High and Low Temperature Studies of Nitrogen Atoms and Singlet Molecular Oxygen

by

Andrew P. Billington, B.Sc., G.R.S.C.

This thesis is submitted to the University of Keele in partial fulfilment of the requirements for the degree of Doctor of Philosphy.

Department of
Chemistry

May 1987

TEXT BOUND CLOSE TO THE SPINE IN THE ORIGINAL THESIS

PAGE NUMBERS ARE CUT OFF IN THE ORIGINAL

The work reported in this thesis was carried out by the author under the supervision of Dr. Peter Borrell. The experimental results in Chapter Eleven were obtained in collaboration with Prof. Nathan Rich, who assisted in recording the spectra. All other work was performed and analysed by the author.

To my parents

Acknowledgements

In presenting this thesis, I would like to thank the following people:

Dr. Peter Borrell for his supervision during the course of this work.

My fellow workers, Dr. Patricia Borrell, Dr. Don Richards, Dr. Andrew Hopkirk and Prof. Nathan Rich, for many helpful conversations.

To my father, Mr. Roy Billington, and his friend Terry Lampard, for their patience, excellent typing and graphic work.

Carole Moch, for patiently reading the text.

The technical staff of the department, in particular Chris Cork, John Wilcox, Ralph Pattison, David Ollivant and Richard Goodwin.

The University of Keele for the award of a studentship.

Last but by no means least Julie Smith, for getting me to put pen to paper.

ABSTRACT

This thesis describes some kinetic and spectroscopic studies of nitrogen atoms and singlet molecular oxygen. These studies were undertaken by observing the emissions in a discharge flow/shock and discharge flow apparatus respectively.

The relative emissivities, $K_{(T)}$, for four transitions in the first positive band system of N_2 have been measured in the temperature range 300 to 1600K. The results were fitted to the expressions:

1 $\log(K_{(T)}) = 3.42 - 1.38 \log(T/K)$ 579 nm
2 $\log(K_{(T)}) = 3.95 - 1.60 \log(T/K)$ 576 nm
3 $\log(K_{(T)}) = 1.61 - 0.64 \log(T/K)$ 586 nm
4 $\log(K_{(T)}) = 3.09 - 1.25 \log(T/K)$ 661 nm

The variation of these emissions with the temperature has been interpreted in terms of the Thrush mechanism modified to include the $N_2(W^3\Delta_u)$state.

The rate constant for the reaction of nitrogen atoms with O_2, has been determined between 300 and 1500K by studying the variation of the first positive and NO(β) emission bands with the time in a mixture of N_2 and O_2.

The rate constant was found to increase with the temperature and was fitted to the Arrhenius equation:

$$k_5/dm^3mol^{-1}s^{-1} = (5\pm0.2) \times 10^9 \exp -(3103\pm310/T)$$

The data has been compared to previous studies and has been considered in terms of doublet/quartet energy surfaces.

The rate constant, k_d^m, for the quenching of $O_2(a^1\Delta_g)$ by m, m = O_2, H_2, D_2, has been measured between 100 and 440K by observing changes in the emissions at 634, 703 and 762 nm with time.

The rate constants increase with the temperature and $k_d^{O_2}$ can be fitted to the Arrhenius equation:

$$k_d^{O_2}/dm^3mol^{-1}s^{-1} = (1896 \pm 65) \exp -(205 \pm 8/T): 100 \text{ to } 440K$$

The quenching rate constant $k_d^{O_2}$ has been examined in terms of the Shin-Maier theory.

The temperature dependence of two simultaneous transitions (634 and 703 nm) has been determined between 100 and 300K. The emissivity is virtually independent of the temperature in this range.

CONTENTS

CHAPTER ONE

1.0 Introduction.

1.1 Structure and Background of the Thesis.

The purpose of the work described in this thesis was to study, over as wide a temperature range as possible, the temperature dependence of several elementary chemical and energy transfer reactions. This thesis is divided into two sections. The first is concerned with a study of nitrogen atom recombination using a combined discharge flow-shock tube. The second describes the temperature dependence of the quenching of singlet molecular oxygen, $O_2(a^1\Delta_g)$ (v=o), by using a variable temperature discharge flow tube.

Nitrogen atom recombination reactions were studied as part of the continued development of the discharge flow shock tube. Previous studies have been concerned with energy transfer reactions, this technique was therefore developed to include reactive species.

Initially, the chemiluminescent reactions of nitrogen atoms were studied since it is intended to use these to measure the concentration of nitrogen atoms. The concentration was followed by measuring the intensity of the resultant Lewis Rayleigh afterglow. Four emissions have been examined (Chapter Six), their relative emissivities were determined between 300 and 1600K. The $N+O_2$ reaction has also been studied. This is a natural extension of the work given in Chapter Six, and is also of considerable interest in high temperature combustion chemistry. The aim of this work was to measure the reaction rate constant over a large temperature range (300-1500K). From these measurements, a comparison with previous determinations could be made, and the quality of the data obtained by the method, for reactions involving reactive species, assessed (Chapter Seven).

A new variable temperature discharge flow tube was constructed in order to study reactions between 100 and 440K (Chapter Nine).

The collisional deactivation of $O_2(a^1\Delta_g)$ (v=o), an example of electronic energy transfer, has been studied using this apparatus to complement work that has been conducted at high temperature. In this study, the collision partners O_2, H_2 and D_2 were used (Chapter Ten).

A study of the temperature dependence of the emissivity for two 'dimol' emissions, from singlet molecular oxygen, has also been made (Chapter Eleven). This provides additional data to work already conducted at both high and low temperature.

There is no simple qualitative model that can be used to describe either recombination or electronic energy transfer reactions. The energy involved in these processes can be converted into vibrational, translational or rotational energy components. The temperature dependence of the reaction rate can follow the exponential (Arrhenius), $T^{\frac{1}{2}}$ (collisional) or $T^{-\frac{1}{2}}$ (vibrational relaxation) forms.

This chapter gives the foundations for some of the theories that are commonly applied to chemical reactions.

1.2 The Temperature Dependence of Chemical Reaction Rates.

The study of the temperature dependence of a chemical reaction provides information as to the nature of the process. Several models are available to describe how the rate constant will vary with the temperature.

1. The Arrhenius Equation.

For the vast majority of reactions, the rate constant increases with the temperature. A convenient way of displaying the temperature dependence for bimolecular reactions is the Arrhenius equation [1, 2, 3];

$$k_{(T)} = A.\exp -(E_{(a)}/RT) \qquad (1.1)$$

where $k_{(T)}$ is the rate constant for the reaction, A is the pre exponential factor and $E_{(a)}$ is the activation energy. The term $\exp -(E_{(a)}/RT)$ gives the proportion of molecules with sufficient energy for the reaction to occur. The quantities A and $E_{(a)}$ are determined experimentally. The equation (1.1) suggests that both of these are temperature independent. It is therefore only an approximation, and over small temperature ranges, 'near-Arrhenius' behaviour can be observed. [4].

2. Simple Collision Theory.

This theory views atoms as 'hard spheres' which collide with one another and, in the process, exchange energy. The rate constant, $k_{(T)}$, is given in terms of the collision cross-section, σ_{AB}, and temperature, T, by the expression:

$$k_{(T)} = \sigma_{AB}(8k_B T/\pi\mu)^{1/2}\exp -(E_{min}/RT) \qquad (1.2)$$

Here, E_{min} represents the minimum energy barrier that must be overcome for the reaction to proceed, μ is the reduced mass, k_B, the Boltzmann and R the universal gas constants.

The equation is qualitatively equivalent to (1.1), except now the pre-exponential factor has a $T^{\frac{1}{2}}$ collisional dependance. If the energy barrier restriction is removed ($E_{min} = O$) then (1.2) reduces to;

$$k_{(T)} = \sigma_{(AB)} C . T^{\frac{1}{2}} \qquad (1.3)$$

where $C = (8 k_B / \pi \mu)^{\frac{1}{2}}$ (1.3 (a))

The disadvantages of this theory are many fold. Steric effects, energy contributions from vibrational and rotational degrees of freedom must be neglected, and the minimum energy cannot be determined independently. Furthermore, the collision cross section must be approximated, since its exact variation with the experimental conditions is difficult to assess [5, 6].

3. Activated Complex Theory

This theory pictures the reaction between two species A and B proceeding by the formation of an activated complex, $AB^{\ddagger}$, a transient with one degree of freedom locked by the interaction [2, 7]. The notion that an activation energy (eqn. 1.1) is extended by assuming a state of equilibrium exists between the reactants and the activated complex. The transient decomposes into the products at a rate $k_{(T)}$, the energy changes that take place are given in figure 1.1 .

In order to find the rate of reaction, several parameters must be known [2]:

(a) The Rate of Passage Through the Transition State.

It is assumed that the distortion which leads to the formation of the products is the vibrational distortion. The frequency of vibration is thus the frequency of passage through the transition state.

Figure 1.1 Formation of an activated complex AB*.

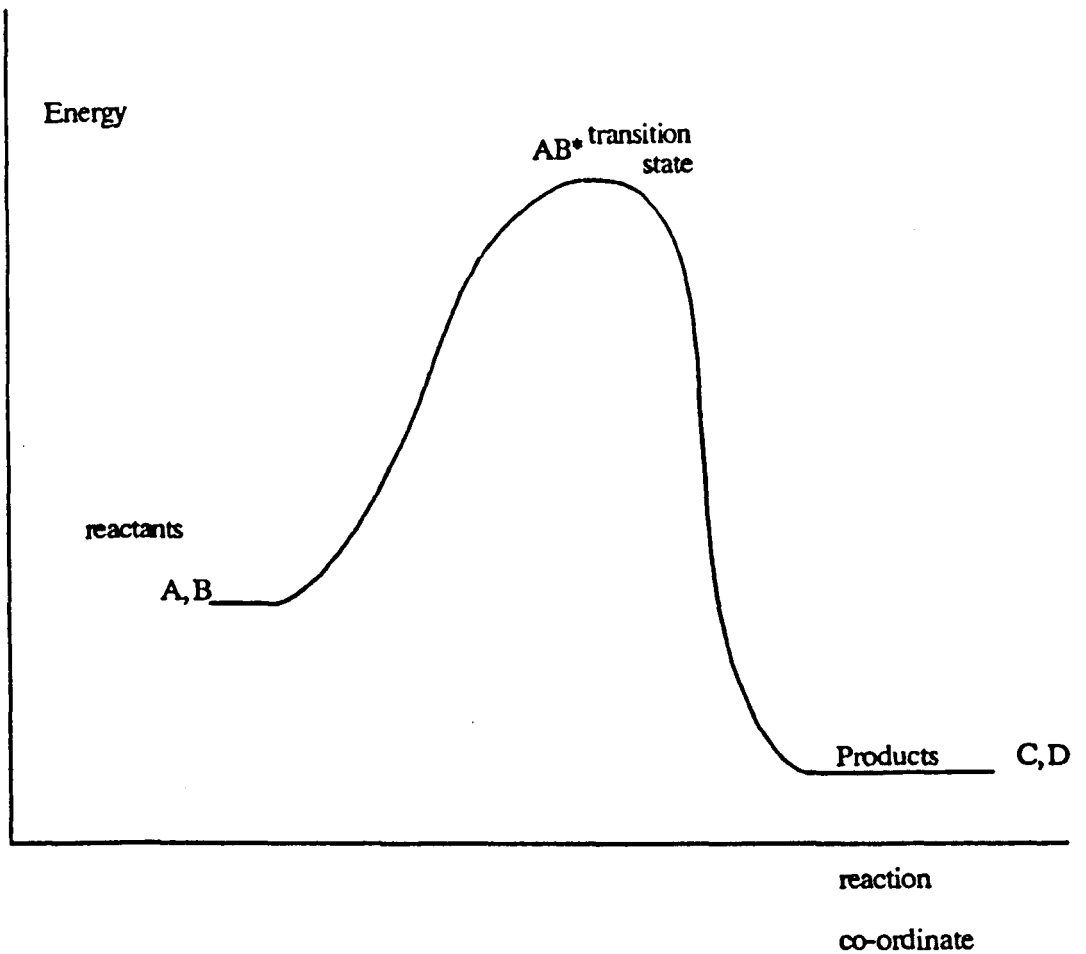

(b) The Concept of an Activated Complex

The state of equilibrium between the reactants and activated complex allows a thermodynamic treatment. The expression for $k_{(T)}$ is given by;

$$k_{(T)} = (k_B T/h) \left(\frac{Q^{\ddagger}_{AB}}{Q_A Q_B}\right) \exp -(E^{\ddagger}/RT) \qquad (1.4)$$

where $Q^{\ddagger}_{AB}$ is the total partition function for the transition state, Q_A and Q_B are the partititon functions for the species A and B, and are calculated from the molecular parameters [8]. The quantity $E^{\ddagger}$ represents the energy barrier for the reaction and is calculated from a potential energy surface. By calculation of the partition functions and then assuming $E^{\ddagger}$ is zero, equation (1.4) reduces to an expression equivalent to (1.3).

A predominant feature of activated complex theory is that molecular parameters enter into the pre exponential factor. This theory is therefore better at predicting the form, rather than the magnitude, of the rate constant as a function of temperature.

4. Vibrational Relaxation Theory.

In addition to the above models, there is also a theory that describes the rate of vibrational energy exchange as a function of temperature.

When a gas is heated, for example in a shock tube, the rotational and translational modes in the molecule can absorb the energy within just a few molecular collisions. The vibrational component does not respond so quickly.

Landau and Teller [9] produced a theory for vibrational energy transfer for colinear collisions between diatomic molecules. The theory they developed considers that energy is transferred on the repulsive part of the intermolecular potential well; attractive forces are neglected. This process is described by;

$$P_{10(T)} = B.\exp -(C/T)^{1/3} \qquad (1.5)$$

where $P_{10(T)}$ is the probability for a transition between the v = 1 and v = O vibrational levels, B and C are constants. The relaxation is therefore dependent upon exp $-(C/T)^{1/3}$. In situations where there is low temperature, intramolecular cohesion, or the presence of a permanent dipole moment, this model becomes inaccurate.

Using these theories it is difficult to predict the temperature dependence of the reaction rate. The presence (or absence) of activation energy barriers, or minimum energy requirements, cannot be accurately predicted. For example, Borrell *et al.* [10, 11, 12] have studied the quenching of $O_2(a^1\Delta_g)$ and $O_2(b^1\Sigma_g^+)$ with a variety of quenchers over a wide temperature range. While $O_2(a^1\Delta_g)$ shows an Arrhenius dependence, $O_2(b^1\Sigma_g^+)$ does not.

Since the predictive capabilities of the various theories is still lacking, the necessity to obtain reliable rate constants, as a function of temperature, is therefore justified.

CHAPTER TWO

2.0 Active Nitrogen and the Lewis Rayleigh Afterglow.

2.1 Introduction.

The purpose of the work to be described in Chapter Six, was to use the yellow part of the first positive emission from nitrogen to measure nitrogen atom concentrations. This chapter gives an account of the origins, spectroscopy and of the effect which experimental parameters have on the Lewis Rayleigh afterglow of atomic nitrogen.

The literature that is concerned with the afterglow is extensive; the review given here is largely confined to studies that are relevant to the work reported in Chapters Six and Seven.

2.2 The Active Species.

There was considerable discussion for many years as to the origin of the yellow afterglow observed when a discharge is passed through nitrogen. It is now accepted that the observed phenomena result from a number of collision processes that involve nitrogen atoms. However, several other species were proposed: these included the N_2^+ ion and the high vibrational levels of the ($x^1\Sigma_g^+$) and ($a^1\pi_g$) states of the N_2 molecule [13].

In 1952, Benson discharged nitrogen with a microwave cavity and then measured the charge density [14]. He compared the energy liberated by the discharged nitrogen with the recombination energy of the N_2^+ ion. These energy calculations showed that if the 'active component' was the N_2^+ ion, then one part in 10^6 must be in this form. The charge density measurements showed that only one part in 10^8 was charged. The observed phenomena could not be due to an ionic species.

Mass spectroscopy was also used to analyse the products of discharged nitrogen. This showed that the atomic species, ^{14}N, was present and in concentrations greater than one thousand times its value in normal N_2 [15]. Jackson and Schiff [16] and Berkowitz [17] showed that nitrogen atoms were present in concentrations between 0.1 and 1% of the N_2 concentration. Berkowitz was also able to show that the intensity of the visible afterglow was proportional to $[N]^2$.

2.3 Spectral Features of the Afterglow.

The transitions that can be observed in the afterglow of active nitrogen are given in fig. 2.1 .

The principal feature of the afterglow is the 'first positive' (1+) emission band system, part of which lies in the visible region (500-700 nm). This was first spectroscopically assigned by Mitra (1945), and is the yellow chemiluminescence that can be observed in a low pressure discharge of N_2. Kurzweg and Broida [18] and Bayes and Kistiakowsky [19] have studied the emission in detail in the visible and near infra red regions of the spectrum respectively. A typical intensity distribution of the bands in the visible afterglow spectrum is in fig. 2.2(a). Plotted in fig. 2.2(b) is the intensity distribution for the first positive bands in an ordinary discharge of nitrogen. From these it is seen that the majority of the visible (1+) emission arises from the $N_2(B^3\pi_g)$ molecule at the vibrational levels v_B=12,11,10 and v_B=7,6,5.

Figure 2.1 Simplified energy diagram of N_2 showing the energy levels and radiative transitions in the afterglow of atomic nitrogen

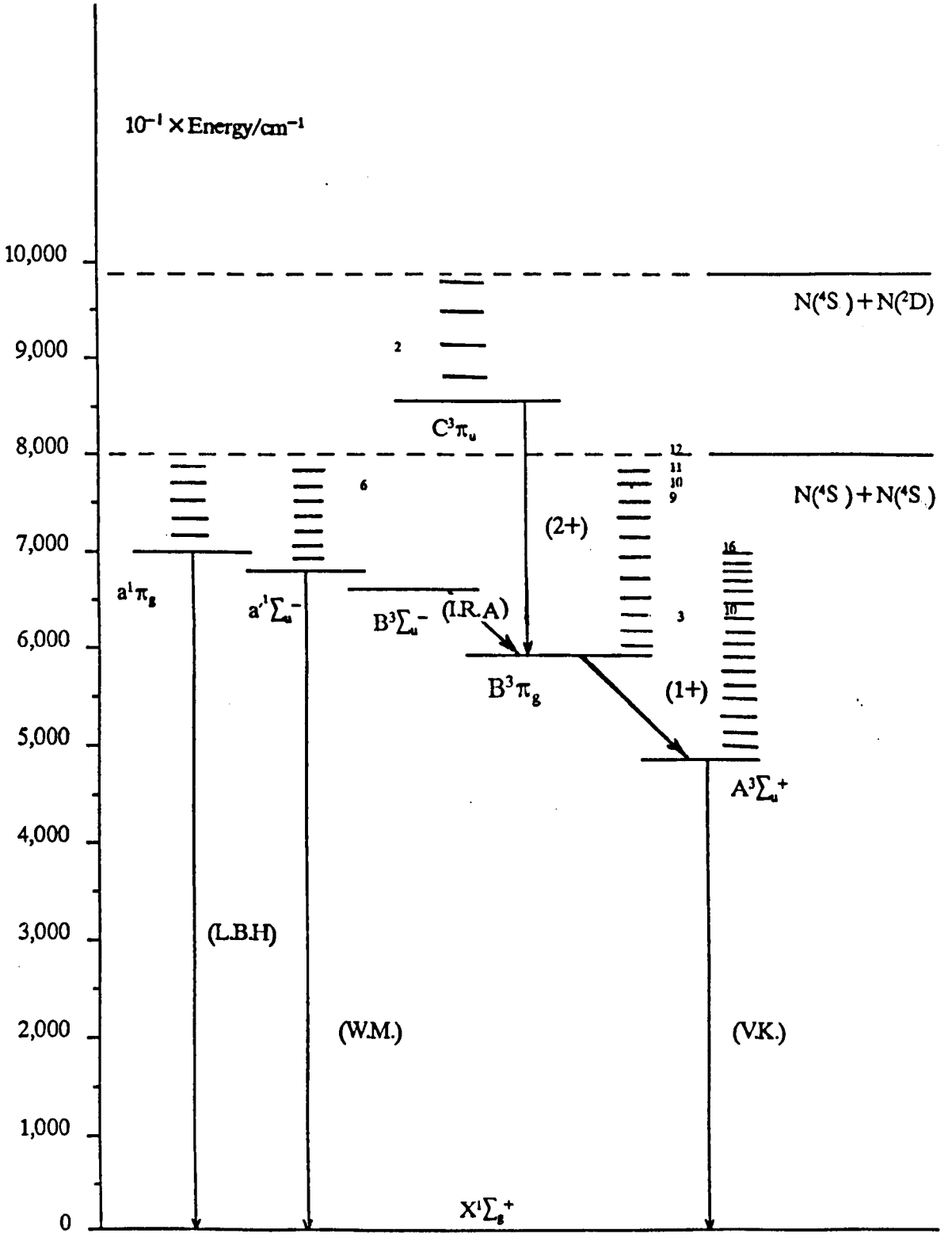

Figure 2.2 The intensity distribution of the (1+) positive band system

Figure 2.2(a)

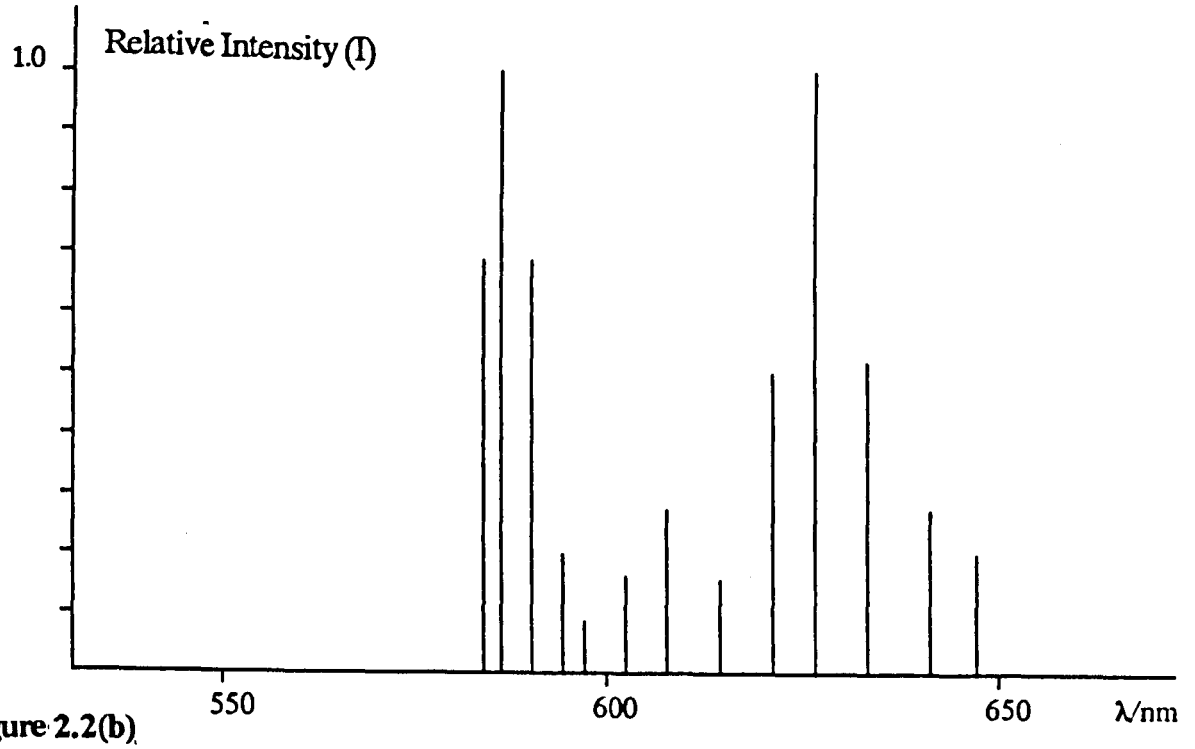

Figure 2.2(b)

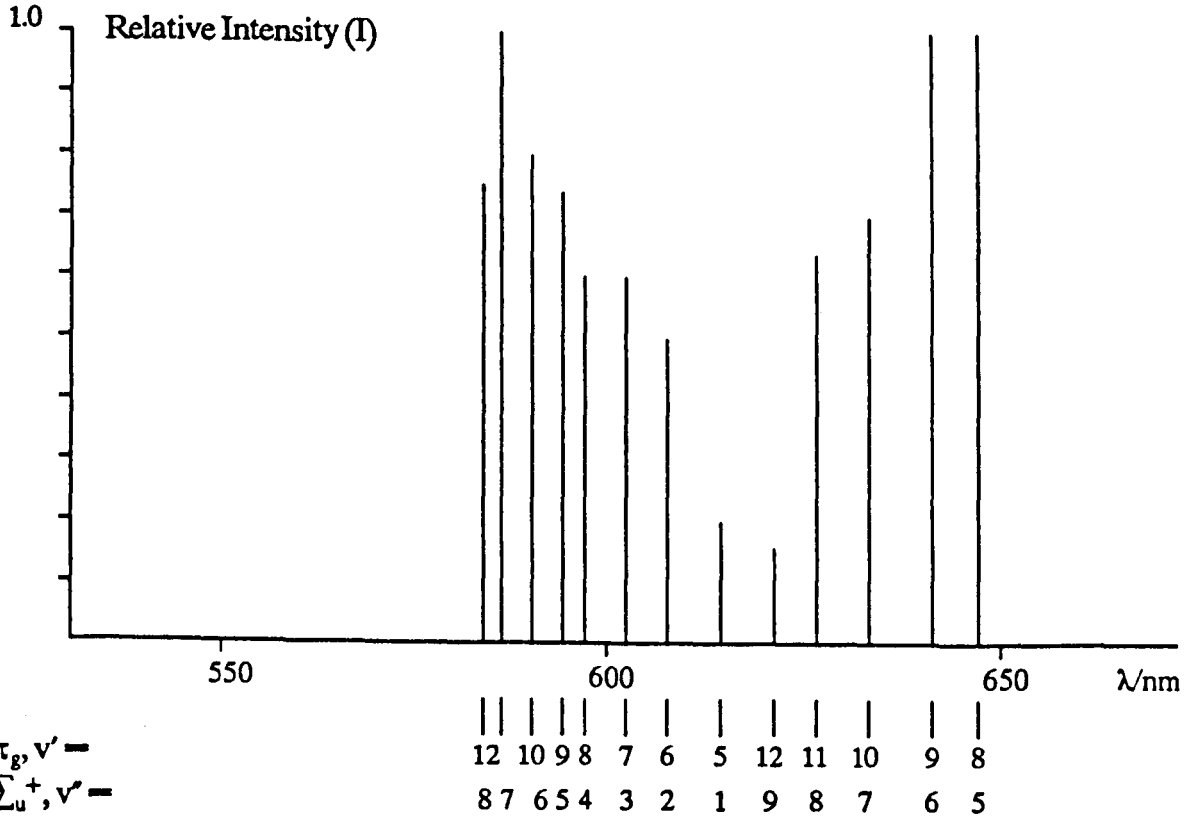

In low pressure discharges (a few torr), at room temperature, several other band systems can be detected (fig. 2.1). They are the infra red afterglow (I.R.A), $N_2(B'^3\Sigma_u^-)$ — $N_2(B^3\pi_g)$ (700-1,100 nm), Wilson-Mulliken-ultraviolet (W.M), $N_2(a'^1\Sigma_u^-)$ — $N_2(x\,^1\Sigma_g^+)$(150-190 nm), and the Lyman-Birge Hopfield (L.B.H), $N_2(a^1\pi_g)$ — $N_2(x\,^1\Sigma_g^+)$ (145-185 nm), emission band systems of N_2. The Vergard Kaplan (V.K), $N_2(A\,^3\Sigma_u^+)$ — $N_2(x\,^1\Sigma_g^+)$ (250-450 nm), and second positive (2+), $N_2(c^3\pi_u)$ — $N_2(B^3\pi_g)$(295-338 nm), systems can be detected in higher pressure and lower temperature discharges respectively.

2.4 The Effect of Pressure and Temperature on the First Positive Band System of N_2.

In the earliest studies, Lord Rayleigh found that when the total pressure was varied between 0.01 and 0.1 torr, the intensity of the (1+) band system was proportional to the pressure [20]. Wentink (1958) also found that the intensity was proportional to the total pressure in the range 0.1-1 torr. Both Campbell and Thrush and Young and Sharpless [21,22] discovered that the first positive emission intensity was independent of the pressure of added N_2, at total pressures above one torr. Furthermore, the intensity was found to be proportional to the square of the nitrogen atom concentration. For the work described in Chapters Six and Seven, measurements were taken in the pressure range 1-8 torr, and the findings of Campbell and Thrush were confirmed.

At room temperature the (1+) emission spectrum consists of a group of bands originating from the vibrational levels, v=12-9, v=7-9 (fig. 2.1) with maxima at v=11 and 6. Upon cooling the maxima sharpen, for the group v=12-9, there is a shift toward the uppermost levels.

Gross, using a discharge flow shock tube [23], has shown that the emission intensity declines as the temperature is increased between 300 and 2000K. Campbell and Thrush, using a cooled discharge flow tube, demonstrated that the emission increased as the temperature was lowered in the range 327 to 196K [21]. Thus, there is a variation in the emissivity with the temperature and hence the work described in (Chapter Six).

2.5 The Mechanism of the Afterglow

In order to interpret the results given in Chapters Six and Seven, the changes in emission intensity and spectral distribution of the (1+) band system must be understood. A mechanism that is capable of explaining these is therefore required.

Gaydon proposed that recombination took place by the formation of an intermediate [24]. He suggested that it was the $N_2(^5\Sigma_g^+)$ state (fig. 2.3), which is shallow bound and correlates to the ground state nitrogen atoms. It was thought that this state crosses over to form the $N_2(B^3\pi_g)$ state at the v = 12 level, and so gives the origin of the first positive band system (fig. 2.1). The $N_2(B^3\pi_g)$ state is therefore the product of the inverse predissociation and is thought to result from the two body interaction:

$$N(^4S) + N(^4S) \xrightarrow{^5\Sigma_g^+} N_2(B^3\pi_g)\,(v = 12,11,10) \qquad (2.5)$$

$$N_2(B^3\pi_g)\,(v \doteq 11) \longrightarrow N_2(A^3\Sigma_u^+)\,(v \doteq 7) + h\nu \qquad (2.6)$$

Benson suggested that there is a high transition probability for the predissociation $N_2(B^3\pi_g) \rightleftharpoons N_2(^5\Sigma_g^+)$, and so the mechanism would not require a third body for the reaction to proceed [25]. The high rotational levels of the $N_2(B^3\pi_g)$ (v = 12) state undergo collision induced relaxation to the lower vibrational levels which would explain the observed population.

Berkowitz modified the previous mechanism to include a third body to stabilise the $N_2(^5\Sigma_g^+)$ molecule [17]. A collision induced transition converts the $N_2(^5\Sigma_g^+)$ into the $N_2(B^3\pi_g)$ state in the vibrational levels v = 12, 11, and 10:

$$N(^4S) + N(^4S) + M \rightleftharpoons N_2(^5\Sigma_u^+) + M \qquad (2.7)$$

$$N_2(^5\Sigma_g^+) + M \rightleftharpoons N_2(B^3\pi_g, v=12,11,10) + M \qquad (2.7(a))$$

As the temperature is reduced, there would be less collisions energetically capable of dissociating the $N_2(^5\Sigma_g^+)$ state, and the observed intensity variation with the temperature could be understood. Furthermore at reduced temperatures the collisions are less capable of removing energy from the higher vibrational levels [26]. The shift of the intensity distribution toward the higher vibrational levels at low temperature is now explicable.

Figure 2.3 Molecular energy states of nitrogen molecules

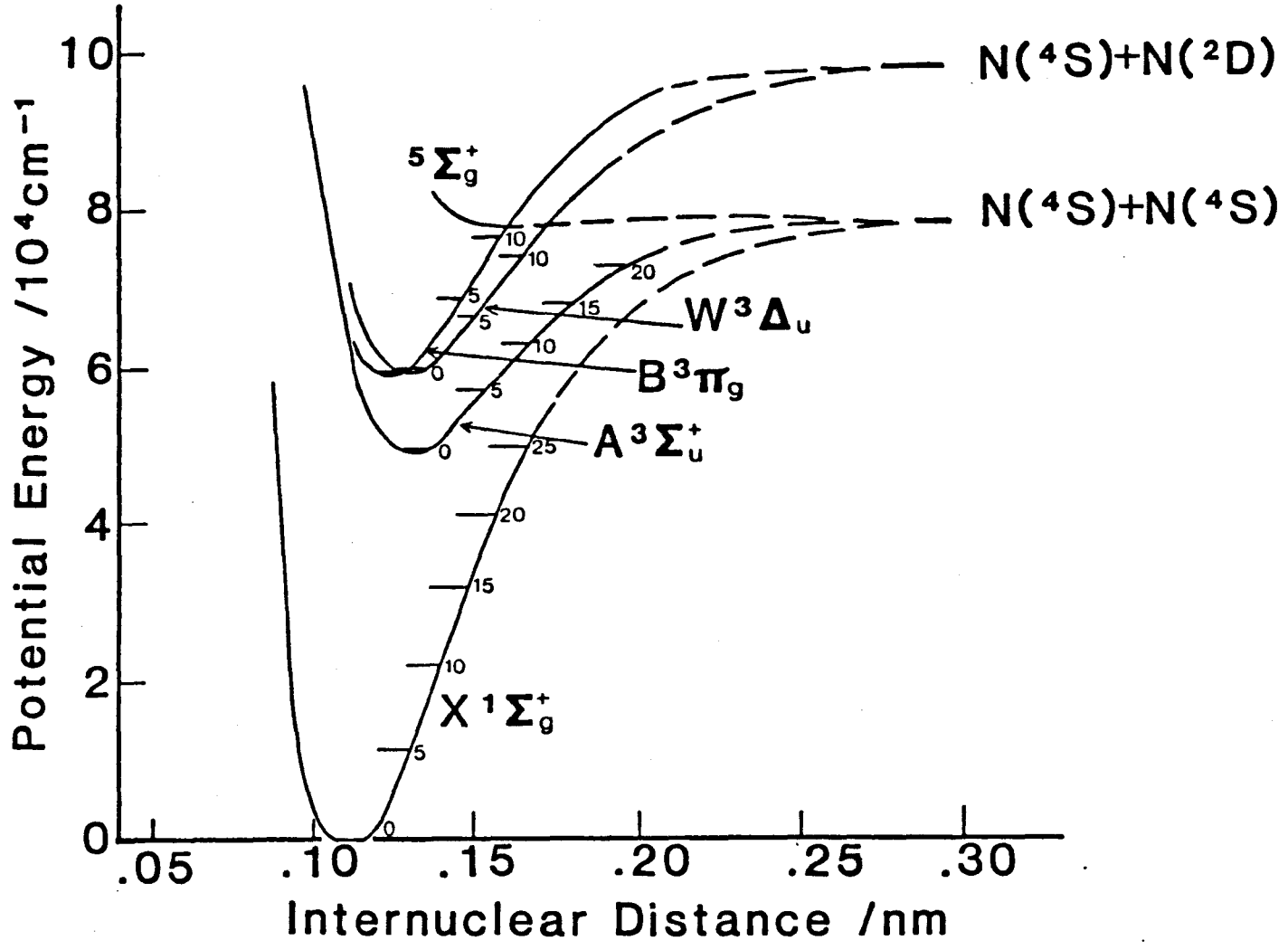

Campbell and Thrush preferred another precursor for the $N_2(B^3\pi_g)$ state [21]; they pointed out that the shallow bound $N_2(^5\Sigma_g^+)$ state could not exist in high enough concentrations to acount for the observed $N_2(B^3\pi_g)$ populations (Chapter Six). Their mechanism is written:

$$N(^4S) + N(^4S) + M \rightleftharpoons N_2(A^3\Sigma_u^+)(v = \text{high}) + M \qquad (2.8)$$

$$N_2(A^3\Sigma_u^+)(v = \text{high}) + M \longrightarrow N_2(A^3\Sigma_u^+)(v = \text{low}) + M \qquad (2.9)$$

$$N_2(A^3\Sigma_u^+)(v = \text{high}) + M \rightleftharpoons N_2(B^3\pi_g)(v = 12,11,10) + M \qquad (2.10)$$

In this scheme, the emission distribution at low temperature is again explained in terms of reduced collisional dissociation. The intensity distribution of the afterglow (fig. 2.2) is complex. This results from the range of energies that can be produced in the newly formed $N_2(A^3\Sigma_u^+)$ state. This model is capable of providing an explanation for the population of the $v = 12, 11, 10$ and 6 levels of $N_2(B^3\pi_g)$, the lowest level is formed by a feeding process from the $N_2(A^3\Sigma_u^+)$ $(v = 16)$ state. Recent work has indicated that there is ready interconversion between the $N_2(B^3\pi_g)$ and the $N_2(W^3\Delta_u)$ states (fig. 2.3). In interpreting the results give in Chapter Six, the Thrush mechanism has been used but it has been modified to include the $N_2(W^3\Delta_u)$ state.

CHAPTER THREE

3.0 Experimental: The Discharge Flow Shock Tube

3.1 Introduction

In this chapter, a description of the discharge flow shock tube is given together with detailed accounts of the flow/shock facilities of the apparatus, the detection equipment and purfication and control systems. The procedure for setting up the apparatus and a safety appraisal are also presented.

3.2 The Combined Discharge Flow Shock Tube Apparatus

The measurements were made by generating nitrogen atoms with a microwave discharge, passing them through a combined discharge flow/shock tube apparatus, and studying the light emission along the tube.

Figure 3.1 shows the apparatus, which consists of a discharge flow tube, with which pre-shock measurements can be taken, modified so that a shock wave can be propagated along its length in order to take post shock measurements at high temperature.

This experimental method has several advantages over other techniques. The species are produced by discharge, and are therefore not shock dependent for their production. The temperature range attainable is between 300-1700 K, and exceeds that obtained by jacketed discharge flow tubes.

3.3 The Discharge Flow System

Discharge flow apparatus have been used extensively for a wide range of kinetic and spectroscopic studies [27]. Due to their relative simplicity, they have remained popular as an experimental technique, despite having been used for over half a century.

The principle behind the discharge flow apparatus is simple — the desired transient species are produced by discharge, and passed into a tube. The flow along the tube sets up a variation in concentation that is spatially rather than time dependent [27]. The concentration of the species is then examined as a function of distance; the time taken for the gas to flow along the tube can be calculated, and so the concentration time relationship for the species can be deduced.

The system used in this part of the thesis is given in figure 3.2 .

Nitrogen atoms are produced by passing purified nitrogen through a microwave discharge, which consists of a microwave cavity (E.M.S. 214L) surrounding an air cooled quartz discharge tube. The cavity is supplied by a Microtron 200 power source, working at 2450 MHz, with an output between 40 and 200 W. The assembly is surrounded by a Faraday cage (see section 3.8), and is located 1.8m from the inlet to the flow tube.

Figure 3.1 A schematic diagram of the apparatus

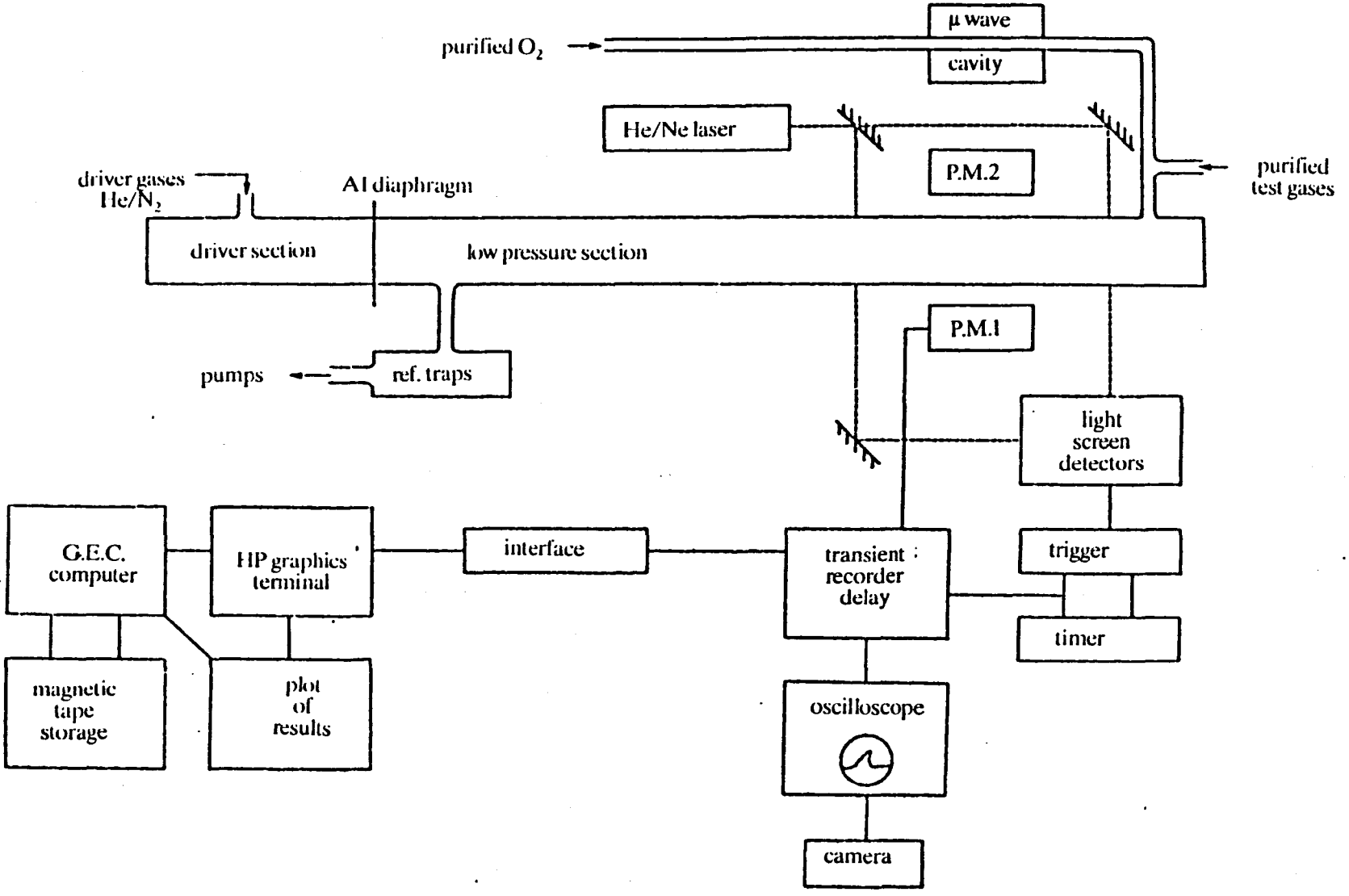

Figure 3.2 The Discharge flow system.

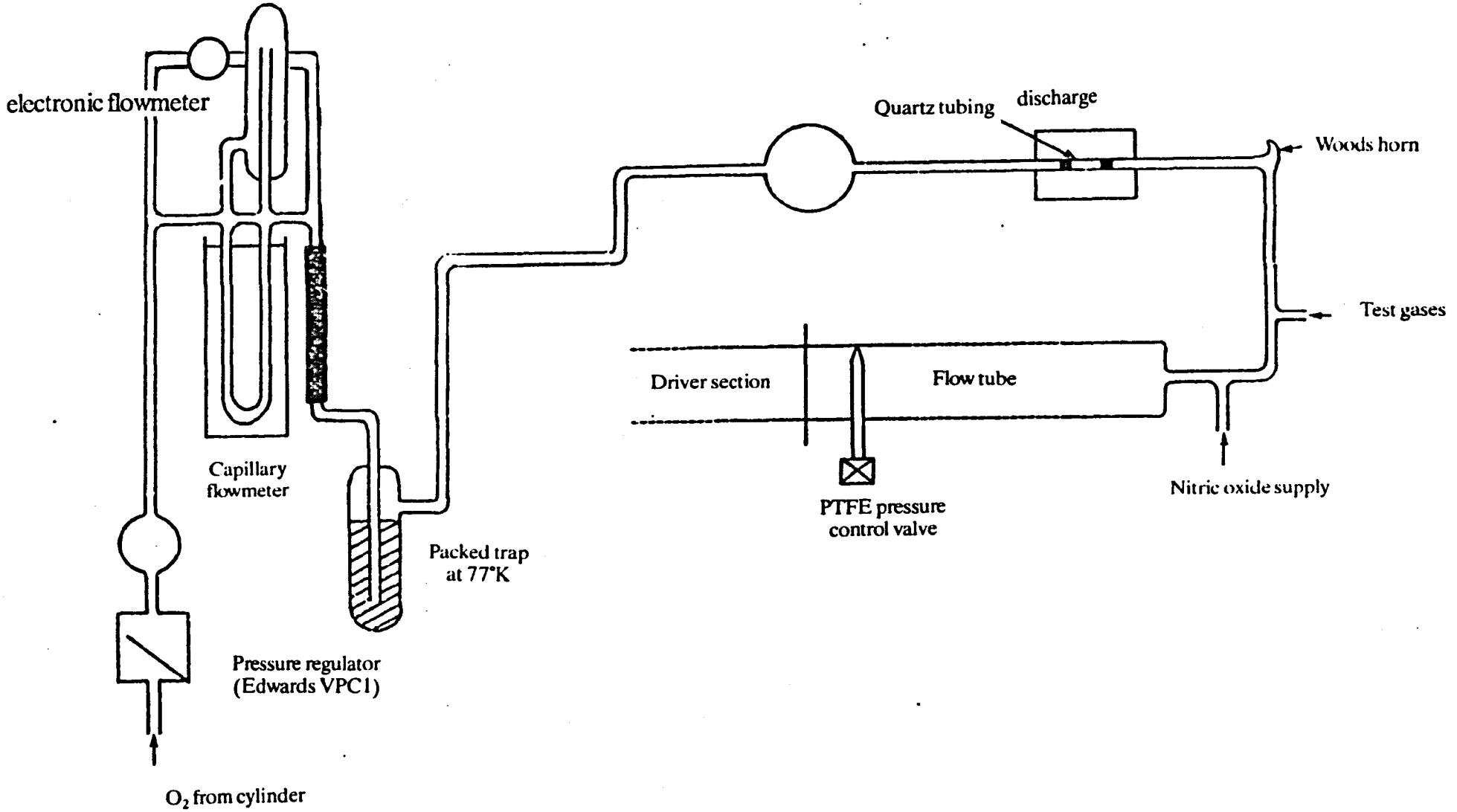

The discharged gas passes into the flow (shock) tube, which consists of a single 5m length of Pyrex glass (i.d=58.8mm). The flow tube and the microwave cavity are pumped by a rotory vacuum pump (Edwards MISC 3000).

The pressure of the flowing test gas can be determined by a diethylpthalate manometer that is continuously pumped (Edwards ED5). The reading is converted to torr by dividing by the density, 1.176×10^3 Kg m^{-3} [28].

The flow rate of the test gas is controlled by use of a needle valve (Edwards); the pressure and hence flow velocity are controlled by using a P.T.F.E. screw valve located at the exit of the flow tube.

3.4 The Shock Tube

The shock tube system used (fig 3.3), consists of a long (5m), straight, uniform tube, divided into two sections by a diaphragm, one, the driver section, made of stainless steel (1.3m long, i.d = 5.8 cm), at a high pressure, the other, the driven section at a relatively low pressure.

A shock wave is generated by bursting a metal diaphragm. This leads to fast expansion of the driver gas as it tries to fill the low pressure driven section. The resultant shock wave moves into the counter flowing test gas, both compressing and heating it [29].

The speed of the shock wave produced, which is determined by the use of laser light screens (section 3.6), can be varied in two ways: either the driver gas composition or the diaphragm thickness (and hence bursting pressure) can be altered to give shock speeds between 0.7 and 1.8 Km s^{-1}. The lower velocity is obtained by using a nitrogen driver with a diaphragm (AL) of thickness 0.051mm. A pure helium driver with the same diaphragm produces a shock wave with a velocity at the upper limit.

Measurements of light intensities are taken, using two photomultipliers, during the time between the arrival of the shock front and contact surface [30]. Observations are made 4.4m from the diaphragm to maximise the observation time without interference from the reflected shock wave [31].

Figure 3.3 The Shock tube.

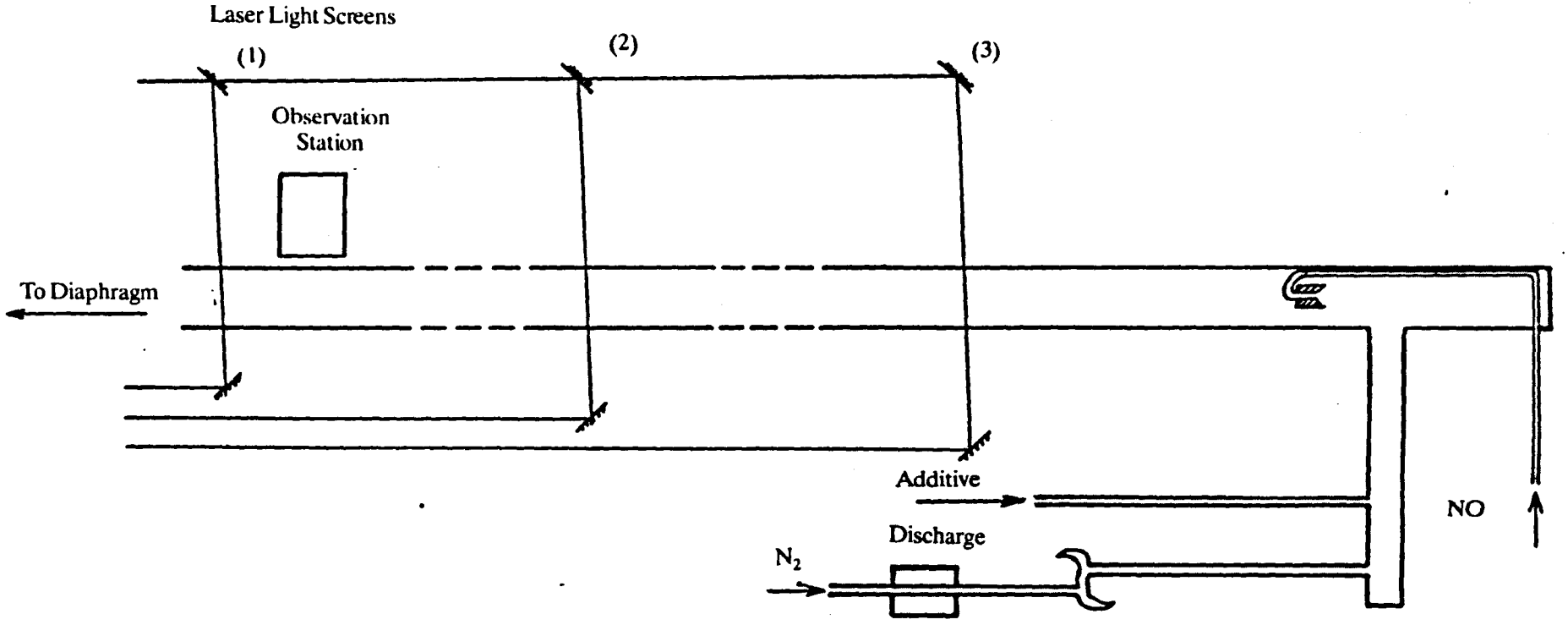

3.5 Purification and Gas Control Systems

The purification and gas handling facilities of the apparatus are divided into two parts, which separately control the main gas flow and additional quencher gas.

The main gas (nitrogen) was taken from a cylinder and regulated by use of a valve (Edwards VPC1), which maintains a constant pressure within the gas reservoir (see fig. 3.2). The gas fills the system up to the control needle valve, which includes the molecular sieve, column and flowmeter.

The gas is dried by use of a molecular sieve (Fisons grade 4a), contained within a glass column (160cm x 1.0cm i.d.) fitted with a heating element and thermometer to enable periodic cleaning.

The flow was monitored by an electronic flowmeter (Brookes 0-2000 ml min^{-1}). The accuracy of this device was checked by comparing it with a capillary flowmeter. The calibration procedure was as follows:

The pressure of a previously evacuated known volume was determined after introducing nitrogen over a measured period of time. The flow rate could be determined since;

$$\text{Flow rate} = V(P_1/P_2)\,t \qquad [3.1]$$

where V = volume of the closed system
P_1 = pressure within the system
P_2 = pressure within the gas handling line
t = time.

A calibration for the capillary is given in fig. 3.4 .

The flow rate through the capillary and the flow meter were then compared. The results are presented in (fig. 3.5); the agreement between the flow rates calculated by each device, is good.

Additive gases (e.g. O_2 (Chapter Seven)) were purified and controlled in a similar but separate gas handling line. The flow rate was measured by an electronic flowmeter (Brookes 0-200 ml min^{-1}). This was checked by a capillary flowmeter by

Figure 3.4 Calibration for the Flow Capillary

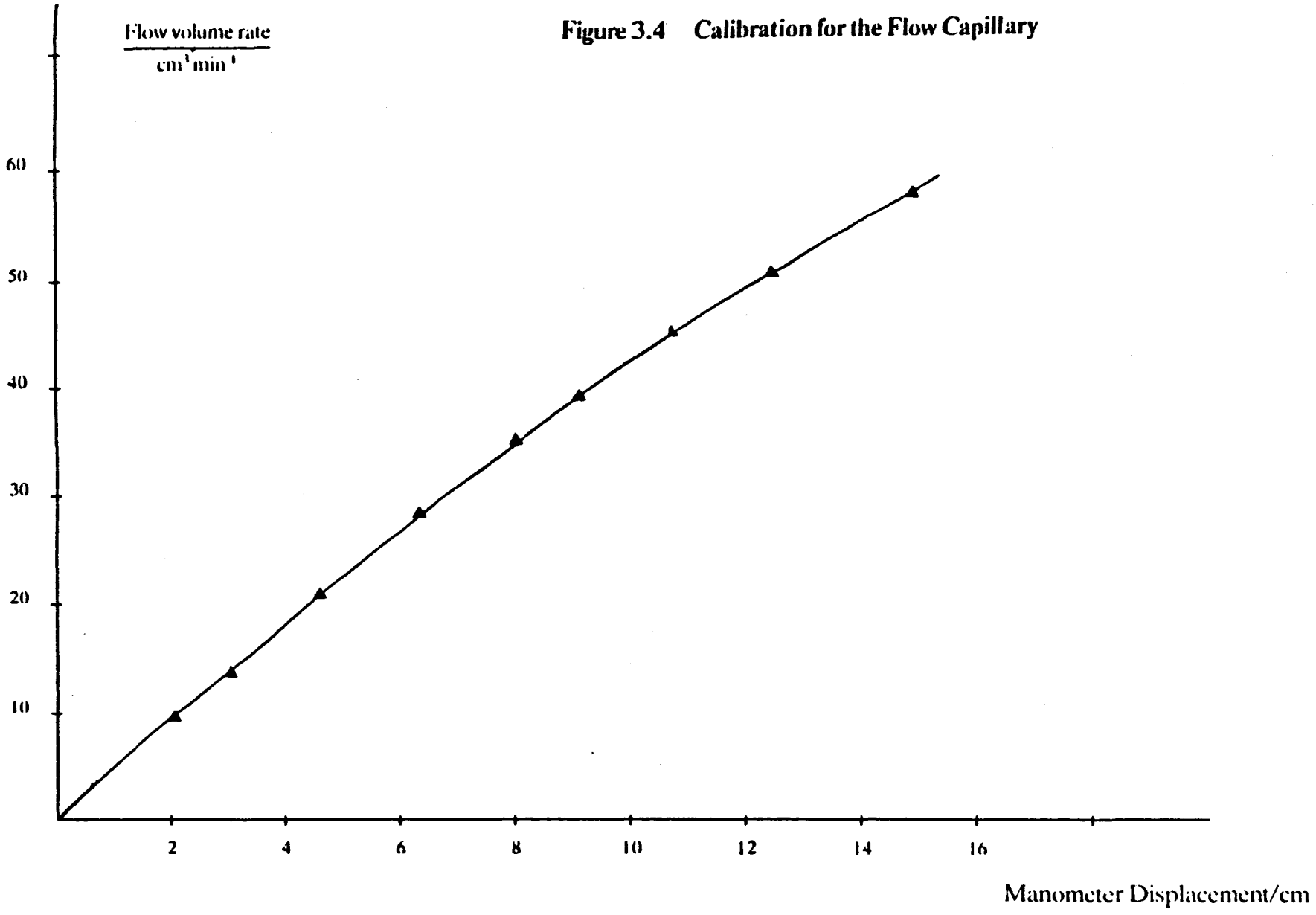

Figure 3.5 Comparison of the Capillary and N_2 Electronic Flowmeter

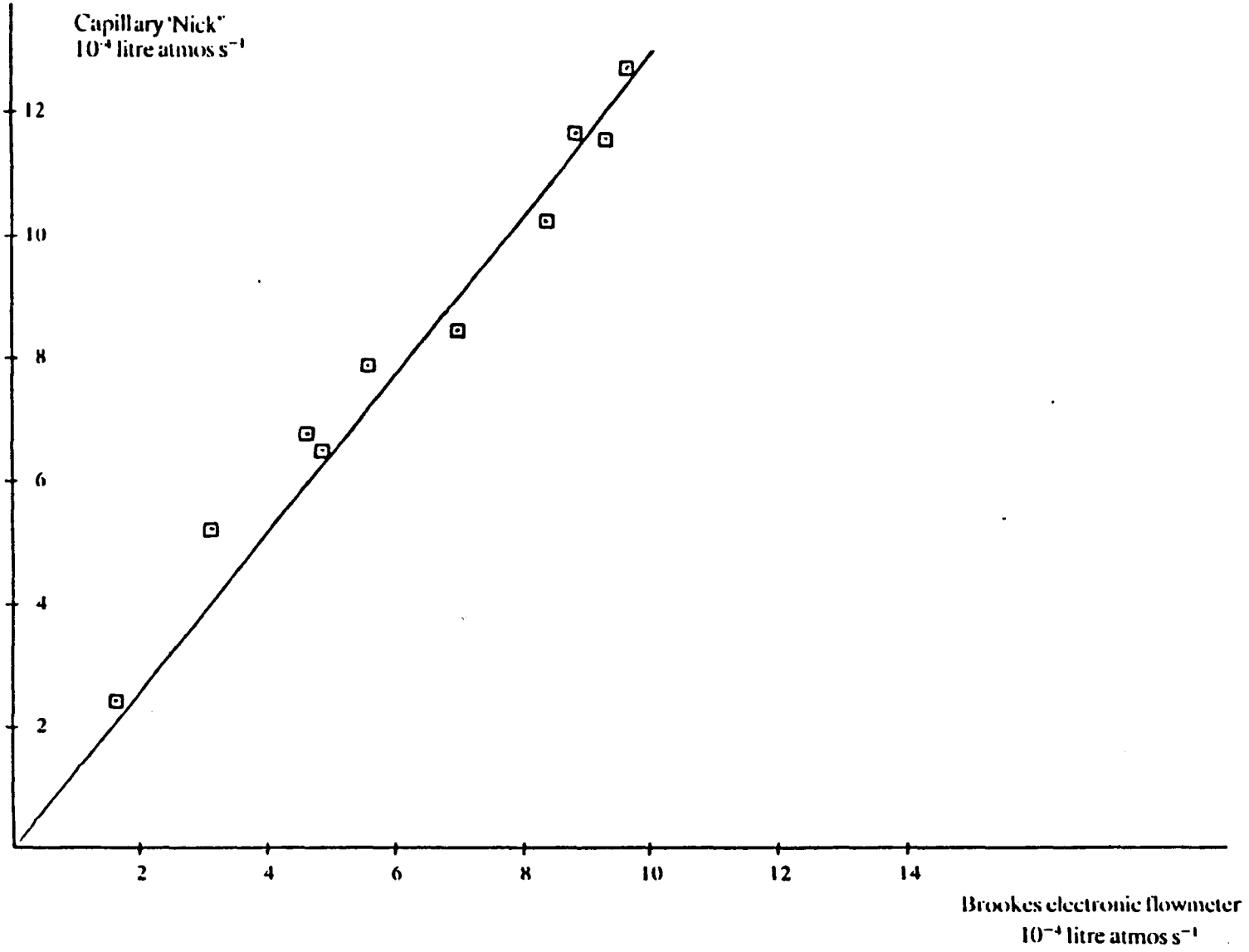

the procedure given previously. The electronic flowmeter was found to measure erroneously, this could be due to earlier measurements using high molecular weight gas additives [28]. A correction for this was constructed since it was used in the experiments described in Chapter Seven. The results are given in figure 3.6 .

Corrosive additives, such as NO, were found to attack the pressure regulator. An alternative regulation system has been used previously and is given in fig. 3.7 . The system consists of a Teflon Sampling bag (All tech associates 41302), connected to a control line by P.T.F.E. tubing. This bag was maintained between ½ and ¾ full, its purpose was to increase gas flow stability.

3.6 The Recording and Detection Equipment

A block diagram of the recording and detection circuit is given in figure 3.8 .

3.6.1 The Detection Components

All of the emissions studied in this work were measured with two photomultipliers (E.M.I 9658 B), which were powered by an E.H.T source (Brandberg 200) at 1300V, and positioned approximately 4.3m from the diaphragm. One was stationary and acted as a reference, the other was mounted on a 2.3m long track, fitted with markers for measuring distances, which ran parallel to the flow tube. The photomultipliers were located within housings to shield them from electrical interference.

The photomultipliers were fitted with either interference filters or with a motor driven monochromator (Bentham BN4) for the work described in Chapter Six. The transmission characteristics of the filters, measured by using a SP8 100 u.v-visible spectrophotometer, are given in figs. 3.9 (a) and 3.9(b) .

A voltage follower was connected to each photomultiplier. The quantum efficiency of the photomultiplier, as a function wavelength [32] is given in figure 3.10 . Both voltage followers (fig 3.11) were, in turn, connected to the transient recorders.

The speed of the shock wave was measured by use of the laser light screens. Two lasers were available for use, the beam from the first was split into two by a semi silvered mirror to make it possible to have three laser beams, and these passed through the tube at an angle of approximately 87° to it. The second beam was 515mm and the

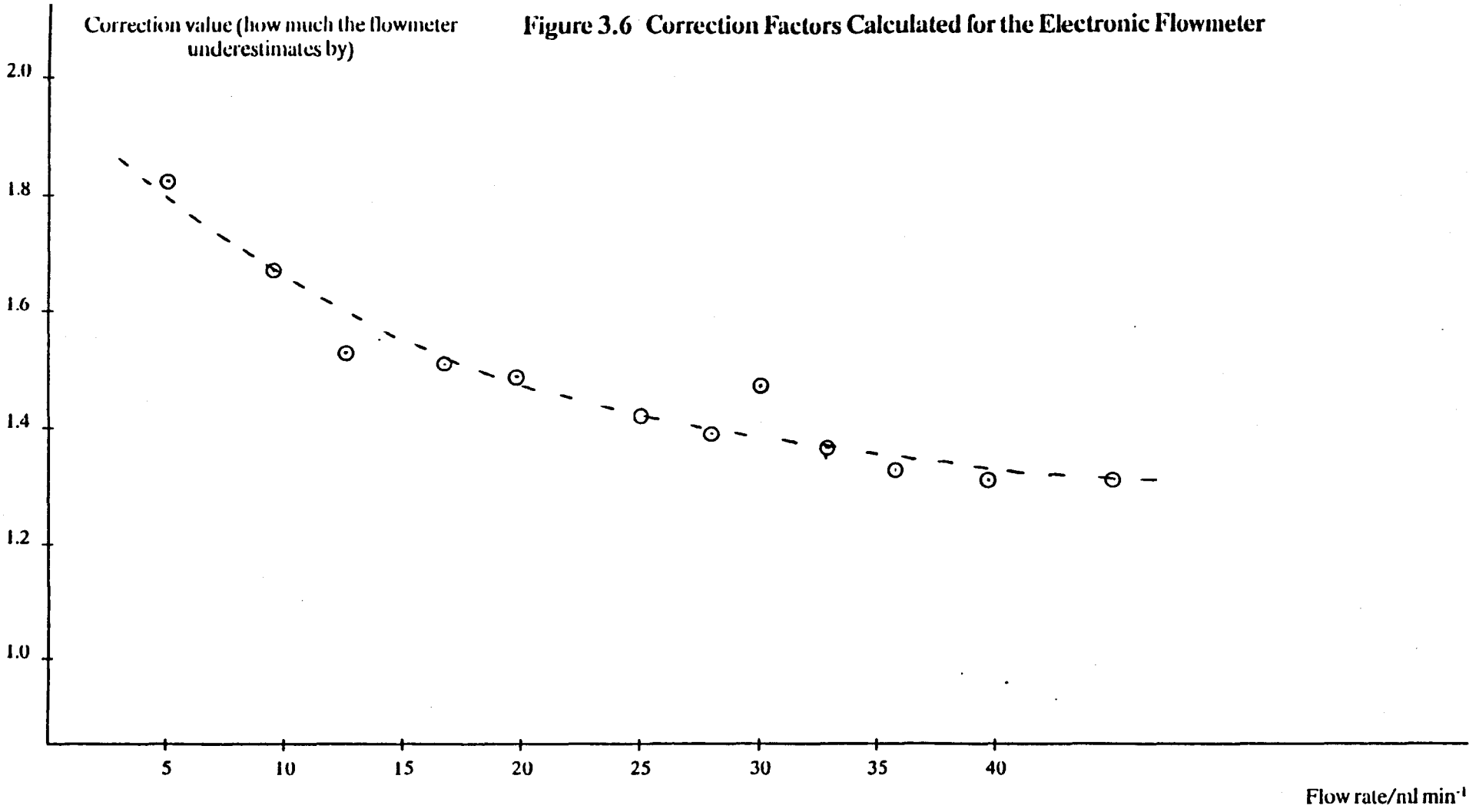

Figure 3.6 Correction Factors Calculated for the Electronic Flowmeter

Figure 3.7 A schematic diagram of the system used to regulate the pressure of corrosive gases

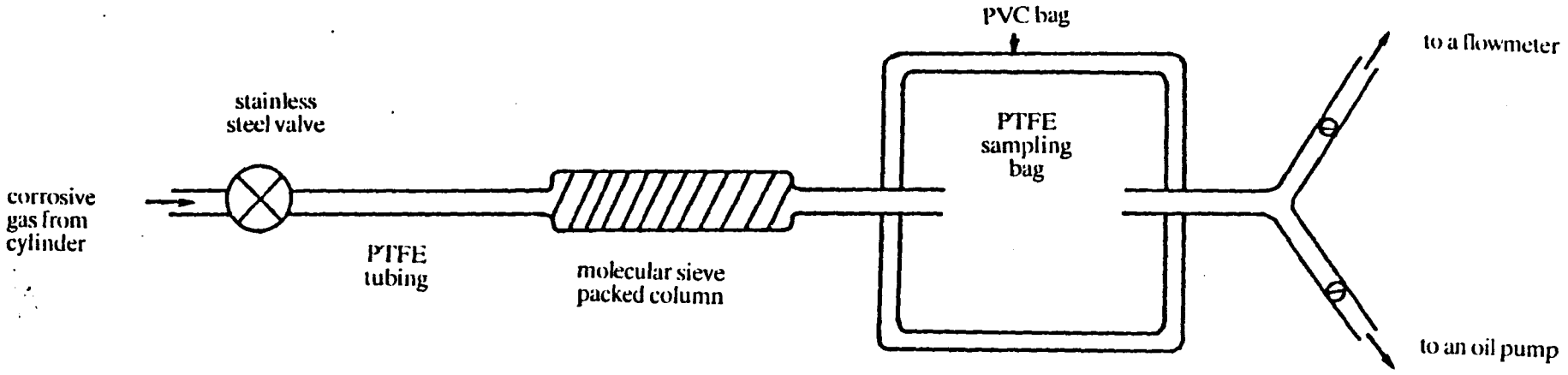

Figure 3.8 Block diagram of the recording and detection circuit

Key: 1, 2, 3; Light screen detectors

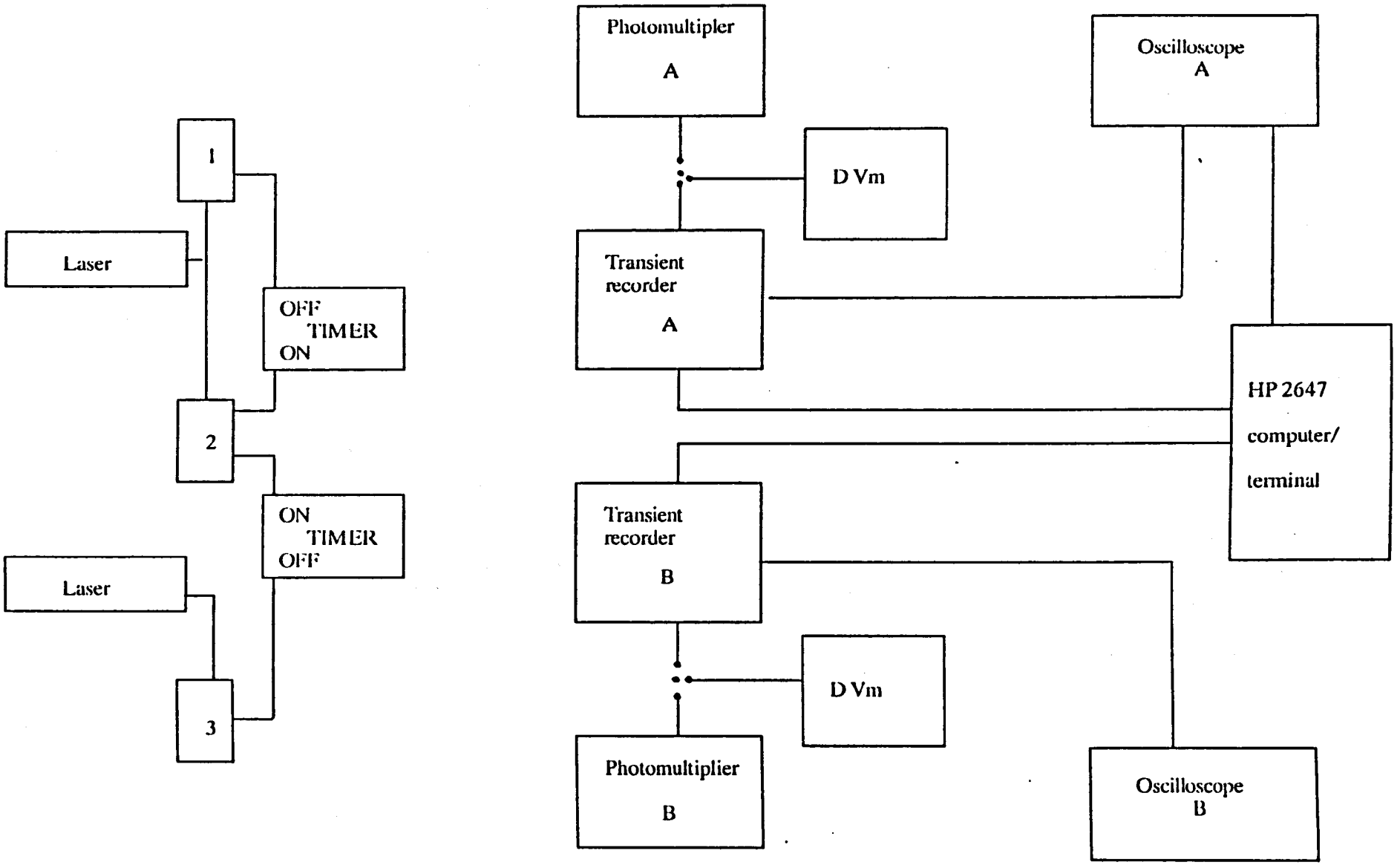

Figure 3.9 Interference Filter Characteristics

a

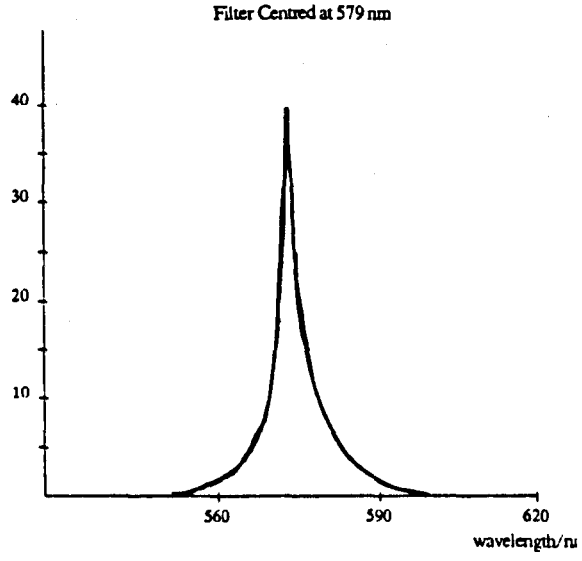

b

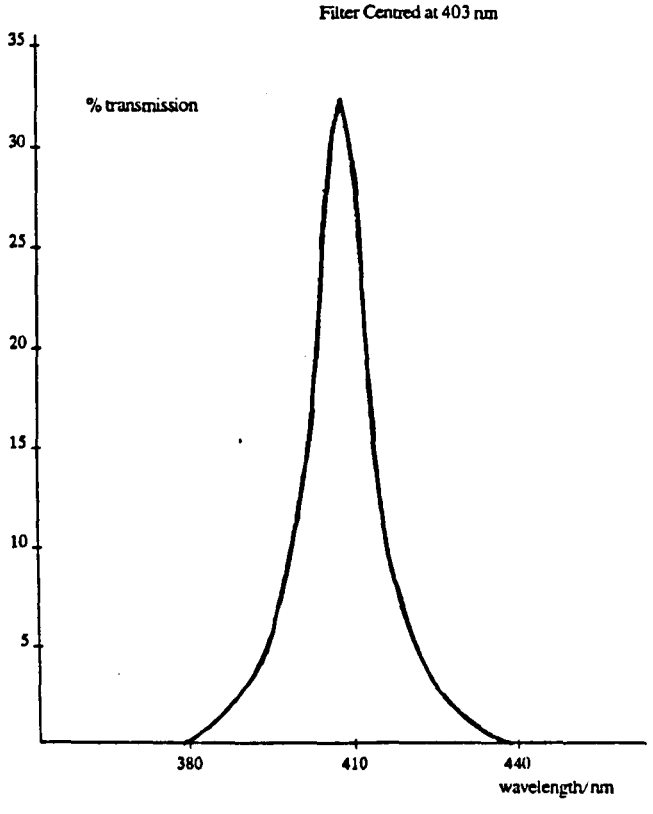

Figure 3.10 Photomultiplier sensitivity as a function of wavelength

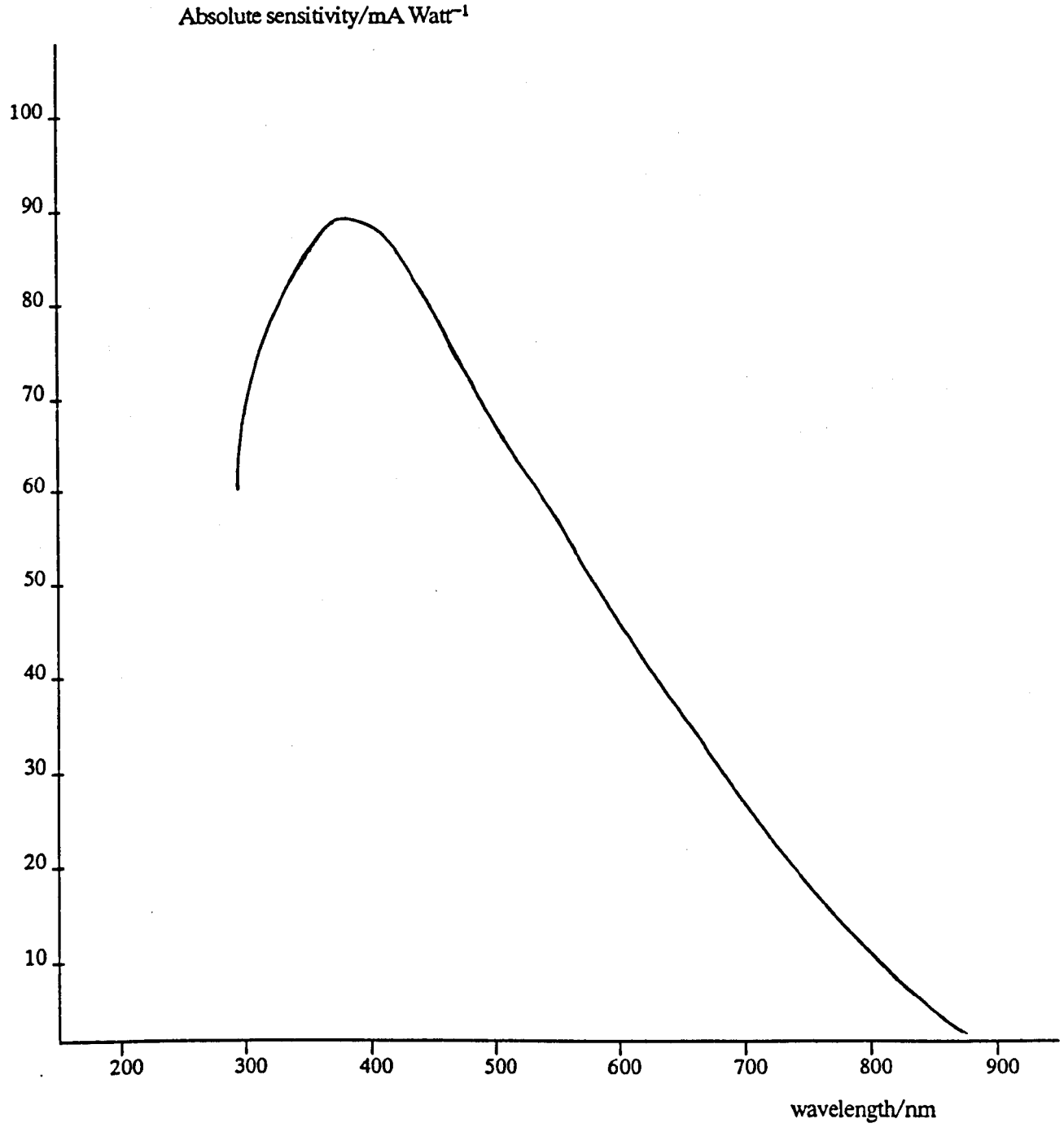

Figure 3.11 The Voltage Follower

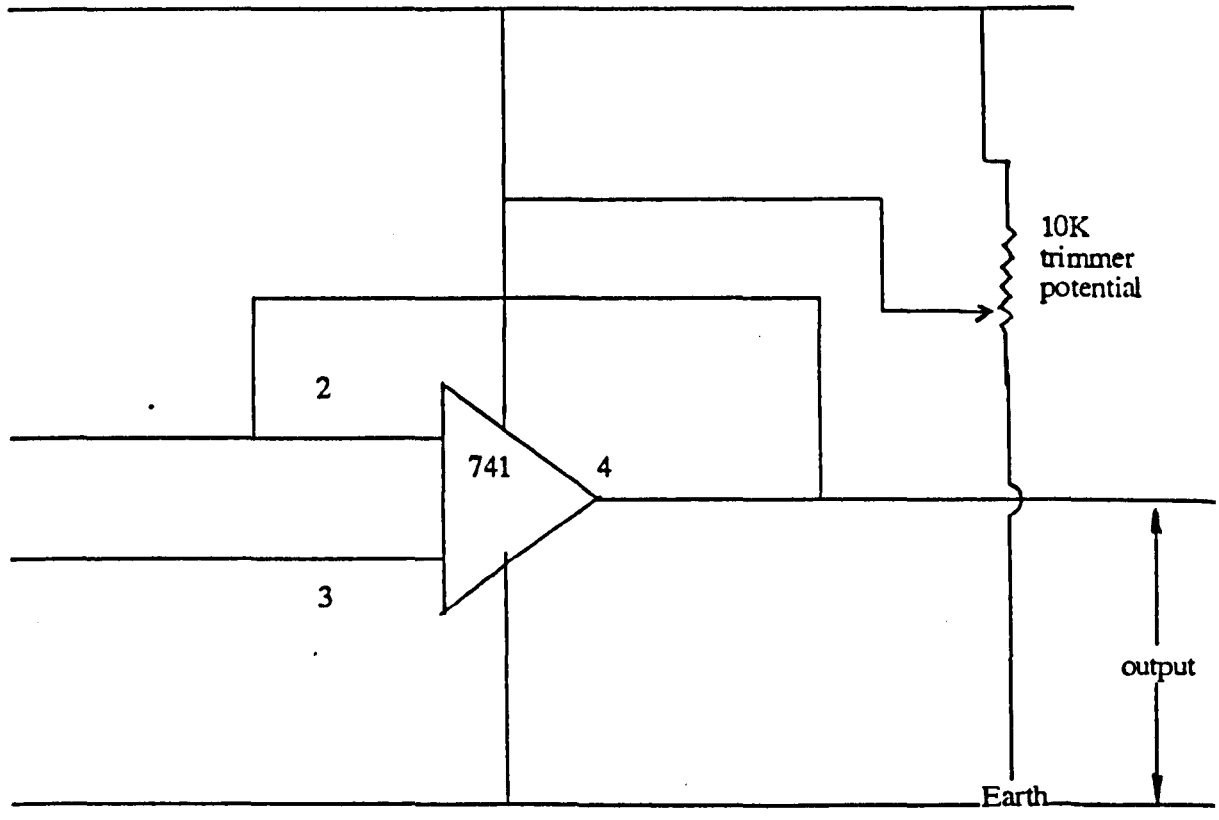

third 815mm from the first. The beams passed via a set of mirrors to three photovoltaic cells; the mirrors were independently mounted to avoid premature triggering by vibration.

As the shock wave moves along the tube it crosses the first laser beam, this causes a sudden increase in density (Chapter Four) which causes reflection and refraction, and in turn, generates a sharp increase in output from the photovoltaic cell as the beam is deflected. This switches on the transient recorders (Datalab 200) and timers. The shock wave moves along the tube to the second beam, this switches off the first timer. The second timer is switched off when the third beam is intersected by the shock front. The speed of the shock wave can be calculated by the time taken for the shock front to travel between the light screens.

The transient recorders are connected to two oscilloscopes (Hewlett Packard series 140), where the post shock data is displayed. It is also transferred to a computer terminal (HP F2647A), and is then stored on magnetic tape.

3.6.2 The Fundamental Measurements

The quality and accuracy of the experimental results depend upon the accuracy of the measurements of voltage, pressure, shock speed and flow rate. Tests of their precision were therefore made.

The pressure was determined by two pressure gauges, one a pumped diethyl pthalate manometer, the other a Speedivac gauge (C.G.3). No pressure gradient between the two was ever observed throughout the experimental range used, the pressure could be calculated to within ± 0.2 torr.

The flow rate was determined by the electronic flowmeters. For the nitrogen flow, the error in the measurement was within ± 5%. For the additional gases (O_2, NO), the flow rate could be determined to ± 10%.

The attenuation of the shock wave was checked by comparing the times taken to cover two pre-measured distances (section 3.6.1). Where times were not obtained, the arrival time for the shock wave could be calculated from the shock trace. In accord with previous workers, the two speed determinations were found to be within experimental error (± 2%).

The output from the transient recorders, oscilloscopes and digital voltmeters were checked against the output from a signal generator (Marconi TF210). They were all examined to ensure they gave the same output compared to the input signal.

The time base of both the oscilloscopes and transient recorders was checked by using the crystal oscillator in the time counter.

3.7 The Set-Up Procedure

A routine set-up procedure was devised for the discharge flow shock tube, this was adhered to throughout the course of this work.

The entire system was evacuated and allowed to stand for 30 minutes. The purification traps were filled with coolant during this period.

The main gas flow (nitrogen) was turned on and adjusted to the desired flow rate (900 ml min^{-1}), which was recorded after the system had been allowed to flush for one minute. The compressed air and microwave power source were turned on, the discharge was initiated with a Tesla coil [33]. Adjustments were made (when necessary) to reduce the reflected power to within 2% of the total. The E.H.T, 12 volt power supply and digital voltmeters were then turned on.

The variation of the intensity of the gas emission along the tube was measured by the mobile photomultiplier, intensities were recorded at positions located by the track markers.

Additional quencher gas was added to the system and the flow rate adjusted. Intensity-distance measurements were recorded after the apparatus had been allowed to settle for 2 minutes. The pressure of the system was recorded along with the flow rates from the electronic flow meters.

The photomultipliers were then returned to their observation positions for the post shock data collection. The light screens and timers were turned on and adjusted. The transient recorders were switched on and adjusted to the expected sweep speed, sensitivity and delay, to optimise the data collection. A measurement of the intensity at the observation station (pre-shock glow) was then made.

The system was then prepared to collect the post shock data. The photomultipliers were connected to the transient recorders, the pressure manometer isolated from the system and the whole recording apparatus reset by the use of the reset button, located near the diaphragm.

Driver gas(es) were loaded into the driver cavity and the pressure was steadily increased, continuous checks were made to ensure that premature triggering had not occured. This was continued until the diaphragm had burst and a shock was propagated along the tube. The driver gas supply, main and quencher gas supplies, light screens and microwave discharge were then switched off.

The times taken for the shock wave to pass between the light screens were recorded along with the photomultiplier dark current. The data within the transient recorders was transferred to magnetic tape through the HP F2647A graphics terminal. The results displayed on the oscilloscope were photographed for future reference.

Both shock tube and driver sections were opened to the atmosphere, a fresh smooth diaphragm inserted, and the whole procedure repeated for the next set of measurements.

3.8 Safety

When working with either discharge flow or shock tube apparatus, certain safety precautions must be taken. The typical hazards of this apparatus can be considered to be both physical and chemical in nature.

3.8.1 Physical

a. Electrical hazards

Electrical hazards arise from the use of high voltage low impedance sources, such as the E.H.T supply used for the photomultipliers. Loose cables and connection lines were tied to the apparatus, to avoid the possibility of accidental contact.

b. Radiation

Two sources of radiation are inherent within the apparatus. The microwave discharge was shielded with a Faraday cage [34], regular checks with a microwave detector were made to ensure that leakages were negligible [35].

The laser sources (Class 3A) were always switched off when not in use; a cut off switch was fitted to the apparatus. Particular care was taken when aligning a beam, those not being aligned were physically blocked to prevent the risk of accidential eye contact.

c. Low pressure

With apparatus at low pressure, particularly those made of glass, the possibility of implosion exists. To reduce the risk of flying debris, the most vulnerable components were covered with insulating tape.

3.8.2 Chemical

Certain experiments, such as those described in Chapter Six , require the use of toxic gases. In particular, NO was used and this was introduced by the method given in section 3.5 . After a series of experiments, the P.T.F.E. Sampling bag and connecting line were pumped out by a water pump. The arrangment was located in a fume cupboard, in case of leakage.

CHAPTER FOUR

4.0 Flow Tube and Shock Wave Theory

4.1 Introduction

In this chapter, the nature of flow and shock tube experiments is examined (Chapters Six, Seven, Ten and Eleven). The first part is concerned with the flow of gas along a typical flow tube. Derivation of the flow velocity under stipulated experimental conditions is given.

The other sections look at the nature and physical effects of shock waves on a test gas, and a derivation of relationships for these is given for a test gas with a temperature independent heat capacity.

4.2 Flow Tube Experiments — A Gas in Motion.

In flow tube experiments, a gas (or liquid) is compelled to flow along a tube, distributing the reactants in space. It is necessary to know both the concentration and flow velocity.

To approach this problem it will be assumed that the plug flow, rather than the parabolic, describes the bulk movement of the gas [36]. Consider a gas flow at one atmosphere, room temperature and volume flow rate labelled by the parameters P_1, T_1 and V_1 respectively. The gas passes into a flow tube where it is mantained at pressure P_2, temperature T_2 and with a linear flow velocity, v.

Under any combination of P_2 and T_2, the density of the gas (ρ) can be calculated by using the ideal gas law [2];

$$\rho = P/RT \qquad \text{mol dm}^{-3} \tag{4.1}$$

where R = universal gas constant.

The law of mass conservation [37] must apply throughout the system, and by equating the mass flow per unit time between the conditions P_1, V_1, T_1 and P_2, V_2, T_2, it can be show that;

$$v = \left(P_1/P_2\right) \frac{V_1}{\pi r_i^2} \left(T_2/T_1\right) \tag{4.2}$$

where r_i is the internal radius of the flow tube.

A conversion between the spatial intervals along the tube and real time valves can now be made since:

$$\text{time} = \text{spatial interval/velocity} \tag{4.3}$$

4.3 Shock Waves and Their Physical Effects

4.3.1 Shock and Sound Waves

A sound wave is propagated through a gas in the form of a weak adiabatic compression [37, 38]. Only small longitudinal displacements of the molecules are involved and there is no net movement of the bulk of the gas. This type of wave is transmitted by collisions between molecules, and its velocity depends upon the random molecular speed of the molecules involved [37].

A shock wave is a pressure disturbance that moves through the sample, with an amplitude that that is much greater than that of a sound wave. Its progress does not depend upon molecular collision, there is a bulk movement of gas and it travels supersonically [37]. A shock wave is an irreversible process and leads to a rise in entropy of the system [31].

4.3.2 Shock Wave Formation

The simplest picture of shock wave formation was given by Becker (1922), who considered a long tube containing a moveable piston. He suggested that the piston moved into the gas, until it reached a velocity, v, in a short but finite time.

Consider the first stage, the piston changes from being at rest until it reaches a velocity dv. As a result, a weak compression wave is sent out into the test gas, also moving at a velocity, dv. The piston accelerates and now obtains a velocity 2dv. A second compression wave is sent in pursuit of the first, travelling faster with respect to the tube than 2dv because it now moves through a slightly warmed sample. This sequence continues until a complete series of waves exist which eventually coallesce to form one common wave travelling at a velocity, v, along the tube.

4.4 Wave Patterns Within a Shock Tube

A diagram for a pressure driven shock tube and the post shock wave patterns produced in it are as given in figure 4.1 . After the diaphragm ruptures, a shock wave is sent, at constant velocity, into the cold low pressure section, where it hits the end plate and is reflected back through the gas. Meanwhile a rarefaction fan spreads out at the other end of the tube and travels through the high pressure driver gas. It too is reflected and then moves with the expanding driver gas, accelerating to a final velocity exceeding that of the initial shock wave.

Figure 4.1 Distance vs. time diagram for a pressure driven shock tube

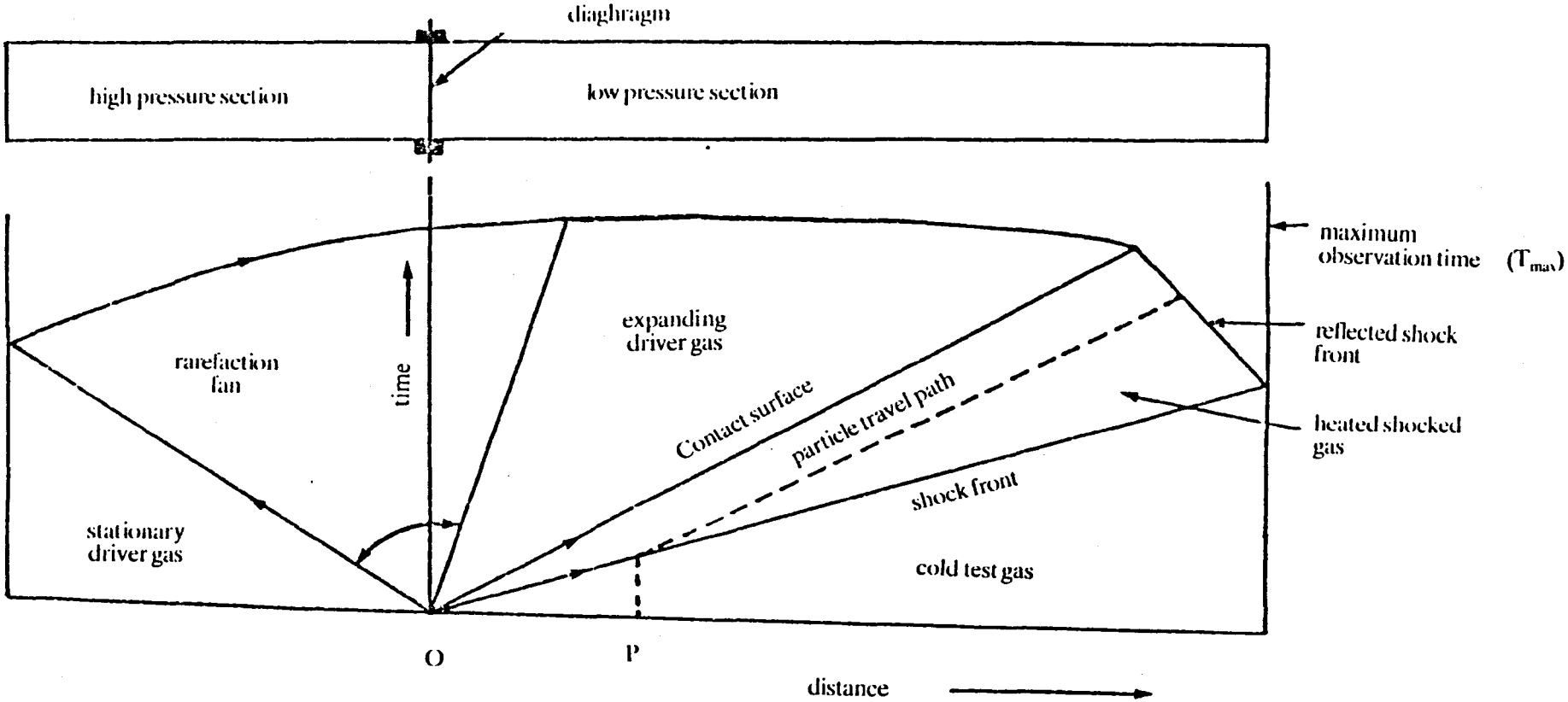

Along with these a contact surface, the leading edge of the gas, moves along the tube in the same direction as the shock wave, but slower than it. Particles behind the shock front travel with a velocity equal to that of the contact surface. This has two important implications: it gives rise to a compression in the observation time (section 4.6.1), and material from upstream (diaphragm end) is swept past the observation section and will show up as a variation in the shock trace (Chapter Five).

The observations that can be taken in a shock tube depend upon the 'hot-flow' time, the time taken between the arrival of the shock front and the contact surface. The maximum observation time is determined by the length of the tube, the location of the measuring instruments and the type of gas involved. This is shown as the height (T max) on figure 4.1 .

4.5 Shock Waves — the Physical Processes

To interpret data from a shock tube system, an understanding of the effect of a shock wave upon a sample is necessary. The derivations for this assume that the flow is steady and that the laws of momentum and mass conservation apply. The control volume used is given in figure 4.2 .

Under fixed shock co-ordinates, the velocity U can be written in terms of the shock wave speed, Ws, and gas flow speed, V, by;

$$U_1 = Ws - V_1 \tag{4.4}$$

$$U_2 = Ws - V_2 \tag{4.5}$$

where U_1 and U_2 are the velocities of the gas sample, defining the control volume, fig 4.2 .

Application of the laws of mass, momentum and energy conservation yield:

$$\rho_1 U_1 = \rho_2 U_2 \tag{4.6}$$

$$P_1 + \rho_1 U_1^2 = P_2 + \rho_2 U_2^2 \tag{4.7}$$

$$H_1 + \tfrac{1}{2}U_1^2 = H_2 + \tfrac{1}{2}U_2^2 \tag{4.8}$$

In the expressions above, ρ denotes the density, P the pressure, H_1 and H_2 are the initial and final enthalpies of the system.

Figure 4.2 Control volume used in the steady flow equations

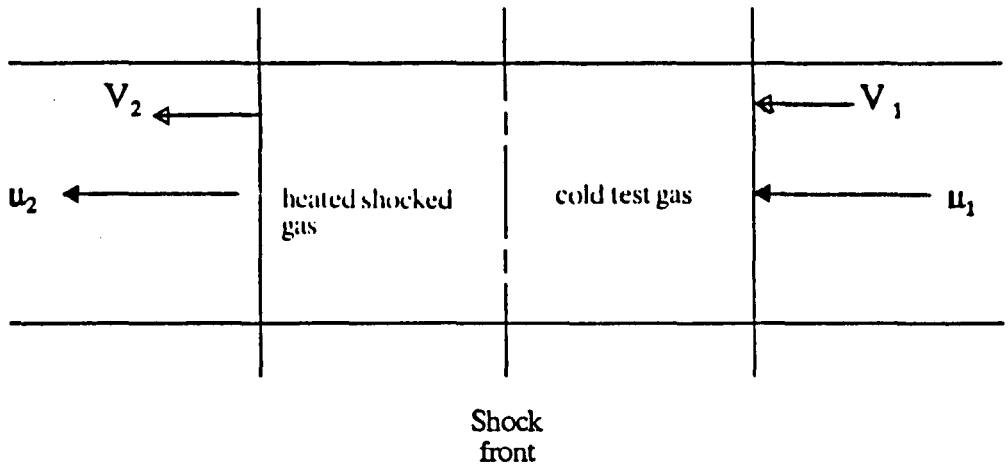

Figure 4.3 Flow relationships through a stationary and uniform shock wave

Post shock	Pre shock
$u_2 > u_1$	u_1
$P_2 > P_1$	P_1
$T_2 > T_1$	T_1
$H_2 > H_1$	H_1

The argument given in expression (4.8) assumes that the heat losses in the system are negligible, this is discussed in section 4.6 . By definition [39], H can be expressed in terms of the internal energy, E, heat capacity per unit volume, R', and temperature, T, by the relationship:

$$H = E + RT \tag{4.9}$$

Providing the sample has a temperature independent specific heat capacity ratio, γ, [40], then equation (4.9) can be written;

$$H = (\gamma/(\gamma-1))\,RT \tag{4.10}$$

or

$$H = (\gamma/(\gamma-1))\,\frac{P}{\rho} \tag{4.11}$$

Using equations (4.8) and (4.11), together with (4.6) and (4.7) to eliminate U_1 and U_2, equation (4.12) can be obtained:

$$\frac{\rho_2}{\rho_1} = \rho_{21} = \frac{(\gamma-1/\gamma+1) + P_2/P_1}{(\gamma-1/\gamma+1)\,P_2/P_1 + 1} \tag{4.12}$$

Equation (4.12) is one of the Rankine-Hugoniot (1870-1887) equations. A combination of (4.6) and (4.7) gives the expression:

$$\frac{P_2}{P_1} = P_{21} = 1 + \frac{\rho_1 U_1^2}{P_2} \tag{4.13}$$

For simplicity, a dimensionless quantity the Mach number, M_1, is introduced, which is related to U_1 and the sound speed, a, by, the equation:

$$M_1 = U_1/a \tag{4.14}$$

It follows from equation (4.4) that if the gas is initially stationary then:

$$M_1 = Ws/a \tag{4.15}$$

By using the expression for the sound speed in terms of ρ_1, γ and P_1 [37], along with equation (4.14), it can be shown that;

$$\frac{P_2}{P_1} = 1 + \gamma M_1^2 \left\{1 - \frac{\rho_1}{\rho_2}\right\} \tag{4.16}$$

now using equations (4.12) and (4.16); (4.17)

$$\frac{P_2}{P_1} = \frac{2\gamma M_1^2 - (\gamma - 1)}{(\gamma + 1)}$$

and the latter two expressions combine to give:

$$\rho_{21} = \frac{(\gamma+1) M_1^2}{(\gamma-1) M_1^2 + 2} \tag{4.18}$$

Finally, using equations (4.17) and (4.18) along with the ideal gas law, the ratio of temperatures of the shocked and unshocked gas is given by:

$$\frac{T_2}{T_1} = T_{21} = \frac{(\gamma M_1^2 - (\gamma-1)/2((\gamma-1)/2 M_1^2 + 1)}{((\gamma+1)/2) M_1^2} \tag{4.19}$$

The relationships have been summarised in fig. 4.3 .

By measuring the pre-shock pressure in the flow tube (P_1), the laboratory temperature (T_1), and determining the shock wave velocity (M_1), the post shock conditions, P_2, ρ_2 and T_2, behind the shock front can be calculated.

4.6 Non Ideal Gases and Shock Wave Theory

In section 4.5 the parameters ρ_{21}, P_{21} and T_{21} were derived for a gas with a temperature independent specific heat capacity. This would be applicable to a rare gas or a polyatomic gas where there is no energy transfer between translational and vibrational or rotational modes. Hence, the analysis given in section 4.5 is not suitable for a diatomic gas (e.g. N_2), and corrections to these calculations must be made.

After shock heating the gas, some of the energy is transferred into the vibrational component. The molar enthalpy, H, can be modelled by a power series using the temperature T. A specific form of this is:

$$H = A + BT + CT^2 + DT^3 \qquad (4.20)$$

The coefficients A, B, C and D can be calculated by fitting the equation (4.20) to known values of H, given in J.A.N.A.F. tables. [41].

The shock parameters are calculated for the 'frozen' case, as described in section 4.50 . These values, along with the coefficients in equation (4.20), are then used. The difference in the original enthalpy calculated is then used to re-evaluate T_2. This process continues until the parameters become self consistent.

4.7 Time Scales Used in the Experiments

Measurements are taken at a fixed observation position on the shock tube. A shock wave moves along the tube at velocity, Ws, the particles behind it are carried along travelling at velocity Wp, where Ws > Wp.

The distinction between these two velocities can be seen more clearly with reference to figures (4.4a) and (4.4b). A shock wave is sent from position A, a distance, x, from the observation point, the time take, ts, for it to reach the observation point from A is given by:

$$ts = x/Ws \qquad (4.21)$$

The particles take a time, tp, moving a velocity, Wp, to travel from A to the observation point given by;

$$tp = x/Wp \qquad (4.22)$$

the difference in time between these two events, td, is given by:

$$td = tp - ts. \qquad (4.23)$$

Figure 4.4 Laboratory and particle times

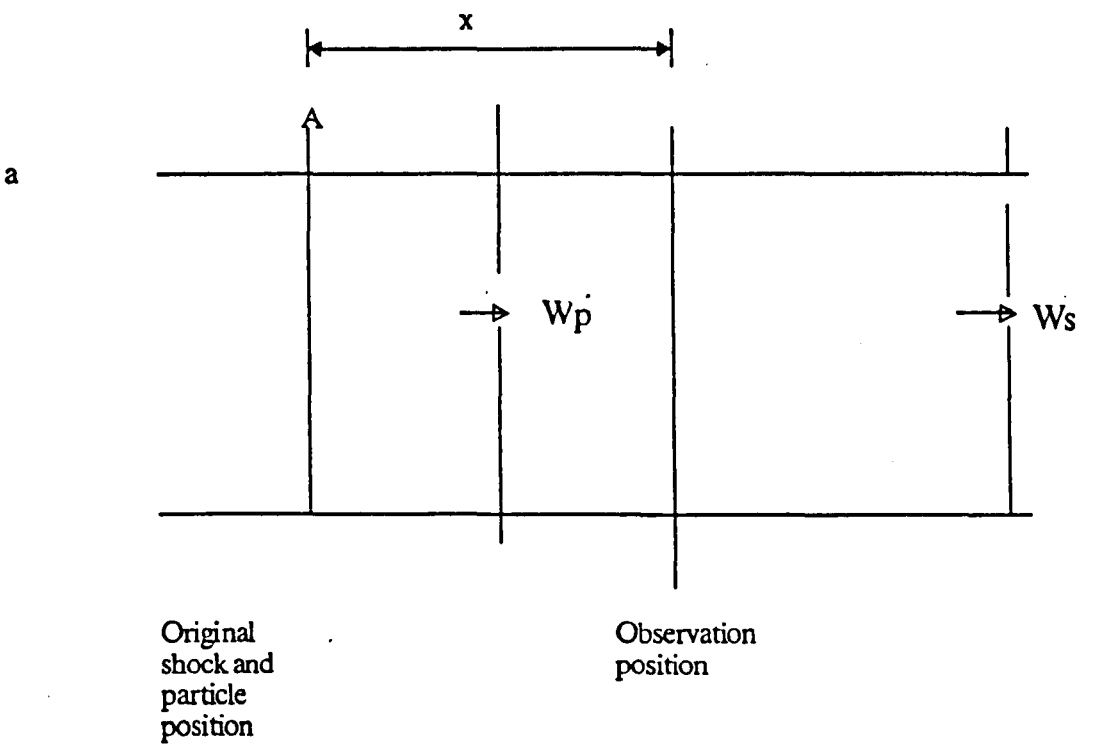

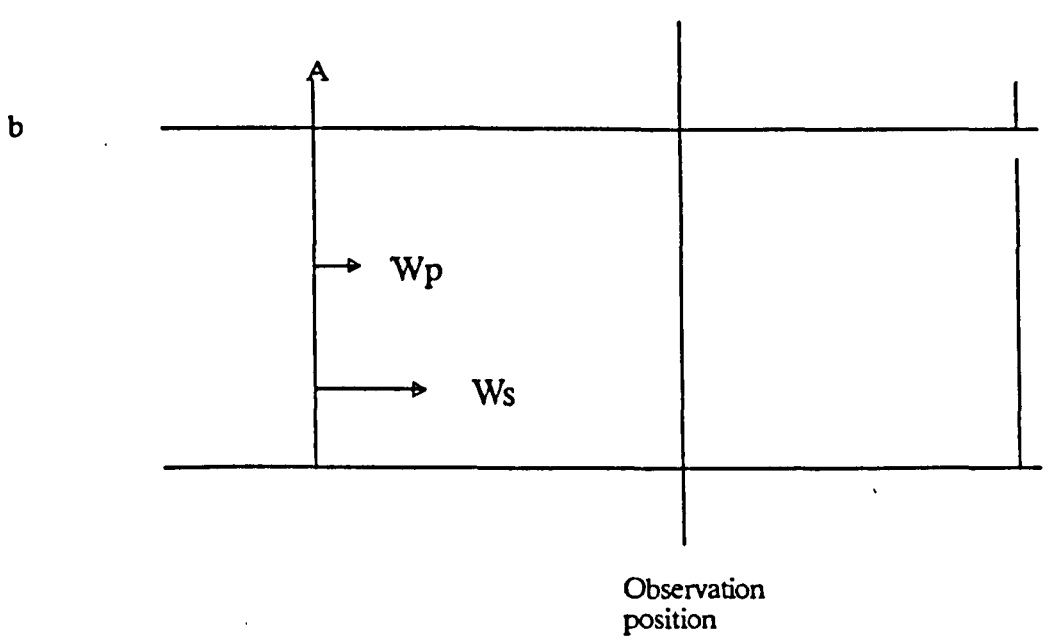

The sample is therefore shock heated for a longer period than the observer realises. It is necessary to convert laboratory time into particle time to derive the kinetics correctly. This is possible since td is determined in laboratory co-ordinates (t_L) and;

$$t_p/t_L = t_p/(t_p - t_s) \tag{4.24}$$

or: $$t_p/t_L = W_s/(W_s - W_p) \tag{4.25}$$

Using fixed shock co-ordinates, and the law of mass conservation:

$$t_p/t_L = \rho_{21} \tag{4.26}$$

The events that occur behind the shock front are the ones of interest in these experiments. A conversion between laboratory and particle time is necessary, and is achieved by using equation (4.26).

In practical terms, the time resolution of the experiment is reduced since $t_p > t_L$. The decay constant in particle time, ϕ_P, and the decay constant in laboratory time, ϕ_L, are linked together by equation (4.26):

$$\phi_P = \frac{\phi_L}{\rho_{21}} \tag{4.27}$$

CHAPTER FIVE

5.0 The Kinetic Models and Analysis Methods Used to Study Nitrogen Atom Reactions

5.1 Introduction

This chapter gives the kinetic equations used to describe nitrogen atom reactions, both at room and high temperature. The chapter concludes by describing the analysis methods that were used to assess the data.

5.2 The Room Temperature Kinetic Models

5.2.1 Atomic Nitrogen Removal Reactions

In the discharge flow tube, nitrogen atom removal reactions occur. The kinetics of these reactions can be examined by looking at the first positive emission from atomic nitrogen [18]. Two systems have been studied, the first with atomic nitrogen in N_2, the second with additional O_2.

5.2.2 Nitrogen Atom Recombination in N_2

The reactions are:

$$N + N \longrightarrow N_2 + h\nu \qquad k_1 \qquad (5.1)$$

$$N + N \longrightarrow N_2 \qquad k_2 \qquad (5.2)$$

$$N + N + N_2 \longrightarrow N_2 + N_2 \qquad k_3 \qquad (5.3)$$

$$N + \text{wall} \longrightarrow \tfrac{1}{2}N_2 \qquad k_4 \qquad (5.4)$$

These reactions have been studied by Campbell and Thrush [21], who found that reaction (5.4), the heterogenous wall process, was slow compared to (5.2) and (5.3). The emission reaction (5.1) can also be removed from the overall scheme since its contribution is also small. Considering only reactions (5.2) and (5.3), the rate of nitrogen atom removal can be written;

$$-\frac{d[N]}{dt} = 2(k_2 + k_3[N_2])[N]^2 \qquad (5.5)$$

or

$$-\frac{d[N]}{dt} = 2\alpha_t [N]^2 \qquad (5.6)$$

where α_t is the psuedo second order rate constant for nitrogen atom recombination.

It has been shown that the intensity from the first positive emission of N_2, in the pressure range $P > 1$ torr, depends upon the square the nitrogen atom concentration [17];

$$^{579}I = B\,[N]^2 \qquad (5.7)$$

where ^{579}I is the intensity of the emission band located at 579nm, and B is a constant determined by the experimental arrangement.

By rearranging and integrating equation (5.6), and then using equation (5.7), the intensity of this emission band at a time t, $^{579}I_t$, is given in terms of the intensity at the start of the measuring zone, $^{579}I_o$, by:

$$(^{579}I_t)^{-\frac{1}{2}} = (^{579}I_o)^{-\frac{1}{2}} + 2\alpha_t/(B)^{\frac{1}{2}} \cdot t \qquad (5.8)$$

In flow tube experiments, distance and time along the flow tube are related by equation (4.3). The intensity along the flow tube length, $^{579}I_l$, is therefore related to the position, l, and linear flow velocity, v, by:

$$(^{579}I_l)^{-\frac{1}{2}} = (^{579}I_o)^{-\frac{1}{2}} + 2\alpha_t/((B)^{\frac{1}{2}}v) \cdot l \qquad (5.9)$$

or $$(^{579}I_l)^{-\frac{1}{2}} = (^{579}I_o)^{-\frac{1}{2}} + 2\alpha_1 \cdot l \qquad (5.9(a))$$

A plot of $(^{579}I_l)^{-\frac{1}{2}}$ against l should give a straight line of slope $2\alpha_t/(B)^{\frac{1}{2}}v$, an example is given in fig. 5.1 .

The psuedo second order rate constant, α_t, is given by:

$$\alpha_t = (k_2 + k_3\,[N_2]) \qquad (5.10)$$

If k_2 and k_3 are independent of the total pressure, (and therefore $[N_2]$), a plot of α_t as a function of $[N_2]$ should give a straight line of slope k_3 and intercept k_2. The results are given and then discussed in Chapter Six.

Figure 5.1 Variation of $I^{-\frac{1}{2}}$ as a function of distance along the tube.

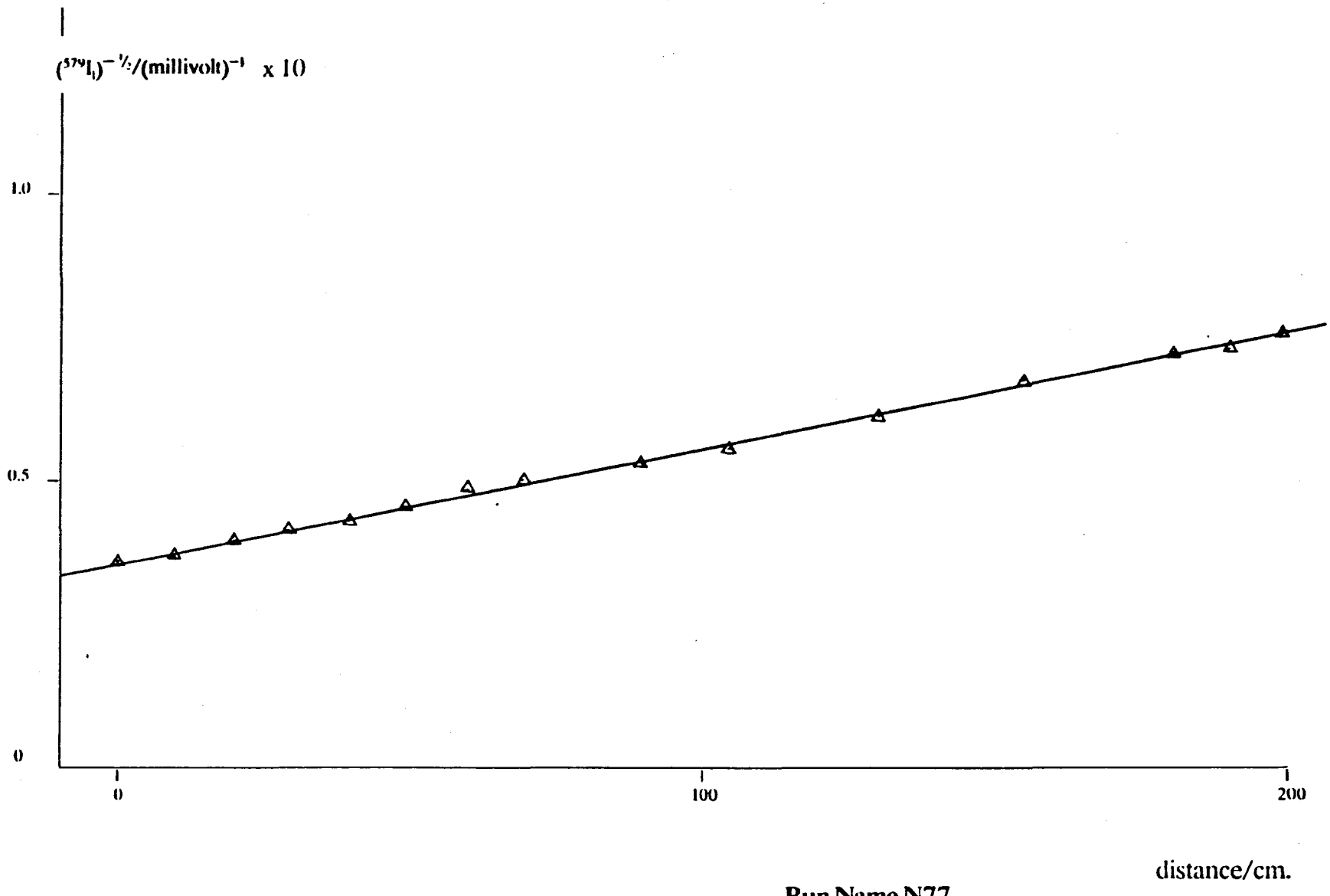

5.2.3 Nitrogen Atom Reactions in Both N_2 and O_2

Oxygen molecules were added to the nitrogen stream 20cm from the start of the measuring zone (Chapter Seven).

Two reactions which will occur are [42, 43]:

$$N + O_2 \longrightarrow NO + O \qquad k_5 \qquad (5.11)$$

$$NO + N \longrightarrow N_2 + O \qquad k_6 \qquad (5.12)$$

In an N_2 stream containing nitrogen atoms with a low oxygen atom concentration (Chapter Seven), reaction (5.12) has been shown to be fast compared to (5.11), other nitrogen atom reactions (5.1−5.4) [44,45,46] and also:

$$N + O + M \longrightarrow NO + M \qquad k_7 \qquad (5.13)$$

which is followed by [21];

$$NO + N \longrightarrow N_2 + O \qquad k_6 \qquad (5.12)$$

Calculations show that the above two catalytic processes contribute to $<10\%$ of the nitrogen atom reaction rate [42,43,46]. This is within experimental error (section 3.6.2) and so can be discounted.

If only (5.11) and (5.12) are considered [42], the rate of N atom removal is given by:

$$-\frac{d[N]}{dt} = k_5 [N][O_2] + k_6 [NO][N] \qquad (5.14)$$

Because reaction (5.12) is fast compared to (5.11), the NO concentration is in a steady state [43], so:

$$[NO] = \frac{k_5 [O_2]}{k_6} \qquad (5.15)$$

Substitution of (5.15) into (5.14) gives the expression:

$$-\frac{d[N]}{dt} = 2\,k_5\,[O_2]\,[N] \qquad (5.16)$$

Clarke and Wayne have shown that reactions (5.1–5.4) are significant under these conditions, and must be accounted for in the reaction scheme.

It was shown (section 5.2.2) that the nitrogen atom recombination rate can be written;

$$-\frac{d[N]}{dt} = 2(k_2 + k_3[N_2])\,[N]^2 \qquad (5.5)$$

Rearranging and integrating eqn. (5.5) gives;

$$\frac{1}{[N]_t} = \frac{1}{[N]_o} + k_a\,t \qquad (5.5(a))$$

or

$$\frac{[N]_o}{[N]_t} = 1 + k_a[N]_o t \qquad (5.5(b))$$

where $[N]_o$ and $[N]_t$ are the nitrogen atom concentrations at times t = o and t respectively and:

$$k_a = 2(k_2 + k_3[N_2]) \qquad (5.5(c))$$

Rearranging eqn. (5.5(b)) gives [43];

$$[N]_t/[N]_o = (1 + k_a[N]_o t)^{-1} \simeq \exp.-k_a[N]_o t \qquad (5.5(d))$$

providing that $k_a[N]_o t < 1$. Taking the logarithm both sides of eqn. (5.5(d));

$$\ln([N]_t/[N_o]) = -k_a[N]_o t \qquad (5.5(e))$$

and then using the emission concentration relationship (section 5.2.2) and rearranging gives the relationship:

$$\tfrac{1}{2}\ln({}^{579}I_t) = \tfrac{1}{2}\ln({}^{579}I_o) - k_a[N]_o t \qquad (5.5(f))$$

A sample plot according to eqn. (5.5(f)) is given in figure 5.2 , for a nitrogen flow in the absence of O_2.This shows that the approximation (eqn. 5.5(d)) is good under these experimental conditions. The total nitrogen atom reaction rate, accounting for reactions (5.1—5.4) and (5.11, 5.12) can therefore be represented by [43];

$$-\frac{d[N]}{dt} = \left\{2k_5[O_2] + k_a^*\right\}[N] \qquad (5.5(g))$$

where $k_a^* = k_a[N]_o$

or

$$-\frac{d[N]}{dt} = k_b[N] \qquad (5.5(h))$$

where $k_b = \{2k_5[O_2] + k_a^*\}$ (5.5(i))

5.2.3.1 Measurements Using the First Positive Emission Band at 579nm.

Measurements of the nitrogen atom concentration can be taken at 579nm (Section 5.2.2). Using relationship (5.7), and then integrating (5.5(g)), it can be shown that;

$$\ln\left\{\frac{{}^{579}I_o}{{}^{579}I_t}\right\} = (4k_5[O_2] + 2k_a^*)t = 2k_b t \qquad (5.17)$$

where ${}^{579}I_o$ and ${}^{579}I_t$ have the same identity as those given in section (5.2.2). Using relationship (4.3), ${}^{579}I_t$ can be expressed as a function of the flow tube length, 1, with a gas linear flow velocity, v, by:

$$\ln\left\{\frac{{}^{579}I_o}{{}^{579}I_t}\right\} = ((4k_5[O_2] + 2k_a^*)/v)1 \qquad (5.18)$$

Figure 5.2 First Order Approximation to the Homogenous and Heterogeneous Recombination Rate.

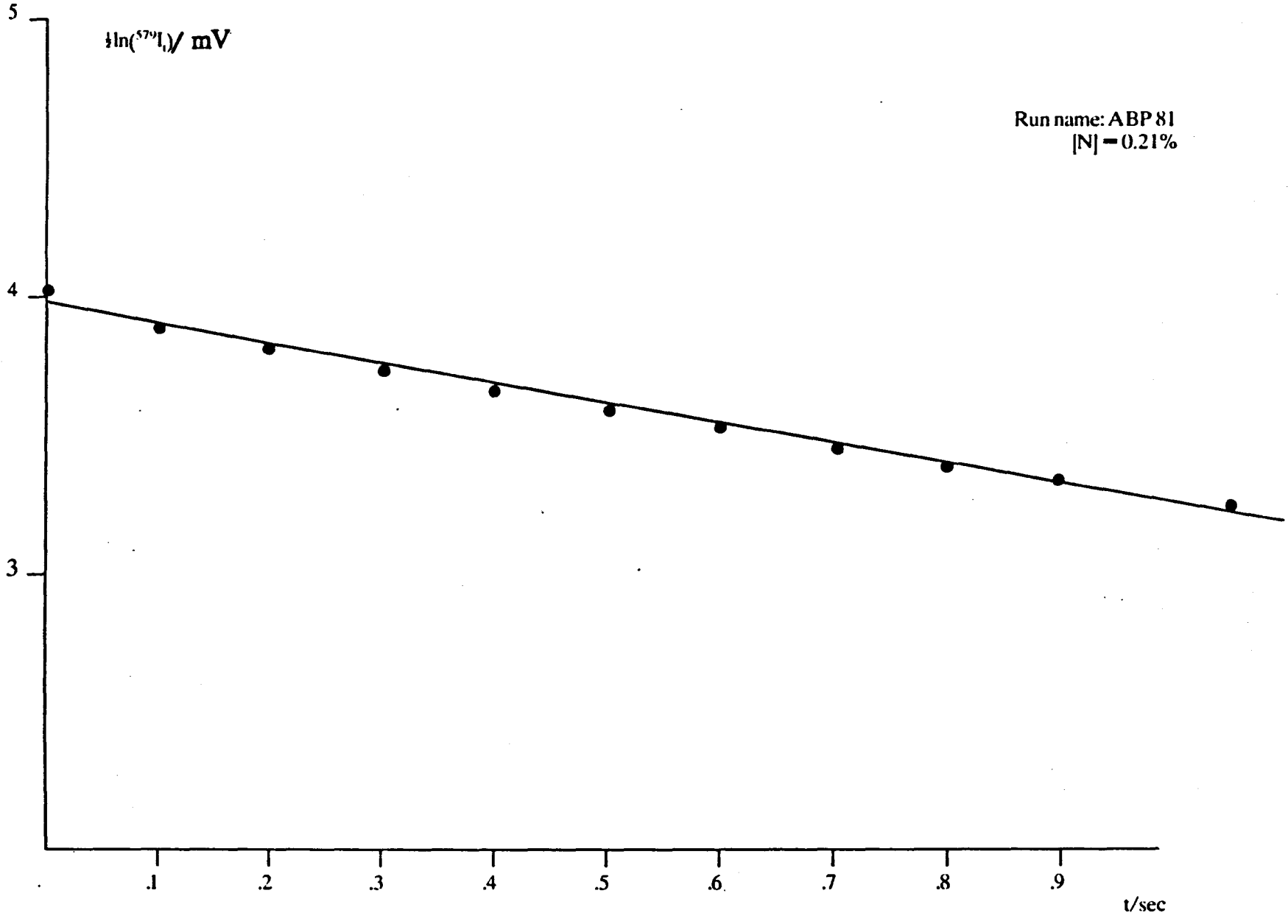

A plot of ln ($^{579}I_o/^{579}I_l$) against l should give a straight line, the value of each slope equal to ($4k_5[O_2]+2k_a^*/v$). A plot is given in fig. 5.3 and shows that a good straight line is produced.

5.2.3.2 Measurements Using the Emission Band at 403 nm.

NO molecules are produced by the reaction. These give rise to NO(ß) band emission [46]; one of these bands is located at 403 nm [47].

The emission arises from the process [46];

$$N+O+M \longrightarrow NO+M \qquad k_7 \qquad (5.13)$$

which is followed by the rapid reaction;

$$NO+N \longrightarrow N_2+O \qquad k_6 \qquad (5.12)$$

and the intensity is represented by [46];

$$^{NO}I = {}^{NO}K\,[N]\,[O]\,[M] \qquad (5.19)$$

where ^{NO}I is the intensity of the NO(ß) band and ^{NO}K is a constant determined by the experimental arrangement.

To predict how the intensity from these bands will vary with time, consider each of the species N and O. The variation of N atoms along the tube, rearranging (5.18) and using (5.7), can be written:

$$[N]_l = [N]_o \exp -((2k_5[O_2]+k_a^*)l/v) \qquad (5.20)$$

Oxygen atoms are produced by reactions (5.11) and (5.12) but are consumed by the reactions:

$$NO+O+M \longrightarrow NO_2+M \qquad k_8 \qquad (5.21)$$

$$O_2+O+O_2 \longrightarrow O_2+O_3 \qquad k_9 \qquad (5.22)$$

$$O+O+N_2 \longrightarrow O_2+N_2 \qquad k_{10} \qquad (5.23)$$

$$O+\text{wall} \longrightarrow \tfrac{1}{2}O_2 \qquad k_{11} \qquad (5.24)$$

$$O+O_2+N_2 \longrightarrow O_3+N_2 \qquad k_{12} \qquad (5.25)$$

$$O+O_3 \longrightarrow 2O_2 \qquad k_{13} \qquad (5.25\,(a))$$

Figure 5.3 Logarithmic intensity variation as a function of distance.

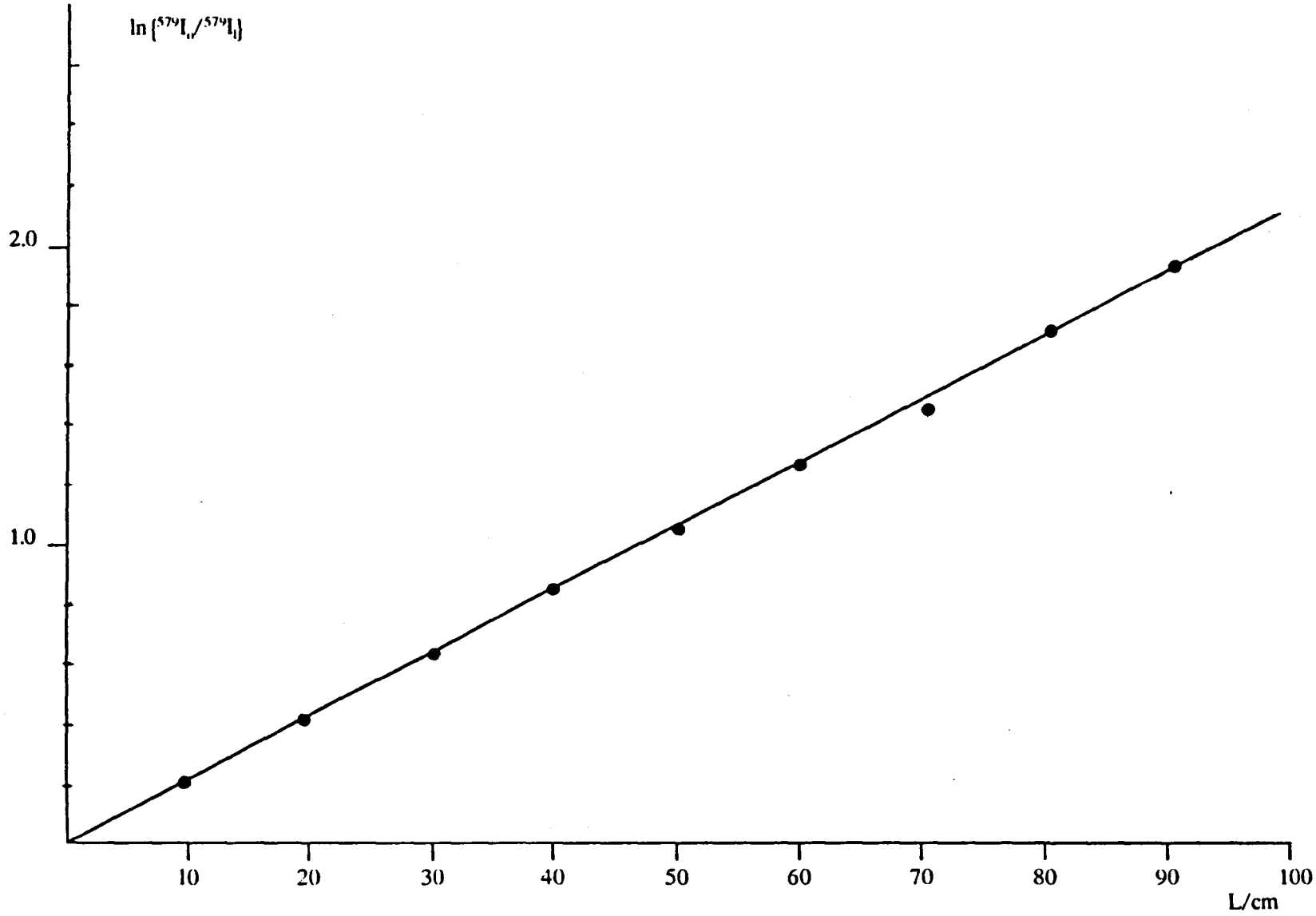

Previous workers have found that reactions (5.21, 5.22, 5.23) are slow under these conditions [42, 43, 47], and therefore can be neglected in the overall kinetic scheme. Hancock *et al.* found that oxygen atoms decayed appreciably in his system and assumed that reaction (5.24) was responsible [48]. Elias *et al.* [49], using a discharge flow system, were able to show that reaction (5.22) was significant and comparable to (5.24). Since the third body efficiences of O_2 an N_2 are similar for O_3 formation, then eqn. (5.25) should be included in the analysis. By assuming that the ozone is kept in steady state, since (5.25 (a)) is fast compared with (5.25) [50, 51], then the rate of O atom removal is given by;

$$-\frac{d[O]}{dt} = \{k_{11} + 2k_{12}[O_2][N_2]\}[O] \qquad (5.26)$$

or $$-\frac{d[O]}{dt} = k_{14}[O] \qquad (5.27)$$

where $k_{14} = k_{11} + 2k_{12}[O_2][N_2]$ (5.27 (a))

The overall rate of oxygen atom removal can now be written, by using eqns. (5.11 and 5.12):

$$-\frac{d[O]}{dt} = k_{14}[O] - 2k_5[O_2][N] \qquad (5.28)$$

The solution to this, assigning the concentration of oxygen atoms at time t, $[O]_t$, and at t = o, $[O]_o$, is;

$$[O]_t = [O]_o \exp -(k_{14}t) + \left(\frac{2k_5[O_2][N]_o}{(k_b - k_{14})}\right) \cdot \aleph \qquad (5.29)$$

where $\aleph = \{\exp -(k_{14}t) - \exp -(k_b t)\}$

and $[N]_o$ is the concentration of nitrogen atoms at the flow tube location t=o.

Combining equations (5.19, 5.20) and (5.29), and then using (4.3), the intensity at a position l, $^{NO}I_l$, will vary as a function of l by;

$$\frac{^{NO}I_l}{^{NO}I_o} = \left\{ 1 + \frac{2A\,k_5\,[O_2]}{(k_b - k_{14})} \right\} \exp -((k_b + k_{14})l/v)$$

$$- \left\{ \frac{2A\,k_5\,[O_2]}{(k_b - k_{14})} \right\} \exp -(2k_b l/v) \qquad (5.30)$$

where $A = [N]_o/[O]_o$
v is the linear flow velocity
$^{NO}I_o$ is the intensity at position l=o
l/v is the time for the reaction at position l.
and $k_b = 2k_5[O_2]+k_a^*$ (see section 5.2.3).

In these experiments l=o (t=o) was taken to be at the photomultiplier observation station and not the beginning of the flow tube. In this way only one determination of A need be made, since it is required for both the room temperature and high temperature post shock condition (see section 5.3.2.2).

The ratio of the intensities $^{NO}I_l$ and $^{NO}I_o$ has been expressed as a function of the flow tube length. The fit of equation (5.30) to the experimental data was achieved by a non linear least squares program, the sub routine is given in appendix 1. A typical experimental plot of the data is given in fig. 5.4 , the solid line through the points represents a fit according to eqn. (5.30).

Under these experimental conditions, k_b will be greater than k_{14} [43,49]. Thus A can be used as an approximate starting value for $P_{(1)}$ (see appendix) in the fitting procedure (section 7.2.2).

The value of k_{14} represents two rate constants;

$$k_{14} = k_{11} + 2k_{12}\,[O_2]\,[N_2] \qquad (5.27\,(a))$$

and so a plot of k_{14} against $[O_2]\,[N_2]$ should give a straight line of intercept k_{11} and slope $2k_{12}$. The results are given and discussed in Chapter Seven.

Figure 5.4 Variation of I/I_0 as a function of distance.

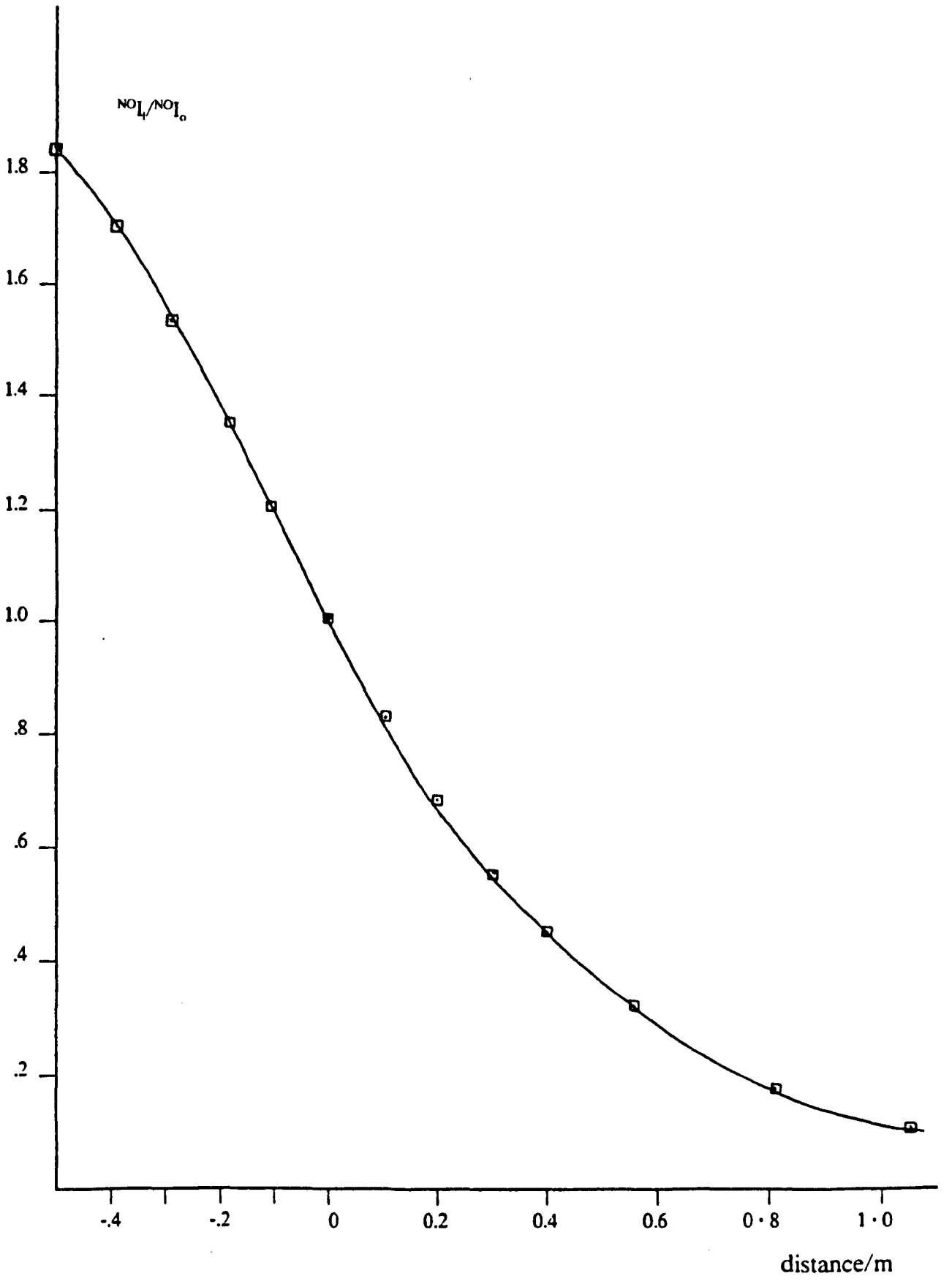

Run name APB83

5.3 The High Temperature Kinetic Models

The models described here refer to the reactions occurring in the post shock regime, at temperature T_2 and in particle time t (see Chapter Four).

5.3.1 Nitrogen Atom Recombination Reactions in N_2

In section 5.2.1 , the nitrogen atom concentration was described as a function of time by the expression:

$$-\frac{d[N]}{dt} = 2\alpha_t [N]^2 \qquad (5.6)$$

At high temperatures, by analogy, the rate of removal of nitrogen atoms is given by;

$$-\frac{d[N]}{dt} = 2\alpha_t'[N]^2 \qquad (5.31)$$

where t refers to the particle time (t) and α_t' is the psuedo second order rate constant for nitrogen atom recombination at high temperature and density (ρ_{21}). Rearranging and integrating (5.31) yields;

$$[N]_t^{-1} = [N]_o^{-1} + 2\alpha_t' \cdot t \qquad (5.32)$$

where $[N]_t$ and $[N]_o$ are the concentrations of nitrogen atoms in particle time t and t=o respectively. The value of $[N]_o$ varies with the tube location, since there is a concentration gradient in the pre-shock condition. Using equation (5.6), $[N]_o$ can be shown to vary as function of t according to;

$$[N]_o^{-1} = [N]_o^{o-1} + 2\alpha_t \cdot t \qquad (5.33)$$

where $[N]_o^o$ is the concentration of N atoms at the observation station immediately after the shock has passed, and α_t is the psuedo second order decay constant suitably corrected for the post shock conditions. Substituting equation (5.33) into (5.32) gives the expression:

$$[N]_t^{-1} = [N]_o^o + 2(\alpha_t + \alpha_t')t \qquad (5.34)$$

If there is no additional deactivation at high temperature, ie $\alpha_t' \approx 0 \ll \alpha_t$, then equation (5.34) reduces to [21]:

$$[N]_t^{-1} = [N]_o^{o-1} + 2\alpha_t t \qquad (5.35)$$

The post shock decay will therefore be a 'snapshot' of the pre-shock concentration gradient. Rearranging (5.35) gives;

$$[N]_t = [N]_o^o/(1+\varphi t) \qquad (5.36)$$

where φ is a constant that describes the variation in the concentration due to the pre-shock concentration gradient.

It was shown that the first positive emission at 579 nm can be modelled by equation (5.7). The emission at high temperature can be represented by the equation;

$$^{579}I = K_{(T)} \cdot B \cdot [N]^2 \qquad (5.37)$$

where $K_{(T)}$ is the enhancement factor at high temperature. More generally for the first positive emission, $^{F\cdot P}I$;

$$^{F\cdot P}I = K_{(T)}\ B'\ [N]^2 \qquad (5.38)$$

where B' is a constant determined by the experimental arrangement and $K_{(T)}$ is the enchancement factor specific to the chosen first positive band. At room temperature, the pre-shock glow, I_{psg}, is given by:

$$I_{psg} = B'[N]_o^2 \qquad (5.39)$$

Correcting for the increase in density (ρ_{21}), and using equation (5.38), the emission intensity immediately post, $^{F\cdot P}I_o$, shock is given by:

$$^{F\cdot P}I_o = I_{psg} K_{(T)} \rho_{21}^2 \qquad (5.40)$$

Using (5.40), (5.36) and (5.7), the intensity of the first positive band of molecular nitrogen at a time t, $^{F\cdot P}I_t$, is related to the pre-shock glow according to:

$$^{F\cdot P}I_t = \frac{K(T)\,\rho_{21}^2\,I_{psg}}{(1+\varphi t)^2} \qquad (5.41)$$

The equation predicts for the shock trace three regions:

1. The steady pre-shock glow, I_{psg}, before the shock impact.
2. An instantaneous rise in emission.
3. Decay as t increases.

A typical shock trace is given in figure 5.5 , it shows the three regions predicted above. The equation predicts correctly conditions (1) and (3), there is not an instantaneous rise in emission (2) since a finite slit width has been used and the electronic circuits do not respond instantaneously. To correct for these, equation (5.41) must be integrated to allow for the rise time, tr, the final expression becomes:

$$^{F.P.}I_t = I_{psg}\rho_{21}^2 K(T) \int_{t-tr}^{t} \frac{(1+\varphi t)^{-2}\,dt}{tr} \qquad (5.42)$$

The expression is numerically evaluated using the interactive computer graphics system, to yield values for tr, φ and K (T). The results are discussed in Chapter Six.

5.3.2 Nitrogen Atom Reactions in Both N_2 and O_2

In sections 5.2.3.1 and 5.2.3.2, the kinetics to describe the first positive and NO(ß) bands, at room temperature, were given. These are now considered at high temperature.

5.3.2.1 Measurements Using the Emission Band at 579nm

In the high temperature post shock regime, the homogenous and heterogenous recombination will be rendered insignificant. Hence, the first order rate constant, k_a^*, need not be included in the kinetic scheme.

Figure 5.5 Shock trace of the emission band at 579 using pure N_2

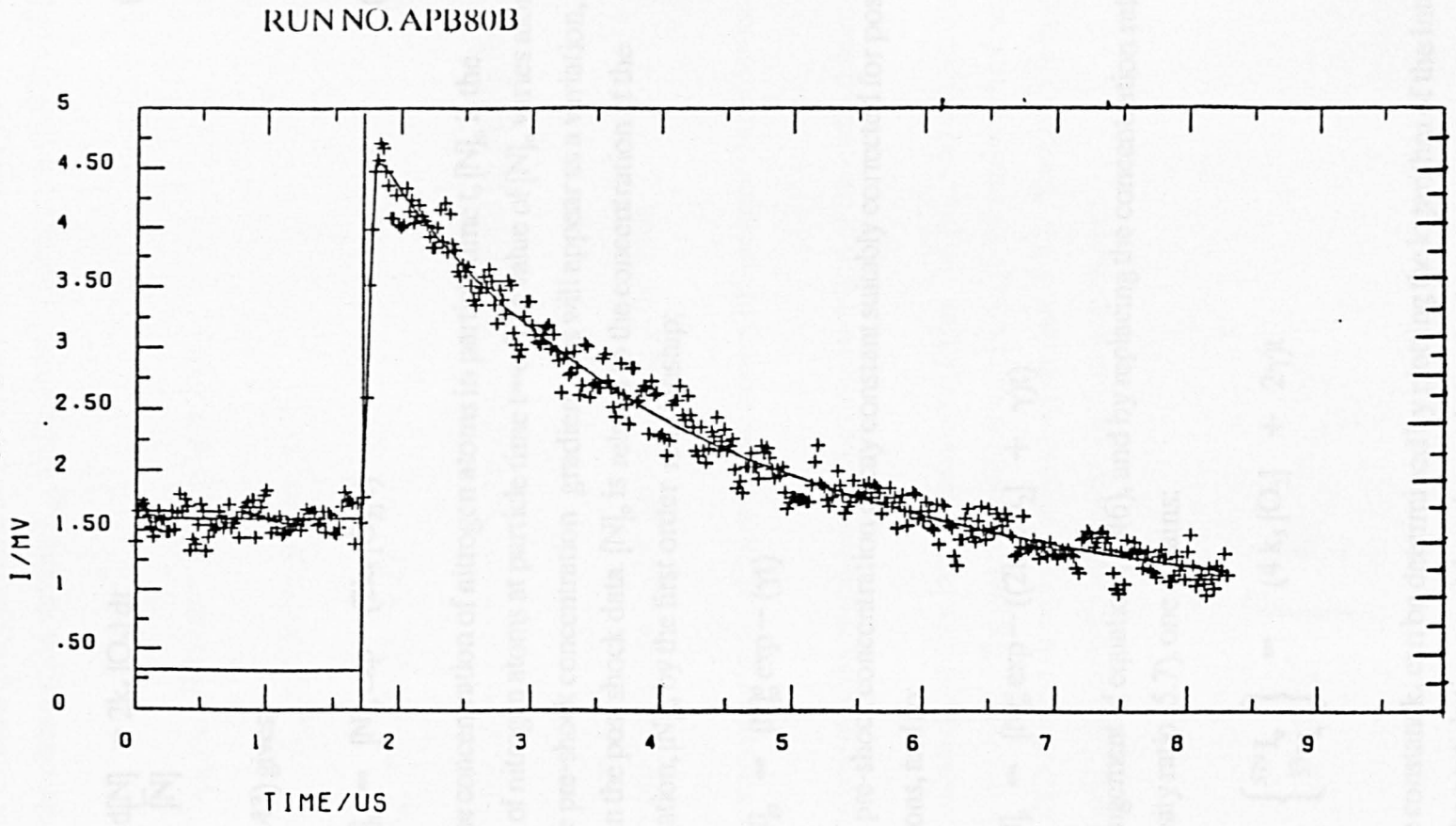

By comparison of the equations given in section 5.2.3 , the N atom removal can be written;

$$-\frac{d[N]}{[N]} = 2k_5[O_2]\,dt \tag{5.43}$$

integrating (5.43) gives;

$$[N]_t = [N]_o \exp -(2k_5[O_2]\,t) \tag{5.44}$$

where $[N]_t$ is the concentration of nitrogen atoms in particle time t, $[N]_o$ is the concentration of nitrogen atoms at particle time t=o. The value of $[N]_o$ varies along the tube due to the pre-shock concentration gradient, this will appear as a variation, in particle time, in the post shock data. $[N]_o$ is related to the concentration at the observation station, $[N]^o_o$, by the first order relationship;

$$[N]_o = [N]^o_o \exp -(\gamma t) \tag{5.45}$$

where γ is the pre-shock concentration decay constant suitably corrected for post shock conditions, and so:

$$[N]_t = [N]^o_o \exp -((2k_5[O_2] + \gamma)t) \tag{5.46}$$

Rearrangement of equation (5.46), and by replacing the concentration ratio with the intensity ratio (5.7), one obtains:

$$\ln \left\{ \frac{^{579}I_o}{^{579}I_t} \right\} = (4k_5[O_2] + 2\gamma)t \tag{5.47}$$

The rate constant k_5 can be determined by plotting the logarithm of the intensity ratio against the particle time, and then determining the increase in the gradient from the decay constant 2γ .

The emission from the first positive band at 579nm at high temperature and immediately post shock, $^{579}I_o$, is given by:

$$^{579}I_o = I_{psg} K(T) \rho_{21}^2 \tag{5.40}$$

The post shock intensity at particle time t, $^{579}I_t$, is related to the cool unshocked gas intensity, at the observation station, I_{psg}, and is given by using eqns. (5.40) and (5.47);

$$^{579}I_t = I_{psg}\,\rho_{21}^2\,K_{(T)}\exp-((4\,k_5\,[O_2[+2\gamma)\,t) \tag{5.48}$$

$$\text{or } ^{579}I_t = I_{psg}\,\rho_{21}^2\,K_{(T)}\exp-(\alpha_{po}\,t) \tag{5.49}$$

$$\text{where } \alpha_{po} = 4\,k_5\,[O_2]+2\gamma \tag{5.49 (a)}$$

Equation (5.49) predicts several key features that should be seen in the shock trace:

1. A steady pre-shock glow (I_{psg}) at the beginning of the trace.

2. An instantaneous rise in emission on the impact of the shock front at t=o.

3. Decay of the intensity which reflects the time variation of the excited species.

The predicted trace has been presented in figure 5.6 (a) , and a typical trace is given in figure 5.6 (b) . The general predictions of eqn. (5.49) are satisfied, with the exception of (2), for the same reasons given in section 5.3.1. To allow for the rise time, equation (5.49) must be integrated, the final equation is:

$$^{579}I_t = I_{psg}K_{(T)}\rho_{21}^2\int_{t-tr}^{t}\exp-\frac{(\alpha_{po}\cdot t)\,dt}{tr} \tag{5.50}$$

Figure 5.7 shows a typical trace taken at 579nm, the full line through the points is a fit to equation (5.50) using the interactive computer graphics system. From each trace values of tr, $K_{(T)}$ and α_{po} can be determined. The constants tr and $K_{(T)}$ can then

Figure 5.6(a) Predicted trace at 579nm.

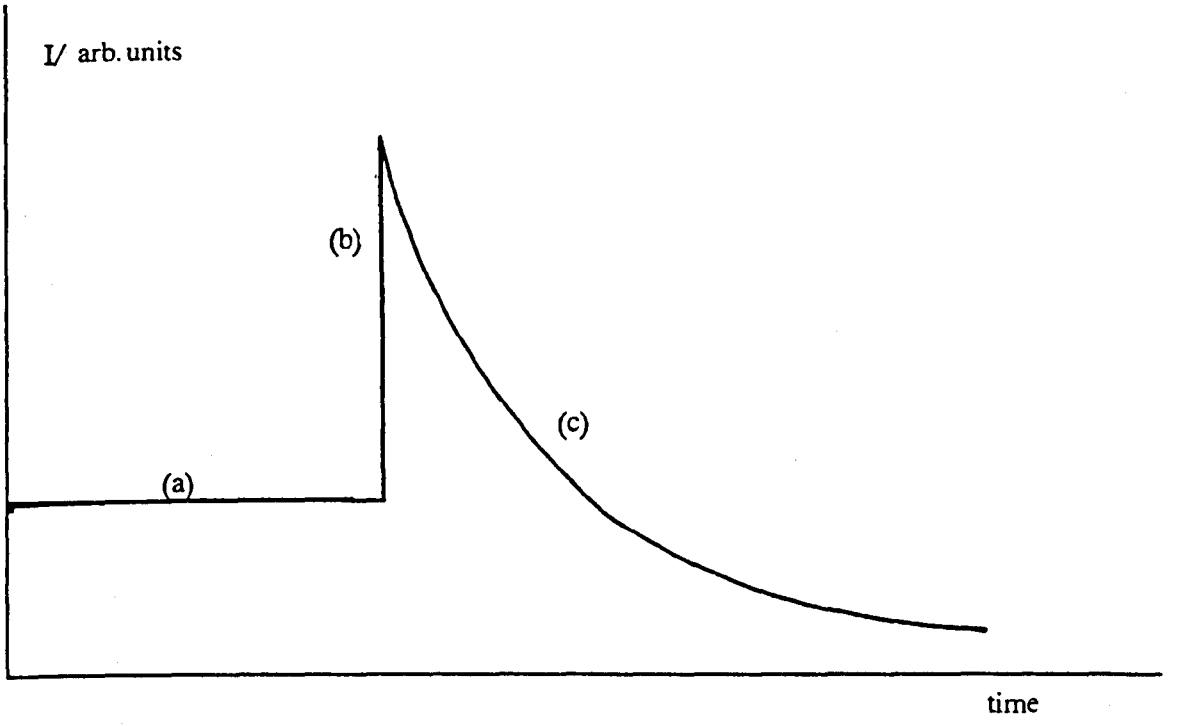

(b) an observed trace at 579nm

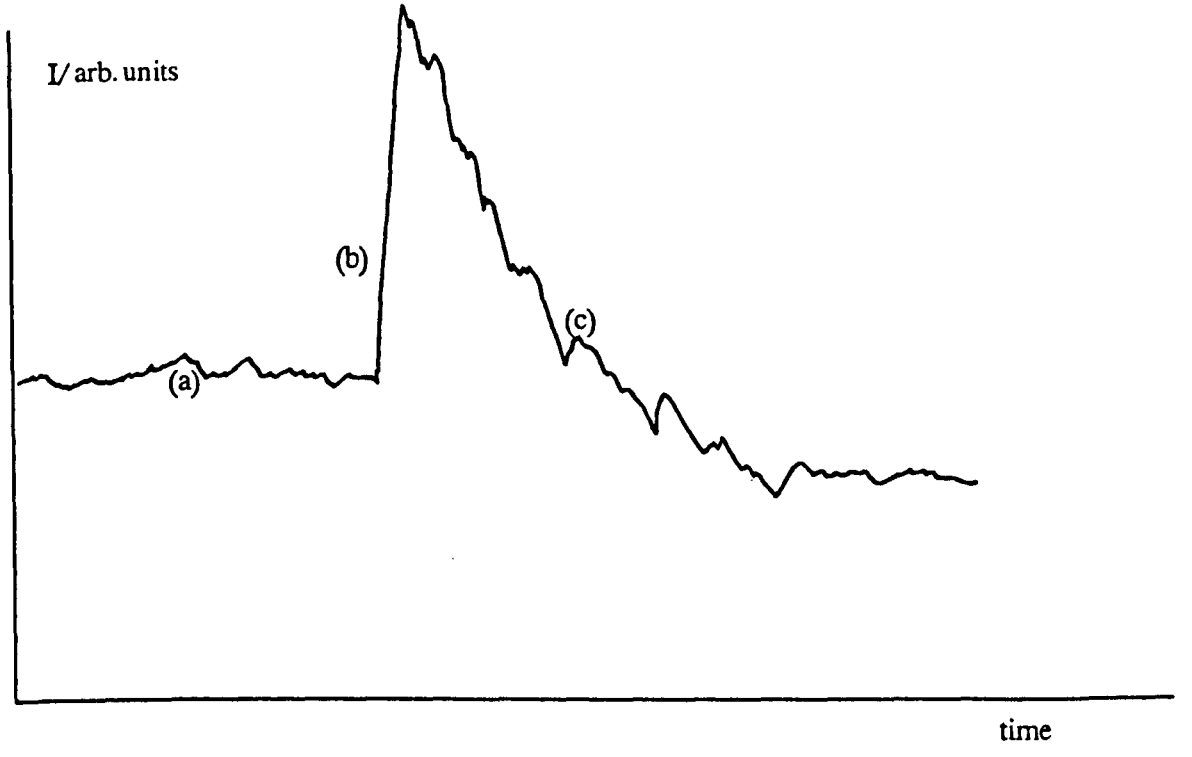

Figure 5.7 Shock trace for the emission band at 579 nm

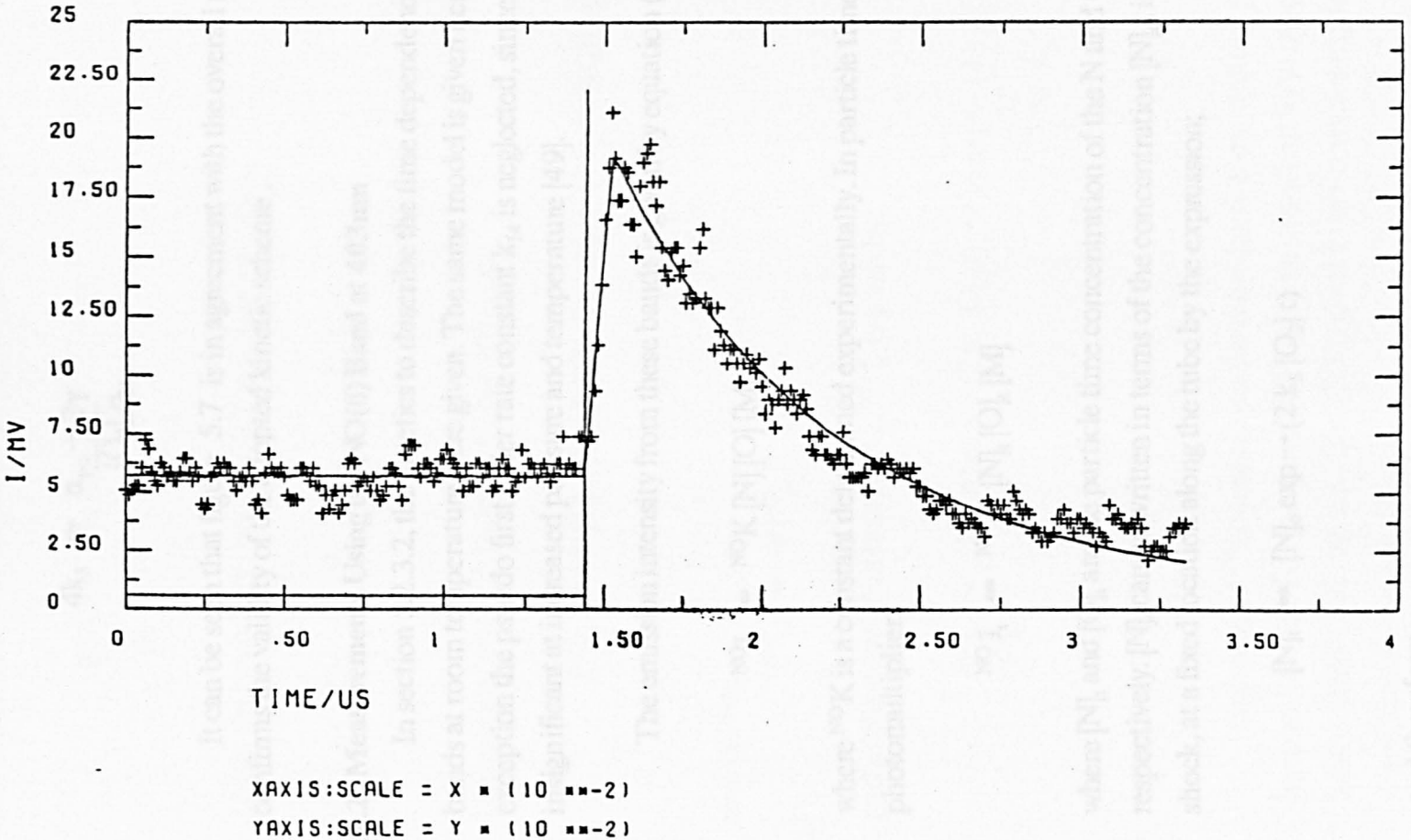

be compared against known values (Section 5.3.1), k_5 can be determined at a known O_2 concentration since (section (4.7)):

$$4k_5 = \frac{\alpha_{po} - 2\gamma}{[O_2]\rho_{21}} \tag{5.51}$$

It can be seen that figure 5.7 is in agreement with the overall model, and so confirms the validity of the adopted kinetic scheme.

5.3.2.2 Measurements Using the NO(ß) Band at 403nm

In section 5.2.3.2, the kinetics to describe the time dependence of the NO(ß) bands at room temperature were given. The same model is given here with the exception the psuedo first order rate constant k_{14} is neglected, since it is rendered insignificant at increased pressure and temperature [49].

The emission intensity from these bands is given by equation (5.19);

$$^{NO}I = {}^{NO}K\,[N]\,[O]\,[M] \tag{5.19}$$

where ^{NO}K is a constant determined experimentally. In particle time using the same photomultiplier;

$$^{NO}I_t = {}^{NO}K\,[N]_t\,[O]_t\,[M] \tag{5.52}$$

where $[N]_t$ and $[O]_t$ are the particle time concentration of the N and O atoms respectively. $[N]_t$ can be written in terms of the concentration $[N]_o$, immediately post shock, at a fixed location along the tube by the expression;

$$[N]_t = [N]_o \exp -(2\,k_5\,[O_2]\,t) \tag{5.44}$$

and therefore;

$$^{NO}I_t = B\,[N]_o\,[O]_t \exp -(2\,k_5\,[O_2]\,t) \tag{5.53}$$

where B is a constant at fixed pressure.

The oxygen atom concentration is governed by two production processes (5.11 and 5.12), the rate of oxygen atom production is therefore:

$$\frac{d[O]}{dt} = 2k_5[O_2][N] \tag{5.54}$$

Using the boundary condition $[O] = [O]_o$ at t=o then:

$$[O]_t = [O]_o + [N]_o\{1 - \exp -(2k_5[O_2]t)\} \tag{5.55}$$

Using equations (5.53 and 5.55), one obtains;

$$^{NO}I_t = B[N]_o\{[O]_o + [N]_o(1 - \exp -(2k_5[O_2]t))\}\exp -(2k_5[O_2]t) \tag{5.56}$$

and at t=o;

$$^{NO}I_o = B[N]_o[O]_o \tag{5.57}$$

and so the relative intensity, $^{NO}I_t / ^{NO}I_o$ is given by;

$$\frac{^{NO}I_t}{^{NO}I_o} = [1+A]\exp -(2k_5[O_2]t) - A\exp -(4k_5[O_2]t) \tag{5.58}$$

where $A = [N]_o/[O]_o$

The value of $^{NO}I_o$ varies along the tube due to the pre-shock concentrations (section 5.2.3.2). The variation of $^{NO}I_o$ can be described by using equation (5.30), substitution of this into equation (5.58) gives a very complex expression, and so a simplification was sought.

The 'post peak' intensity can be modelled by;

$$\ln(^{NO}I_o) = a - b \cdot t \tag{5.59}$$

where a = ln (I_{psg}), I_{psg} is the pre-shock glow, t is the time, and b is a constant. A typical plot is given in figure 5.8 and shows that the relationship is good. From eqn. (5.59):

$$\ln ({}^{NO}I_o) = \ln (I_{psg}) - bt \tag{5.60}$$

or

$${}^{NO}I_o = I_{psg} \exp -(bt) \tag{5.61}$$

Defining the post-shock intensity at t=o, I_o^o, then the post-shock emission is:

$${}^{NO}I_o = I_o^o \exp -bt \tag{5.62}$$

The pre-shock glow and I_o^o are related by the expression [28, 31, 46];

$$I_o^o = I_{psg} \rho_{21}{}^{3\,NO}K_{(T)} \tag{5.63}$$

where ${}^{NO}K_{(T)}$ is the enchancement factor for the NO(β) band, and so substitution of (5.63), (5.62) and (5.58) finally gives;

$$\frac{{}^{NO}I_t}{I_{psg}\rho_{21}{}^{3\,NO}K_{(T)}} = \left\{1+A\right\} \exp -((2\,k_5\,[O_2]+b)\,t) - A \exp -((4\,k_5\,[O_2]+b)\,t) \tag{5.64}$$

where $A = [N]_o/[O]_o$

and b is the pre-shock decay constant suitably corrected for post shock conditions.

Equation (5.64) predicts four regions in the shock trace:

a. The start of the trace, a steady pre-shock glow, I_{psg}
b. Instantaneous rise in intensity on the arrival of the shock front.
c. Attainment of the intensity maximum, dependent upon the parameters.
d. Decay, which reflects the variation of both the N and O atoms with time.

A comparison of the model (eqn. 5.64) with a typical shock trace is given in figures 5.9 (a) and 5.9 (b) . Conditions a, c and d are satisfied, b is not observed, for the same reasons described in section 5.3.1 . To allow for the rise time, tr, equation (5.64) must be integrated, the final form now becomes:

Figure 5.8 Linear approximation of the pre-shock decay at 403nm

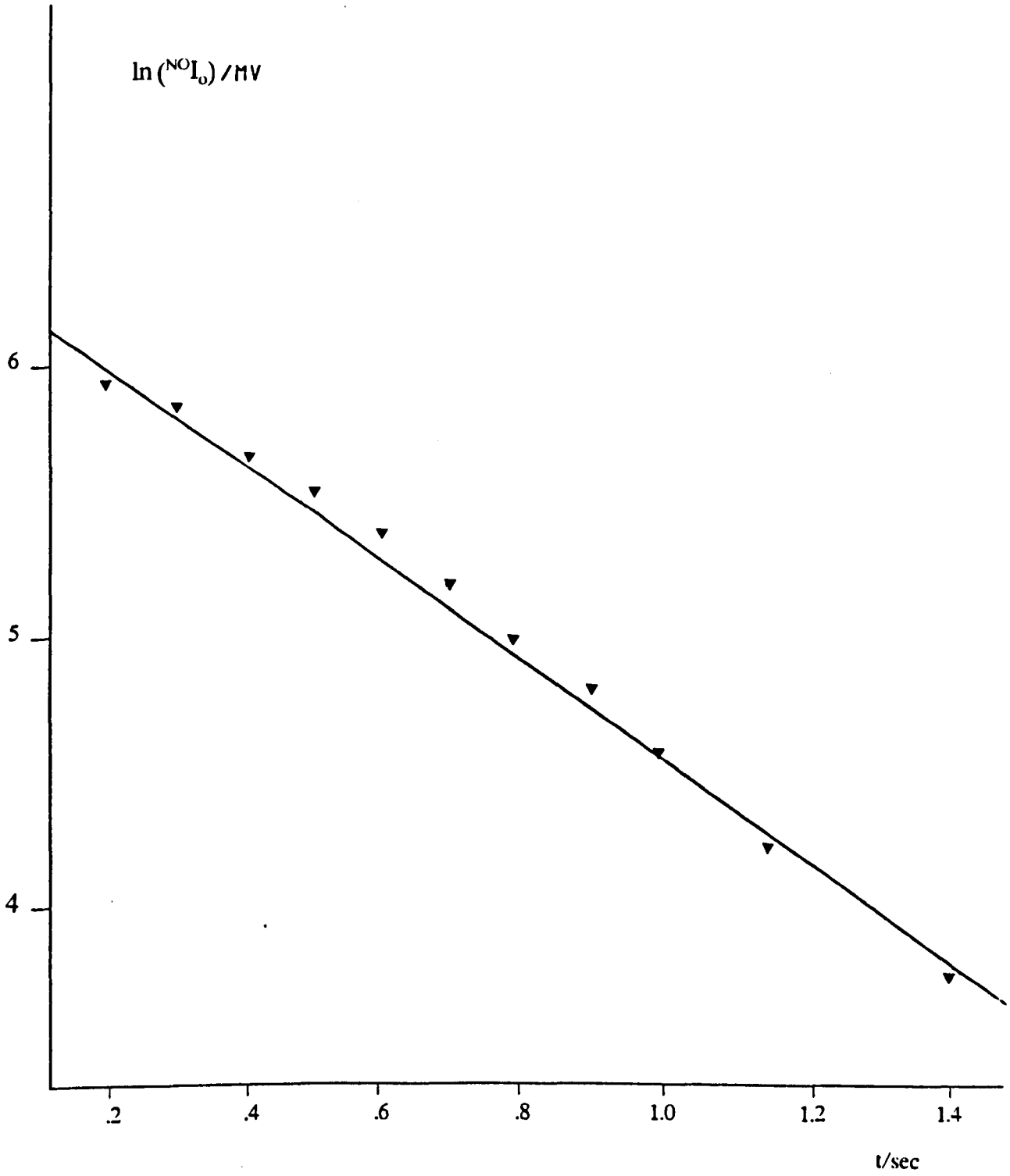

Figure 5.9(a) Predicted trace at 403 nm.

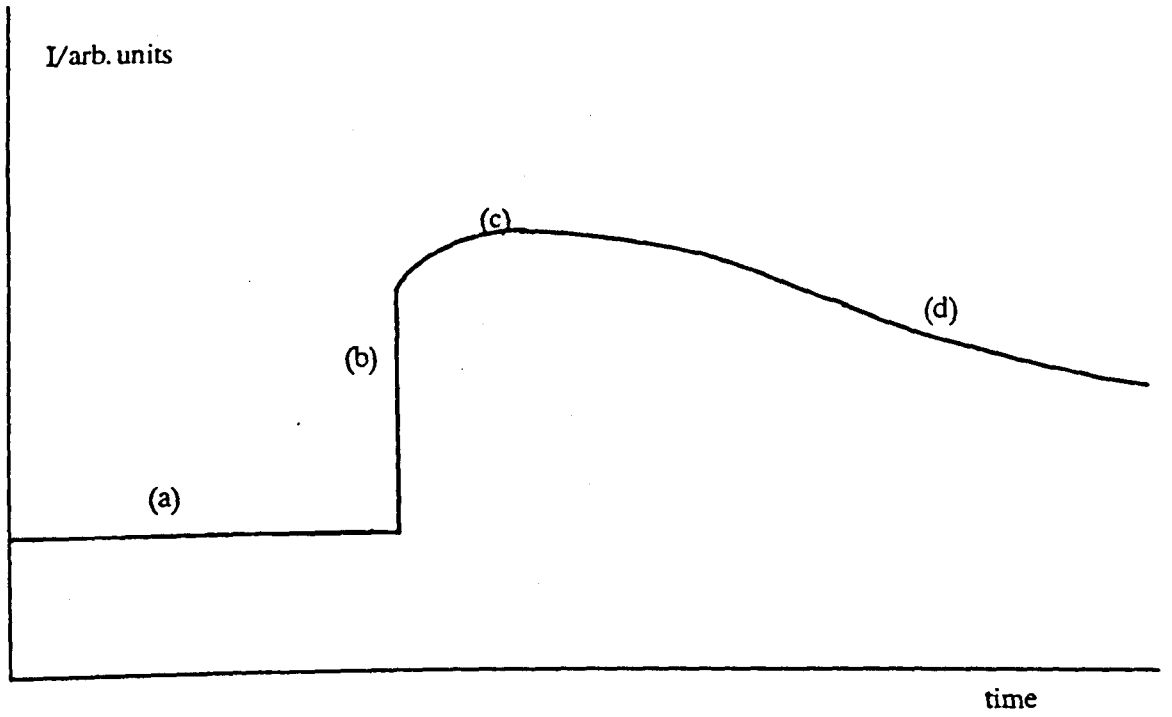

(b) an observed trace at 403nm

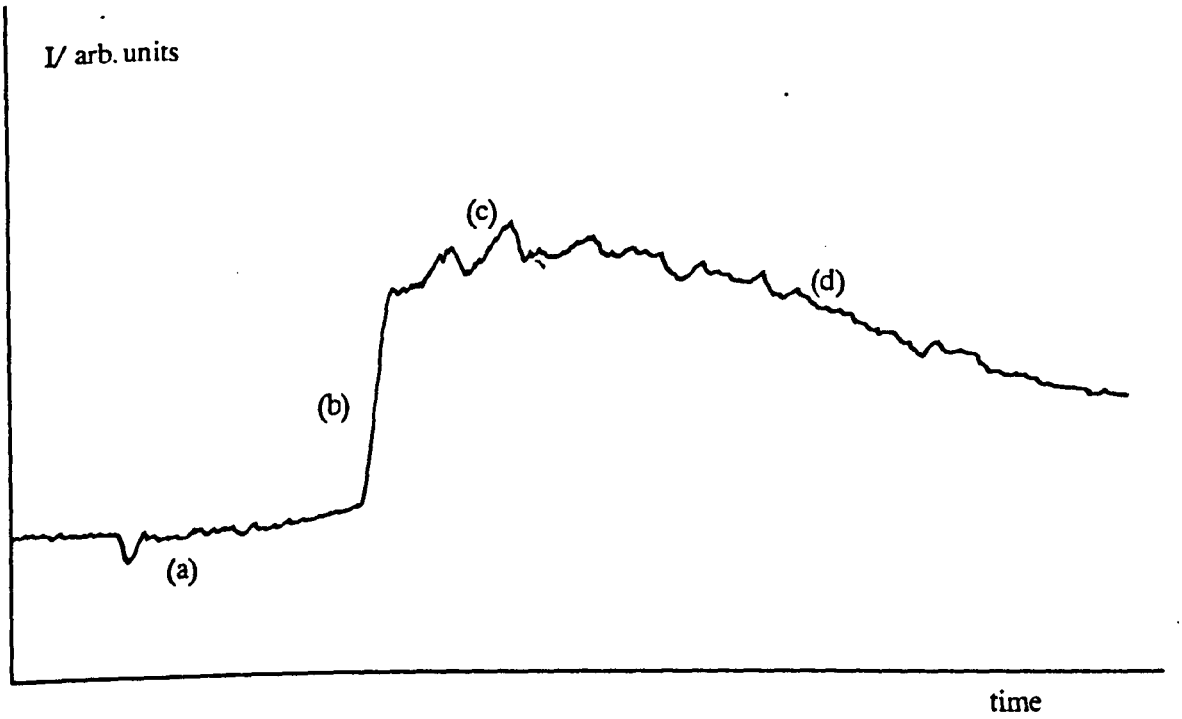

$$\frac{^{NO}I_t}{I_{psg}\,\rho_{21}{}^{3\,NO}K_{(T)}} = \int_{t-tr}^{t} \frac{\{1+A\}\exp-((2k_5[O_2]+b)t)\,dt}{tr} - \int_{t-tr}^{t} \frac{A\exp-((4k_5[O_2]+b)t)\,dt}{tr} \qquad (5.65)$$

Figure 5.10 shows a trace, obtained at 403nm, the full line through the data points was fitted using equation (5.65), by use of the interactive computer graphics system. From each trace, values of tr, $^{NO}K_{(T)}$ and $2k_5[O_2]$ can be obtained. k_5 can then be determined if $[O_2]$ is known.

5.4 Computer Analysis of the Post Shock Data

Two programs are used for the storage and treatment of the post shock data. One is concerned with the data transfer and allocation, the second is for analysis.

5.4.1 The Transfer and Storage of Data

After the data has been stored on magnetic tape [52], it is allocated disc space within the G.E.C. 4080 computer. The digitised points, 1024 in total, are transferred using the HP2647A graphics terminal. The points are converted to millivolt and time co-ordinates, and along with the sweep speed, sensitivity and run name stored on the D1005 disc.

5.4.2 The Data Analysis

The equations that have been developed for the high temperature post shock behaviour are analytically solved by non-linear least squares. The analysis system is designed to work with both the HP2647 and Volker Craig terminals.

Figure 5.10 Emission trace of the $N+O_2$ reaction at λ=403nm

RUN NO. APB105B

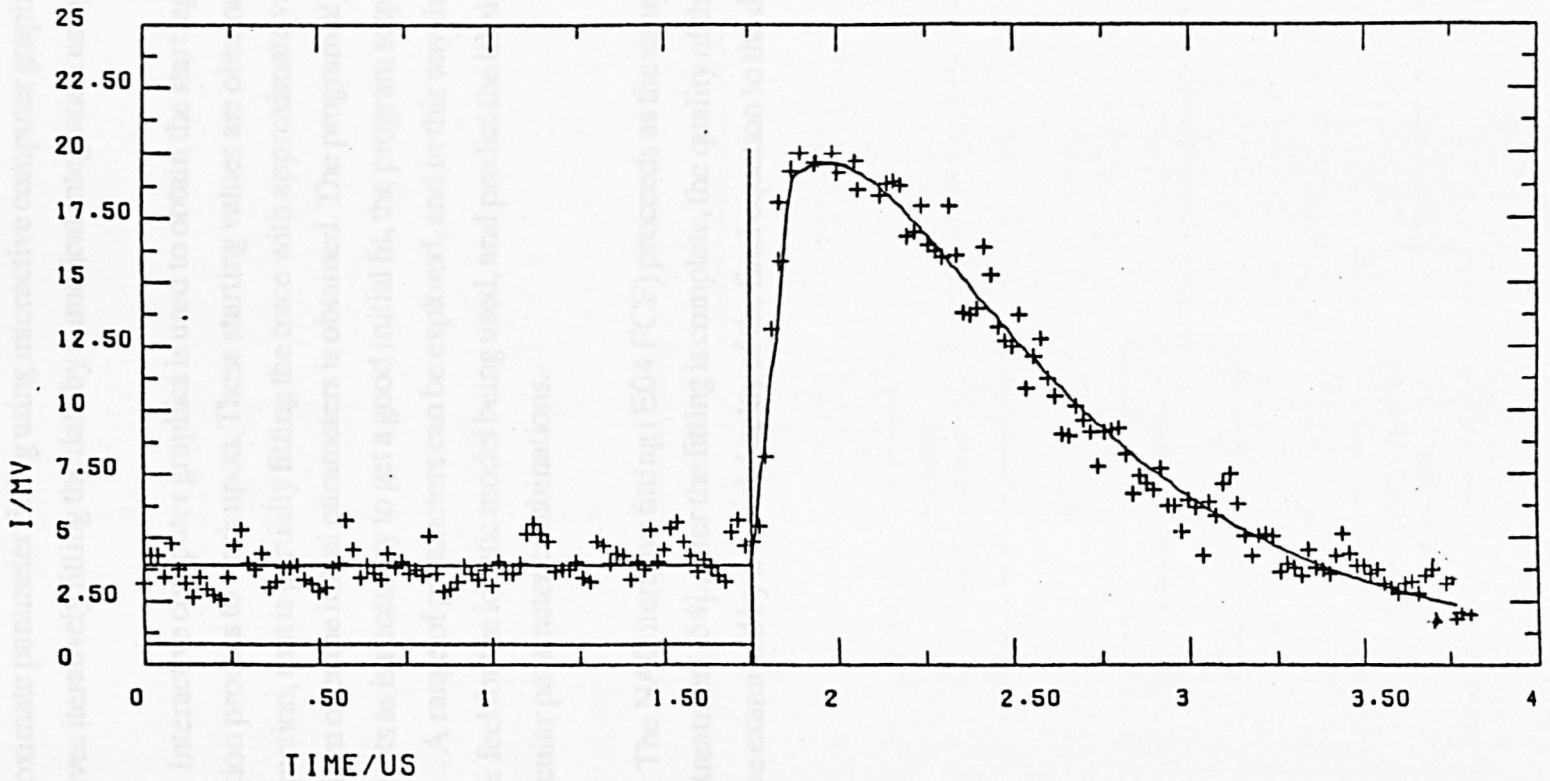

The analysis is divided into two sections. The first is concerned with approximate parameter fitting using interactive computer graphics [52]. The second involves iteratively fitting the data by numerical integration using Simpson's rule [53].

Interactive computer graphics is used to obtain the starting values for the iteration process to work upon. These starting values are obtained by visual interaction, that is partially fitting the trace with approximate values. In this way, freedom over the initial parameters is obtained. The program allows as many attempts as is necessary to get a good initial fit, the program sequence is given in figure 5.11 . A range of parameters can be explored, and in this way the controller can gain a better feel for the kinetic model being used, and predict the likely outcome of particular parameter combinations.

The NAG iterative fitting (E04 FCF) proceeds as the usual 'blind methods' of data treatment [54]. After the fitting is complete, the quality of the fitted parameters can be examined by a visual display of the final equation to the data points.

Figure 5.11 Block diagram of the interative computer graphics system.

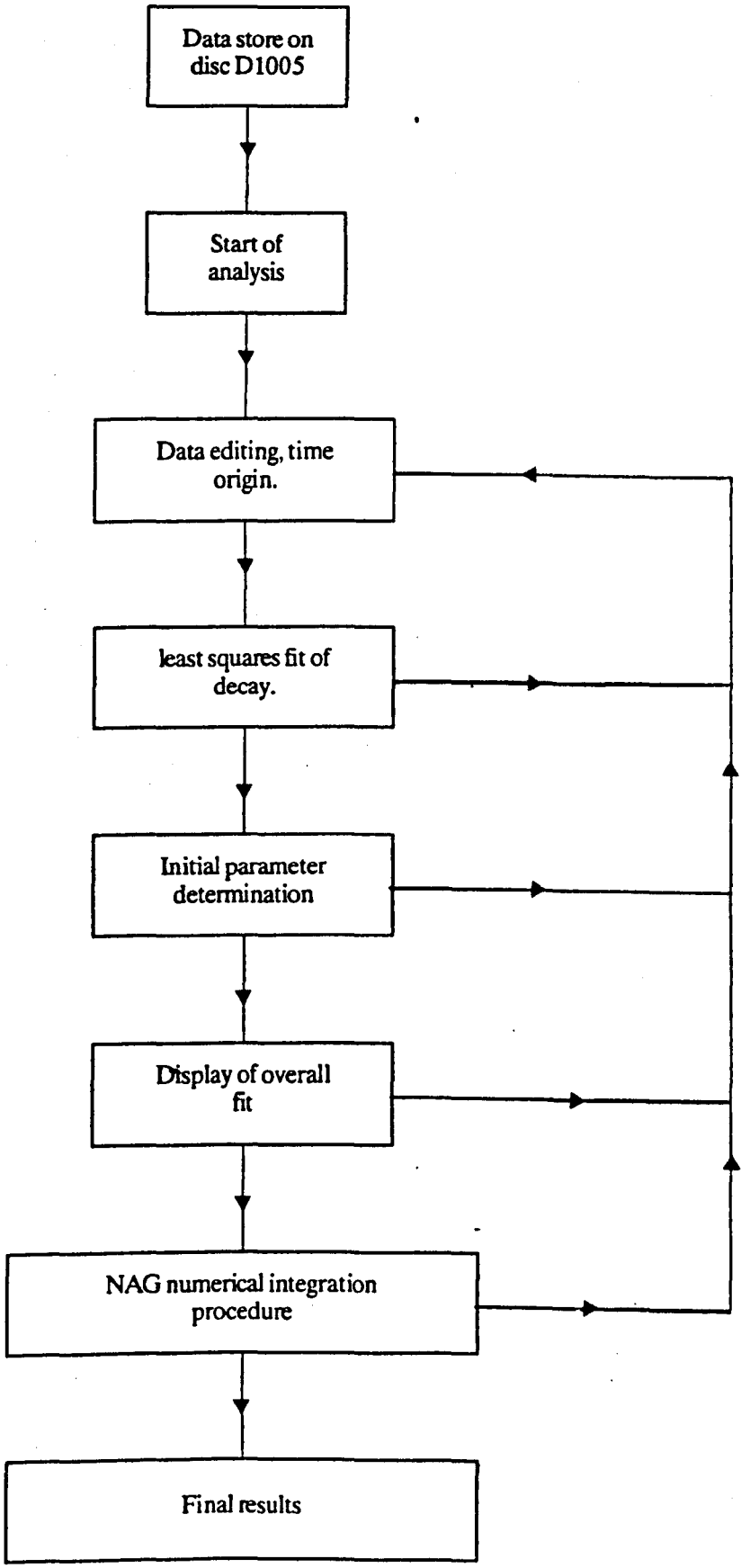

CHAPTER SIX

6.0 The Temperature Dependence of the Lewis Rayleigh Afterglow of Atomic Nitrogen.

6.1 Introduction.

The first positive emission (1+) of atomic nitrogen was studied with a view to developing a method for investigating nitrogen atom reactions at high temperature.

The first positive emission has been used to estimate the nitrogen atom concentration. A variation of the emissivity with the temperature had been reported previously (Chapter Two). The aim was therefore to measure the emissivity and compare the results against those of Gross [23], obtained at high temperature using a discharge flow shock tube. The current measurements were found to be wavelength dependent, the temperature dependence was investigated for several emission bands and the results then interpreted in the light of the currently accepted theory.

6.2 Experimental.

Nitrogen was passed through a microwave discharge and into a discharge flow tube at a linear flow velocity between 0.5 and 2.3 ms^{-1}.

Pre-shock conditions were established, the concentration gradient along the tube was determined by measuring the emission intensity with a mobile photomultiplier, fitted with an interference filter (Balzers), centred at 579 nm.

Shock waves were run into the nitrogen flow at velocities between 0.7 and 1.725 km s^{-1}, giving a temperature range between 500 and 1600 K. The post-shock emission was measured by two photomultipliers. One was fitted with an interference filter (579 nm) and was used to monitor the emission from N_2 ($B^3\pi_g$) (v=11) [18,19]. The other was fitted to a monochromater (Bentham BN4, 3 nm bandwidth); this was used to isolate the emissions at 576, 586 and 661 nm, which correspond to transitions from the N_2 ($B^3\pi_g$) molecule at the vibrational levels v=12, 10 and 6 respectively [18,19].

Nitrogen atom concentrations were determined by titration with NO by the reaction [55]:

$$N + NO \longrightarrow N_2 + O \qquad (6.1)$$

The NO was added to the nitrogen atom stream ($\sim 2x10^{-3}$ millimol s^{-1}) by using the reverse flow injector (Chapter Three). For a given discharge power and nitrogen flow rate, the NO flow rate was adjusted until the emission was completely extinguished and the titration therefore complete.

6.3 The Room Temperature Data.

Plots of $(^{579}I_l)^{-\frac{1}{2}}$ against flow tube length gave good straight lines at all of the pressures studied. Sample plots are given in figure 6.1 .

The second order rate constant, α_1, determined from the slope of the plot (Chapter Five) is given by;

$$\text{Slope} = 2\alpha_1 \qquad (6.2)$$

Figure 6.1 The variation of $I^{-\frac{1}{2}}$ with flow tube length.

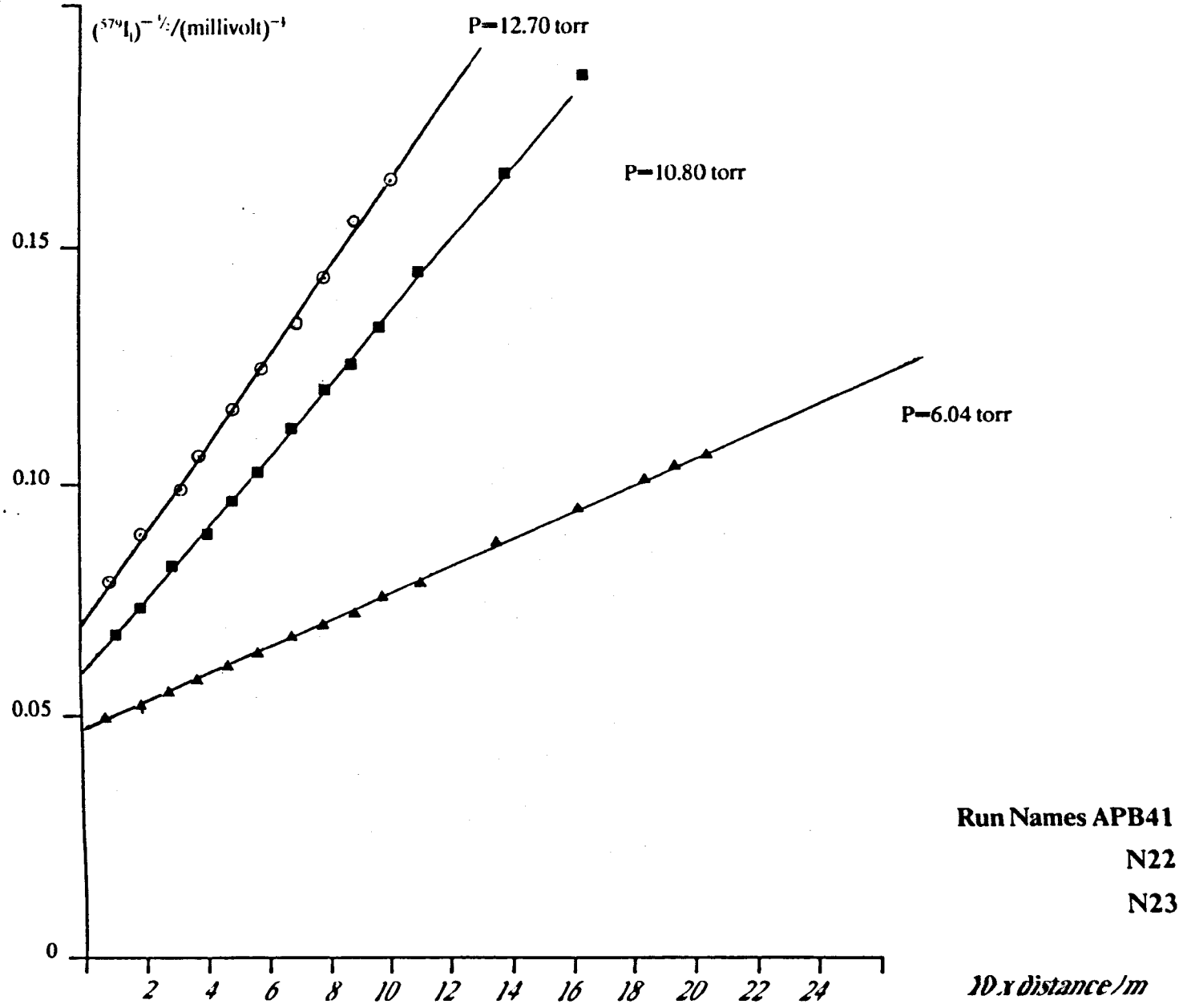

Table 6.1 Room Temperature Determinations of the Rate Constants α_1 and α_t

Run Name	$(2\alpha_1) \times 10^4$ / $mV^{i}cm^{-1}$	Pressure / torr	Flow velocity / $cm\ s^{-1}$	$(2\alpha_t/B^{i}) \times 10^2$ / $mV^{i}s^{-1}$
APB 41	2.21	6.04	101.1	2.24
42	2.47	6.56	93.1	2.30
43	2.37	4.544	112.3	2.66
44	2.73	6.74	90.7	2.48
45	2.99	6.91	88.4	2.6
46	2.99	6.91	88.4	2.6
47	1.844	5.53	114.1	2.173
48	1.9	5.35	114.3	2.17
49	2.61	6.91	88.4	2.3
50	3.86	9.24	66.1	2.55
80	2.17	5.8	105.3	2.24
79	2.31	5.8	105.3	2.43
78	2.09	5.8	105.3	2.17
77	2.63	5.8	105.3	2.74
76	2.09	5.8	105.3	2.17
75	2.22	5.8	105.3	2.31
74	2.2	5.8	105.3	2.28
73	2.2	5.8	105.3	2.28
54	2.93	5.8	105.3	3.08
55	2.88	5.8	105.3	3.03
56	2.29	5.8	105.3	2.42
57	2.40	5.8	103.3	2.52
58	2.10	5.8	105.3	2.21
59	2.06	5.8	105.3	2.17
60	2.54	5.8	105.3	2.67
61	2.47	5.8	105.3	2.60
62	2.1	5.8	105.3	2.21
63	2.25	5.8	105.3	2.35

Table 6.1

(Continued from previous page)

Run Name	$(2\alpha_i) \times 10^4$ / $mV^{-1}cm^{-1}$	Pressure / torr	Flow velocity / $cm\ s^{-1}$	$(2\alpha_i/B^i) \times 10^2$ / $mV^{-1}s^{-1}$
APB 64	1.899	5.8	105.3	1.98
65	1.92	5.8	105.3	2.02
66	2.0	5.8	105.3	2.106
67	2.06	5.8	105.3	2.176
68	2.1	5.8	105.3	2.21
69	2.1	5.8	105.3	2.21
70	2.1	5.8	105.3	2.21
71	2.1	5.8	105.3	2.21
N 28	2.6	6.65	91.9	2.85
29	2.53	5.01	120.0	3.036
30	5.40	4.23	144	1.853
31	6.33	4.67	63.2	3.49
32	1.97	5.4	113.2	2.23
33	1.45	2.59	236	3.42
8	2.7	5.61	101.5	2.74
9	2.67	3.8	148	3.95
10	2.88	3.02	186	3.35
11	2.19	3.65	154	3.37
12	2.01	4.2	114.2	2.295
13	5.34	9.97	58.16	3.10
14	8.01	10.4	54.0	4.32
15	2.24	4.75	128	2.86
16	2.40	5.57	95.8	2.29
18	2.96	6.48	86.7	2.566
23	9.27	12.7	44.2	4.10
22	8.20	10.8	52.0	4.27
21	5.65	9.07	61.9	3.50
19	3.02	6.03	93.1	2.82
27	2.06	2.41	252.7	4.81
26	2.13	3.37	181	3.88

the values of $2\alpha_1$ from each experimental run are given in table 6.1 .

The psuedo-second order rate constant, α_t is related to α_1 by the expression;

$$2\alpha_t = 2\alpha_1 B^{\frac{1}{2}} v \qquad (6.3)$$

where v is the linear flow velocity (cm s^{-1}) and $B^{\frac{1}{2}}$ is a constant.

Values of $2\alpha_t/B^{\frac{1}{2}}$ were determined from the slope each plot and are given in table 6.1 .

The constant B was determined by titration, eqn. (6.1). The results were averaged and gave a value:

$$B = (5.0 \pm 1.9) \times 10^{15} \text{ mV dm}^6 \text{ mol}^{-2}.$$

The end point of each titration was determined to within ± 10% error, the error limit given is the standard error of the mean.

The psuedo-second order rate constant, α_t, is also (Chapter Five);

$$\alpha_t = k_2 + k_3 [N_2] \qquad (6.4)$$

where k_2 and k_3 are the second and third order rate constants for the reactions (Chapter Five):

$$N + N \longrightarrow N_2 \qquad k_2 \qquad (6.5)$$

$$N + N + N_2 \longrightarrow N_2 + N_2 \qquad k_3 \qquad (6.6)$$

From a linear plot of α_t against $[N_2]$ or pressure (eqn. 6.4), the rate constants k_2 and k_3 can be determined from the intercept and slope respectively. A plot of the data according to this form is given in figure 6.2 .

Figure 6.2 The variation of α_t with pressure.

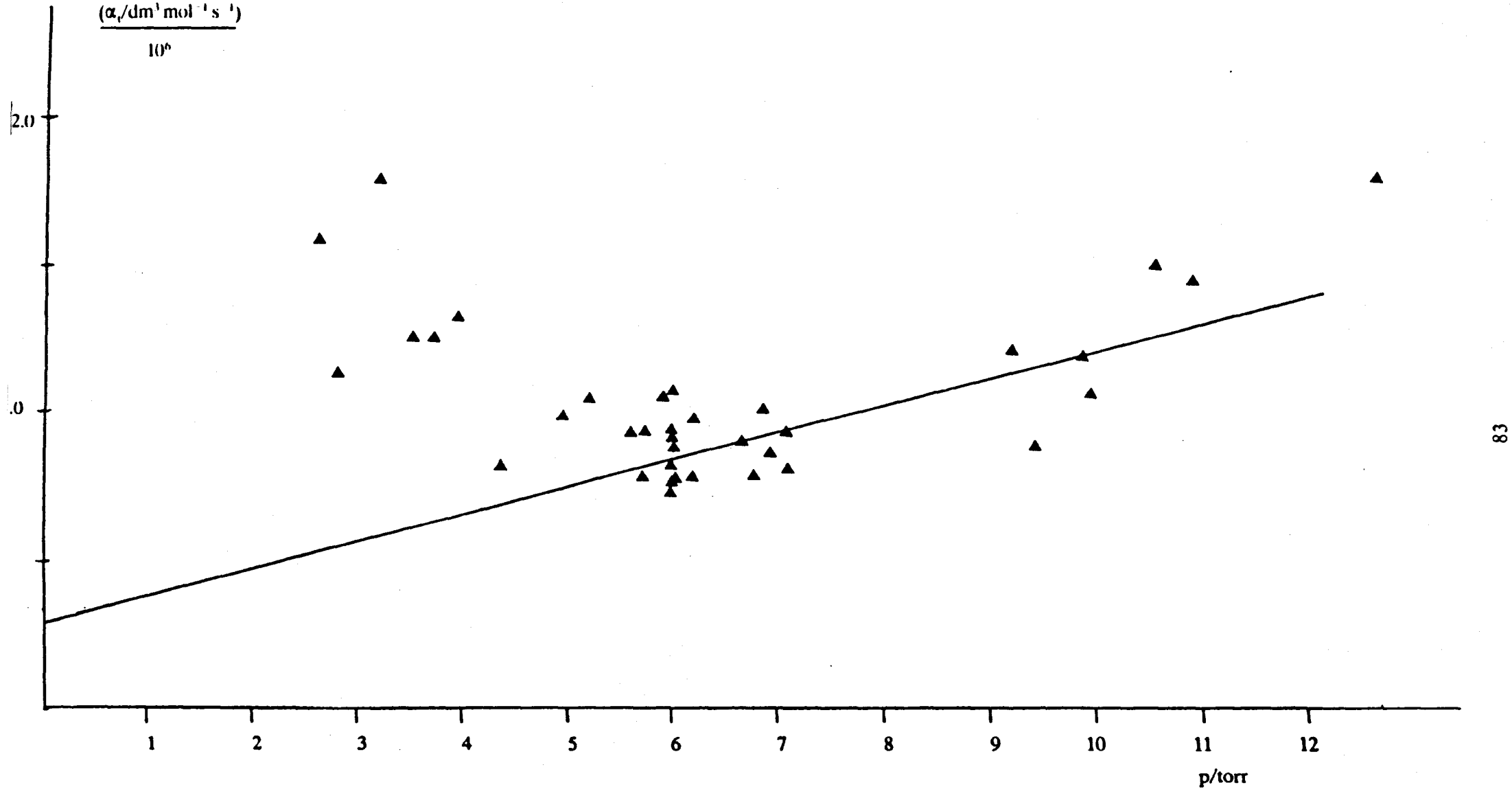

Using the values for the slope and intercept, determined by linear least squares analysis of the data between 5.8 and 12.7 torr, the rate constants k_2 and k_3 are:

$$k_3 = (1.71 \pm 0.18) \times 10^9 \text{ dm}^6 \text{ mol}^{-2}\text{s}^{-1}$$

$$k_2 = (3.14 \pm 0.66) \times 10^5 \text{ dm}^3 \text{ mol}^{-1}\text{s}^{-1}$$

the error limits are 2σ (95%) confidence values.

6.4 Discussion of the Room Temperature Data.

It was shown in section 6.3 , that plots of $(^{579}I)^{-1}$ against t gave good lines, and this was consistent with the model given in Chapter Five. Previous workers have found curvature in plots equivalent to these. Brennon *et al.* [56] attributed these non-linearities to a significant first order wall recombination rate (k_4). Both impurities and short lived intermediates have also been postulated to explain these effects [57,58,59,60]. The results obtained in this study show that the model adopted is reasonable; nitrogen atom recombination can be modelled in this system by equations that are second order with respect to nitrogen atoms.

In these experiments, the pre shock concentration gradient was measured in a large apparatus that is frequently opened to the atmosphere. Although the measurements were not designed to obtain the rate constants k_3 and k_2, a comparison of the data against previous estimates is still worthwhile. A series of determinations of k_3, the homogenous recombination rate constant, are given in table 6.2 . The value obtained in this work is in good agreement with the determinations of Clyne and Stedman, and the recommended value of Campbell and Thrush.

The value of k_2, the heterogenous recombination rate, is a factor of two below the value of Campbell and Thrush [21]. Their determination was carried out in a smaller diameter tube (D = 26.6mm). Correcting for the difference in size between the apparatus, the current value of k_2 becomes approximately the same as theirs.

Table 6.2 Room Temperature Determinations of the Homogenous Third Order Rate Constant k_3

$\frac{k_3 \times 10^{-8}}{dm^6\,mol^{-1}\,s^{-1}}$	Authors	Ref
18.0	Clyne & Stedman	61
44.0	Dunford	62
7.0	Harteck	59
7.7	Kretchmer & Peterson	63
13.8	Campbell & Thrush	21
27.0	Marshall	64
17.1	This work	—

Recommended value (Baulch): $k_3 = 1.38 \times 10^9 dm^6 mol^{-2} s^{-1}$

The rate constants k_2 and k_3 were determined from the second order plot (fig. 6.2). From the model (eqn. 6.4), a straight line would be expected, in accord with both Campbell and Thrush and Clyne and Stedman, and a straight line was obtained at higher pressures (P> 5 torr). The majority of the measurements were conducted at 5.8 torr and since only a few determinations of α_i were made at pressures above this, greater errors in the value of k_2 and k_3 will be incurred.

It was necessary to measure both the pre-shock glow and decay constant at pressures below those at which most of the work was conducted (5.8 torr). The decay constant α_i was measured, plotted (fig. 6.2), and found to give curvature at pressures P<5 torr.

The effect of impurities at low pressure has been considered [58], and would be negligible in this system. Furthermore, a pink afterglow region [65,66,67] was observed downstream of the discharge, and this is indicative of purity. It is noted however that the purity control imposed in these experiments is not as strict as that of Campbell and Thrush [21].

Curvature in plots equivalent to fig. 6.2 have been reported. Brennon and Shane [56] have suggested that the homogenous rate constant k_3, is in fact the sum of two separate rate constants. Using a mechanism equivalent to Campbell and Thrush, but including the possibility for recombination directly into the ground state, they were able to show;

$$k_3 = k_G + k_A \left\{ \frac{1 + a\ [N_2]}{1 + a'\ [N_2]} \right\} \qquad (6.7)$$

where k_G is the rate constant for the formation of the ground state molecule and k_A is the rate constant for the formation of $N_2(A^3\Sigma_u^+)$ state, a and a′ are constants.

By suitable selection of the parameters a and a′ they were able to produce a rate constant k_3 that increased at low pressure (~ a factor of two between 5 and 1 torr).

The present work appears to support the contention of Brennon and Shane [56]. However, the purpose of the work was to measure the emissivity at high temperature, a more detailed analysis was not possible since no further measurements were taken.

6.5 The High Temperature Results.

A typical high temperature trace, taken using an interference filter centred at 579 nm, is given in fig. 6.3 . It shows the steady pre-shock glow, a sharp increase in emission with the arrival of the shock front and then decay which reflects the pre-shock concentration gradient. Each trace was fitted using the equation (Chapter Five);

$$ {}^{F.P}I_t = I_{pre}\,\beta_1^2\,K_{(T)} \int_{t-tr}^{t} (1+\varphi t)^{-2} \cdot dt \qquad (6.8) $$

where ${}^{F.P}I_t$ is the post shock emission intensity at particle time t, $K_{(T)}$ is the relative emissivity at temperature T_2 relative to room temperature T_1, φ is a constant that describes the variation of the emission due to the pre-shock concentration gradient and tr is the integration time for the system.

The fit from each trace determines the constants $K_{(T)}$, φ and tr. The values of φ and tr can be compared against experimental values and hence $K_{(T)}$ obtained.

A series of shocks were performed looking at the emission at 579 nm. The values of $K_{(T)}$, determined by the method given above, are given in table 6.3 . It can be seen at high temperature that all of the values of $K_{(T)}$ are less than one. The results have been plotted on a log ($K_{(T)}$) against log (T) graph and are given in figure 6.4 . Also plotted are the results of P.M. Borrell [68], who used an interference filter centred at 579 nm; the agreement between the data is excellent. The results of Gross [23], who used an interference filter that encompassed several emission bands are also given. It was realised at this point (see section 6.6) that the principal difference between these measurements and those of Gross was the possible wavelength dependence of the emissivity. Further measurements were made in order to test this hypothesis.

A series of measurements, using the monochromator (3nm bandwidth) to isolate the emissions at 576nm (v=12), 586nm (v=10) and 661nm (v=6), were made. A sample trace, taken at 661nm, is given in figure 6.5 . It shows more scatter than the 579nm trace, due to the reduced emission intensity (approximately a factor of 50).

Figure 6.3 Shock trace for the emission band at 579 nm

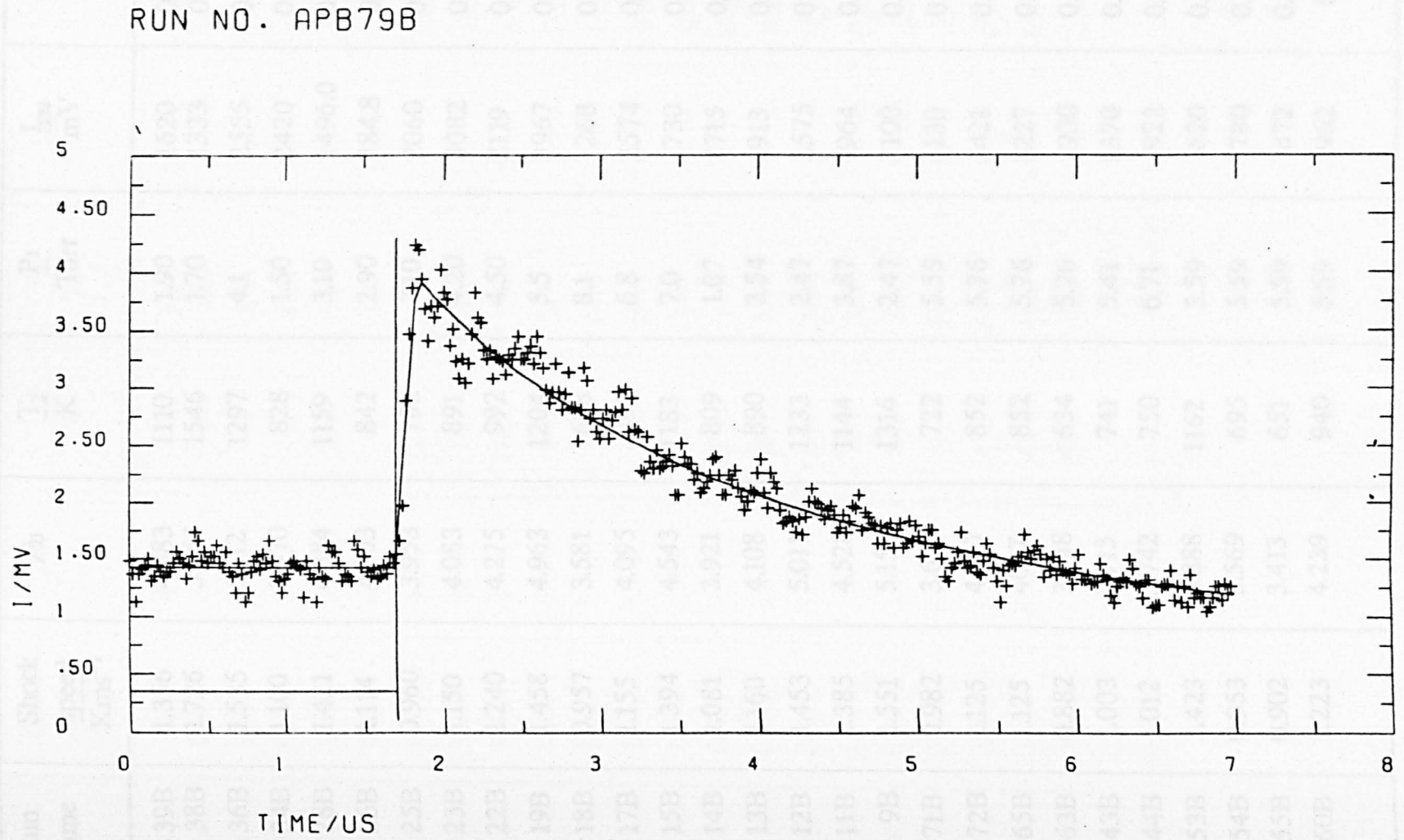

Table 6.3 Shock Parameters for the Enhancement Data at 579 nm (filter). (15 nm bandwidth)

Run Name	Shock speed / Kms^{-1}	ρ_{21}	T_2 / K	P_1 / Torr	I_{psg} / mV	$K_{(\eta)}$
APB 39B	1.356	4.483	1110	1.90	1620	0.202
38B	1.726	5.464	1546	1.70	1333	0.1186
36B	1.535	5.112	1297	4.1	2555	0.1032
34B	1.100	3.970	828	1.50	2420	0.387
28B	1.421	4.884	1159	3.10	1496.0	0.207
26B	1.114	4.003	842	2.90	284.8	0.232
25B	0.960	3.953	702	2.10	2060	0.352
23B	1.150	4.083	891	4.20	3082	0.273
22B	1.240	4.275	992	4.50	2119	0.243
19B	1.458	4.963	1204	5.5	3967	0.131
18B	0.957	3.581	698	8.1	1268	0.30
17B	1.155	4.095	895	6.8	2574	0.260
15B	1.394	4.543	1183	7.0	1730	0.153
14B	1.081	3.921	809	1.07	2715	0.345
13B	1.160	4.108	890	3.54	1913	0.340
12B	1.453	5.011	1233	2.47	2575	0.137
11B	1.385	4.528	1144	3.87	1964	0.158
9B	1.551	5.153	1316	2.47	3100	0.130
71B	0.982	3.658	722	5.59	1130	0.273
72B	1.125	4.027	852	5.76	1421	0.190
65B	1.125	4027	852	5.76	1227	0.194
63B	0.882	3.348	634	5.76	930	0.535
43B	1.003	3.715	741	5.41	1370	0.231
44B	1.012	3.742	750	6.71	922	0.271
53B	1.423	4.888	1162	5.59	620	0.115
54B	0.953	3.569	695	5.59	780	0.271
55B	0.902	3.413	651	5.59	872	0.32
60B	1.223	4.239	940	5.59	962	0.187

Table 6.3 *(Continued from previous page)*

(15 nm bandwidth)

Run Name	Shock speed / Kms^{-1}	ρ_{21}	T_2 / K	P_1 / Torr	I_{psg} / mV	$K_{(T)}$
APB 61B	1.237	4.269	971	5.59	1155.0	0.154
62B	0.962	3.599	704	5.59	987.0	0.372
47B	0.903	3.413	651	5.50	842.0	0.372
49B	0.874	3.321	627	6.88	953.0	0.371
57B	1.000	3.709	739	5.59	800.0	0.263
58B	1.114	4.003	842	5.80	1246.0	2.00
59B	1.459	4.963	1204	5.80	1377.0	0.100
66B	1.128	4.036	857	5.59	1291.0	0.21
68B	1.442	4.930	1185	5.59	1010.0	0.097
69B	1.156	4.099	885	5.59	760.0	0.202
70B	1.003	3.715	735	5.59	1138.0	0.270
80B	1.092	3.850	820	5.59	1277.0	0.190
79B	1.077	3.911	813	5.59	1076.0	0.224
78B	0.987	3.669	726	5.59	1202.0	0.263
77B	0.899	3.400	647	5.59	642.0	0.259
76B	0.891	3.374	640	5.59	1267.0	0.314
75B	1.013	3.742	750	5.59	1264.0	0.264
48B	0.897	3.394	645	5.33	882.0	0.352
7B	0.858	3.266	614	6.6	117.4	0.501
6B	0.880	3.341	632	4.78	2147.0	0.447
5B	0.878	3.334	630	5.28	352.0	0.406
4B	0.930	3.502	670	3.63	569.0	0.304

Figure 6.4 Log ($K_{(T)}$) against log (T) at 579 nm (filter).

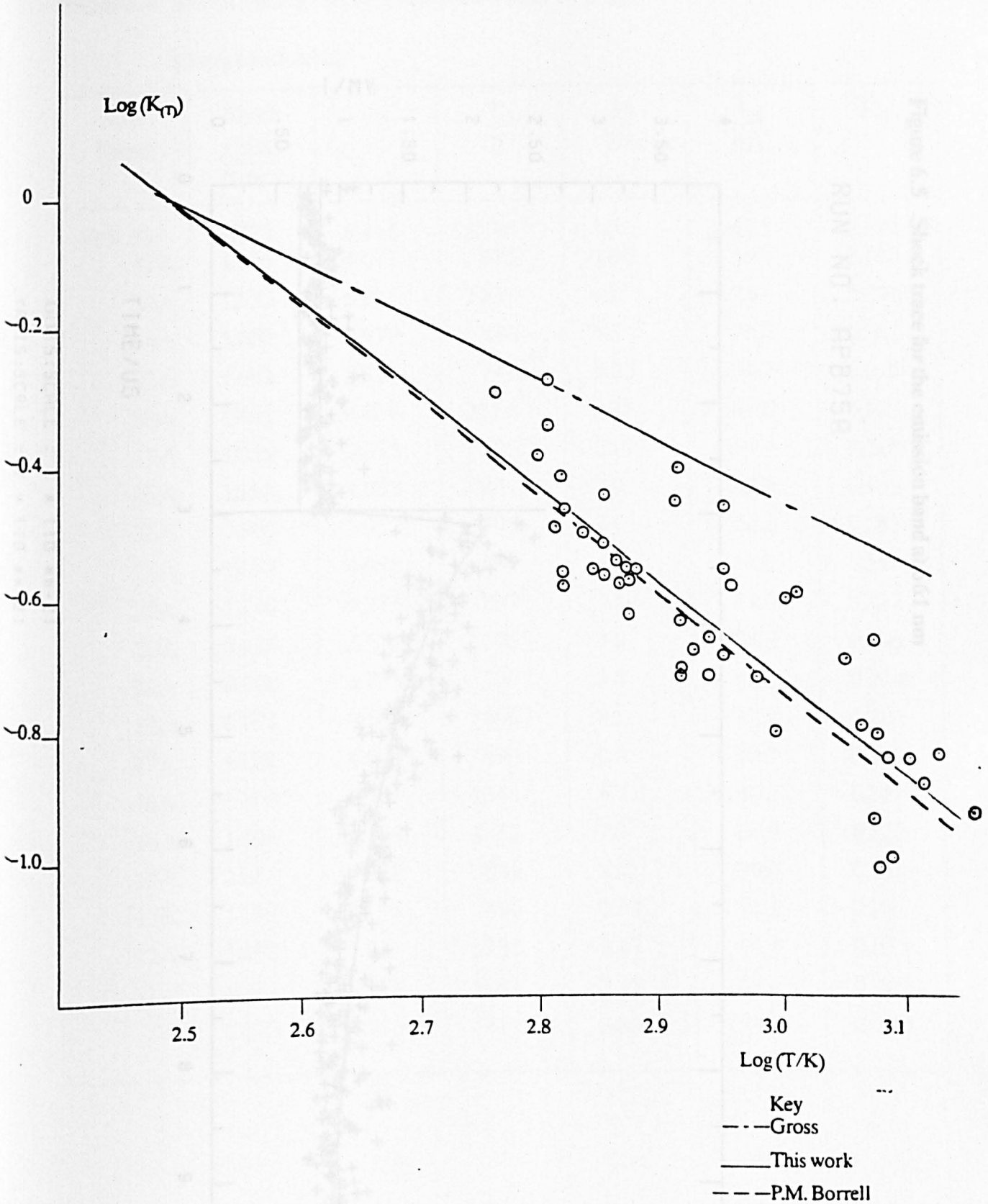

Figure 6.5 Shock trace for the emission band at 661 nm

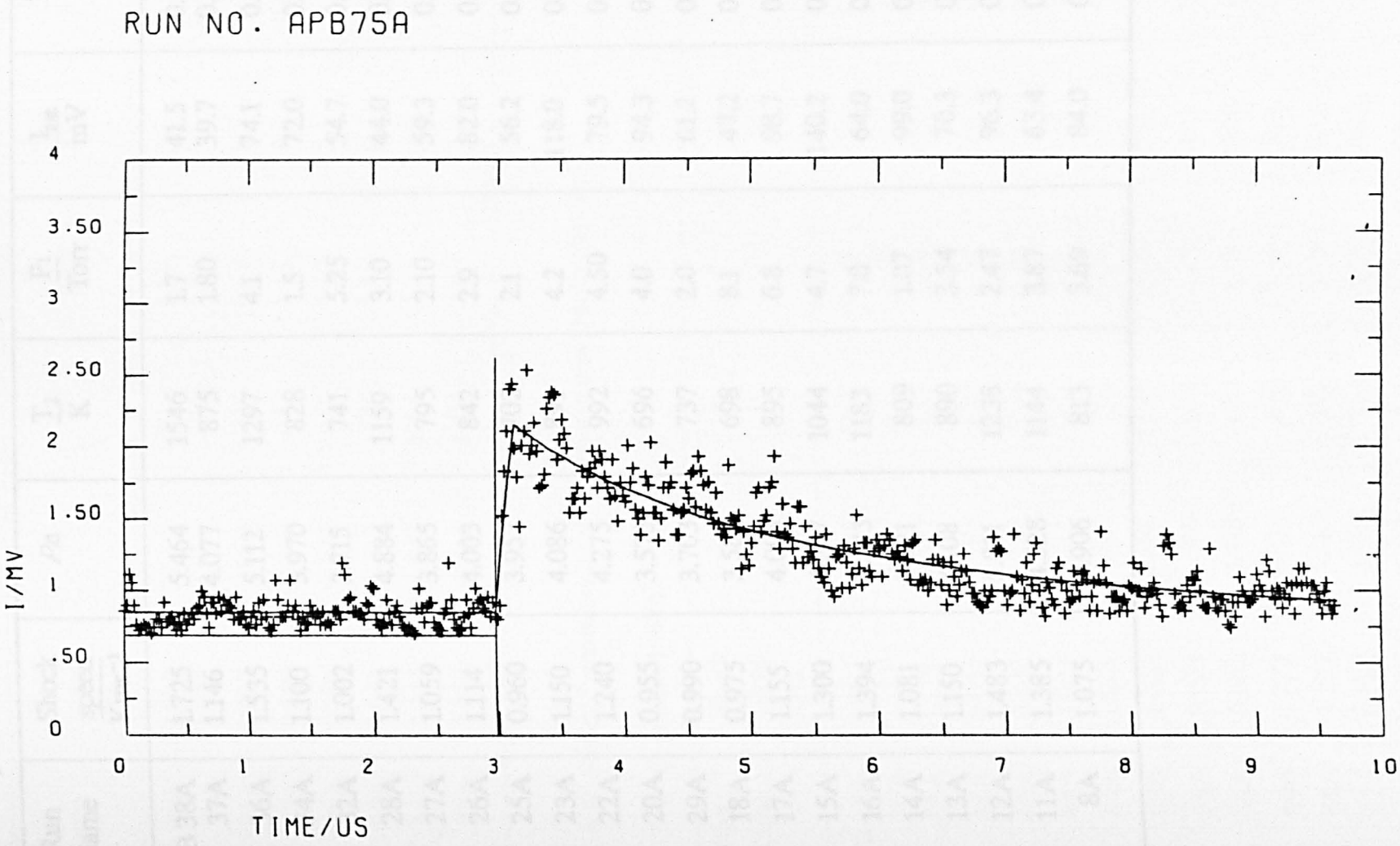

Table 6.4 Shock Parameters for Enhancements at 576nm.

(3 nm bandwidth)

Run Name	Shock speed / Kms^{-1}	ρ_{21}	T_2 / K	P_1 / Torr	I_{peak} / mV	$K_{(T)}$
APB 38A	1.725	5.464	1546	1.7	41.5	0.125
37A	1.146	4.077	875	1.80	39.7	0.188
36A	1.535	5.112	1297	4.1	74.1	0.0906
34A	1.100	3.970	828	1.5	72.0	0.183
32A	1.002	3.715	741	5.25	54.7	0.197
28A	1.421	4.884	1159	3.10	44.0	0.13
27A	1.059	3.865	795	2.10	59.3	0.209
26A	1.114	4.003	842	2.9	82.0	0.165
25A	0.960	3.953	702	2.1	56.2	0.183
23A	1.150	4.086	891	4.2	118.0	0.191
22A	1.240	4.275	992	4.50	79.5	0.132
20A	0.955	3.575	696	4.0	94.3	0.198
29A	0.990	3.703	737	2.0	61.2	0.124
18A	0.975	3.581	698	8.1	47.2	0.261
17A	1.155	4.095	895	6.8	98.7	0.149
15A	1.300	4.387	1044	4.7	140.2	0.167
16A	1.394	4.543	1183	7.0	64.0	0.120
14A	1.081	3.921	809	1.07	99.0	0.180
13A	1.150	4.108	890	3.54	70.3	0.17
12A	1.483	5.011	1238	2.47	96.3	0.073
11A	1.385	4.528	1144	3.87	63.4	0.209
8A	1.075	3.906	813	3.69	84.0	0.203

Table 6.5 Shock Parameters for the Enhancement Data at 586 nm.

(3 nm bandwidth)

Run Name	Shock speed / Kms^{-1}	ρ_{21}	T_2 / K	P_1 / Torr	I_{psc} / mV	$K_{(T)}$
APB 80A	1.092	3.950	820	5.59	17.2	0.579
79A	1.077	3.950	813	5.59	14.1	0.498
78A	0.987	3.669	726	5.59	15.7	0.702
77A	0.899	3.400	647	5.59	8.3	0.667
76A	0.891	3.374	640	5.59	15.4	0.741
72A	1.013	3.742	750	5.59	16.2	0.673
74A	1.425	4.892	1164	5.59	9.9	0.254
73A	1.458	4.963	1204	5.59	11.10	0.285

Table 6.6 Shock Parameters for the Enhancement Data at 661 nm.

(3 nm bandwidth)

Run Name	Shock speed / Kms^{-1}	ρ_{21}	T_2 / K	P_1 / Torr	I_{psc} / mV	$K_{(T)}$
APB 71A	0.982	3.658	722	5.59	42.0	0.339
75A	1.125	4.027	852	5.76	45.7	0.277
65A	1.125	4.027	852	5.59	41.10	0.300
64A	0.957	3.581	698	5.59	40.90	0.373
63A	0.882	3.348	634	5.76	30.62	0.679
43A	1.003	3.715	741	5.41	15.0	0.253
44A	1.012	3.742	750	6.71	13.8	0.313
53A	1.423	4.888	1162	5.59	23.8	0.161
54A	0.953	3.569	695	5.59	30.1	0.340
55A	0.902	3.413	651	5.59	32.4	0.402
60A	1.223	4.239	940	5.59	36.0	0.221
61A	1.237	4.267	971	5.59	43.6	0.218
62A	0.962	3.599	704	5.59	36.5	0.338
47A	0.903	3.413	651	5.50	26.5	0.417

Table 6.6 *(Continued from previous page)*

(3 nm bandwidth)

Run Name	Shock speed / Kms^{-1}	ρ_{21}	T_2 / K	P_1 / Torr	I_{psg} / mV	$K_{(T)}$
APB 49A	0.874	3.321	627	6.88	27.1	0.480
57A	1.00	3.709	739	5.59	32.5	0.342
58A	1.114	4.003	842	5.59	44.7	0.281
59A	1.459	4.963	1204	5.59	51.2	0.12
66A	1.128	4.036	859	5.59	45.0	0.253
68A	1.442	4.930	1185	5.59	36.1	0.151
69A	1.156	4.099	885	5.59	28.1	0.271
70A	1.003	3.715	735	5.59	41.8	0.350

Figure 6.6 log ($K_{(T)}$) against log (T) at 576 nm (monochromator).

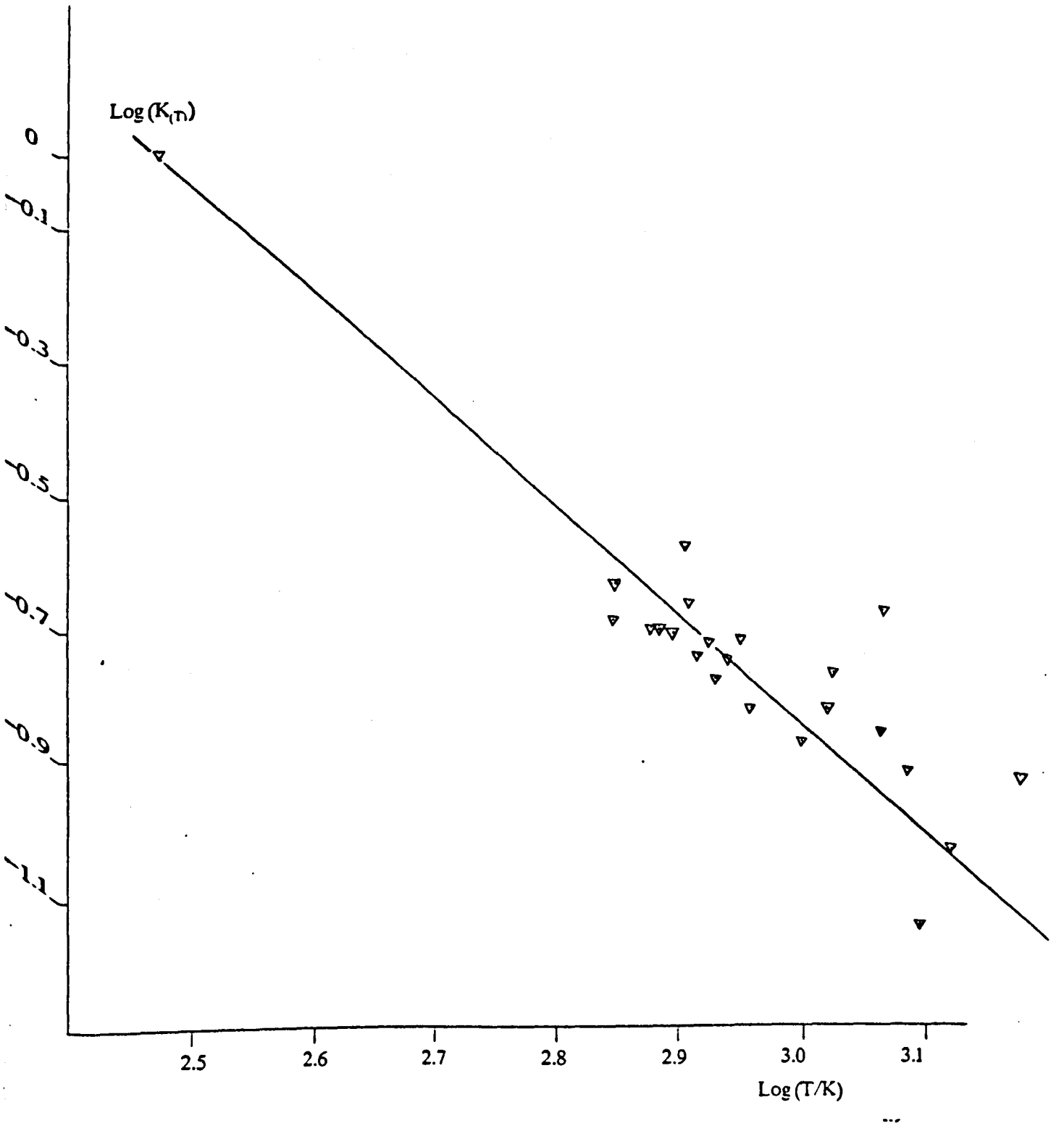

Figure 6.7 Log ($K_{(T)}$) against log (T) at 586 nm (monochromator).

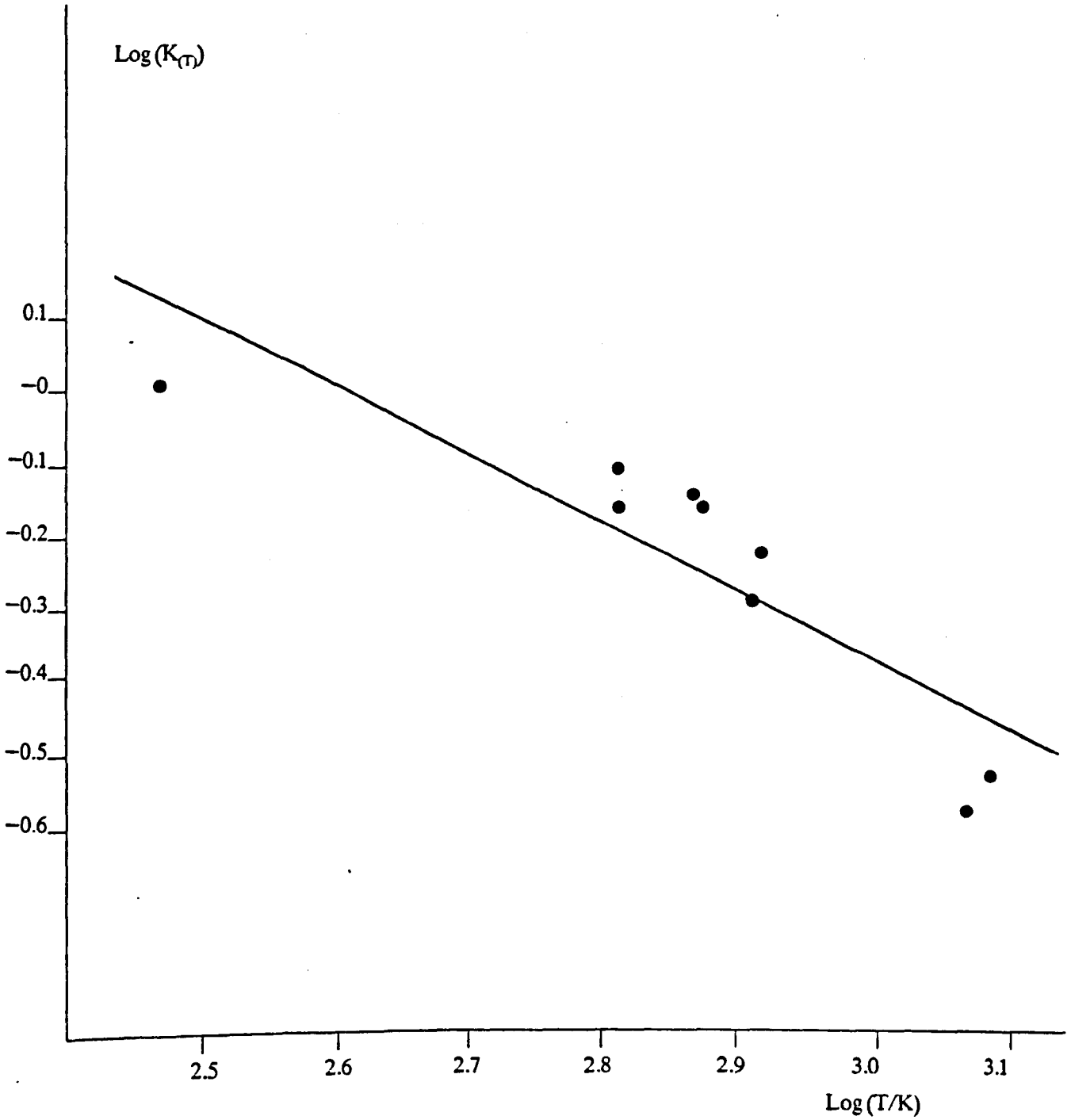

Figure 6.8 Log ($K_{(T)}$) against log (T) at 661 nm (monochromator).

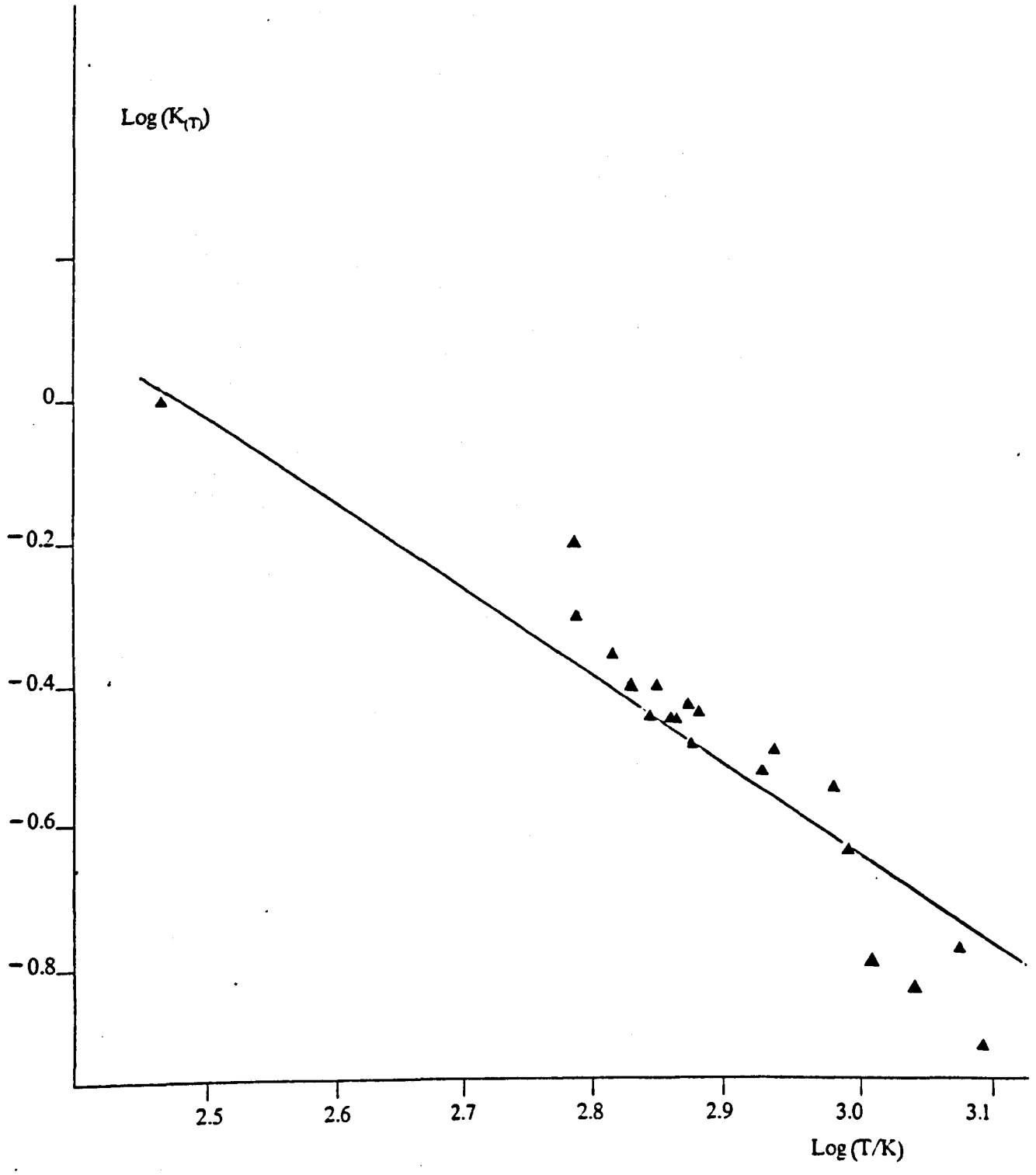

For each wavelength studied, values of $K_{(T)}$ were calculated by the method described. The values have been listed in tables 6.4, 6.5 and 6.6 ; the result for these bands have also been plotted on log ($K_{(T)}$) against log (T) graphs and are given in figures 6.6, 6.7 and 6.8 . Linear least squares analysis of the data gave the relationships:

$$\log(K_{(T)}) = 3.42 - 1.38.\log(T/K)$$

Interference filter, 579nm

$$\log(K_{(T)}) = 3.95 - 1.60.\log(T/K)$$

monochromator, 576nm

$$\log(K_{(T)}) = 1.61 - 0.64.\log(T/K)$$

monochromator, 586nm

$$\log(K_{(T)}) = 3.09 - 1.25.\log(T/K)$$

monochromator, 661nm.

An alternative expression was found to represent the data more accurately;

$$K_{(T)} = P_{(1)} + P_{(2)}T + P_{(3)}T^2 \qquad (6.9)$$

where $P_{(1)}$, $P_{(2)}$ and $P_{(3)}$ are constants. The data was fitted to equation (6.9) by a non linear least squares procedure and is given in appendix 2. The results for the analysis are given in table 6.7 , the results at 579nm are plotted on figure 6.9 .

From figures 6.6, 6.7, 6.8 and 6.4 , it can be seen that the points fall along a straight line. For a variety of experiments conducted between 1.0 and 8.1 torr, varying the nitrogen atom concentration between 0.46 and 0.11%, the emission is represented by:

$$I \propto [N]^2 \qquad (6.10)$$

These findings are in agreement with previous workers who have also observed a second order emission dependence between 1 and 10 torr [21,17], in the temperature range 196 to 327K, and so extends the range of validity of relationship (6.10) up to 1546 K.

Table 6.7 Curve parameters for equation (6.9)

Wavelength nm.	$P_{(1)}$	$P_{(2)}$ K	$\cdot P_{(3)}$ K^2
576	1.745± 0.964	−2.95E-3 ±2.11E-4	1.293E-6 ±141E-7
579	1.6870± 3.811E-2	−2.70E-3 ± 1.221E-4	1.149E-6 ±8.05E-8
586	1.2330± 7.948E-2	−7.92E-4 ±2.80E-3	1.89E-8 ±8.275E-9
661	1.538± 9.54E-2	−2.168E-3 ±3.54E-4	8.275E-7 ± 2.74E-7

The error limits are 2σ (95%) confidence values.

Figure 6.9 The Variation of $K_{(T)}$ with the temperature at 579 nm

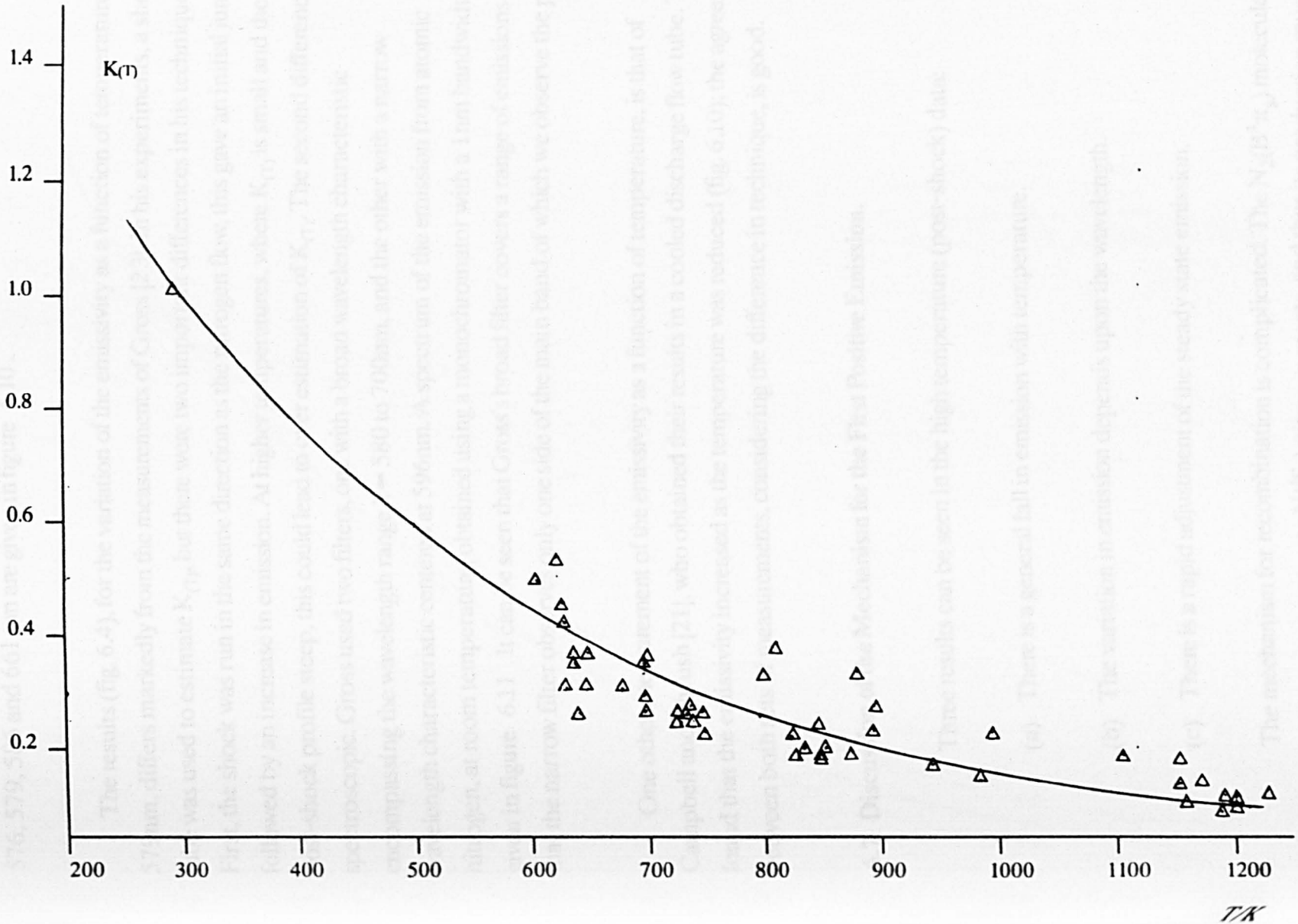

6.6 Discussion of the High Temperature Data.

The variation of the relative emissivities with temperature for the emission bands at 576, 579, 586 and 661 nm are given in figure 6.10 ..

The results (fig. 6.4), for the variation of the emissivity as a function of temperature at 579nm, differs markedly from the measurements of Gross [23]. In his experiments, a shock tube was used to estimate $K_{(T)}$, but there were two important differences in his technique. First, the shock was run in the same direction as the nitrogen flow, this gave an initial jump followed by an increase in emission. At higher temperatures, where $K_{(T)}$ is small and the post-shock profile steep, this could lead to over estimation of $K_{(T)}$. The second difference is spectroscopic. Gross used two filters, one with a broad wavelength characteristic encompassing the wavelength range $\lambda = 580$ to 700nm, and the other with a narrow wavelength characteristic centered at 596nm. A spectrum of the emission from atomic nitrogen, at room temperature, obtained using a monochromator with a 1nm bandwidth,is given in figure 6.11 . It can be seen that Gross's broad filter covers a range of emissions and that the narrow filter observes only one side of the main band of which we observe the peak.

One other measurement of the emissivity as a function of temperature, is that of Campbell and Thrush [21], who obtained their results in a cooled discharge flow tube. They found that the emissivity increased as the temperature was reduced (fig. 6.10); the agreement between both sets of measurements, considering the difference in technique, is good.

6.7 Discussion of the Mechanism for the First Positive Emission.

Three results can be seen in the high temperature (post-shock) data:

(a) There is a general fall in emission with temperature.

(b) The variation in emission depends upon the wavelength.

(c) There is a rapid adjustment of the steady state emission.

The mechanism for recombination is complicated. The $N_2(B^3\pi_g)$ molecule does not correlate to ground state $N(^4S)$ nitrogen atoms, and thus its production must involve curve crossing [69]. Two mechanisms have been proposed to explain the observed pressure dependence for the population of the $N_2(B^3\pi_g)$ vibrational levels.

Figure 6.10 The Variation of $K_{(T)}$ with the temperature at 576,579,586 and 661nm

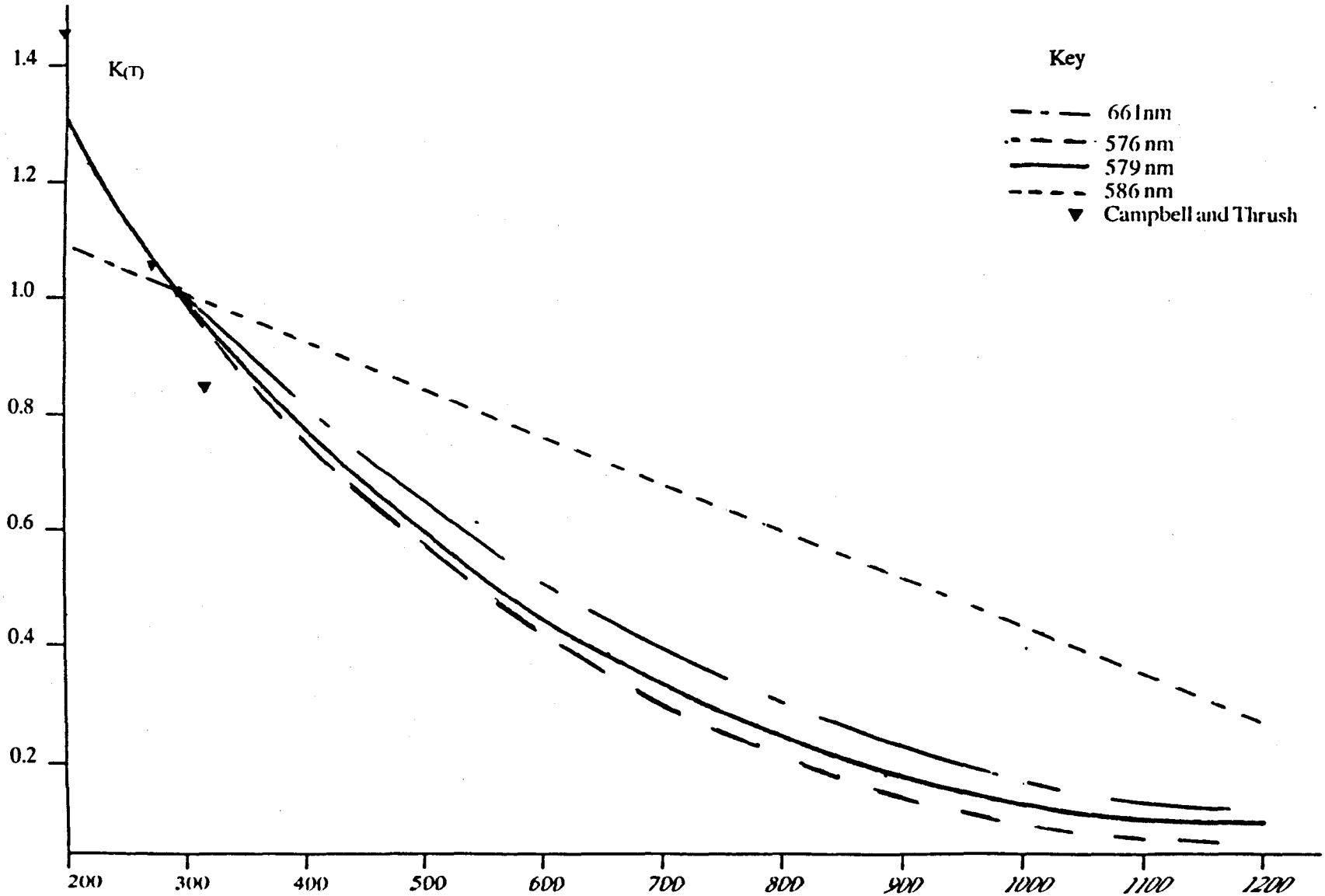

Figure 6.11 The Emission spectrum from active Nitrogen at T=295K

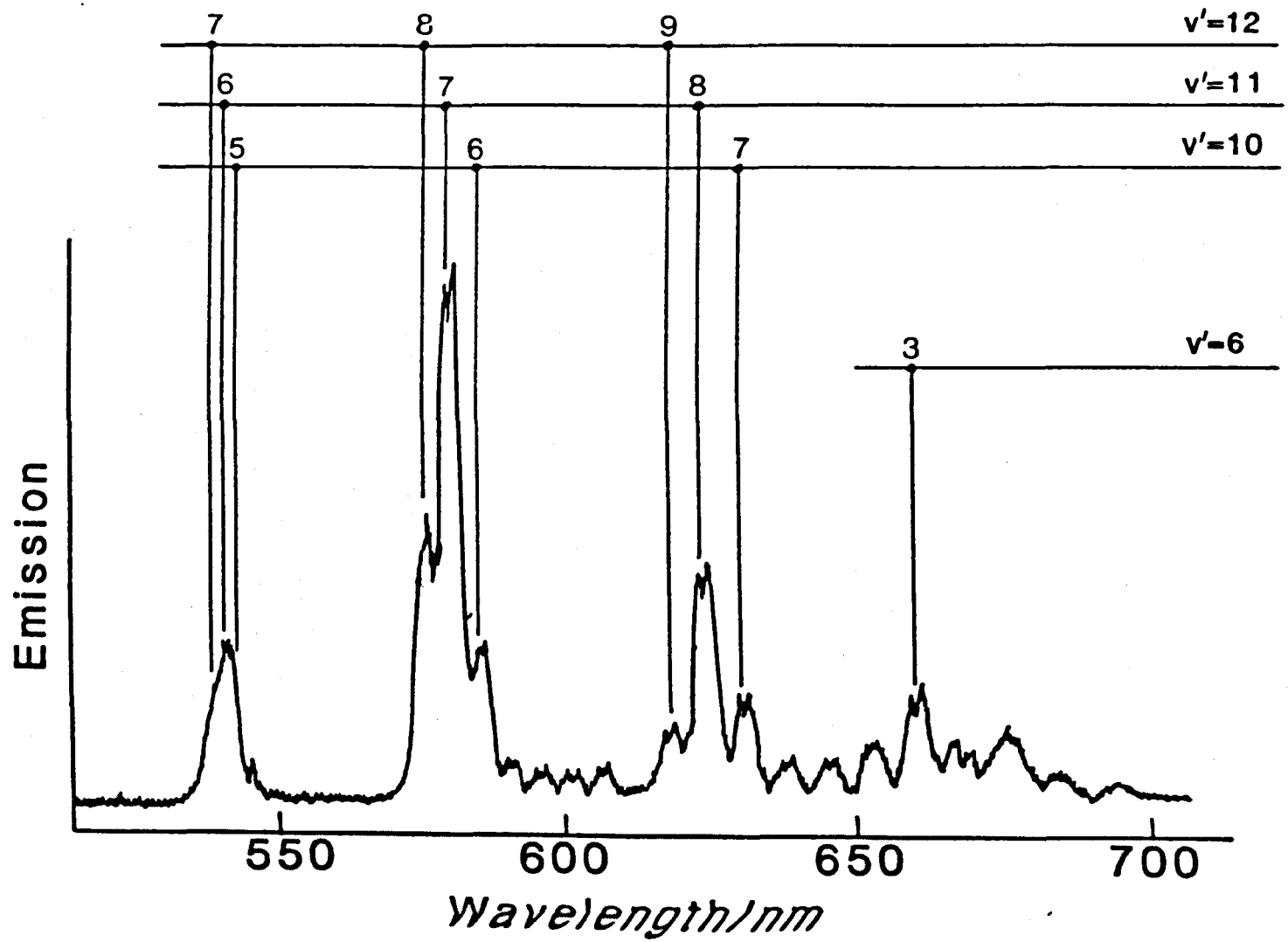

(a) Two nitrogen atoms approach one another along an attractive potential, this is followed by a collision induced transition into the $N_2(B^3\pi_g)$ state.

(b) The presence of a steady state of nitrogen molecules in the precursor state. The $N_2(B^3\pi_g)$ is populated collisionally from the precursor. This is maintained in steady state by collision induced redissociation, quenching and third order combination.

The first mechanism must be rejected since it does not satisfy the experimental observations. Bayes and Kistiakowsky[19] found that the intensity distribution is shifted to lower vibrational levels on the addition of an inert gas. Since the initial energy distribution is governed by the quantity of energy that is removed by the third body, this observation would not be consistent with mechanism.

The second mechanism requires a precursor molecule. There are three possible precursors, $N_2(x^1\Sigma_g^+)$, $N_2(^5\Sigma_g^+)$ and $N_2(A^3\Sigma_u^+)$. The first molecule, $N_2(x^1\Sigma_g^+)$, does not lie close to the $N_2(B^3\pi_g)$ state in the appropriate energy range. Collision induced population of the $N_2(B^3\pi_g)$ molecule from the high vibrational levels of $N_2(x^1\Sigma_g^+)$ is therefore unlikely. The molecule $N_2(^5\Sigma_g^+)$ is a shallow bound state with a binding energy of $7x10^2cm^{-1}$. Its steady state population could not be high enough to account for the high rate of $N_2(B^3\pi_g)$ formation. The last molecule, $N_2(A^3\Sigma_u^+)$, is therefore favoured as the precursor since it has a high binding energy and lies close to the $N_2(B^3\pi_g)$ molecule.

The preferred model of Golde and Thrush [69] from a model presented by Campbell and Thrush [21], is given in figures 6.12 and 6.13 . In the recombination occurs in the high vibrational levels of the $N_2(A^3\Sigma_u^+)$ state. This provides a single explanation for the formation of both the upper v=12, 11, 10 and lower v=6 vibrational levels. The mechanism is shown in figure 6.13 but has been modified to include the $N_2(w^3\Delta_u)$ state, which is a new feature in the overall scheme. The rate constants follow earlier numbering [21].

Recombination occurs at ~v=26 in the $N_2(A^3\Sigma_u^+)$ molecule. This process must be reversible so that it is consistent with the second order emission dependence observed at pressures $>$ 1 torr. The radiative lifetime of the $N_2(A^3\Sigma_u^+)$state is in the order of 1 second. Electronic quenching of this state by N_2 is considered to be

Figure 6.12: The Modified Reaction Scheme of Thrush

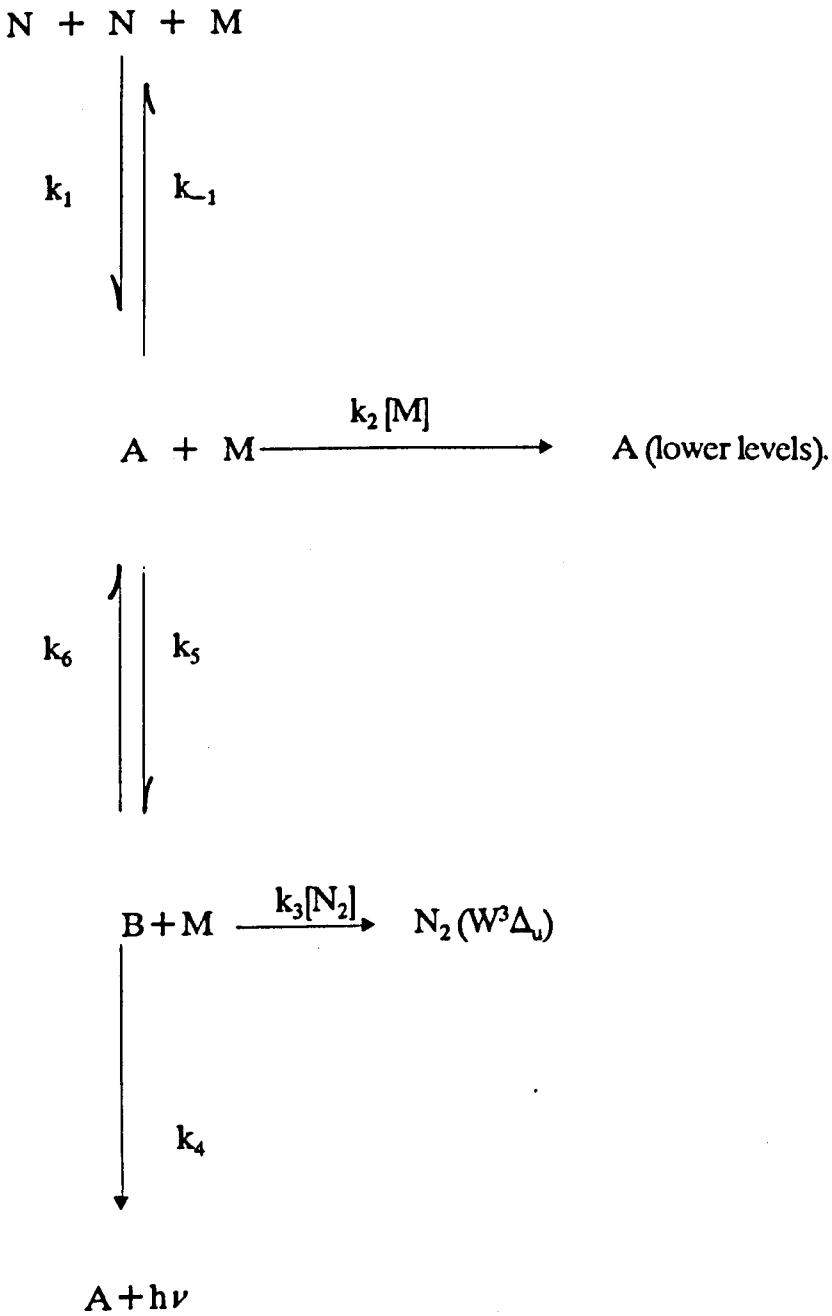

Figure 6.13 Nitrogen atom recombination including the $N_2(w^3\Delta_u)$ state.

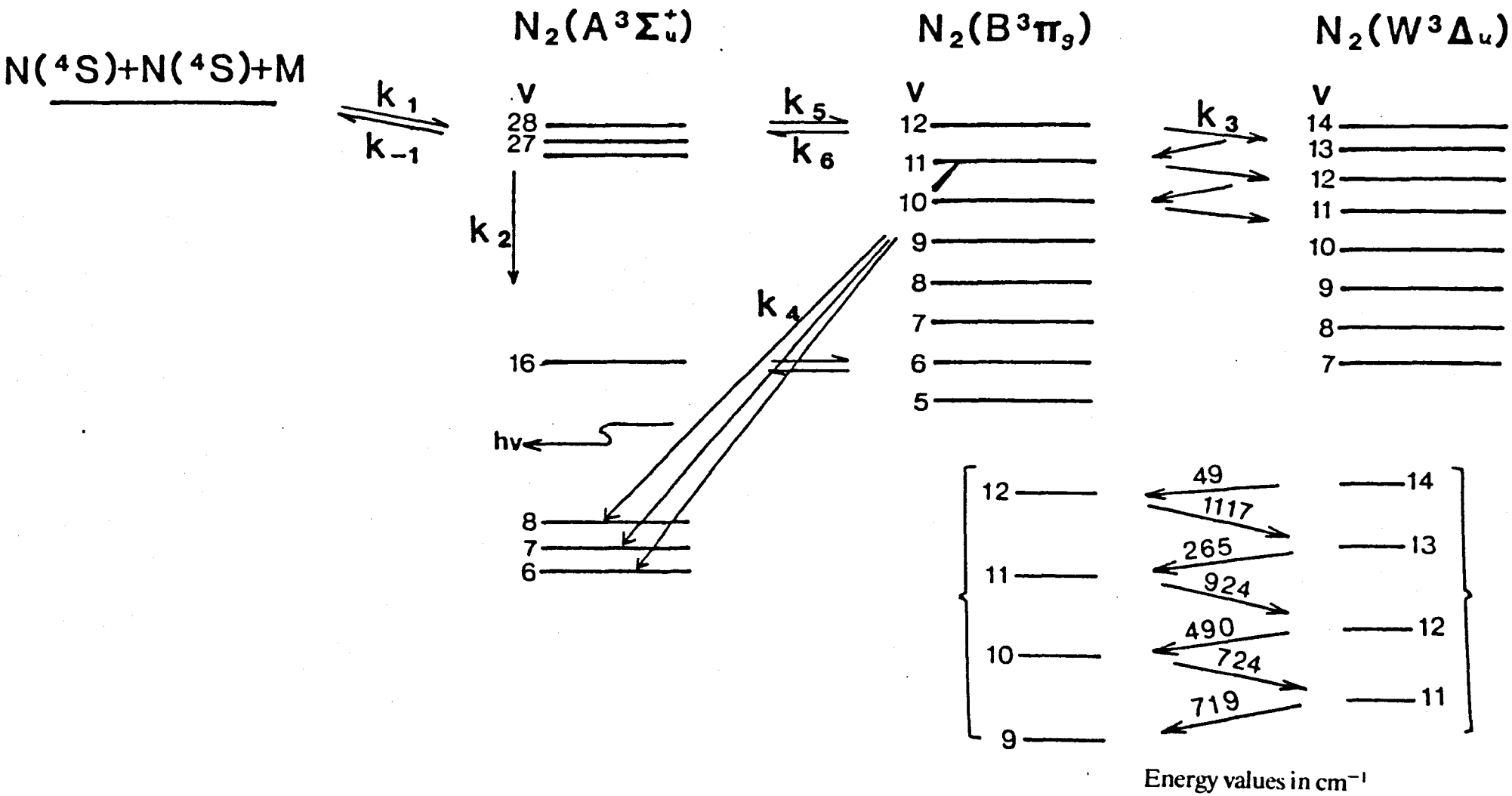

negligible since its emission can be detected in pure N_2 [70,71]. The $N_2(A^3\Sigma_u^+)$ state can be vibrationally deactivated or undergo collisional crossover to form the $N_2(B^3\pi_g)$ state, which itself can undergo collisional deactivation or emit. Collisional transfer between these two states has been considered to be important, since $N_2(B^3\pi_g)$ does not correlate to ground state $N(^4S)$ atoms.

Earlier workers realised that the deactivation of $N_2(B^3\pi_g)$ must be fast compared with the emission. Jeunehomme and Duncan [72] found that N_2 quenches the $N_2(B^3\pi_g)$ state at a rate of one in every twenty collisions. The vibrational relaxation could not be faster than this since they were unable to find longer radiative lifetimes at lower vibrational levels. Bayes and Kistiakowsky[19], using a rare gas quencher, concluded that vibrational relaxation would have to occur around 1 in every 100 collisions. This estimate is unreasonably high for a molecule with a vibrational spacing of $1.4 \times 10^3 cm^{-1}$. Vibrational relaxation is therefore probably too slow.

Sadeghi *et al.* and Roten, Rosewaks and Nadler have studied the laser induced fluorescence of the $N_2(B^3\pi_g)$ molecule [73,74]. They were able to explain their results by introducing rapid coupling between the $N_2(B^3\pi_g)$ and $N_2(W^3\Delta_u)$ states. Evidence has also been found by these workers for coupling to the $N_2(B'^3\Sigma_u^-)$ molecule, the third in the triplet manifold $N_2(B^3\pi_g)$, $N_2(W^3\Delta_u)$, $N_2(B'^3\Sigma_u^-)$. However its contribution is thought to be small and only the $N_2(W^3\Delta_u)$ need be considered. A diagram illustrating both $N_2(B^3\pi_g)$ and $N_2(W^3\Delta_u)$ potential wells is given in figure 6.14 ; the energy for the vibrational levels of both states has been calculated and is given in table 6.8 .

The radiative lifetimes of the $N_2(B^3\pi_g)$ molecule have been shown to be around 5μsec [69]. Calculations using the rate constant of Sadeghi and Setser for the lower vibrational levels, predict a collisional lifetime $\sim 10^{-2}$μ seconds under these conditions. This is consistent with the experimental data since no relaxation is observed in the shock trace.

The reactions of the $N_2(B^3\pi_g)$ (v=12) state can be treated with the simplified mechanism of Thrush to give the emission intensity, I, in terms of the various rate constants. Using the rate constants given in fig. 6.13 , the intensity is given by:

$$I/[N]^2 = k_1 k_4 k_5 \{k_{-1} + k_2 + k_5 (k_3 + k_6 + k_4/[N_2]) - k_5 k_6\}^{-1} \qquad (6.11)$$

Figure 6.14 Vibrational Energy levels of the N_2 ($B^3\pi_g$) and N_2 ($W^3\Delta_u$) Molecules

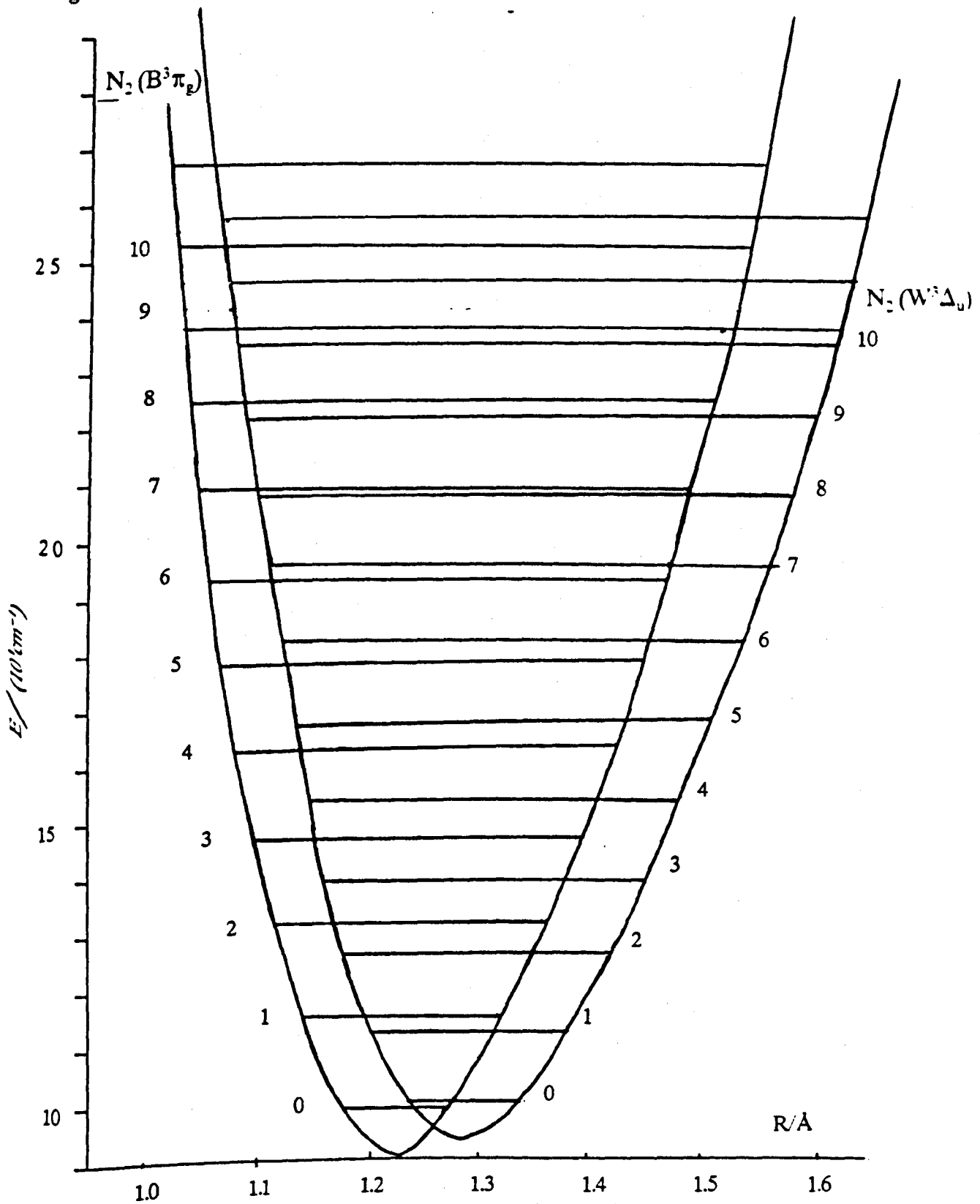

Taken from ref. [101]

Table 6.8 Energy Levels for Several States of N_2

$N_2(W^3\Delta_u)$		$N_2(B^3\pi_g)$		$N_2(A^3\Sigma_u^+)$	
v	E/cm^{-1}	v	E/cm^{-1}	v	E/cm^{-1}
0	9625	0	9551	7	9447
1	11106	1	11256	8	10686
2	12563	2	12933	9	11897
3	13995	3	14580	10	13080
4	15402	4	16199	11	14235
5	16785	5	17788	12	15363
6	18143	6	19348	13	16464
7	19477	7	20879	14	17535
8	20187	8	22381	15	18500
9	22073	9	23853	16	19597
10	23335	10	25296	17	20586
11	24572	11	26709	18	21547
12	25786	12	28093	19	22480
13	26975	13	29445	20	23386
14	28141	14	30770	21	24264
				22	25114
				23	25937
				24	26732
				25	27499
				26	28238
				27	28950
				28	29634

Zero level taken from $N_2(A^3\Sigma_u^+)$.

Taken from ref. [101]

Nitrogen atoms have been shown to be more efficient quenchers of the lower vibrational levels of the $N_2(A^3\Sigma_u^+)$ state than nitrogen molecules. Golde and Thrush illustrated that since the emission depends upon $[N]^2$ for the upper vibrational levels, here they must have similar quenching efficiencies to the N_2 molecules. The measurements (section 6.5) support this hypothesis up to 1546K.

The temperature dependence for the emission will be a complex function involving all of the rate constants. However, all of the emissions depend upon the rate constant, k_1, which should be similar to the overall recombination rate, k_R, the recommended value of Baulch is [75]:

$$k_R \ dm^6 mol^{-2} s^{-1} = 3 \times 10^8 \exp(500/T) \ : T=100-600K \qquad (6.12).$$

The value of k_R, relative to room temperature, has been plotted in figure 6.15 . Also given are the values of $K_{(T)}$ for the emission band at 579 nm. It can be seen from the two curves that the overall recombination rate k_R is probably the principal factor influencing the emission dependence.

The intensity distribution has been plotted as a function of the temperature in figure 6.16 . The room temperature distribution shows maxima at v=11 and v=6, but it can be seen that the distribution for the upper group shifts to lower vibrational levels as the temperature is raised. Further, Bayes and Kistiakowsky [19] observed that the distribution moved toward the upper vibrational levels as the temperature is reduced, and Broida [18] found that at 77K the majority of the emission came from the v=12 level. These changes give an insight into how the values of k_3, k_5 and k_6 change with both the vibrational levels and the temperature. A qualitative indication of the behaviour can be obtained from the energy level diagram between the $N_2(B^3\pi_g)$ and $N_2(w^3\Delta_u)$ states, which is inset in fig. 6.13 .

Miller and Bondeyby have suggested that the product of the Franck-Condon factor and exponential energy gap, $\exp(-|\Delta E|/RT)$, can be used to identify strong

Figure 6.15 Variation of the emission band at 579 nm compared to the recombination rate constant.

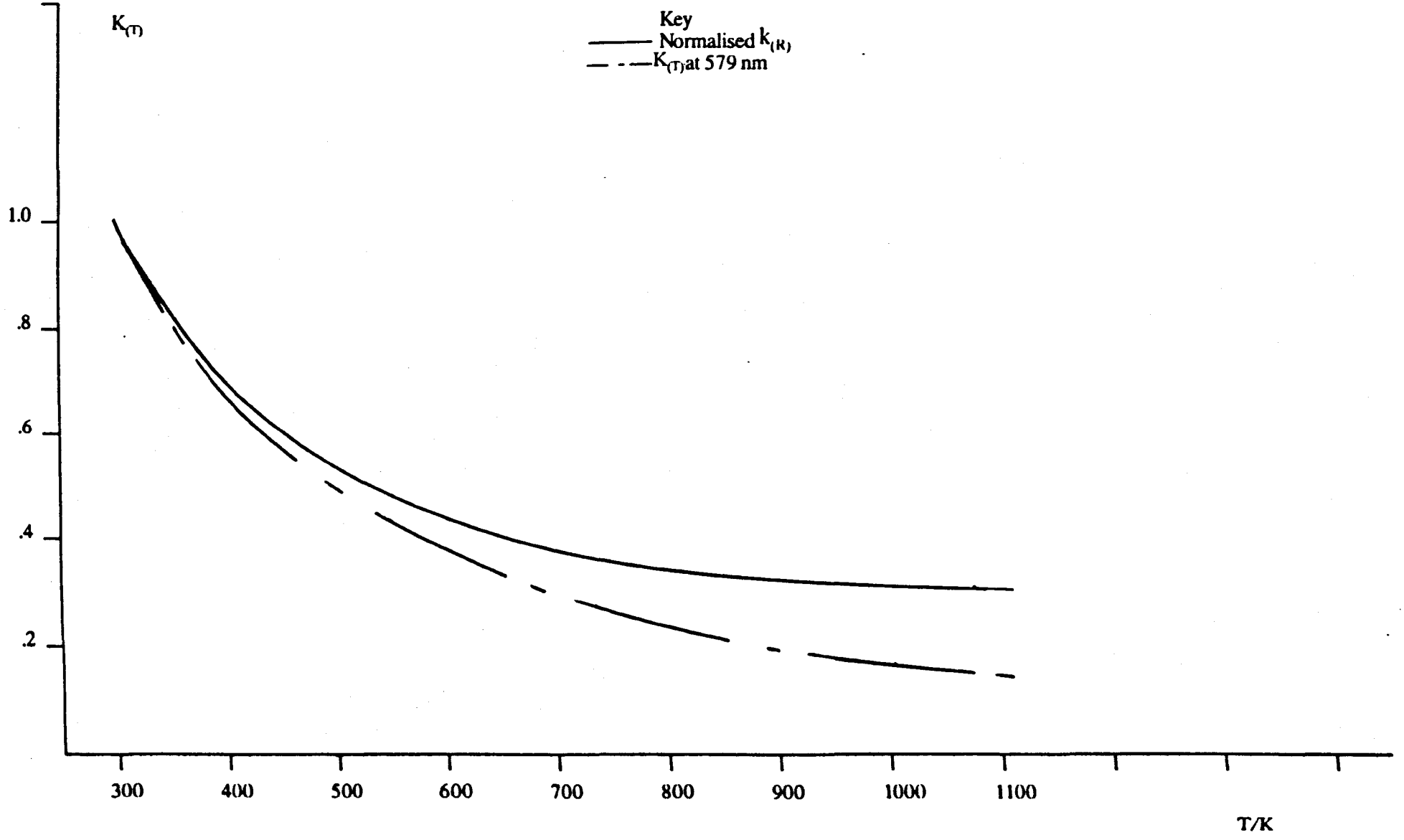

Figure 6.16 Relative Intensity distributions in the Lewis Rayleigh afterglow

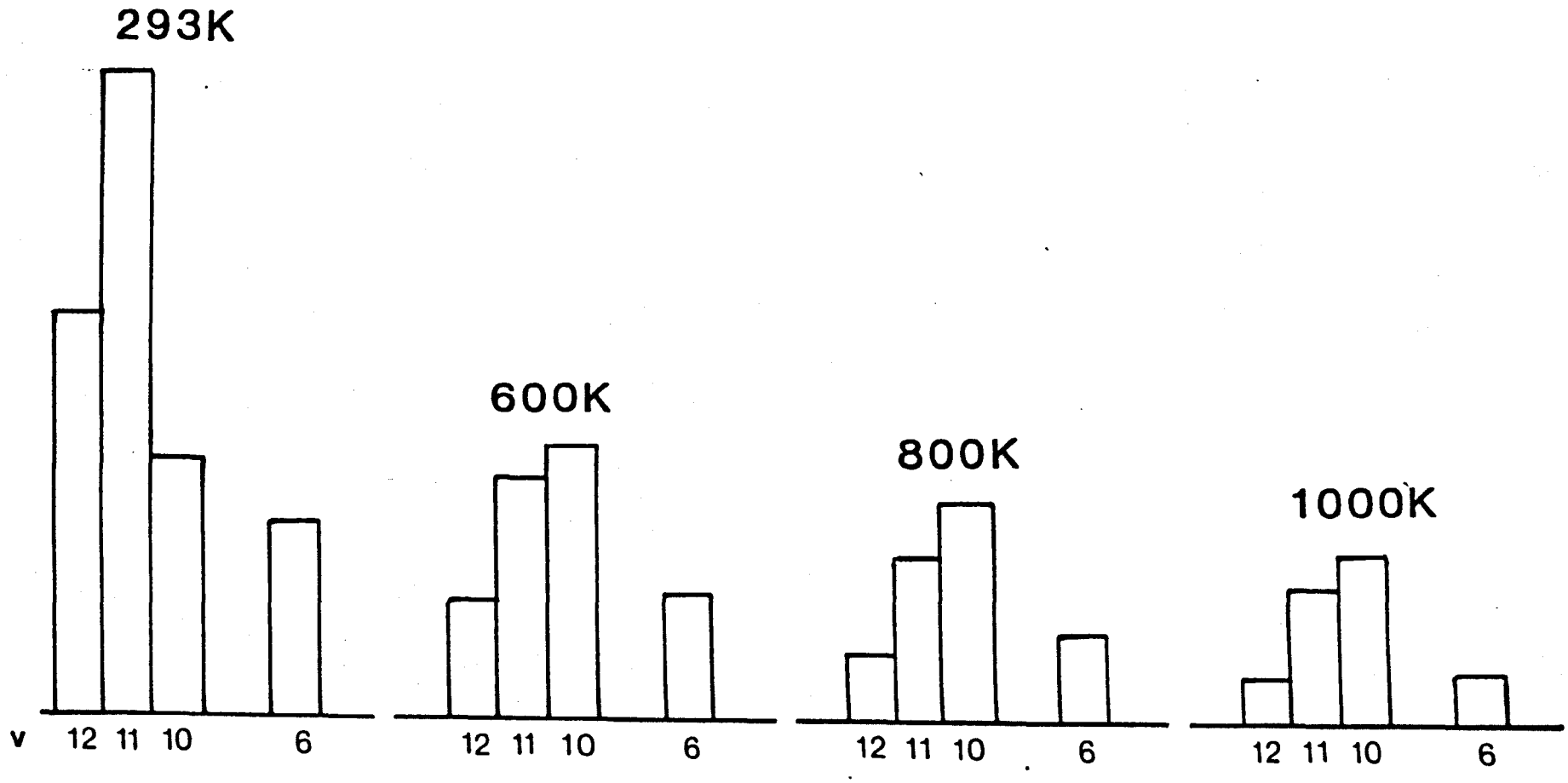

coupling pathways between two manifold levels [76]. Since we are concerned with comparative measurements, the electronic coupling between the vibrational levels of the two states can be represented by exp- ($|\Delta E|/RT$), where $|\Delta E|$ is the modulus value of the energy gap. This term applies to both the up and down energy processes. When comparing couplings, those with larger $|\Delta E|$ values will change more rapidly with temperature, than those with small $|\Delta E|$ values.

Inspection table 6.8 and figure 6.13 shows that the deactivation of N_2 ($B^3\pi_g$) (v=12) will increase more with temperature than the deactivation of the v=11 vibrational level, and the deactivation of the v=11 will be greater than the v=10. Conversely, the feeding process to v=10 changes faster than to v=11 as the temperature increases.. Quantitatively, the observed spectral shift can now be understood, and is consistent with the coupling model.

Quantitative analysis of the spectral distribution, and its variation with temperature, would be difficult. Sadeghi and Setser suggest that the Franck-Condon factor, along with the energy gap, are important in determining the coupling strengths between vibrational states of electronically excited molecules. In addition, there must also be a factor that is capable of accounting for the mixture of electronic wave functions of the two states involved [73].

In the model, it has been assumed that only the N_2 ($B^3\pi_g$) (v=12) state is fed directly, and the lower vibrational levels are populated as a result of a cascade involving the $N_2(W^3\Delta_u)$ state. Some direct population of the lower levels is possible, but the result of Broida [18] at 77K suggests that this contribution will be small. Furthermore, the $N_2(W^3\Delta_u)$ state may be fed directly from the N_2 ($A^3\Sigma_u^+$) molecule and is itself an emission precursor.

All of the models envisage that the N_2 ($B^3\pi_g$) (v=6) molecule is fed from the N_2 ($A^3\Sigma_u^+$) (v=16) state, where there is near resonant crossover. It is generally agreed that this vibrational level represents a separate feeding process from the N_2 ($A^3\Sigma_u^+$) molecule. The results show that the temperature dependance for the N_2 ($B^3\pi_g$)(v=6) level is almost identical to the v=11 level. More detailed measurements of the rate constants by laser fluorescence are therefore required at the lower vibrational levels. Further experiments are also needed on the v=7 and 8 levels of N_2 ($B^3\pi_g$), so that confirmation of this model at the lower vibrational levels can be made.

CHAPTER SEVEN

7.0 The Temperature Dependence of the $N+O_2$ Reaction

7.1 Introduction

Measurements of the $N+O_2$ reaction rate constant were made in the temperature range 300 to 1500K, by observing with time changes in the first positive (1+) and NO (β) emission bands (Chapter Five). These experiments were made so that the discharge flow shock tube could be assessed as an experimental technique for investigating reaction systems involving nitrogen atoms. The data obtained has been compared with previous determinations and has been examined in terms of the current theory.

7.2 Room Temperature Measurements of the $N+O_2$ Reaction Rate Constant.

Prior to any high temperature measurements, the reaction rate constant k_5 (Chapter Five), for the $N+O_2$ reaction, was determined at room temperature.

7.2.1 Experimental

The variation of both the first positive (1+) and NO(β) band emissions (Chapter Five), as a function of the flow tube length, was determined by using the mobile photomultiplier fitted with an interference filter centred at either 579 or 403nm. Measurements were taken in N_2/O_2 mixtures (up to 3.3% O_2 in N_2), with linear flow velocities in the range $0.6-1.4 ms^{-1}$. The total pressure of the system was varied between 4.20 and 8.20 torr, the molar flow rate of the N_2 was maintained at 0.6 millimol sec^{-1}.

7.2.2 Results and Treatment of the Data

In Chapter Five it was shown that the variation of the emission intensity as a function of the flow tube length could be modelled for both the first positive (1+) and NO(β) bands.

A typical plot of $\ln({}^{579}I_o/{}^{579}I_l)$, for the (1+) emission band at 579nm, against the flow tube length for an N_2/O_2 mixture, is given in fig. 7.1 . Good straight lines were obtained for all of the experimental conditions used.

The slope of each plot was shown to be (section 5.2.3.1):

$$\text{Slope} = 2k_b/v \tag{7.1}$$

where $$k_b = \{2k_5[O_2] + k_a^*\} \tag{7.2}$$

$$k_a^* = 2(k_2 + k_3[N_2])[N]_o \tag{7.3}$$

k_5, k_2 and k_3 refer to the reactions:

$$N + O_2 \xrightarrow{k_5} NO + O \tag{7.4}$$

$$N + N \xrightarrow{k_2} N_2 \tag{7.5}$$

$$N + N + N_2 \xrightarrow{k_3} N_2 + N_2 \tag{7.6}$$

The determined values of $2k_b$ are listed in table 7.1 . Thus, a plot of $k_b/2$ against $[O_2]$ should give a slope equal to k_5 and an intercept equal to $k_a^*/2$ (eqn. (7.2)).The results have been plotted in fig. 7.2 ,it can be seen that a straight line is produced and there is a positive intercept.

Table 7.1 Room Temperature Determination of k_5, 579 nm.

Run Name	$[O_2] \times 10^6$ / mol dm^{-3}	Pressure / torr	L.F.V / ms^{-1}	$2k_b$ / sec^{-1}	$k_b/2$ / sec^{-1}
APB 127	5.89	5.27	1.067	2.292	0.573
126	5.86	5.24	1.067	1.905	0.476
124	5.82	5.24	1.041	2.227	0.556
123	5.82	5.24	1.041	2.285	0.571
122	5.82	5.24	1.041	2.453	0.613
121	5.82	5.24	1.04	2.236	0.559
120	5.82	5.24	1.049	2.136	0.534
119	5.28	5.93	0.944	2.551	0.637
118	5.21	5.24	1.03	2.168	0.542
117	10.24	7.08	0.741	3.6	0.8
116	11.74	8.12	0.646	3.82	0.88
115	10.59	4.20	1.25	3.82	0.955
114	10.36	4.20	1.25	4.252	1.063
113	10.36	4.22	1.25	4.6	1.15
112	12.54	5.78	0.917	5.12	1.28
111	12.54	3.78	0.917	4.72	1.18
110	9.38	4.32	1.230	3.68	0.92
109	7.75	4.32	1.40	2.93	0.73
108	10.80	6.04	0.914	3.48	0.87
107	8.10	4.49	1.35	2.81	0.70
106	10.11	5.93	1.018	3.03	0.76
105	9.62	5.33	1.135	3.34	0.835
104	11.65	6.45	0.937	3.31	0.827
103	7.11	4.55	1.32	2.21	0.55
102	6.47	4.73	1.27	2.70	0.675
101	10.29	4.75	1.27	2.08	0.52
100	7.2	4.40	1.38	1.42	0.35

Figure 7.1 Logarithmic intensity variation as a function of distance.

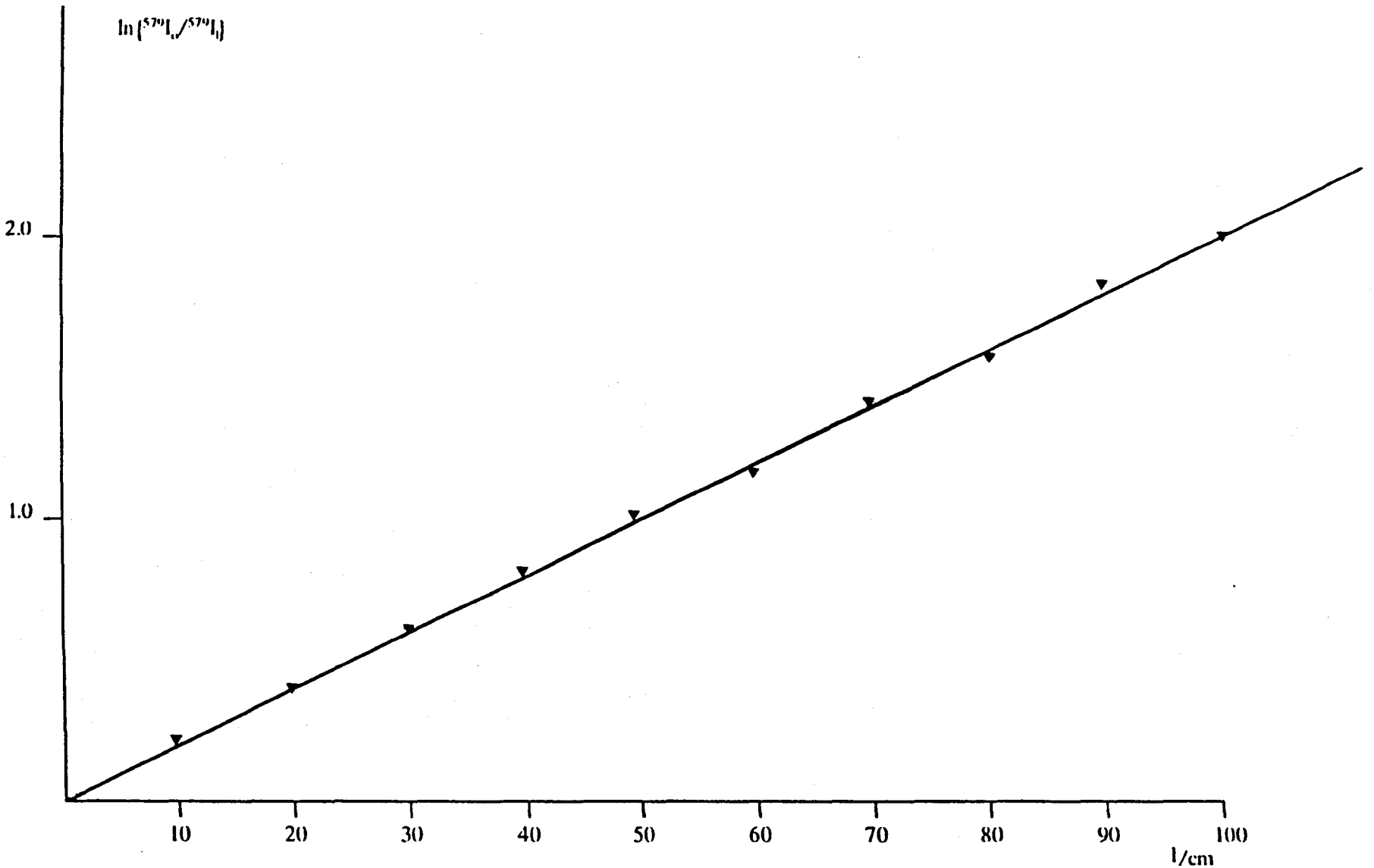

Figure 7.2 Determination of k_5 at T=292K

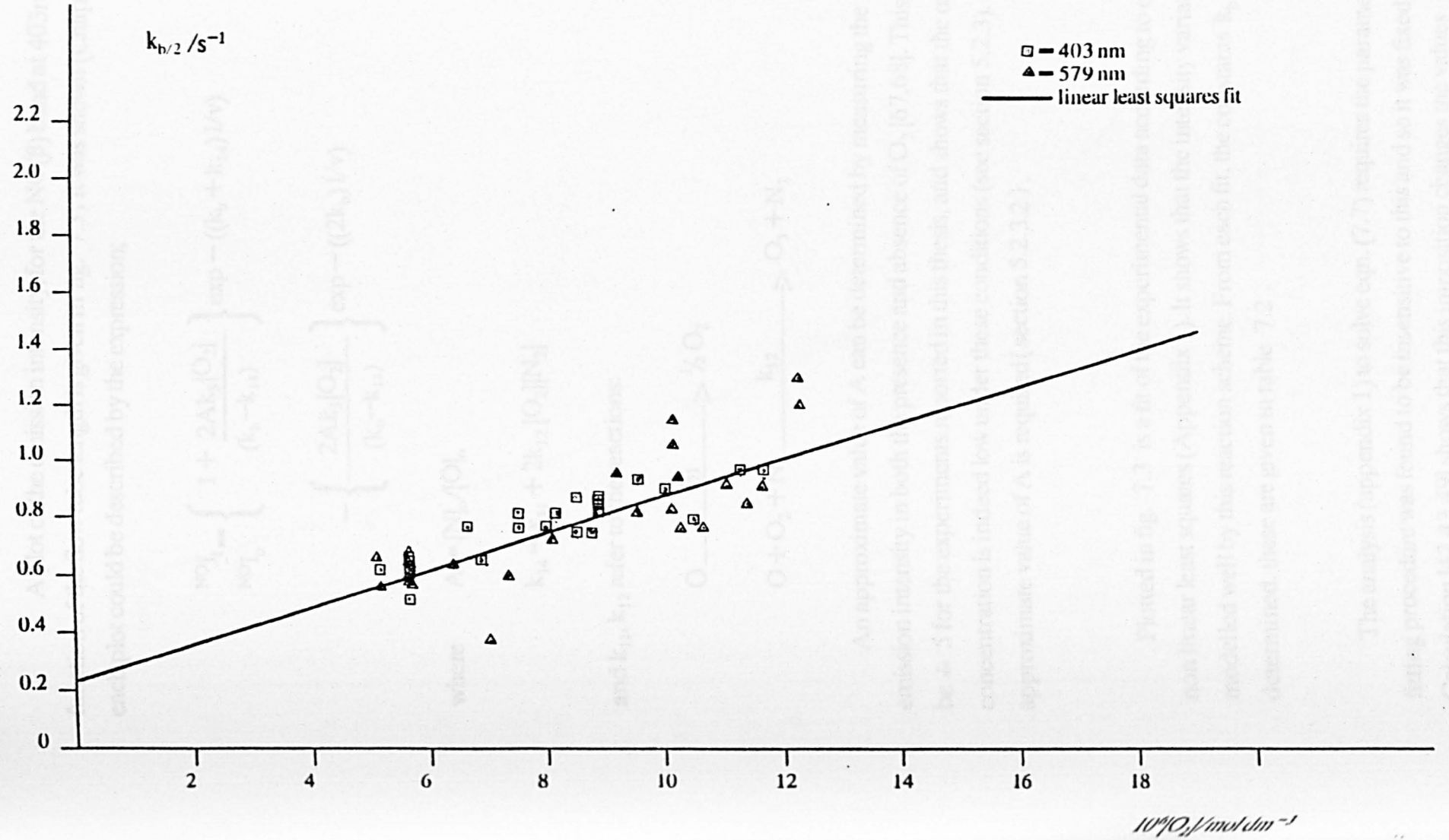

A plot of the emission intensity, for the NO(β) band at 403nm, $^{NO}I_1$, as a function of the flow tube length is given in fig. 7.3 , It was shown (Chapter Five), that each plot could be described by the expression;

$$\frac{^{NO}I_1}{^{NO}I_o} = \left\{ 1 + \frac{2Ak_5[O_2]}{(k_b - k_{14})} \right\} \exp -((k_b + k_{14})\, l/v)$$

$$- \left\{ \frac{2Ak_5[O_2]}{(k_b - k_{14})} \right\} \exp -((2k_b)\, l/v) \qquad (7.7)$$

where $A = [N]_o/[O]_o$

$$k_{14} = k_{11} + 2k_{12}\,[O_2][N_2] \qquad (7.8)$$

and k_{11}, k_{12} refer to the reactions:

$$O \xrightarrow{k_{11}} \tfrac{1}{2} O_2 \qquad (7.9)$$

$$O + O_2 + N_2 \xrightarrow{k_{12}} O_3 + N_2 \qquad (7.10)$$

An approximate value of A can be determined by measuring the first positive emission intensity in both the presence and absence of O_2 [67,68]. This was found to be ≃ 5 for the experiments reported in this thesis, and shows that the oxygen atom concentration is indeed low under these conditions (see section 5.2.3). Only an approximate value of A is required (section 5.2.3.2).

Plotted in fig. 7.3 is a fit of the experimental data according to eqn. (7.7) using non linear least squares (Appendix 1). It shows that the intensity variation can be modelled well by this reaction scheme. From each fit, the constants $k_b/2$ and k_{14} were determined, these are given in table 7.2 .

The analysis (appendix 1) to solve eqn. (7.7) requires the parameter $P_{(1)}$. The fitting procedure was found to be insensitive to this and so it was fixed to equal A Calculation [42,43,49] shows that this imposition changes the values of k_b and k_{14} by less than the experimental error (± 10%).

Figure 7.3 Variation of $^{NO}I_t/^{NO}I_o$ as a function of distance.

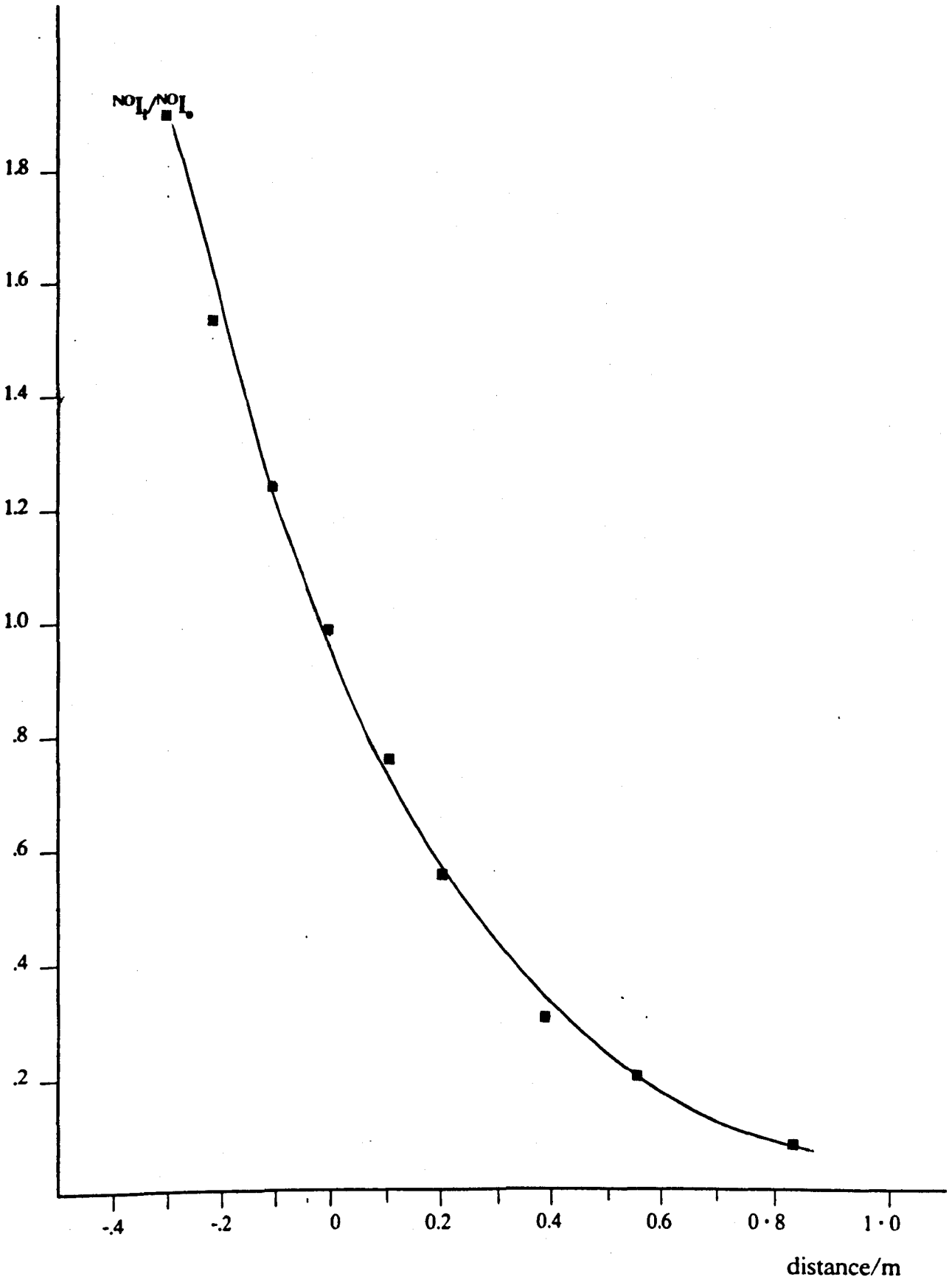

Run name APB 108

Table 7.2 Room Temperature Determination of k_5, 403 nm.

Run Name	$[O_2] \times 10^6$ / mol dm^{-3}	Pressure / torr	L.F.V / ms^{-1}	k_{14} / sec^{-1}	$k_b/2$ / sec^{-1}
APB 88	9.72	6.19	0.961	1.37	0.9
90	9.72	6.19	0.961	1.29	0.904
91	8.37	5.33	1.075	0.794	0.771
92	8.37	5.33	1.075	1.00	0.833
93	7.43	4.73	1.212	0.958	0.788
94	10.21	6.50	1.212	1.26	0.865
95	7.97	5.07	1.131	0.929	0.816
96	8.65	5.50	1.042	0.903	0.753
87	8.78	5.59	1.025	1.10	0.842
86	8.78	5.59	1.025	1.01	0.80
85	8.78	5.39	1.025	1.21	0.853
84	8.78	5.59	1.025	1.04	0.842
83	8.59	5.59	1.025	1.45	0.842
118	5.21	5.24	1.03	0.938	0.591
119	7.07	5.93	0.944	0.650	0.650
120	5.82	5.24	1.049	0.820	0.627
122	5.82	5.24	1.041	0.595	0.762
123	5.82	5.24	1.041	0.621	0.659
125	5.82	5.24	1.041	0.742	0.699
126	5.868	5.24	1.067	0.631	0.630
102	6.47	4.73	1.182	0.632	0.762
103	7.11	4.55	1.228	0.688	0.641
104	11.65	6.45	0.866	1.082	0.937
105	9.62	5.33	1.048	0.831	0.887
106	10.71	5.93	0.942	1.105	0.785
107	8.10	4.49	1.245	0.607	0.782
108	10.8	6.04	0.926	1.389	0.788
109	7.75	4.32	1.214	0.653	0.712

From a linear plot of $k_b/2$ against $[O_2]$ (eqn. 7.2), the rate constants k_5 and $k_a^*/2$ can be determined from the slope and intercept respectively (fig. 7.2). The agreement between the data obtained by using both (1+) and (NOβ) emission bands is good, linear least squares analysis of the data gave the values;

$$k_5/dm^3\ mol^{-1}\ s^{-1} = (6.58 \pm 1.5) \times 10^4$$

$$k_a^*/s^{-1} = (0.42 \pm 0.1)$$

the error limits are 2σ (95%) confidence values.

The psuedo first order rate constant for the recombination oxygen atoms, k_{14}, is the sum of two rate terms (eqn. 7.8). From a linear plot of k_{14} against $[O_2][N_2]$ (Chapter Five), the rate contants k_{11} and k_{12} can be determined from the intercept and slope respectively. The data (table 7.3) has been plotted in fig. 7.4 ; a straight line was obtained and linear least squares analysis of the data gave;

$$k_{11}/s^{-1} = (0.294 \pm 0.045)$$

$$k_{12}/dm^6\ mol^{-2}\ s^{-1} = (1.25 \pm 0.22) \times 10^8$$

the error limits are 2σ (95%) confidence values.

7.2.3 Discussion of the Room Temperature Data.

A series of determinations of k_5 are given in table 7.4 . The result obtained in this work agrees well with the value of Becker *et al.* [78], who measured the reaction rate constant by monitoring the first positive emission band as a function of time in the pressure range 10^{-4} to 10^{-1} torr. This work is also in good agreement with the value of Clark and Wayne [43], which was also determined in a discharge flow system.

The current determination supports the upper values of k_5 listed with the exception of that of Monat *et al.* [45]. This high value was obtained from an extrapolation of their high temperature data. Since the data was scattered, extrapolation from this would be expected to give error.

It was seen that the combined heterogenous and homogenous first-order decay constant, k_a^*, is significant under these conditions. Calculations show that in this pressure

Table 7.3 Determination of the Rate Constants k_{11} and k_{12} at Room Temperature.

Run Name	k_{14} sec^{-1}	$[O_2] \times 10^6$ $mol\ dm^{-3}$	$[N_2] \times 10^4$ $mol\ dm^{-3}$	$[O_2][N_2] \times 10^9$ $mol^2 dm^{-6}$
APB 88	1.37	9.72	3.39	3.295
90	1.29	9.72	3.39	3.295
91	0.794	8.37	2.92	2.44
92	1.00	8.37	2.92	2.44
93	0.958	7.43	2.59	1.924
94	1.26	10.21	2.59	2.64
95	0.929	7.97	2.78	2.215
96	0.903	8.65	3.02	2.612
87	1.10	8.78	3.07	2.695
86	1.01	8.78	3.07	2.695
85	1.21	8.78	3.07	2.695
84	1.04	8.78	3.07	2.695
83	1.45	8.59	3.07	2.695
118	0.938	5.21	2.87	1.495
119	0.650	7.07	8.26	2.304
120	0.820	5.82	2.87	1.67
122	0.595	5.82	2.87	1.67
123	0.621	5.82	2.87	1.67
125	0.742	5.82	2.87	1.67
126	0.631	5.86	2.87	1.67
102	0.632	6.47	2.59	1.675
103	0.658	7.11	2.498	1.776
104	1.082	11.65	3.54	4.124
105	0.831	9.62	2.92	2.809
106	1.105	10.71	3.25	3.48
107	0.607	8.10	2.465	1.996
108	1.389	10.8	3.31	3.5717
109	0.653	7.75	2.37	1.836

Figure 7.4 Variation of k_{14} with $[O_2]\,[N_2]$.

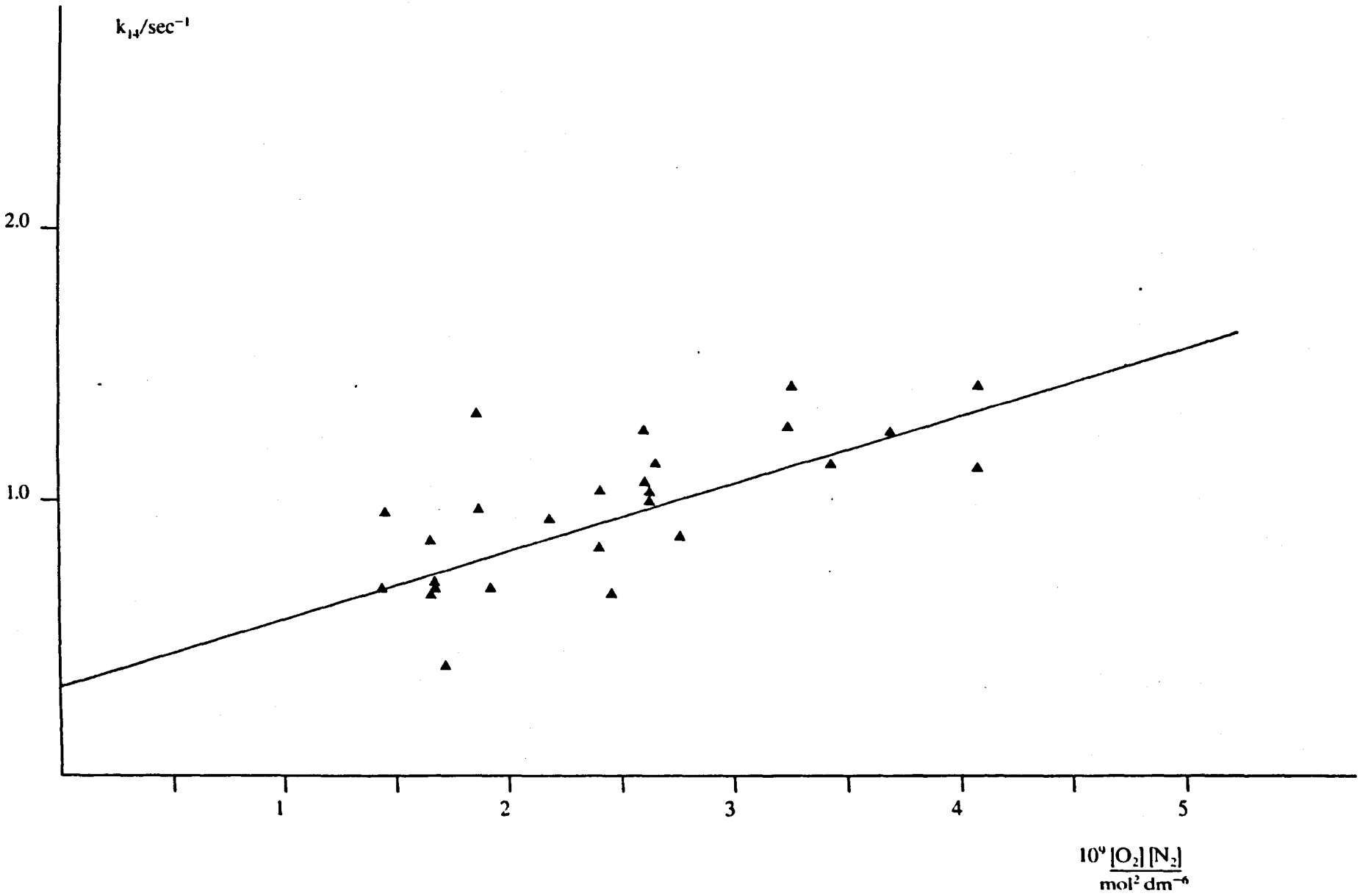

Table 7.4 Room temperature rate constants for k_5.

$\frac{k_5 \times 10^{-4}}{dm^3mol^{-1}s^{-1}}$	Author	Reference
5.8	Kistiakowsky & Volpi (1959)	55
5.5	Kaufman & Decker (1959)	57
5.2	Clyne & Thrush (1961)	42
2.8	Kretchmer (1963)	79
2.3	Wilson (1969)	80
4.37	Clark & Wayne (1970)	43
6.7	Becker *et al.* (1976)	78
36.34*	Monat *et al.* (1980)	45
6.58	This work (1986)	—

* Extrapolation from high temperature data

Table 7.5(a) Room temperature rate constants for k_{12}.

$\frac{k_{12} \times 10^{-8}}{dm^6mol^{-2}s^{-1}}$	Author	Third body	Reference
2.2	Harteck (1953)	O_2	81
0.78	Benson & Axworthy (1967)	O_2	50
1.1	Kretchmar (1958)	O_2	82
1.0	Elias *et al.* (1959)	O_2	49
1.9	Jones & Davidson (1959)	O_2	83
0.86	Urbach *et al.* (1959)	O_2	84
2.0	Kaufman (1958)	N_2	85
1.0	Elias *et al.* (1959)	N_2	49
1.25	This work (1986)	N_2	—

Table 7.5 (b) Room Temperature Values for γ (pyrex surface).

$\gamma/10^{-5}$	Authors	Ref
7.7	Elias, Ogryzlo & Schiff	49
1.6	Morgan, Elias & Schiff	89
12.0	Linnett and Marsden	90
3.0	Kaufman	85
3.17	This work	—

range (4.2–8.2 torr), and with the observed nitrogen atom concentrations (0.4μmol dm^{-3}), a value of 0.5 sec^{-1} would be expected. Furthermore, variation due to the experimental conditions would give a fluctuation of 30% to this value. Considering the error limits of determined quantity (section 7.2.2), and the approximation involved, the constant k_a^* is consistent with the work reported in Chapter Six and the findings of Clark and Wayne.

The rate constant k_{12}, for the formation of ozone in the presence of N_2, was determined from the slope of fig. 7.4 . Previous determinations of this rate constant, using the third bodies O_2, N_2, have been listed in table 7.5(a) . The third body efficiency of both of these molecules has been shown to be similar at room temperature [86,87,88], and so a comparison between the present work and all of the listed values can therefore be made. From table 7.5(a) it can be seen that there is an excellent agreement between this work and that of Kretchmer and Elias *et al.* [82,49]. The reported values vary between 0.7 and 2.2×10^8 dm^6 mol^{-2} s^{-1}; this due to the differences in the experimental techniques that have been employed in the determination. The value reported here supports the lower values of k_{12} reported.

The rate constant, k_{11}, represents a surface efficiency, γ, for the recombination of oxygen atoms on a Pyrex surface of 3.2×10^{-5} since [51];

$$\gamma = \frac{2k_{11}r}{\bar{c}} \qquad (7.11)$$

where $\bar{c}$ is the mean speed of oxygen atoms at T = 292K [2] and r = 2.54cm.

Values of γ, determined by previous workers, are given in table 7.5(b) . The value of the surface efficiency depends upon the history and cleanliness of the glass; efficiency values have been reported in the range 10^{-5} to 10^{-4}, the value determined in this study lies in this range.

7.3 The High Temperature — Post Shock Data.

In Chapter Five models were given to describe the variation with time of both the first positive and NO(β) band emissions in the high temperature - post shock regime.

A typical high temperature trace, taken by observing the emission at 579nm (1+), is given in fig. 7.5 . This shows the steady pre-shock glow, a rise in the emission with the arrival of the shock front and then decay, which is due to a time dependent variation in the nitrogen atom concentration. Each trace was fitted to the equation (Chapter Five);

$$^{579}I_t = I_{psg}\, p_{21}^2\, K_{(T)} \int_{t-tr}^{t} \frac{\exp-(\alpha_{po}\cdot t)\cdot dt}{tr} \qquad (7.12)$$

where α_{po} is the post-shock decay constant, I_{psg} is the pre-shock glow, $K_{(T)}$ is the enhancement factor and tr is the integration time.

The solid line given in fig. 7.5 is a fit of the data according to eqn. (7.12). The quality of this fit shows that eqn. (7.12) accurately describes the emission intensity, $^{579}I_t$, as a function of the time. From each trace the constants $K_{(T)}$, tr and α_{po} were determined. It was shown (Chapter Five) that the rate constant k_5 was related to the post and pre shock decay constants by;

$$4k_5 = (\alpha_{po} - 2\gamma)/p_{21}[O_2] \qquad (7.13)$$

where γ is the pre-shock decay constant suitably corrected for the post-shock conditions. The calculated values of k_5 are given in table 7.6 for a series of experiments.

A high temperature trace, taken by observing the NO(β) band located at 403 nm, is given in fig. 7.6 . This shows a steady pre-shock glow, an increase in the emission with the arrival of the shock front, relaxation and then eventually decay. Each trace was fitted to the equation (Chapter Five);

$$\frac{^{NO}I_t}{I_{psg}\, p_{21}{}^3\, ^{NO}K_{(T)}} = \int_{t-tr}^{t} \frac{[1+A]\exp-((2k_5[O_2]+b)t)\cdot dt}{tr} - \int_{t-tr}^{t} \frac{(A)\exp-((4k_5[O_2]+b)t)\cdot dt}{tr} \qquad (7.14)$$

Figure 7.5 Shock trace of the $N+O_2$ reaction system (579 nm)

Run Name APB 126A

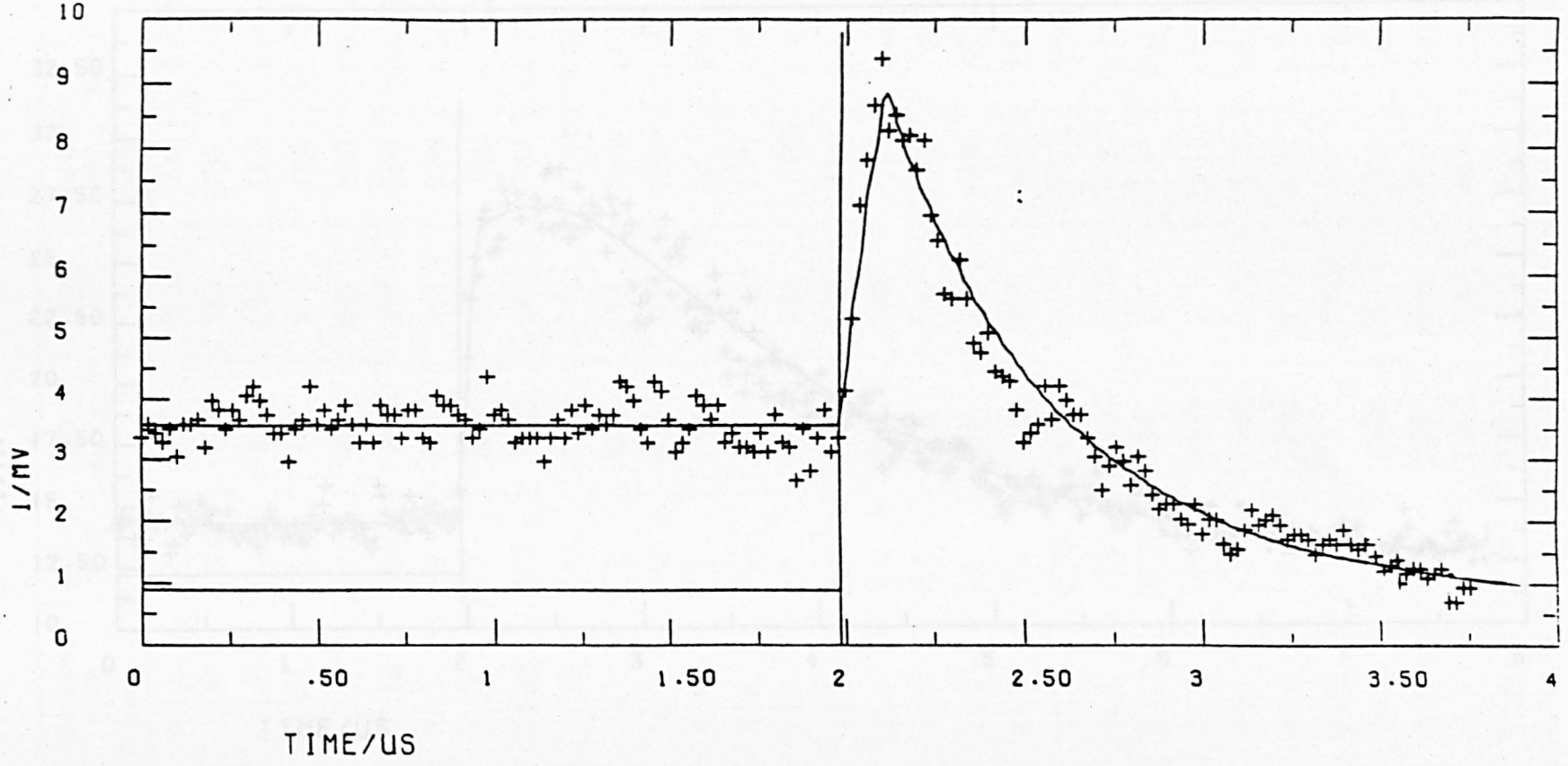

Figure 7.6 Shock trace of the $N+O_2$ reaction system (403 nm)

Run Name APB 93A

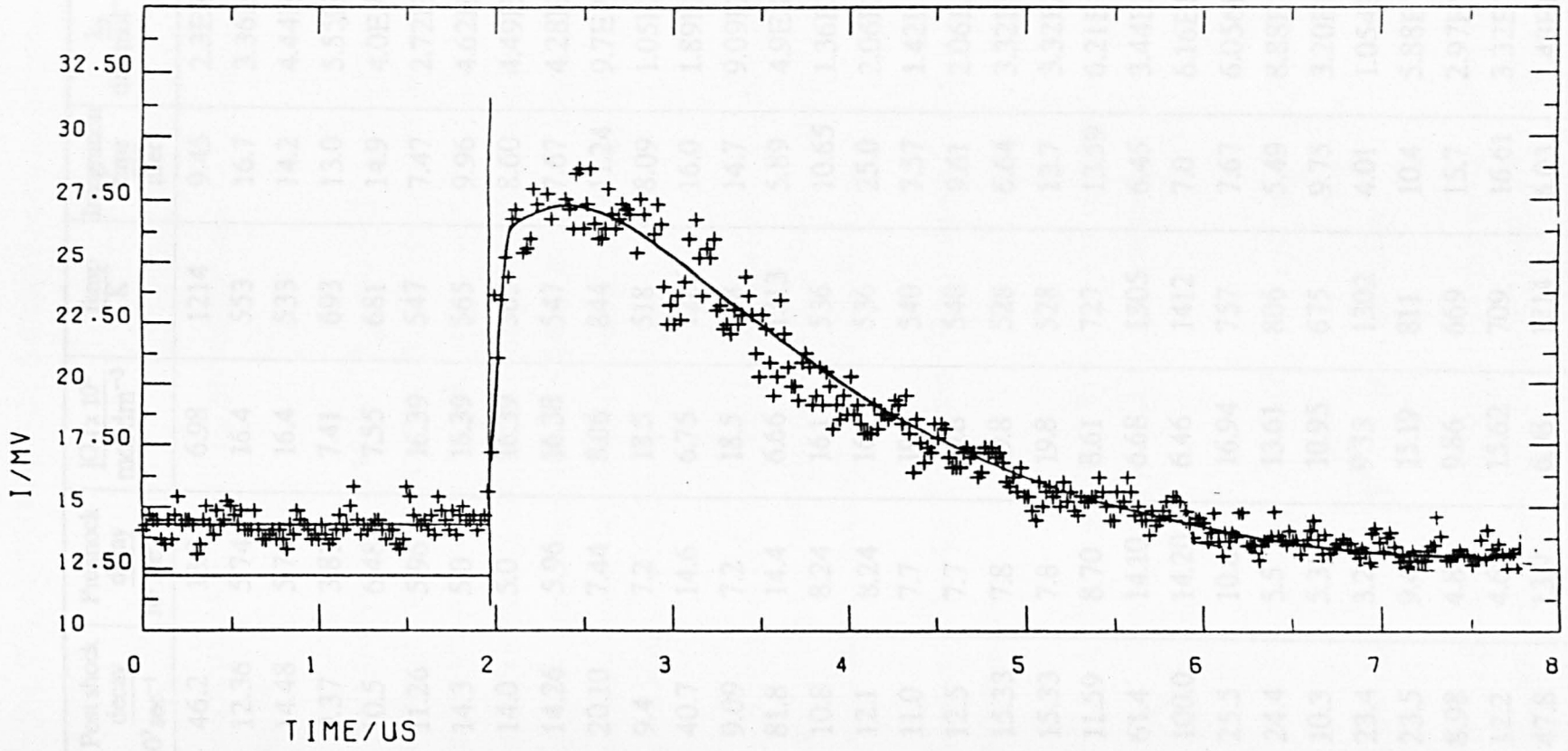

Table 7.6 High Temperature Determination of k_5 (579 nm).

Run Name	Post shock decay $10^3 sec^{-1}$	Pre shock decay $10^3 sec^{-1}$	$[O_2] \times 10^6$ mol dm^{-3}	Temp K	Integration time μsec	k_5 $dm^3 mol^{-1} s^{-1}$	$K_{(T)}$
122A	46.2	13.9	6.98	1214	9.45	2.3E8	0.101
113B	12.36	5.74	16.4	553	16.7	3.36E7	0.348
113A	14.48	5.74	16.4	533	14.2	4.44E7	0.427
118A	9.37	3.81	7.41	693	13.0	5.55E7	0.292
119A	10.5	6.48	7.55	681	14.9	4.0E7	0.314
114B	11.26	5.96	16.39	547	7.47	2.72E7	0.518
115A	14.3	5.0	16.39	565	9.96	4.62E7	0.432
115B	14.0	5.0	16.39	565	8.60	4.49E7	0.411
114A	14.26	5.96	16.38	547	7.67	4.28E7	0.421
121A	20.10	7.44	8.06	844	11.24	9.7E7	0.205
116B	9.4	7.2	18.5	518	8.09	1.05E7	0.498
129A	40.7	14.6	6.75	1286	16.0	1.89E8	0.236
116A	9.09	7.2	18.5	518	14.7	9.09E6	0.483
124A	81.8	14.4	6.66	1313	5.89	4.9E8	0.092
117B	10.8	8.24	16.1	536	10.65	1.36E7	0.414
117A	12.1	8.24	16.1	536	25.0	2.06E7	0.466
111A	11.0	7.7	19.8	540	7.57	1.42E7	0.407
111B	12.5	7.7	19.8	540	9.61	2.06E7	0.398
112B	15.33	7.8	19.8	528	6.64	3.32E7	0.437
112A	15.33	7.8	19.8	528	13.7	3.32E7	0.517
120A	11.59	8.70	8.61	727	13.59	6.21E7	0.278
123A	61.4	14.10	6.68	1305	6.45	3.44E8	0.078
126A	100.0	14.20	6.46	1412	7.0	6.16E8	0.097
104A	25.5	10.89	16.94	757	7.67	6.056E7	0.256
105A	24.4	5.5	13.61	806	5.49	8.88E7	0.219
100A	10.3	5.36	10.95	675	9.75	3.20E7	0.30
107A	23.4	3.2	9.33	1302	4.01	1.054E8	0.0638
106A	23.5	9.4	15.19	811	10.4	5.88E7	0.235
102A	8.98	4.88	9.86	669	15.7	2.97E7	0.297
109A	12.2	4.68	15.62	709	16.61	3.32E7	0.266
122B	47.8	13.9	6.98	1214	6.03	2.43E8	0.101

where $^{NO}K_{(T)}$ is the enhancement factor for the NO(β) band, I_{psg} is the pre-shock glow, $A = [N]_o/[O]_o$ and b is the pre-shock decay constant corrected for the post-shock conditions.

The solid line give in fig. 7.6 is a fit of the data according to eqn. (7.14). This shows that the form of the intensity varation can be accurately represented by this equation.

From each fit the constants $^{NO}K_{(T)}$ and $2\,k_5[O_2]$ and tr can be determined. The analysis relies upon the representation of the pre-shock emission by a first order equation which is characterised by a decay constant b. It was shown (section 5.3.2.2) that this is a valid approximation in the post peak regime. The values of $^{NO}K_{(T)}$, k_5 and tr determined from each experiment, are given in table 7.7 .. The constants were found to vary little with small changes in the value of A. Thus A need only be known approximately (see section 7.2.2).

The values of k_5 have been plotted as a function of the temperature in fig. 7.7 . From this it is seen that k_5 increases with the temperature and that the agreement between the data, from both emission bands, is good.

7.4. Discussion of the High Temperature Reaction Rate Constants for the $N+O_2$ Reaction.

An Arrhenius plot (fig. 7.8) was constructed from the data given in tables 7.6 and 7.7 . A straight line was fitted to the data by linear least squares analysis and gave the relationship;

$$k_5/dm^3mol^{-1}s^{-1} = (5.0 \pm 0.2) \times 10^9 \exp -(3103 \pm 380/T) \qquad (7.15)$$

the error limits are 2σ (95%) confidence values.

An alternative expression has been used by previous workers to describe the data in the temperature range T=300 to 2000K; a plot of $\ln(k_5/T)$ against $1/T$ was made and is given in fig. 7.9 . This gave a reasonable straight line, the solid line given in the plot represents the recommended value of k_5 between T=300 and 2000K [75] and shows the data reported here is in good agreement with this. Also plotted in fig.

Table 7.7 High Temperature Determination of k_5 (403 nm).

Run Name	Post shock decay 10^3 sec^{-1}	Pre shock decay 10^3 sec^{-1}	$[O_2] \times 10^6$ mol dm^{-3}	Temp K	Integration time μsec	k_5 dm^{3}mol^{-1}s^{-1}	$^{NO}K_{(T)}$
108B	111.8	14.65	15.9	1257	8.9	7.5E8	0.04
93B	24.3	5.83	10.07	886	5.52	2.89E8	0.093
125B	66.5	10.1	6.63	1285	4.85	8.9E8	0.037
96B	93.1	10.2	9.43	1250	6.21	1.08E9	0.034
101B	4.8	2.1	19.7	674	9.46	3.45E7	0.209
94B	94.3	14.9	12.4	1198	7.0	8.21E8	0.045
93A	23.2	5.8	10.2	882	6.1	2.72E8	0.09
120B	2.10	0.9	10.9	675	19.9	2.71E7	0.159
123B	50.7	10.0	6.45	1314	4.4	7.51E8	0.031
119B	18.9	4.84	10.1	681	11.82	2.7E7	0.152
104B	8.83	10.8	17.00	757	9.501	6.6E7	0.10
95A	21.37	6.41	10.71	900	7.0	2.4E8	0.067
91A	2.2	4.33	12.33	736	17.4	2.4E7	0.10
91B	1.76	4.33	12.33	736	25	1.92E7	0.103
109B	3.72	2.40	15.72	709	18.86	3.26E7	0.104
105B	12.87	3.20	13.61	806	12.36	1.21E8	0.09
87B	3.73	5.65	15.10	692	12.47	3.48E7	0.183
95B	22.1	6.14	10.7	900	8.0	2.44E8	0.065
96A	100.5	10.3	8.37	1250	9.7	1.44E9	0.037
106B	14.06	4.74	15.19	811	6.11	1.16E8	0.105
107B	48.3	56.6	8.33	1302	7.32	4.8E8	0.034
88B	4.67	6.26	14.62	639	10.0	4.71E8	0.196
103B	9.52	3.21	15.10	750	8.7	1.20E8	0.07

Figure 7.7 Variation of log (k_5) with the temperature.

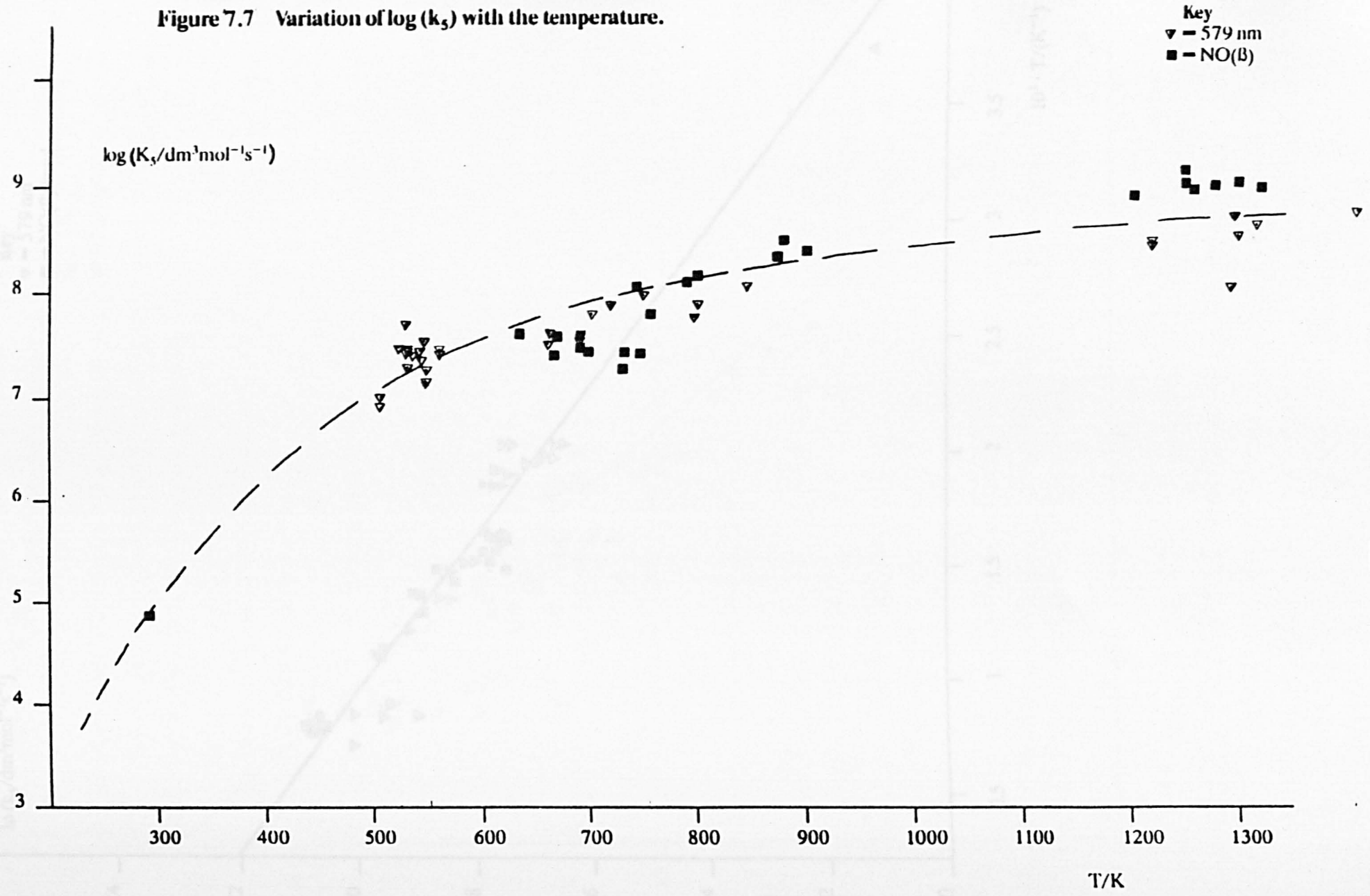

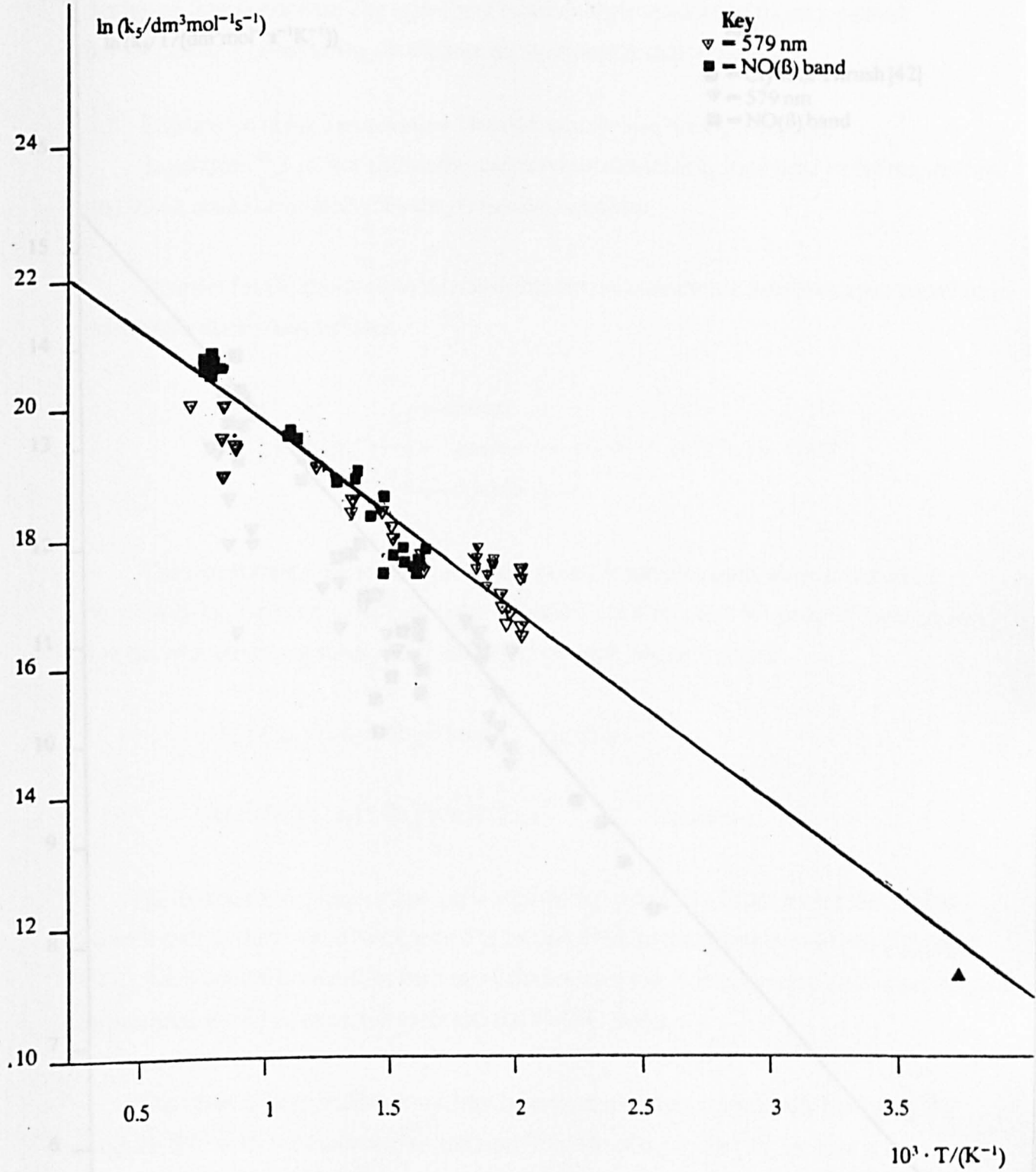
ln (k_5/dm^{3}mol^{-1}s^{-1})
Key
▽ = 579 nm
■ = NO(ß) band
24
22
20
18
16
14
12
10
0.5
1
1.5
2
2.5
3
3.5
$10^3 \cdot T/(K^{-1})$

Figure 7.9 Variation of ln (k_5/T) vs. 1/T for the N+O_2 reaction rate constant.

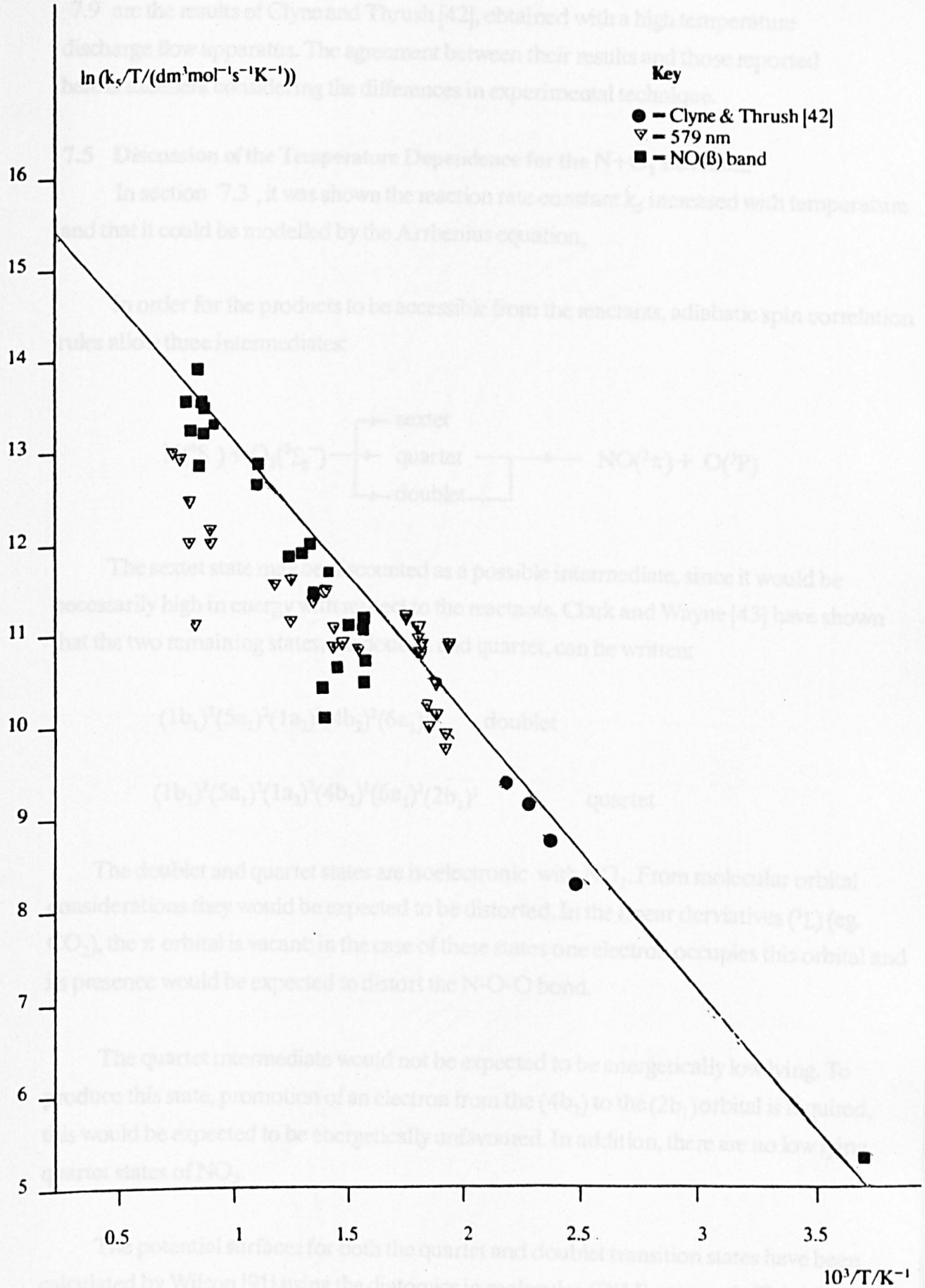

7.9 are the results of Clyne and Thrush [42], obtained with a high temperature discharge flow apparatus. The agreement between their results and those reported here is excellent considering the differences in experimental technique.

7.5 Discussion of the Temperature Dependence for the $N+O_2$ Reaction.

In section 7.3 , it was shown the reaction rate constant k_5 increased with temperature and that it could be modelled by the Arrhenius equation.

In order for the products to be accessible from the reactants, adiabatic spin correlation rules allow three intermediates:

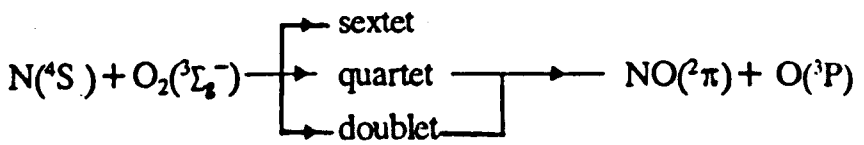

The sextet state may be discounted as a possible intermediate, since it would be necessarily high in energy with respect to the reactants. Clark and Wayne [43] have shown that the two remaining states, the doublet and quartet, can be written:

$(1b_1)^2(5a_1)^2(1a_2)^2(4b_2)^2(6a_1)^1$ doublet

$(1b_1)^2(5a_1)^2(1a_2)^2(4b_2)^1(6a_1)^1(2b_1)^1$ quartet

The doublet and quartet states are isoelectronic with NO_2. From molecular orbital considerations they would be expected to be distorted. In the linear derviatives ($^1\Sigma$) (eg. CO_2), the π orbital is vacant; in the case of these states one electron occupies this orbital and its presence would be expected to distort the N-O-O bond.

The quartet intermediate would not be expected to be energetically low lying. To produce this state, promotion of an electron from the ($4b_2$) to the ($2b_1$)orbital is required, this would be expected to be energetically unfavoured. In addition, there are no low lying quartet states of NO_2.

The potential surfaces for both the quartet and doublet transition states have been calculated by Wilson [91] using the diatomics in molecules (DIM) approach. This is a semi empirical formulation of valence bond theory applied to the quantum mechanics of tri and polyatomic species. The computed potential surface for the 2^2B_2 'ring state' and $2\,^4B_2$ intermediates are given in figures 7.10(a) and 7.10(b) respectively.

Figure 7.10 Potential energy surfaces for (a) doublet and (b) quartet states of NO_2

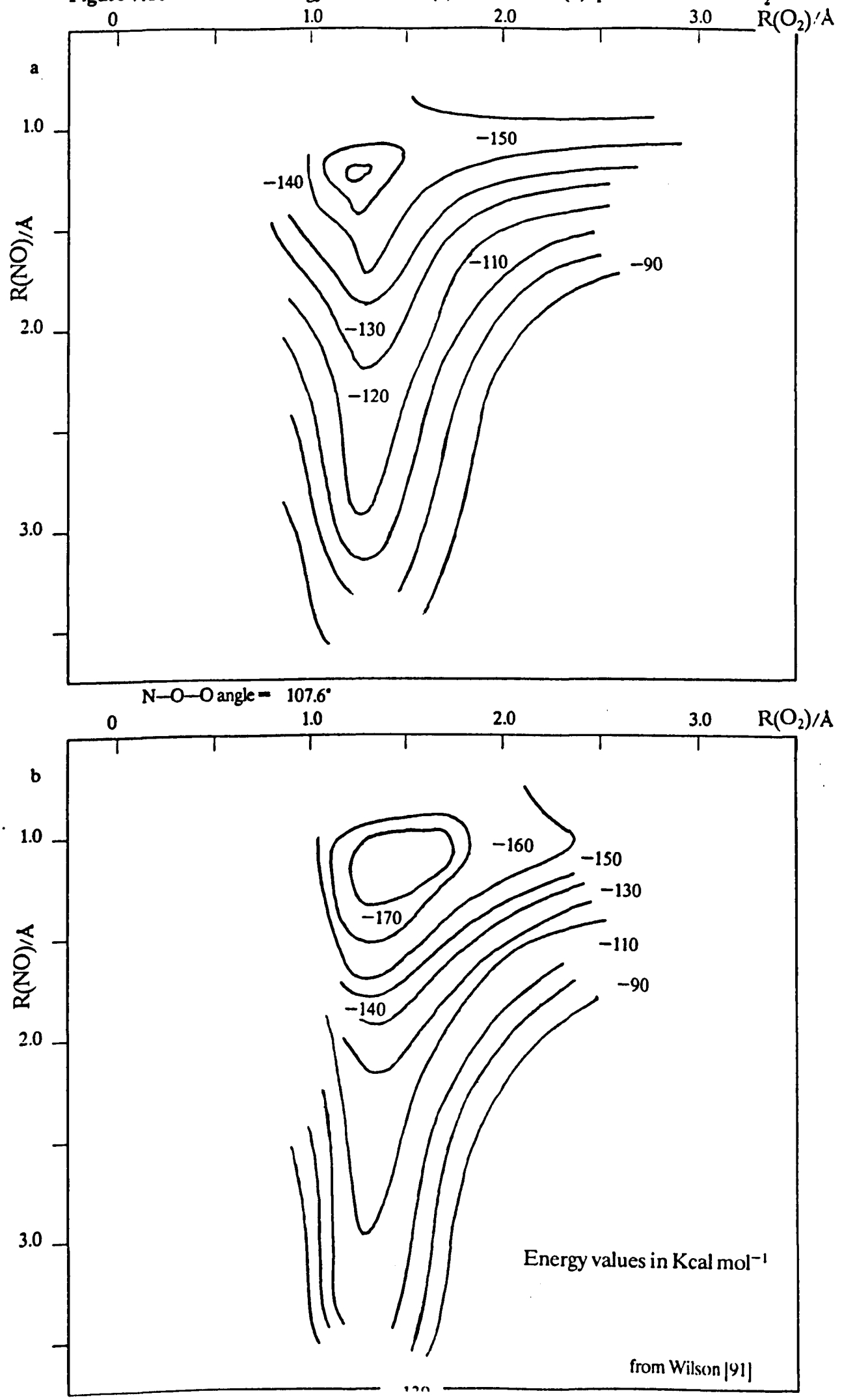

The conclusions that can be drawn from these potentials are interesting. From the position of the minimum in figure 7.10(a) , the reaction would be considered to be dynamically forbidden from occurring. The nitrogen atom accelerates toward the O_2 molecule (up the page) without any energy barrier at all. Forces do not rise along the O-O bond; it can be shown that $R_e(NO) = R(NO) + 0.2Å$ and $R_e(O_2) = R(O_2)$, where the quantities R and R_e refer to the unperturbed and perturbed bond lengths respectively. As a result, the nitrogen atom simply bounces off of the O_2 molecule and so reaction does not take place.

For the quartet intermediate (fig. 7.10(b)), a different situation exists. As the nitrogen atom accelerates toward the O_2 molecule, the O-O bond stretches. Energy analysis shows that 143 $KJmol^{-1}$ are required to reach the product asymptote from the bound quartet state. The internal energy modes have only 123 $KJmol^{-1}$, leaving an energy deficit of 20 $KJmol^{-1}$, which acts as an activation energy barrier. This analysis is in good agreement with the measured activation energy of 25 $KJmol^{-1}$.

Benioff has approached the $N+O_2$ reaction by using the Multi-Configuration Self Consistent Field (MCSCF) approach [92,93]. In this, the minimum energy pathway is calculated from the various matrix group elements that contribute to the total energy of the system. Their calculations show [92] that the energy of the doublet and quartet states lie 48 and 73 $KJmol^{-1}$ above the reactant asymptote. Correcting for the difference in zero point energy (~12 $KJmol^{-1}$), the doublet pathway requires an extra 36 $KJmol^{-1}$ to reach the product asymptote. This is also in fair agreement with the measured activation energy. It is clear that from this calculation the doublet surface is preferred, in accord with the suggestions of Clyne and Thrush [42].

There has been considerable interest as to whether the $N+O_2$ reaction is responsible for the observed concentration of NO in the atmosphere D region [92,93]. At altitudes of 100Km (T=200K), the concentration of NO has been measured to be 6×10^7 molecules cm^{-3} [94]. If it is assumed that reactions (7.4) and (7.16) are the production and removal processes;

$$N + O_2 \xrightarrow{k_5} NO + O \qquad (7.4)$$

$$NO + N \xrightarrow{k_6} N_2 + O \qquad (7.16)$$

then the concentration of NO is given by (Chapter Five);

$$[NO] = \frac{k_5[O_2]}{k_6}$$

Under these conditions, $k_6 = 1.2 \times 10^{-13} cm^3 molecule^{-1} sec^{-1}$, $[O_2] = 2 \times 10^{12}$ molecule cm^{-3} and k_5, calculated from this study at T = 200K, equal to 3×10^{-20} cm^3 $molecule^{-1}$ sec^{-1}. The values give an NO concentration of 5.2×10^5 molecule cm^{-3}, which is considerably lower than the observed value. The NO in the atmospheric D region is therefore not controlled by reactions (7.4) and (7.16).

Ferguson has reported a value for the rate constant [96];

$$O_2^+ + N_2 \xrightarrow{k_{15}} NO^+ + NO \qquad (7.17)$$

where $k_{15} > 6 \times 10^{-18}$ cm^3 $molecule^{-1}$ sec^{-1}. Assuming that reaction (7.16) is the removal process for NO then the concentration is given by;

$$[NO] = \frac{k_{15}\,[N_2][O_2^+]}{k_6\,[N]} \qquad (7.18)$$

which must have a value of $\sim 6 \times 10^7$ molecule cm^{-3}. Using a value of $[N_2] = 8 \times 10^{12}$ molecule cm^{-3}, then the ratio $[O_2^+]/[N] = 0.13$ is required. Unfortunately there are no reliable estimates of this but a recent approximate value gives some support to this mechanism [95]. Furthermore the reaction;

$$O_2(a^1\Delta_g) + N \longrightarrow NO + O \qquad (7.19)$$

may also be of importance, a reliable measurement of this will be required in future evaluations [43,97].

CHAPTER EIGHT

8.0 Singlet Molecular Oxygen.

8.1 Introduction.

This chapter describes the electronic structure, spectroscopy and reactions of singlet molecular oxygen. Production methods and detection of the species are also considered. This review of singlet molecular oxygen is not intended to be a comprehensive one, and is concerned only with the literature that is relevant to this study.

8.2 The Electronic Structure of the Oxygen Molecule.

The molecular orbital diagram for O_2 is given in figure 8.1 . The O_2 molecule has sixteen electrons. The four innermost (KK) retain their atomic character. The remaining twelve are valence electrons, molecular orbital theory requires them to occupy the lowest available bonding and anti-bonding orbitals. The electronic structure of O_2 is written:

$$KK.(2s\sigma_g)^2(2s\sigma_u^*)^2(2p\sigma_g)^2(2p\pi_u)^4(2p\pi^*_g)^1(2p\pi^*_g)^1$$

The 2s atomic orbitals interact weakly to give the $2\sigma_u$ and $2\sigma_g$ molecular orbitals, each containing a pair of electrons. The p_z atomic orbitals form the $2p\sigma_g$ molecular orbital, which also contains a pair of electrons. This gives rise to a strong σ bond, that defines the co-ordinates of the molecular orbitals. In addition there are two $1\pi_u$ degenerate bonding molecular obitals which contain two electron pairs, and two degenerate $1\pi_g^*$ antibonding molecular orbitals each of which contain one of the two remaining electrons.

The electrons in the two degenerate π anti-bonding molecular orbital, $1\pi_g^*$, can be arranged in several ways (table 8.1). Molecular oxygen is in the ground state, $O_2(^3\Sigma_g^-)$, when the two electrons are unpaired and have parallel spin [98], in the first excited state, $O_2(a^1\Delta_g)$, when the two electrons are paired and are in the same orbital and in the second excited state, $O_2(b^1\Sigma_g^+)$, when the two electrons are paired but are in different orbitals.

The distribution of electrons in the $1\pi_g^*$ antibonding orbital determines the overall symmetry, angular momentum and total spin character of the molecule [99]. The total energy of the O_2 molecule depends upon the relative orientations of the spin and orbital angular momentum. Hund's rule [100] states that the term state with maximum multiplicity lies lowest in energy, and for states of equal multiplicity, that with the greater angular momentum will lie the lowest. With reference to table 8.1 , it is seen that the order of increasing energy for the first three molecular states is:

$$O_2(x^3\Sigma_g^-):O_2(a^1\Delta_g):O_2(b^1\Sigma_g^+).$$

Figure 8.2 gives an energy level diagram for these electronic species.

Figure 8.1 Electronic Structure of the O_2 molecule.

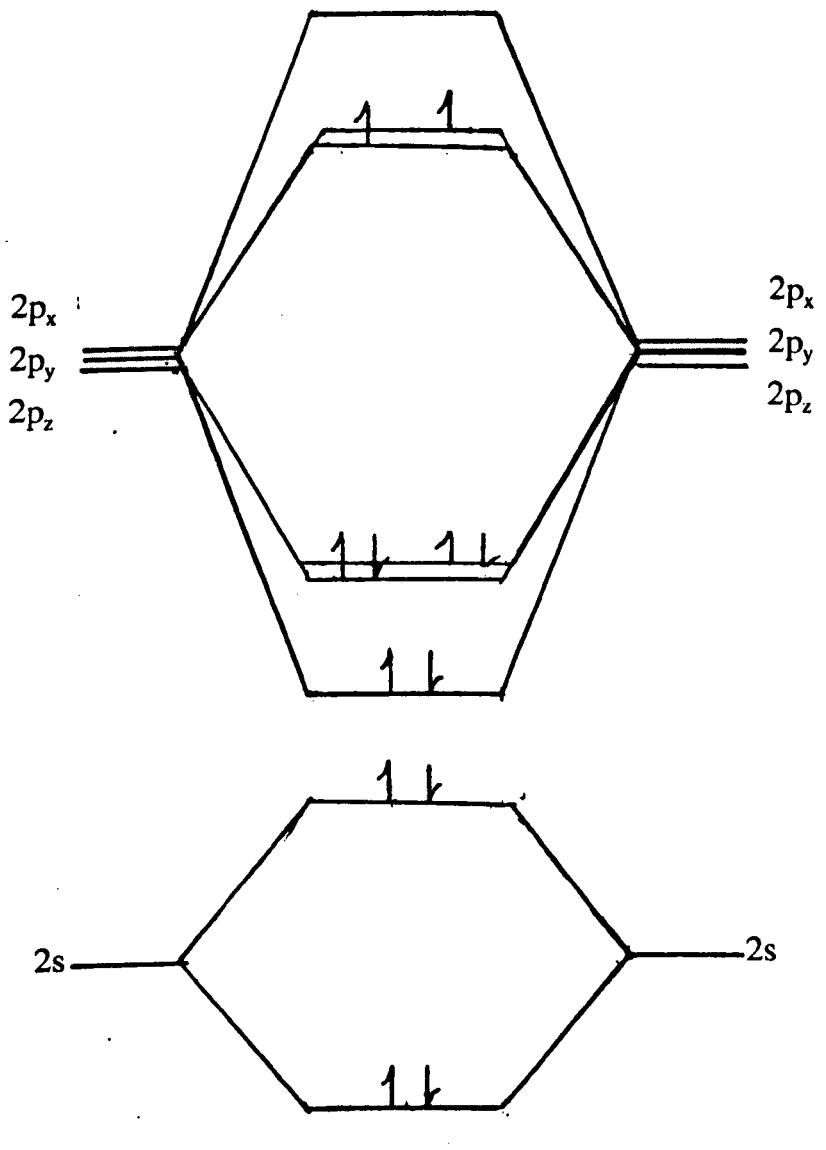

Electronic configuration:

$$KK.\ (2s\sigma_g)^2\ (2s\sigma_u^*)^2\ (2p\sigma_g)^2\ (2p\pi_u)^4\ (2p\pi_g^*)^1\ (2p\pi_g^*)^1$$

Figure 8.2 Potential energy diagram for some molecular oxygen states

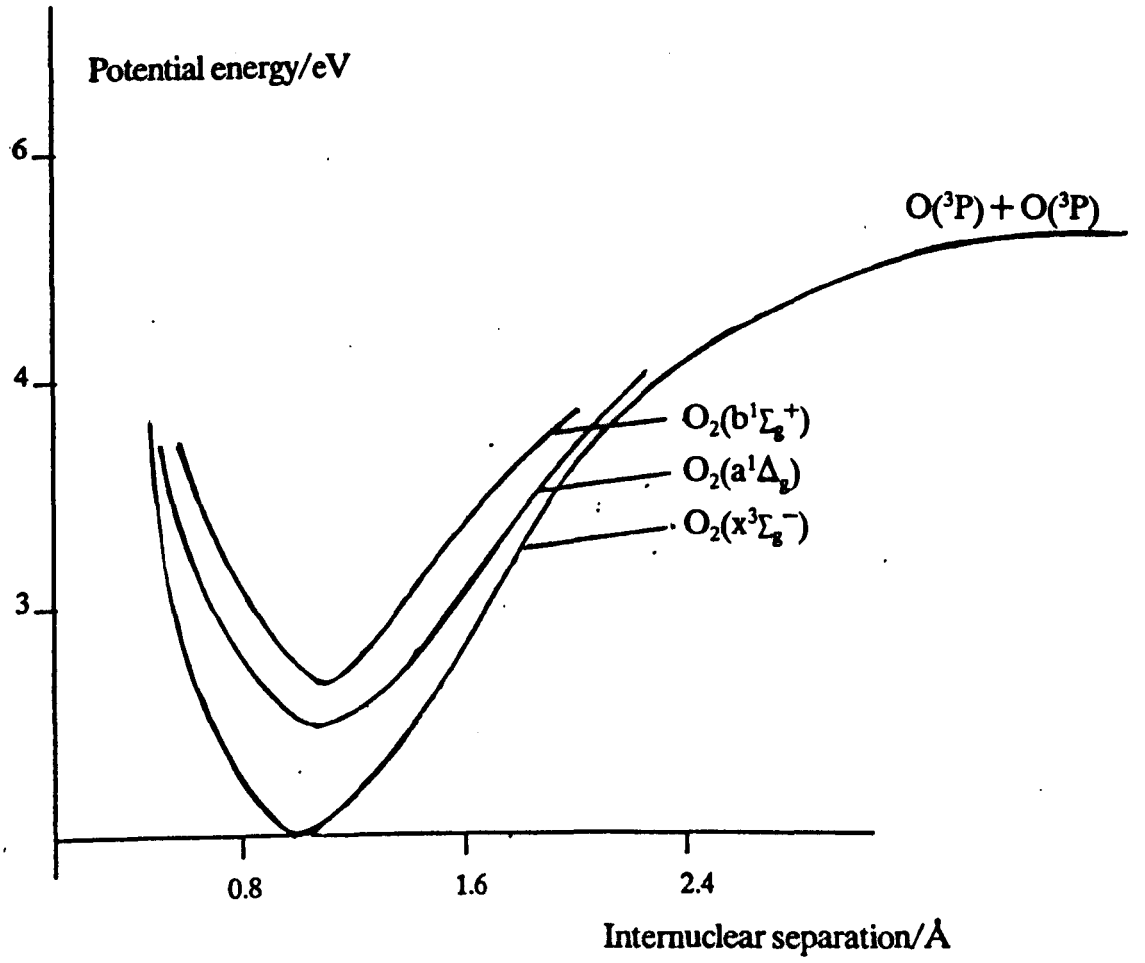

Table 8.1

Molecular State	$2p\pi_g$ arrangement	momentum		$\frac{E}{eV}$
		Orbital	Spin	
$b^1\Sigma_g^+$	$\underline{\uparrow}\ \underline{\downarrow}$	0	0	1.63
$a^1\Delta_g$	$\underline{\uparrow\downarrow}\ \underline{\ }$	2	0	0.98
$x^3\Sigma_g^-$	$\underline{\uparrow}\ \underline{\uparrow}$	0	1	0

8.3 The Optical Transitions of Singlet Molecular Oxygen.

The optical transitions of singlet molecular oxygen that are relevant to this thesis are given in table 8.2..

These transitions are strictly forbidden electric dipole processes [101]. As a consequence, the intensity from them is low and the free singlet molecular oxygen species are long lived. The molecules $O_2(a^1\Delta_g)$ and $O_2(b^1\Sigma_g^+)$ have measured free radiative lifetime of 44 mins [102] and 7 seconds [103] respectively (eqns. 8.1 and 8.2).

$$O_2(a^1\Delta_g) \longrightarrow O_2(x^3\Sigma_g^-) + h\nu \quad (\lambda = 1270\ nm) \tag{8.1}$$

$$O_2(b^1\Sigma_g^+) \longrightarrow O_2(x^3\Sigma_g^-) + h\nu \quad (\lambda = 762\ nm) \tag{8.2}$$

The electric dipole transitions from singlet molecular oxygen to the ground state are both symmetry and spin forbidden [28]. In the case of $O_2(a^1\Delta_g)$, there is an additional orbital restriction. These processes therefore occur as magnetic dipole transitions, and have much lower probability than allowed electric dipole transitions [101].

The spin restriction can be removed in the case of a simultaneous transition. The singlet oxygen - singlet oxygen interactions give rise to the unusual and interesting 'dimol' emission [104]:

$$2O_2(a^1\Delta_g) \longrightarrow 2O_2(x^3\Sigma_g^-) + h\nu \tag{8.3}$$

In these reactions, two singlet species interact and combine their excitation energy to emit one photon. The wavelength of emission from the combined molecular pair is half of the single molecule transition (table 8.2).

The emission was reported by Seliger (1960) from the reaction between aqueous hydrogen peroxide and sodium hypochlorite (eqn. 8.9). The correct identification of the band was suggested by Arnold, Ogryzlo and Witzke (1964). They passed gaseous oxygen through a discharge and recorded emission bands at 634, 703, 760 and 860 nm. The last two emissions came from the (0,0) and (0,1) transitions of $O_2(b^1\Sigma_g^+)$, and these were rapidly quenched when water was added to the system. They

Table 8.2 Some Emissions from Singlet Molecular Oxygen

MOLECULAR TRANSITION	Wavelength nm
$O_2(a^1\Delta_g)(v=o) \longrightarrow O_2(x^3\Sigma_g^-)(v=o) + h\nu$	1270
$O_2(a^1\Delta_g)(v=o) + O_2(a^1\Delta_g)(v=o) \longrightarrow O_2(x^3\Sigma_g^-)(v=o) + O_2(x^3\Sigma_g^-)(v=o) + h\nu$	634
$O_2(a^1\Delta_g)(v=o) + O_2(a^1\Delta_g)(v=1) \longrightarrow O_2(x^3\Sigma_g^-)(v=o) + O_2(x^3\Sigma_g^-)(v=o) + h\nu$	579
$O_2(a^1\Delta_g)(v=o) + O_2(a^1\Delta_g)(v=o) \longrightarrow O_2(x^3\Sigma_g^-)(v=1) + O_2(x^3\Sigma_g^-)(v=o) + h\nu$	703
$O_2(b^1\Sigma_g^+)(v=o) \longrightarrow O_2(x^3\Sigma_g^-)(v=o) + h\nu$	762

concluded that the bands at 634 and 703 nm must come from the $O_2(a^1\Delta_g)$ molecule and suggested an O_4 dimer, stabilised by Van der Waals forces (eqn. 8.3).

Further work [105] suggested that the colliding molecules were not bound, since the emission was found to increase with the temperature. Borrell *et al.* have studied these emissions in a combined discharge flow tube and also found that the emission increased above room temperature [106]. Furthermore, up to 1000K the results suggested that the process was collisional, above 1000K, the emission increased further and this was attributed to the presence of vibrational 'hot bands.'

McKellar, Rich and Welsh have studied the absorption of several dimol transitions at low temperature. They found that down to 120K, the absorption hardly changed at all, but below 120K, there was a sharp increase of the absorption with the temperature [107].

In the light of these studies, it was considered worthwhile to study the emission at low temperature. It was found that between 100 to 300K, the emissivity remains virtually independent of the temperature. These and the high temperature results of Borrell have been considered in terms of the Van Kranendonk theory for collision induced transitions (Chapter Eleven).

8.4 Generation of Singlet Molecular Oxygen

For the experiments described in this thesis, singlet molecular oxygen was produced by flowing purified O_2 through a microwave discharge. Both $O_2(a^1\Delta_g)$ and $O_2(b^1\Sigma_g^+)$ are produced; $O_2(a^1\Delta_g)$ can result from the exothermic oxygen atom recombination [108], $O_2(b^1\Sigma_g^+)$ is produced downstream by the energy pooling reaction [109]:

$$O_2(a^1\Delta_g) + O_2(a^1\Delta_g) \longrightarrow O_2(b^1\Sigma_g^+) + O_2(x^3\Sigma_g^-) \qquad (8.4)$$

Most of the gas phase work that has been done on singlet molecular oxygen has involved the species production by a microwave discharge [110]. Other discharges (R.F, D.C) have been employed, but microwave cavities can maintain more stable production rate over a wider pressure range [110].

Previous workers have shown that the concentration of the singlet molecular oxygen can be greatly enhanced by allowing the oxygen to become saturated with mercury vapour prior to discharge [49]. Oxygen atoms are produced by the discharge, these are efficient deactivators of singlet molecular oxygen. The mercury vapour reacts with the oxygen atoms according to [110]:

$$Hg + O \longrightarrow HgO \qquad (8.5)$$

$$Hg + O \longrightarrow HgO + O_2(a^1\Delta_g) \qquad (8.6)$$

Since one is concerned with kinetic measurements, it is of paramount importance to ensure that the O_2 stream is free of impurities. Contamination with the species O and O_3 can be problematic when using discharge methods [111]. The measurements that were made in the system used here (Chapter Nine) were taken with an oxygen stream containing mercury, and also at a distance from the discharge. This allows the oxygen atoms to be removed by both the HgO ring and by wall deactivation [49].

Singlet molecular oxygen can be produced by laser excitation [112]. Both singlet molecular oxygen states, $O_2(a^1\Delta_g)$ and $O_2(b^1\Sigma_g^+)$, can be selectively produced by using a laser source of suitable wavelength. The use of tuneable dye lasers have meant that particular vibrational levels can be selected for study. In recent work, $O_2(a^1\Delta_g)$ was produced by a Nd/YAG laser system [113], the $O_2(b^1\Sigma_g^+)$ state has also been produced by photolysis of $O_2(x^3\Sigma_g^-)$, using a vacuum ultra violet hydrogen laser [114]. These production methods carry the benefit not only of vibrational state selection but also the freedom from oxygen atom and ozone impurity.

Ozone photolysis can also be used to produce singlet molecular oxygen, and it is thought that this reaction may be significant in the production of the species in both the lower and upper atmosphere [115]. Irradiation of ozone results in the formation of singlet molecular oxygen;

$$O_3 + h\nu\ (\lambda = 310 - 330\,nm) \longrightarrow O_2(a^1\Delta_g) + O(^3P) \qquad (8.7)$$

and at shorter wavelengths:

$$O_3 + h\nu\ (\lambda = 210 - 310\,nm) \longrightarrow O_2(a^1\Delta_g) + O(^1D) \quad (8.8)$$

Energy transfer from the $O(^1D)$ species can produce $O_2(b^1\Sigma_g^+)$, if $O_2(x^3\Sigma_g^-)$ is present as an energy acceptor. This method provides a simple experimental route by which $O_2(b^1\Sigma_g^+)$ can be produced. However, it suffers from the oxygen atom impurity that can be present with discharge methods.

Findlay and Snelling produced $O_2(a^1\Delta_g)$, in the gas phase, by irradiation of oxygen/benzene mixtures at 254 nm [116]. The $O_2(a^1\Delta_g)$ is formed by the quenching of triplet benzene by the ground state oxygen molecule [117]. Although this method has the advantage that oxygen atom and ozone impurities are eliminated, it introduces benzene as an additional quenching species. Triplet sulphur dioxide has also been used to produce $O_2(a^1\Delta_g)$ by photosensitisation [118]. These reactions are of considerable importance since they are thought to be involved in the production of singlet molecular oxygen in polluted atmospheres [110].

In solution, singlet molecular oxygen can be produced by the reaction between sodium hypochlorite or chlorine in aqueous hydrogen peroxide [119]:

$$NaOCl + H_2O_2 \longrightarrow NaCl + H_2O + {}^1O_2 \quad (8.9)$$

The singlet molecular oxygen produced is almost exclusively in the $O_2(a^1\Delta_g)$ state, since water rapidly quenches the $O_2(b^1\Sigma_g^+)$ molecule. Organic reactions of $O_2(a^1\Delta_g)$ in solution are studied by using organic sensitisers, and reaction (8.9) remains little more than a curiosity rather than a general production process [120].

8.5 Detection and Measurement.

In the gas phase there are a number of techniques that can be used to detect and measure singlet molecular oxygen.

The molecule $O_2(a^1\Delta_g)$ is paramagnetic by virtue of its orbital angular momentum, and has been analysed by use of paramagnetic resonance. Falik *et al.* used this technique and estimated that 10% of their discharged oxygen was in the $O_2(a^1\Delta_g)$ state [121]. They were also able to monitor the formation of $O_2(b^1\Sigma_g^+)$ from triplet sensitisers (naphthalene, quinoxaline and per fluoro–naphthalene).

Singlet molecular oxygen can be detected by calorimetry. In this method, a heated wire is inserted into the oxygen gas flow and the amount of energy liberated by the excited molecules on the wire is used to calculate their concentration. Arnold [122] has shown that cobalt coated wire is more than 95% efficient in deactivating $O_2(a^1\Delta_g)$. The disadvantages of this method are two-fold. In the gas stream there may be other excited species, ie $O_2(b^1\Sigma_g^+)$, that deactivate on the wire. This method is more difficult to use for temperature dependent studies, since the variation in quenching efficiency of the wire probe is uncertain [105].

Photo ionisation was first used to detect singlet molecular oxygen by Cairns and Samson [123] and then by McNeal and Cook [124,125]. It was found that singlet molecular oxygen, $O_2(a^1\Delta_g)$ and $O_2(b^1\Sigma_g^+)$, could be detected and have ionisation potentials 1 and 1·6 eV less than the ground state respectively. Clark and Wayne greatly improved the technique by employing rare gas resonance lines to excite the oxygen molecules [126]. The 1165 Å line of krypton excites only $O_2(b^1\Sigma_g^+)$, whereas the argon 1067 and 1048 Å resonance lines excite both $O_2(a^1\Delta_g)$ and $O_2(b^1\Sigma_g^+)$, but not the ground state O_2 molecule. The photo ionisation technique is very sensistive but it has the limitation in that it cannot be applied to systems containing organic molecules, oxides of nitrogen or other molecules which have excitation potentials below 11 eV.

The emissions from singlet molecular oxygen have been used to detect and follow the concentration of the species [127,128,110]. When sufficiently high concentrations of $O_2(a^1\Delta_g)$ are present, the emission bands at 762, 1270 and 634 and 703 nm can easily be detected [30,31,117,129,110]. The advantage of emission spectroscopy is that it can be used to examine individual species and that its use is not limited by the presence of other molecules, or by the pressure of the system under study [130]. This method was used for the work reported in Chapters Ten and Eleven, since the emission bands at 634, 703 and 762nm are sufficiently intense under our conditions [28,30,31].

Chemical methods are less common than the physical for the detection and determination of singlet molecular oxygen. Since chemical additives must be state specific, react rapidly and be impurity free, the variety of detecting species is distinctly limited. The reaction of 2-3 dimethyl but-2-ene has been used to measure $O_2(a^1\Delta_g)$, it is rapid and does not undergo side reactions [110]:

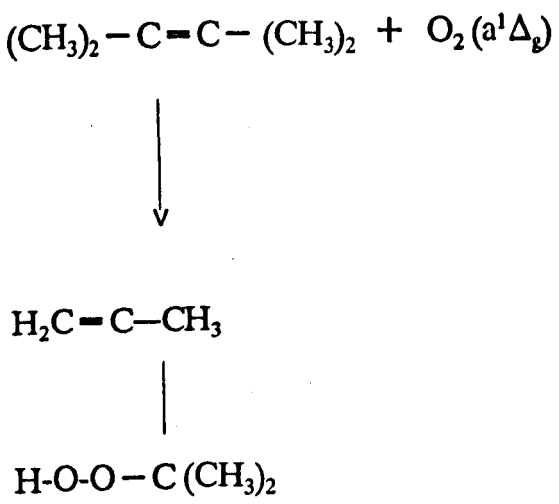

(8.10)

8.6 Reactions of Singlet Molecular Oxygen in the Gas Phase.

There have been numerous studies of the quenching of singlet molecular oxygen in the gas phase. These fall into two categories, physical and chemical quenching. In this section physical quenching is considered since it is relevant to the work reported in Chapter Ten.

The temperature dependence of the quenching of singlet molecular oxygen has been studied over a limited temperature range, around room temperature, by a variety of methods [112]. At high temperature (300-1300K), studies have been made by using a combined discharge flow shock-tube [30,11,12]. The temperature range 100 to 450K can now be covered by the new variable temperature discharge flow apparatus (Chapter Nine), and several collision partners have been investigated by this technique (Chapter Ten).

Physical quenching is the process by which electronic energy is lost by a non-reactive collision. This can occur by both molecular and surface interaction :

$$O_2(a^1\Delta_g) + m \longrightarrow O_2(x^3\Sigma_g^-) + m \qquad (8.11)$$

$$O_2(a^1\Delta_g) \xrightarrow{\text{wall}} O_2(x^3\Sigma_g^-) \qquad (8.11(a))$$

$$O_2(b^1\Sigma_g^+) + m \longrightarrow O_2(a^1\Delta_g) + m \qquad (8.12)$$

A series of rate constants for both singlet species are given in table 8.3 . It can be seen that the quenching rate varies markedly with the quenching species and the quenching rate constants for $O_2(b^1\Sigma_g^+)$ are considerably larger than those of $O_2(a^1\Delta_g)$.

For the quenching of $O_2(a^1\Delta_g)$, the process requires spin inversion which is forbidden [101]. The quenching of $O_2(b^1\Sigma_g^+)$ to $O_2(a^1\Delta_g)$ has been verified experimentally by Kear and Abrahamson who detected the development of the dimol emission during the course of the reaction [138]. For the quenching of this molecule the spin restriction has been removed and so the quenching rate constants are greater than those for the $O_2(a^1\Delta_g)$ species.

Kohse-Höinghaus and Stuhl have studied the temperature dependence for the quenching of $O_2(b^1\Sigma_g^+)$ by H_2, NH_3, CH_3 and HCl between 200 and 350K. They found that the data could be fitted to a simple Arrhenius expression [114]. Borrell *et al.* have studied the quenching of $O_2(b^1\Sigma_g^+)$ by the molecules O_2, N_2, CO_2 and N_2O [112]. In this study the inefficient room temperature quenchers, O_2, N_2, were found to become more efficient at high temperature. The quenchers CO_2 and N_2O, efficient at room temperature, were on the other hand found to become less efficient at high temperature. Their studies have shown that the quenching of $O_2(a^1\Delta_g)$ increases with temperature and for a variety of molecules can be fitted to the Arrhenius equation.

Ogryzlo plotted the logarithm of the rate constant against the boiling point of the quencher. This empirical plot gave a reasonably good correlation [139] and no other physical property investigated was found to better it.

Davidson and Ogryzlo plotted the logarithm of the quenching rate constant against the highest fundamental frequency of the quencher [140] (table 8.3). Good correlations were obtained for both $O_2(a^1\Delta_g)$ and $O_2(b^1\Sigma_g^+)$, a sample plot is given in figure 8.3 . This suggests that the vibrational frequency of the quencher molecule is an important factor in the quenching process.

Thomas and Thrush have used a statistical approach [112,141]. They compared the fraction of quenching collisions, which gave rise to a particular vibrational level, with the calculated probability for that level. A surprisal plot of this against the fraction of energy being released gave a straight line for both species, and this was observed using the quenchers H_2O, D_2O, C_2H_2, NH_3, N_2O, CO_2, NO, CO and HCL. From this analysis they concluded that the deactivation mechanism was non specific and that resonant energy transfer was not important. They also concluded that the quenching took place under the influence of short range forces, on the repulsive part of the molecular potential well.

Table 8.3 Deactivation Rate Constants for the Quenching of Singlet Molecular Oxygen at T=292K.

(a) Quenching of $O_2(a^1\Delta_g)$

Quenching rate constant $dm^3\ mol^{-1}s^{-1}$		Reference	Highest fundamental frequency/cm^{-1}
He	4.8	131	—
H_2	2.8E3	116	4405
O_2	9.4E2	30	1580
H_2O	3.4E3	116	3576
CO_2	1.5E3	132	2344
N_2O	<45	116	2224
NO	2.7E4	133	1904
CO	5.0E3	134	2168
D_2	2.3E3	28	3118

(b) Quenching of $O_2(b^1\Sigma_g^+)$

Quenching rate constant $dm^3\ mol^{-1}s^{-1}$		Reference	Highest fundamental frequency/cm^{-1}
He	6E3	135	—
H_2	2.4E8	135	4405
O_2	2.4E4	136	1580
H_2O	2.4E9	135	3576
CO_2	1.8E8	137	2344
N_2O	4.5E7	134	2224
NO	2.6E7	137	1094
CO	2.6E6	137	2168
D_2	1.0E7	138	3118

Figure 8.3 Variation of log (K) against the highest fundamental frequency of the quencher. ($O_2(b^1\Sigma_g^+)$)

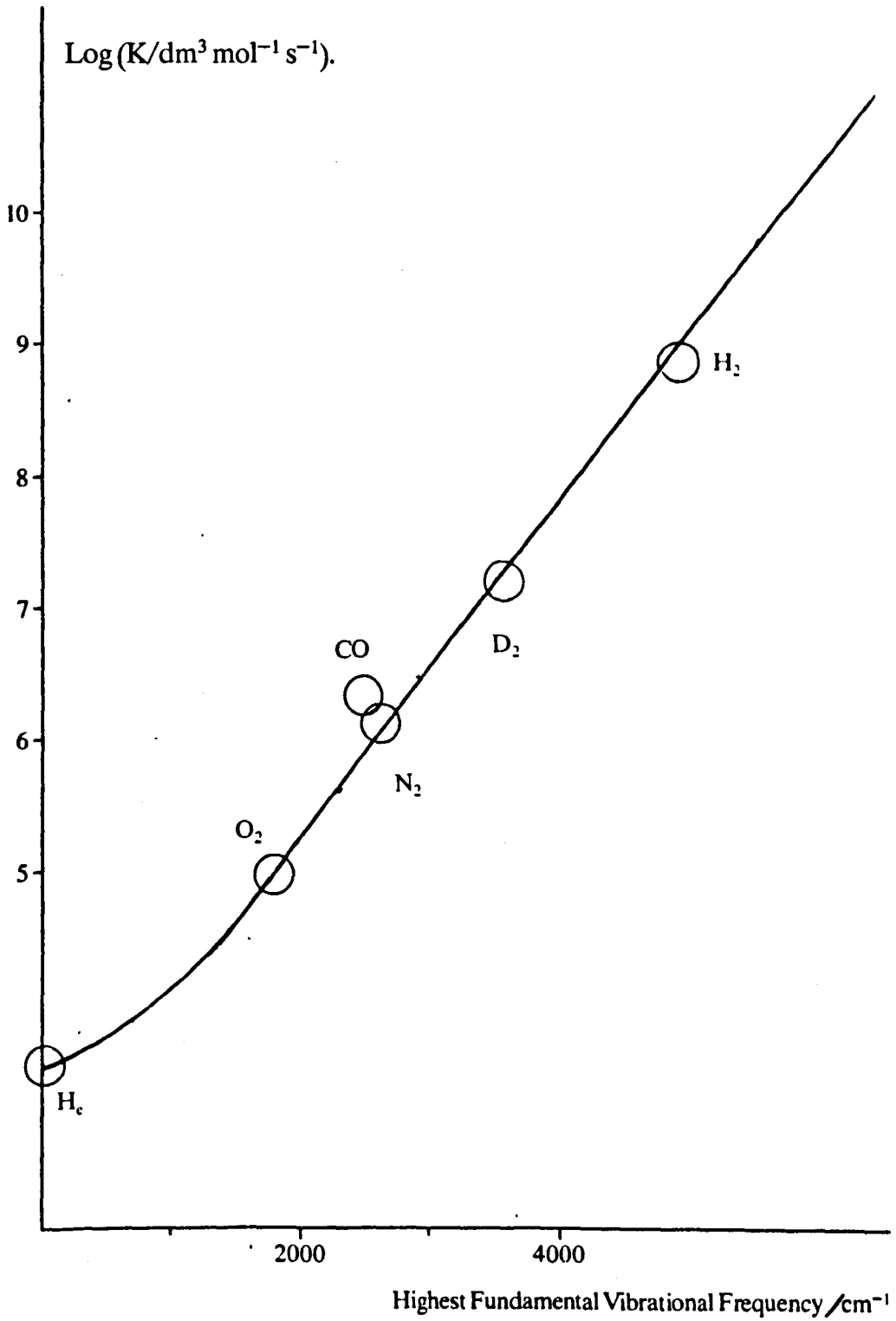

Kear and Abrahamson have investigated the quenching of $O_2(b^1\Sigma_g^+)$ [138]. In their approach they calculated the collision cross sections for diatomic molecules. They assumed that short range repulsive forces were dominant in the energy exchange process. The calculated rate constants for most gases was an order of magnitude too low, in the case of O_2 the theoretical rate was very much lower than the experimental.

The effect of long range interactions has been considered by Braithwaite, Davidson and Ogryzlo [142]. They envisaged energy transfer taking place between the transition dipole of the excited molecule and the transition dipole or quadrupole of the quencher. The results for the calculated rate constants were in good agreement with the experimental values, however the rate constant for O_2 was again still too small.

The temperature dependence for the quenching of $O_2(b^1\Sigma_g^+)$, using the collision partners H_2 and HBr, has been investigated [143,144]. From this study it was concluded that although long range forces play an important part in the quenching, short range interactions are also important. The best fit to the data was achieved by combining both of these interactions. The calculations also show that the main contributions to the quenching are those that convert the maximum amount of energy into vibration, and the minimum into translation and rotation.

In recent work, Maier [145] has used a model for relaxation that is a development of the earlier work of Shin [146] (Chapter Ten). Quenching is viewed as the conversion of the electronic energy into the maximum amount of vibration and the minimum into translation. Using this model, he has been able to provide a convincing explanation of the differences observed for the quenching of $O_2(a^1\Delta_g)$ by two different oxygen isotopes [147].

These various contributions have shown that the quenching of singlet molecular oxygen is still not completely understood. The problem still remains as to what one would expect for the temperature dependence for the quenching of these molecules. More experimental work is therefore required so that the contributions from the various interactions can be examined (Chapter Ten).

CHAPTER NINE

9.0 Experimental: The Variable Temperature Discharge Flow Apparatus.

9.1 Introduction

Measurements in the temperature range 100 to 440K were made by using a new variable temperature discharge flow apparatus. Singlet molecular oxygen was generated by a microwave discharge and then passed into a variable temperature flow tube. Measurements of the light emission as a function of distance along the flow tube were then conducted under a variety of experimental conditions.

This chapter gives an account of the construction and operation of the apparatus. The technique is described, an outline of the apparatus is given including details of the temperature regulating flow tube, purification and control and the detection systems. The use of a microcomputer to collect and analyse the results is also described.

9.2 The Discharge Flow Apparatus

The apparatus (fig 9.1) is a variable temperature discharge flow tube, constructed by the modification of a room temperature discharge flow tube by the addition of thermostating and insulating jackets.

Singlet molecular oxygen is produced by passing oxygen over mercury and then through a microwave discharge, which is supplied from a variable power source (Microtron 200), operating at 2450 MHz. The discharge consists of a microwave cavity (E.M.S.) surrounding a quartz discharge tube which is cooled by a compressed air supply. The whole section is surrounded by a protective Faraday cage [34].

The discharged oxygen is passed into the flow tube after having been exposed to an HgO ring (section 9.4.2), to remove any oxygen atoms, and then through a Woods light horn, which reduces stray light from the discharge [148]. The discharge flow tube, microwave cavity and connecting line are maintained at low pressure by a rotary vacuum pump (Genevac GNV 12).

The oxygen flow rate is controlled by a needle valve (Edwards), the pressure, and hence linear flow velocity, is controlled by a screw tap (Rotaflow) which is positioned between the exit of the tube and the main rotary pump. The pressure within the system is measured using a pressure gauge (C.G.3), and was checked against a diethyl ether manometer. The conversion between the manometer reading and torr valves was made by using a conversion factor of 0.0825mm $torr^{-1}$. A comparison between the pressure read by each device is given in figure 9.2 .

9.3 The Temperature Regulated Discharge Flow Tube.

9.3.1 The Design of the Flow Tube.

Calculations were made to ascertain whether it would be possible to maintain the test gas at a constant temperature, equal to that of the regulating jacket.

Temperature regulation depends upon the ability of the gas to diffuse to the cooling (or warming) surface. The diffusion rate increases as the radius of the tube is reduced; a small diameter tube was therefore chosen. Calculations show that under these pressues and flow rates, the gas should rapidly attain the temperature of the tube [43,110,149].

Figure 9.1 The variable temperature discharge flow tube

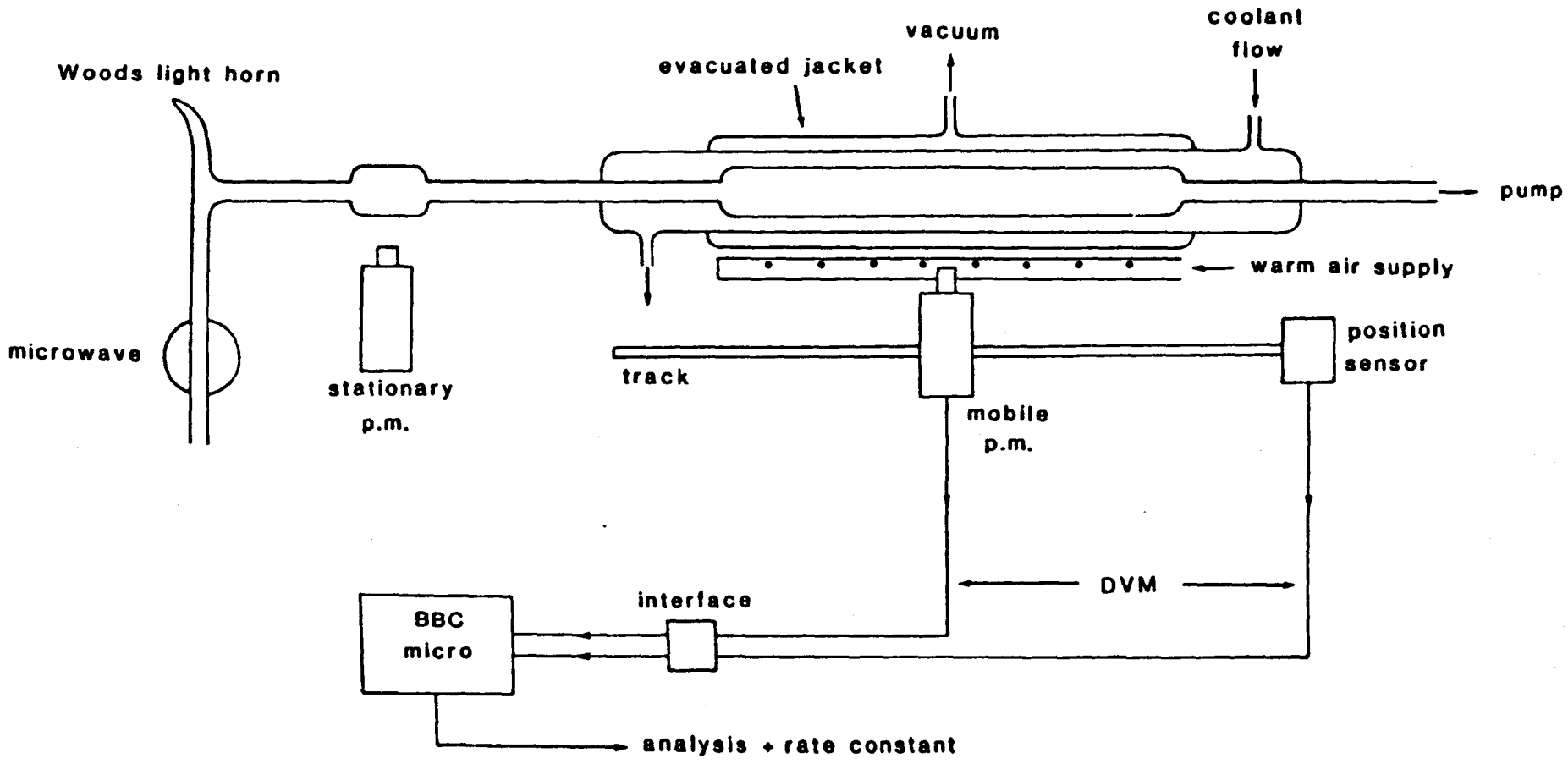

Figure 9.2 Comparison of the manometer and speedivac pressure gauges

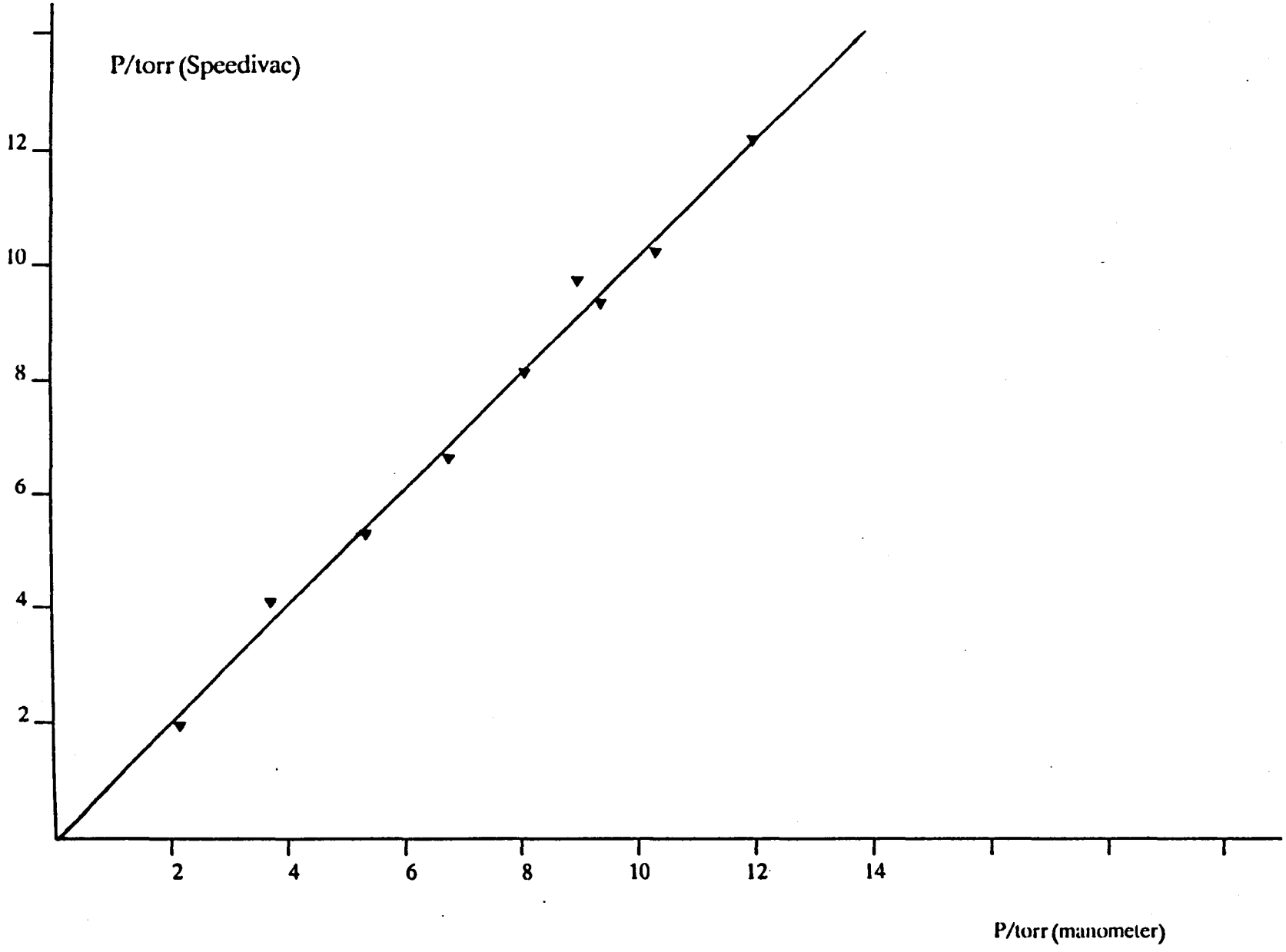

The calculations were verified experimentally. The temperature of the thermal jacket was measured by inserting four copper constantan thermocouples along its length and then connecting them to a silver junction box (Croprico). A calibration for the thermocouples was made by measuring the voltage they developed at a known temperature, the results are given in figure 9.3 .. This thermocouple arrangement was used for all of the temperature determinations. The output from the thermocouples was measured by using a digital voltmeter (Solartron 7040). Two thermocouples were then inserted into the flow tube and were connected with those in the jacket to the junction box. The temperature of the O_2 test gas was measured (>3cm downstream of the inlet), within experimental error, to be the same as the jacket throughout the pressure and temperature range. This is in accord with the experience of both Heidner and Hack [148,150]. The discrepancy in the temperature between one end of the flow tube and the other was measured and at the lowest temperature (100K) was ± 4K.

The vessel construction was as follows. The discharge flow tube, length 40cm (i.d = 3.20cm) was surrounded by a temperature regulating jacket, length 70cm (i.d = 4.20cm) and vacuum jacket, length 40cm (i.d = 5.20cm).

The discharge flow tube was connected to the thermal jacket by small diameter tubing, length 15cm (i.d = 1.0cm), one of the sections ensures rapid thermal equilibration between the test gas and the jacket (fig. 9.4).

The thermal jacket was supplied with coolant or warming agent by two supply and two exit pipes (i.d = 1.0cm). These were located at each end of the thermal jacket, and angled at approximately 45° to the walls of the jacket to improve the flow.

The vacuum jacket is pumped by a separate vacuum line using an Edwards (ED4) and an oil diffusion pump. The pressure within the jacket was maintained at 10^{-3} torr and was monitored with a McLeod gauge.

The first designs of this system were made by using Pyrex glass throughout. It was found that the strain imposed by contraction and expansion gave only a limited lifetime, the following modifications were therefore made. The end joints, between the thermal jacket and small diameter connecting tubes, were replaced by flexible rubber bulkheads and sealed by silicone rubber. The vacuum jacket remained of entirely glass

Figure 9.3 Thermocouple calibration graph

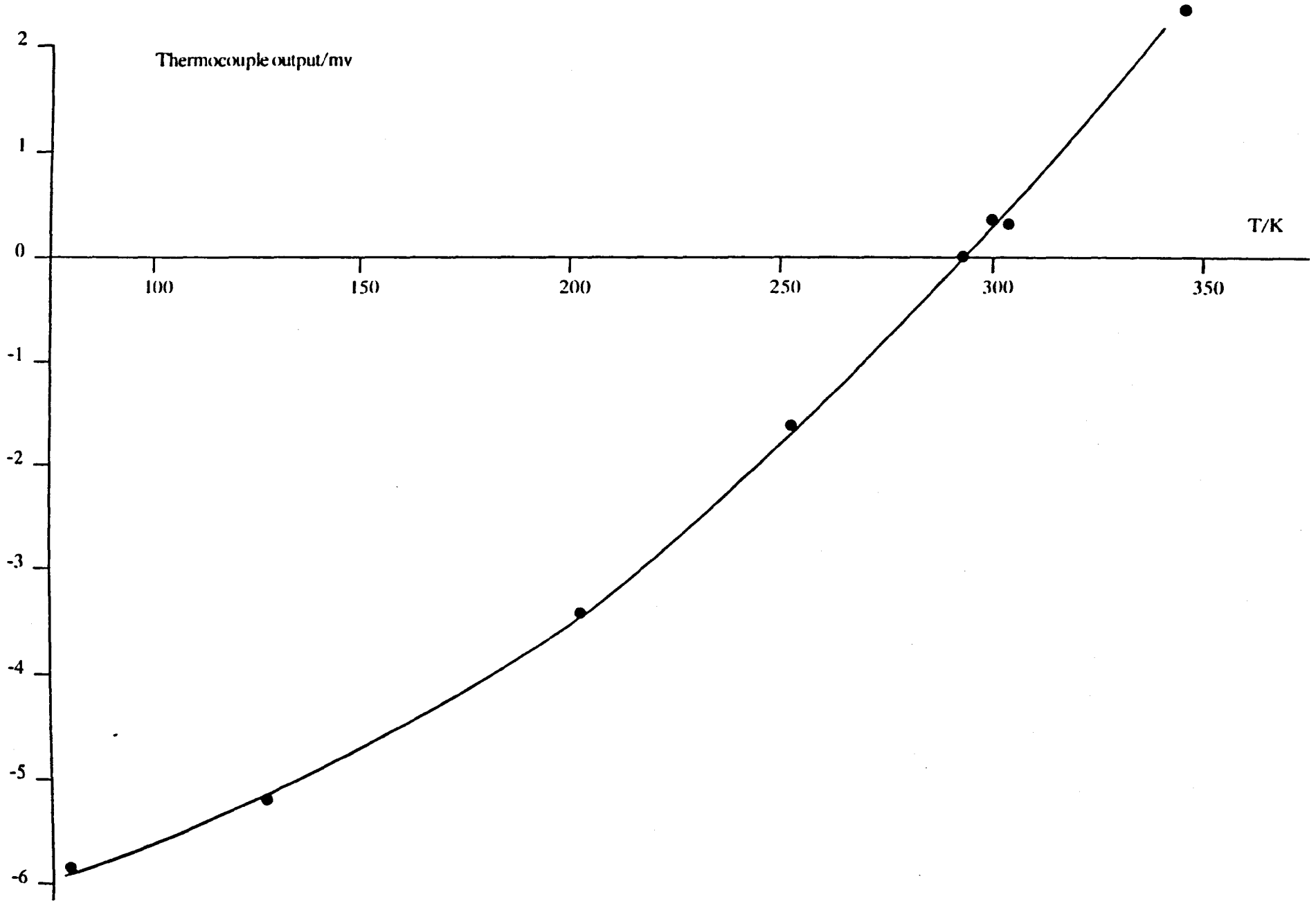

Figure 9.4 The variable temperature discharge flow tube.

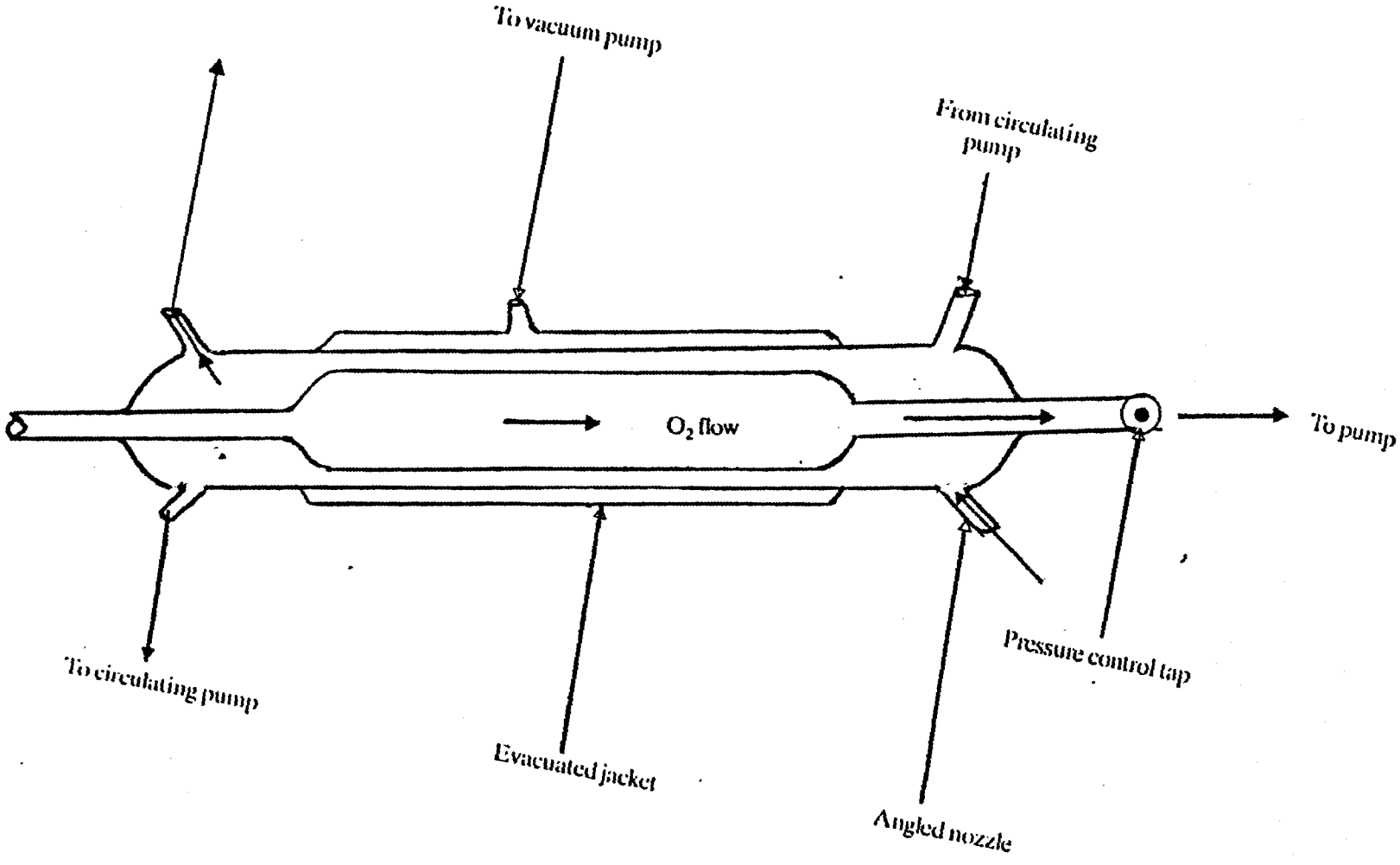

construction. Although this arrangement extended the lifetime, it was not totally leakproof and condensation within the thermal jacket at low temperature became problematic during long experimental runs.

9.3.2 Temperature Regulation of the Discharge Flow Tube

A cooling circuit was fitted to the apparatus and is shown in figure 9.5 . Temperature reduction was obtained by closed loop circulation of nitrogen gas, chilled by passing it through a heat exchanger immersed in liquid nitrogen. The gas was circulated by a pump (N.G.K. PSR4) with a sweep volume of 450 cm^3 sec^{-1}.

The temperature was controlled by changing the level of immersion of the heat exchanger. When fully immersed the flow tube could be reduced to 100K (±4K). A control heater was fitted to the circuit and located immediately after the heat exchanger. This heater (30 ohm), supplied with 70V, was found to raise the temperature of the flow tube by 50K, it also assists in temperature stabilisation over long experimental runs (ie $>$ 1 hour). The liquid nitrogen reservoir was kept at constant level by supplying it continuously from a 25 litre portable tank (B.O.C.).

The temperature of the discharge flow tube was maintained without thermostating. It was found that at times greater than fifteen minutes after initiation of the coolant circulation, the system would attain thermal stability.

A second heating coil was fitted to the circuit before the pump inlet. A 750W coil, insulated and wrapped on a copper pipe was used to protect the pump from the cold nitrogen gas and thus prevent damage due to freezing.

Temperatures above 292K were obtained either by circulating paraffin or silicone oil, or by gas circulation. The highest temperature used was 440K and this was known to ± 1K.

9.4 Purification and Control

9.4.1 The Purification and Gas Control system

Diagrams of the purification and gas control systems are given in figures 9.6 and 9.7 .

Figure 9.5 The Cooling Circuit

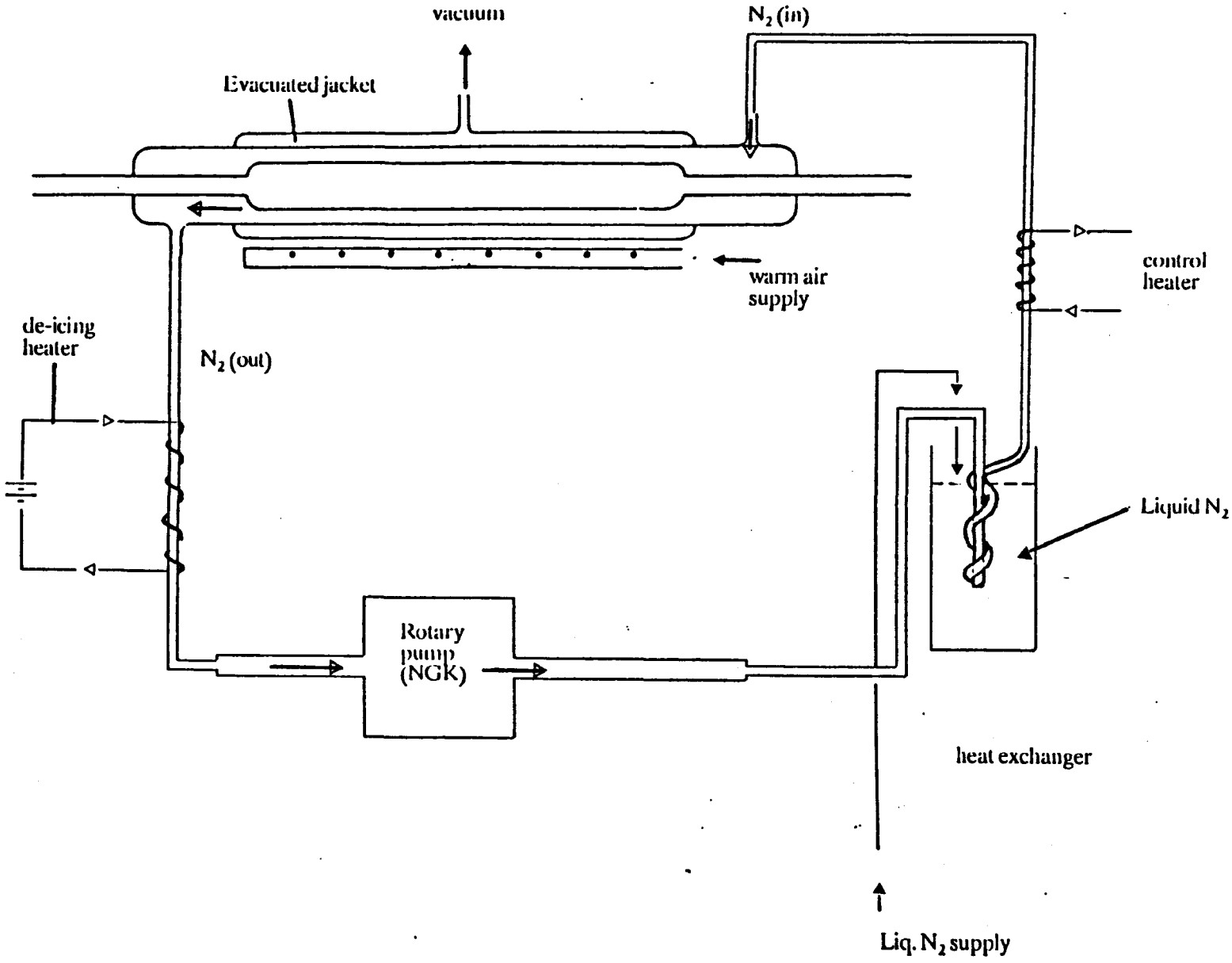

Figure 9.6 The purification and control line

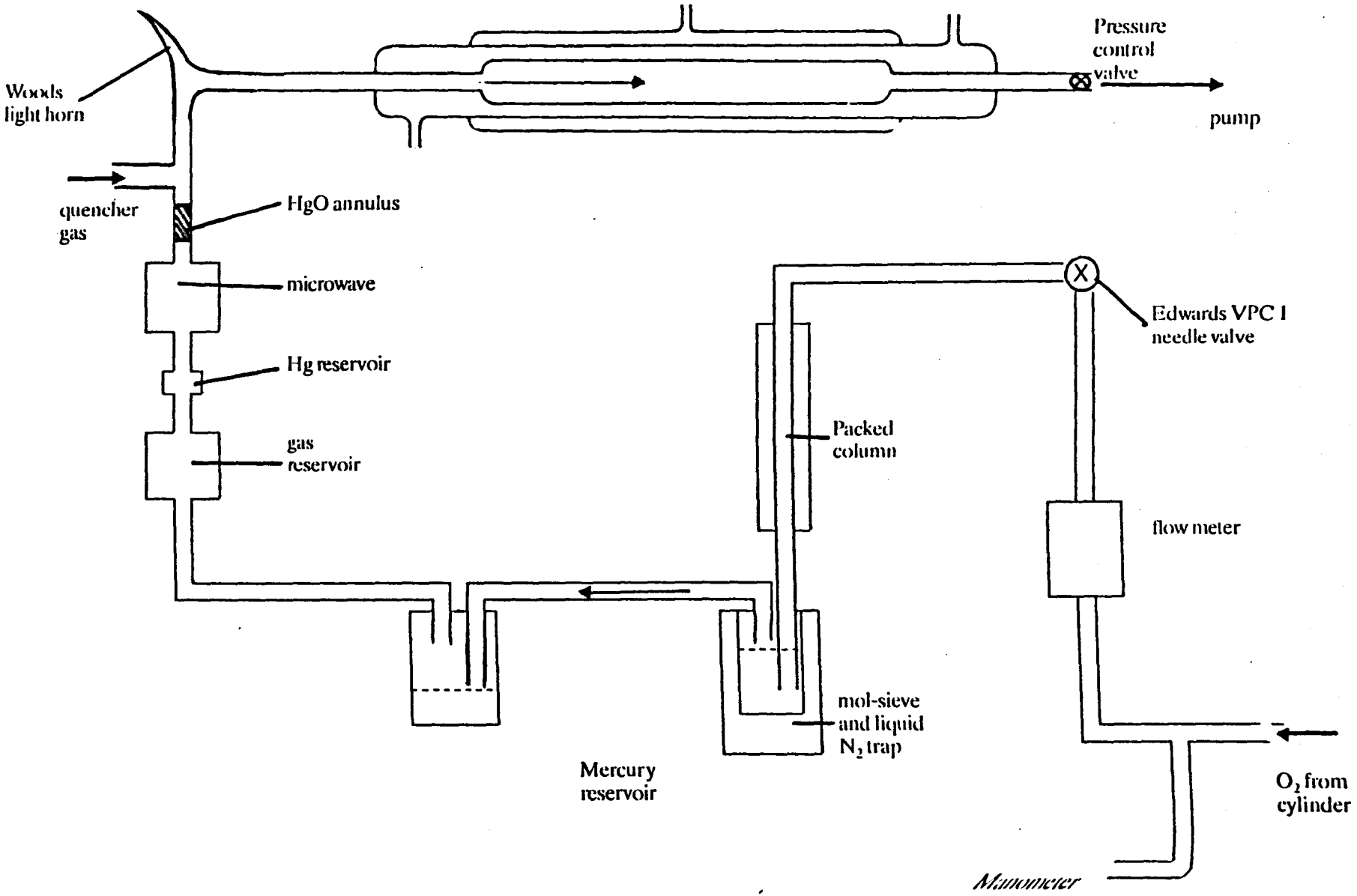

Figure 9.7 · Quencher gas purification and control line.

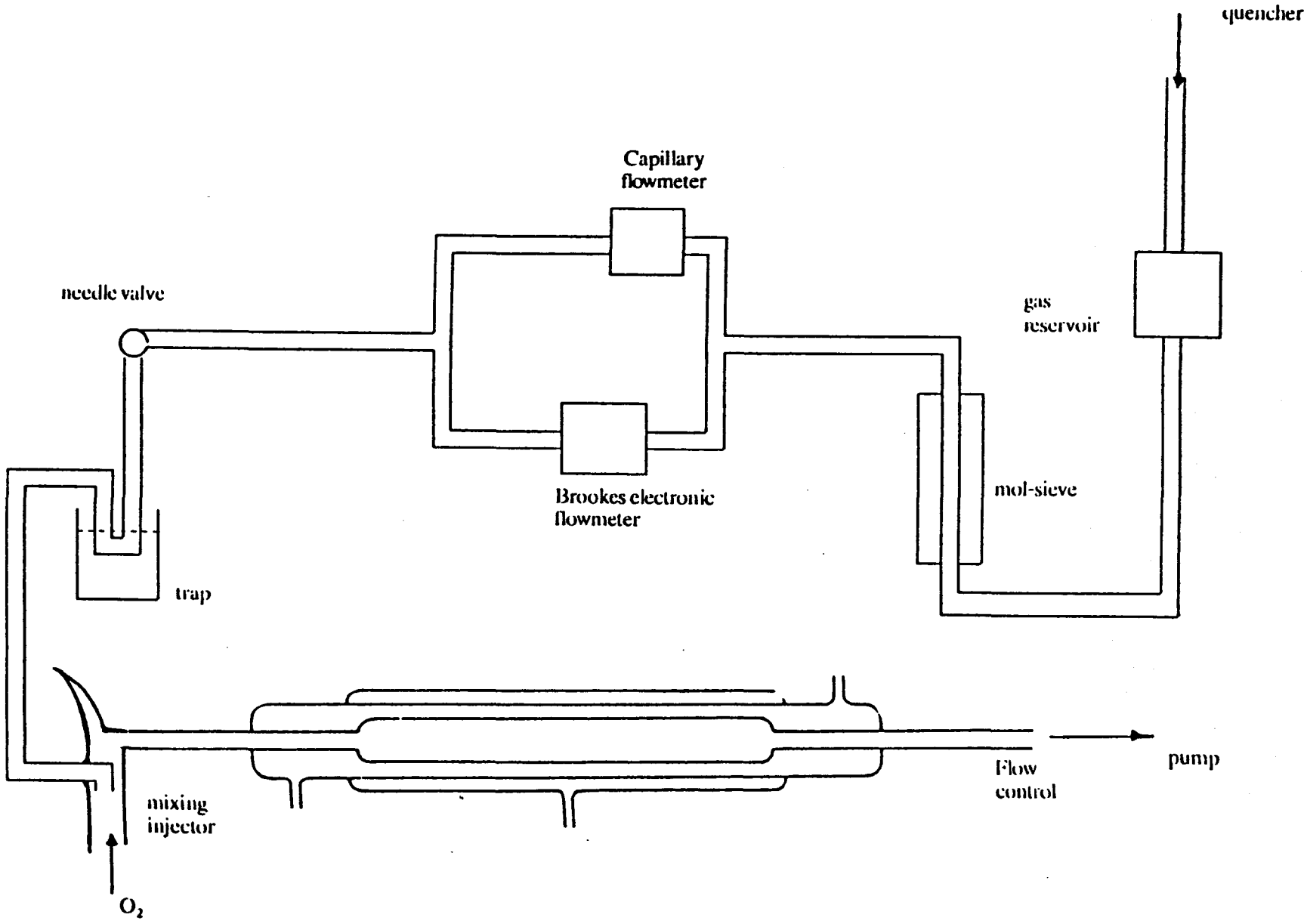

Oxygen (B.O.C. grade) was taken from a cylinder and regulated to one atmosphere. The flow rate was measured by a capilliary flowmeter, a calibration for capillary is given in figure 9.8 , and this was used for all of the work reported using this apparatus. The flow rate was controlled by a needle valve (Edwards).

The low pressure side of the line contains a drying column (i.d = 1.0cm), 60cm long, fitted with a molecular sieve (Fisons grade 4a). This sieve was frequently regenerated by passing dry nitrogen gas through the column, whilst the sieve was maintained at 200°C by the fitted heating element. A trap, also containing this molecular sieve, is fitted downstream and is cooled by immersion in a liquid nitrogen reservoir.

The dry O_2 passes into a reservoir, where the flow becomes saturated with mercury vapour. This is kept at constant level, the mercury is changed frequently. The gas flow then passes to a gas bulb and then on to the microwave discharge.

The gas line used to control and purify quencher gases is shown in figure 9.7 . It is similar to that used for the oxygen system.

9.4.2 The HgO Ring

The last 'purification' process occurs at the HgO ring. The mercury vapour removes oxygen atoms from the stream, leaving O_2 and singlet molecular oxygen (section 8.4).

Before any measurements were made, a clean HgO surface was deposited on the glass walls downstream of the microwave discharge. This was done by dismantling the discharge section, washing the entire region with both nitric and chromic acids and then re-assembling followed by discharge and redeposition. The absence of oxygen atoms at pressures above 3.5 torr was confirmed by the lack of air afterglow on the addition of NO to the discharged gas flow [110].

At pressures below 3.5 torr, the presence of oxygen atoms was detected by this method. The HgO ring was therefore less effective at these pressures, and so experimentation was not undertaken in this region [30].

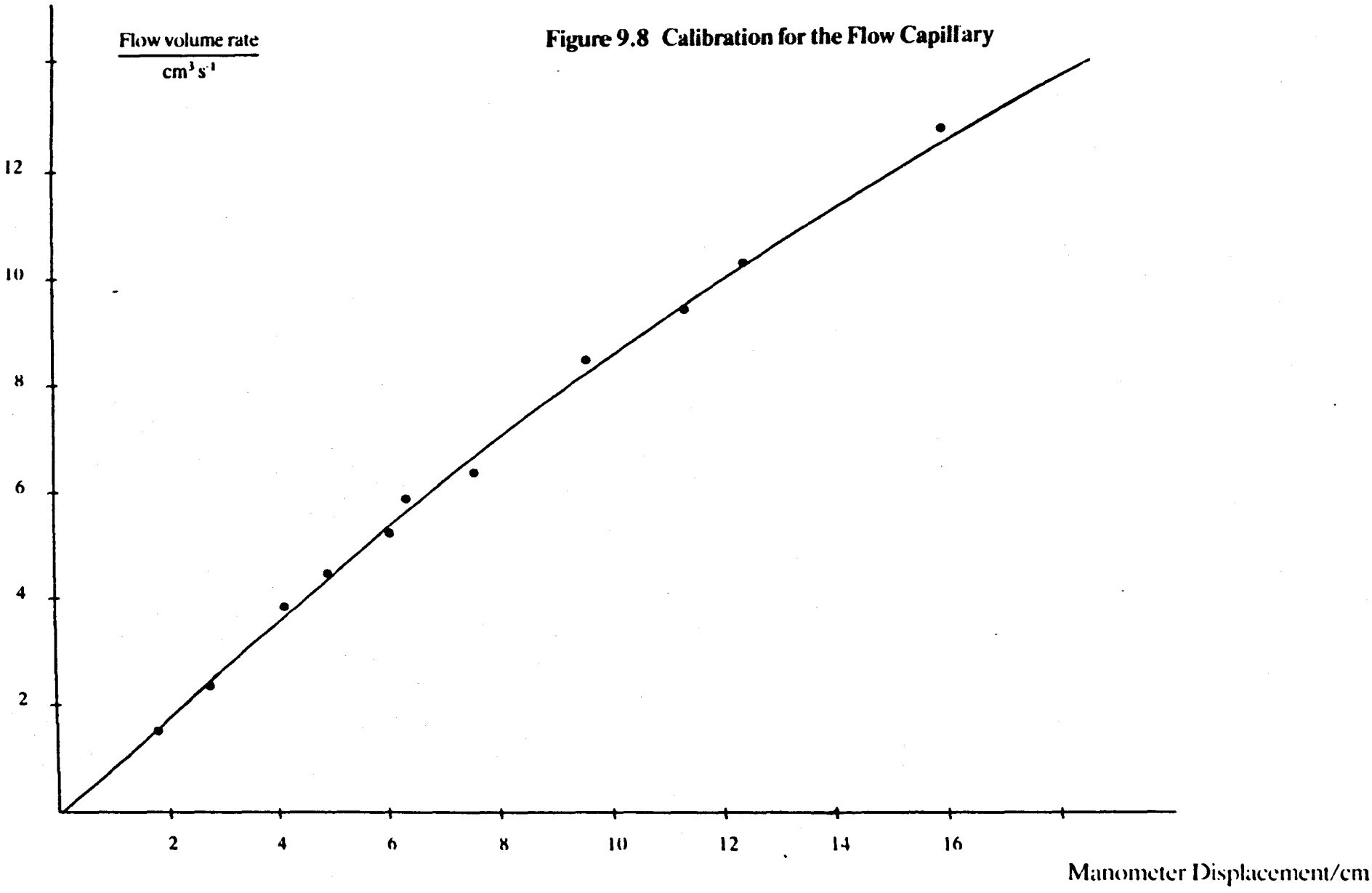

Figure 9.8 Calibration for the Flow Capillary

9.5 Light Intensity, Position and Time Measurements

The equipment that was used to measure and record the data is now considered. The measurements are intensity (volts), position along the tube and the flow rate.

All of the emission studied in this work were observed by using two photomultipliers (E.M.I. 9558 B), fitted with adjustable slits and interference filters. The transmission characteristics of the three filters, centred at 703, 634 and 762nm are given in figures 9.9 (a), 9.9 (b) and 9.9 (c) , the results were taken using a DMS−100 spectrophotometer.

Of the two photomultipliers one is stationary to act as a reference and was positioned between the microwave discharge and the observation tube. The second was mobile and was used to determine the concentration gradient along the tube. This was mounted on a track parallel to the tube, which was fitted with a motor drive so that the photomultiplier could be moved automatically. The track ran along the length of the tube, a fixed distance scale was attached to it.

The photomultipliers were operated using an E.H.T. supply (Brandberg 470), working at a voltage specified by the photomultiplier manufacturer (~ 1300V) [32]. The quantum efficiency of these photomultipliers as a function of wavelength is given in table 9.1 .

A block diagram for the measuring instruments is given in figure 9.10 . The photomultiplier output was fed to a digital voltmeter (Beckman 3030). These digital voltmeters were checked by a calibrated voltage source (Weir 651). The output from the photomultiplier was also fed to a B.B.C. microcomputer system [151,152], the voltage read by this was checked in a similar manner.

The flow rate was determined by the calibration, given in figure 9.8 . From this the flow rate was calculated and for the conditions used, could be determined to within ± 5%.

9.6 The Computer System

9.6.1 Computerised Data Acquisition

The computer and disc drive system are shown in figure 9.10 . A B.B.C. microcomputer was chosen to measure the light intensity and position simultaneously;

Figure 9.9 Interference Filter Characteristics

a

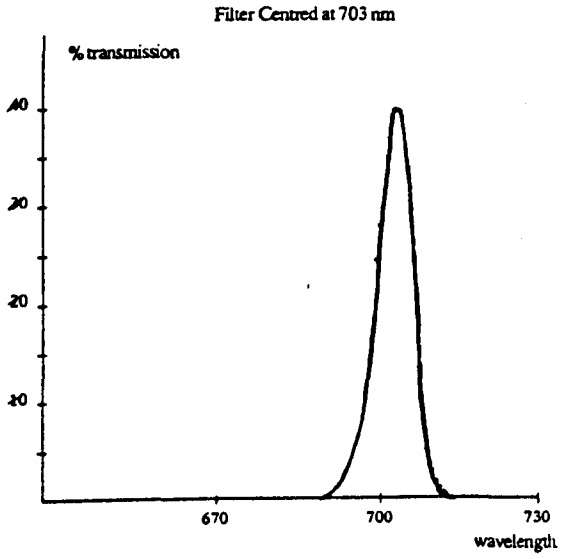

b

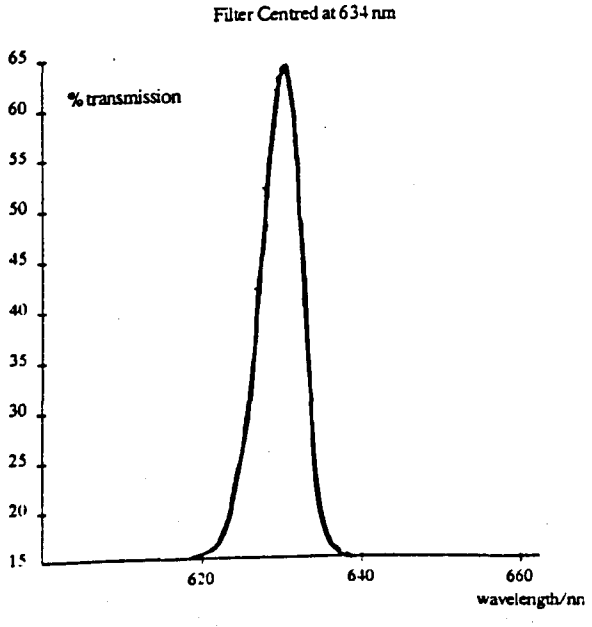

c

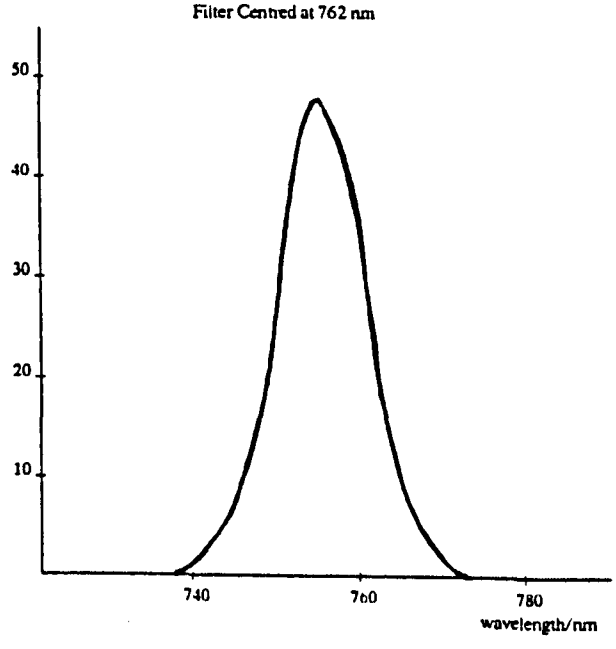

Table 9.1 Relative Sensitivity of the E.M.I. 9558B Photomultiplier Tube.

Wavelength/nm	Sensitivity
762	0.42
634	0.78
703	0.53
579	1

Figure 9.10. Block diagram of the sensing and recording equipment.

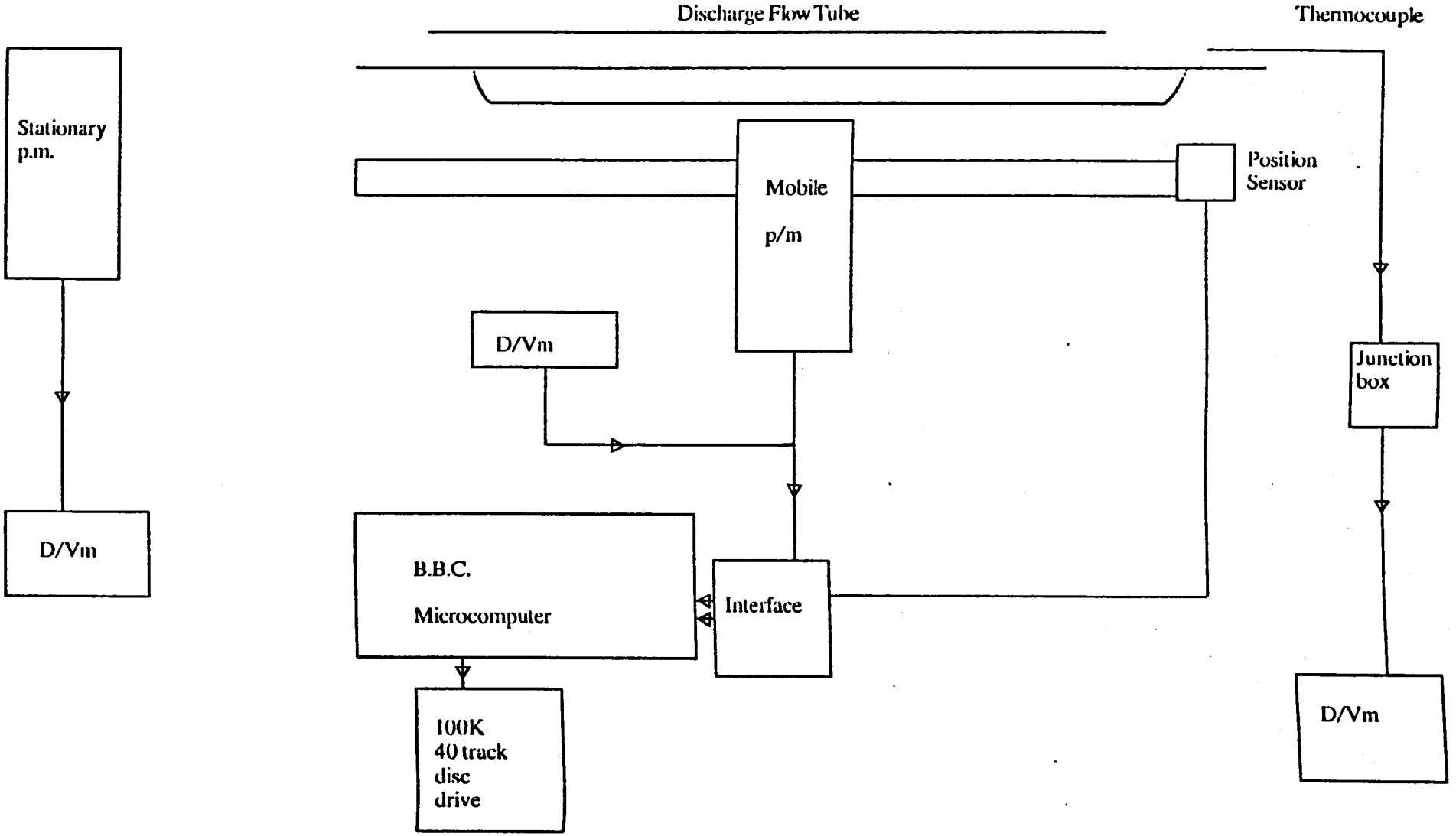

the data is stored automatically on a 40 track single disc drive. The program to read data through the analogue to digital interface is given in the appendices.

9.6.2 Installation of the System

The computer is capable of measuring between 0 and + 1.80 volts to a resolution of 0.45mv [151]. This was sufficient since the photomultipliers can be adjusted to give an output in this voltage range. However this is negative with respect to earth and therefore requires inversion. A diagram of the voltage inverter is given in figure 9.11 (a) . The voltage inverter was connected to the computer by use of a 'D' type plug [33], shown in figure 9.11 (b) . The position of the photomultiplier along the tube was determined with a 10 turn, variable resistance potentiometer, situated on the tracking screw. The output from this arrangement was also fed to the computer.

Figure 9.11(a) The Voltage Inverter

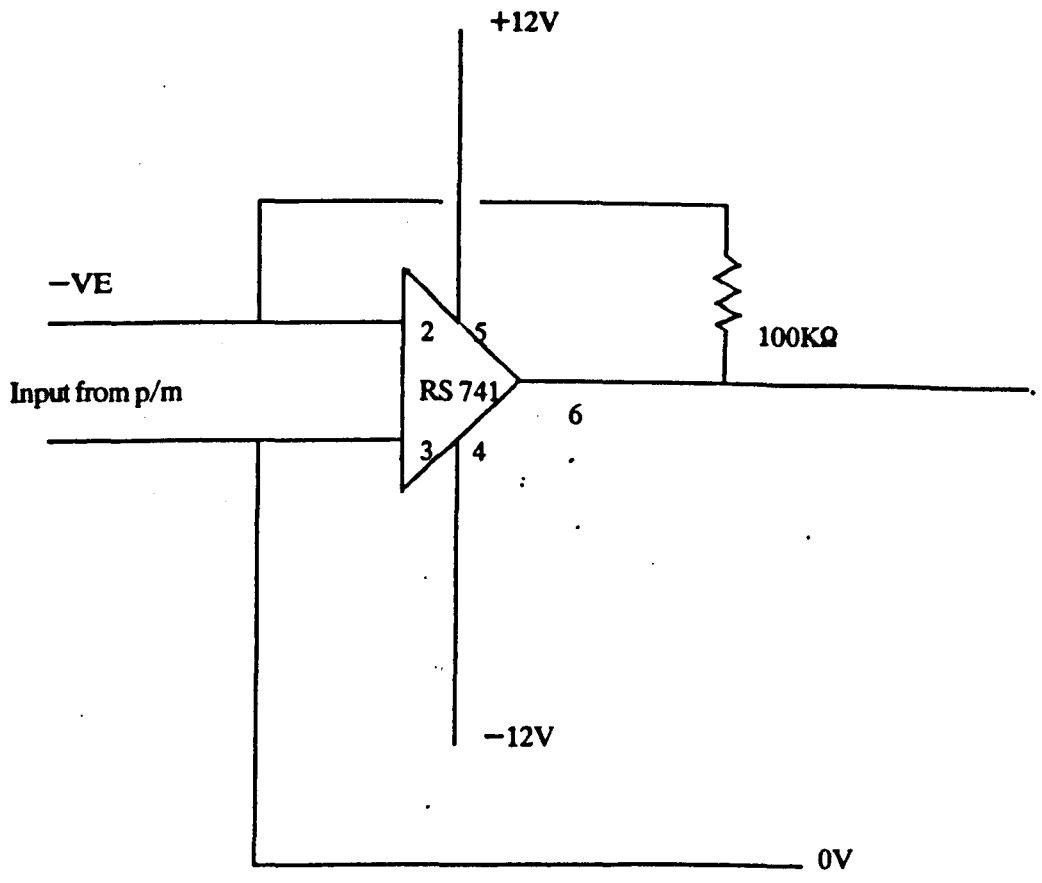

Figure 9.11(b)

Plug Connections for the Voltage Inverter

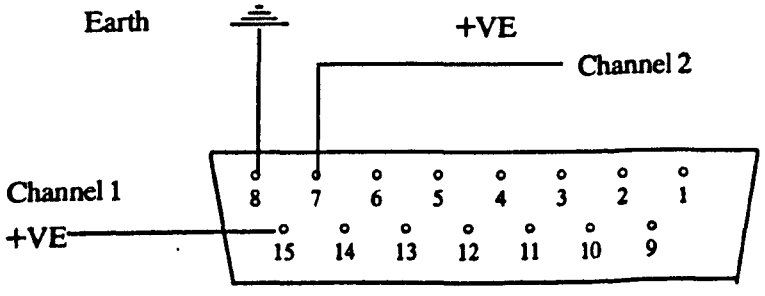

CHAPTER TEN

10.0 The Collisional Quenching of O_2 ($a^1\Delta_g$) (v=o).

Vibrational excitation of the quenching species has been suggested to be an important factor in the quenching mechanism of singlet molecular oxygen [140]. Evidence for this electronic to vibrational energy transfer could be obtained by studying the quenching rate constant with a variety of different quenchers. There are several theoretical approaches, these consider the long and short range interactions [142,138] and conversion of electronic energy in to the maximum amount of vibration, the minimum translation [147] (Chapter Eight).

The present study was undertaken to give experimental data on the temperature dependence for the quenching of $O_2(a^1\Delta_g)$, by various quenchers at low temperature. This may provide an insight into the nature of the quenching process, and also complements the work already conducted at high temperature [28,30,31].

10.1 Introduction: The Collisional Quenching of O_2 ($a^1\Delta_g$) (v=o) by O_2.

The variable temperature discharge flow tube was used to measure $k_d^{O_2}$, the collisional quenching rate constant for the quenching of O_2 ($a^1\Delta_g$) (v=o) by O_2. The concentration gradient of the O_2 ($a^1\Delta_g$) (v=o) was measured along the tube as a function of the pressure and the flow rate, measurements were taken in the temperature range 100 to 440K.

10.2 The Kinetic Model for the Collisional Deactivation of O_2 ($a^1\Delta_g$) (v=o)

Collisional deactivation of O_2 ($a^1\Delta_g$) (v=o) occurs at both the surface of the flow tube and by molecular collision. These processes can be written;

$$O_2(a^1\Delta_g)(v=o) \xrightarrow{k_w} O_2(x^3\Sigma_g^-) \qquad (10.1)$$

$$O_2(a^1\Delta_g)(v=o) + m \xrightarrow{k_d^m} O_2(x^3\Sigma_g^-) + m \qquad (10.2)$$

where m is a quenching species.

The radiative and energy pooling processes have been shown to be slow under these conditions [112]. The rate of removal of O_2 ($a^1\Delta_g$) (v=o) with respect to time is therefore;

$$-\frac{d[O_2(a^1\Delta_g)(v=o)]}{dt} = [O_2(a^1\Delta_g)(v=o)](k_d^m[m] + k_w) \qquad (10.3)$$

$$\text{or} \quad -\frac{d[O_2(a^1\Delta_g)(v=o)]}{dt} = [O_2(a^1\Delta_g)(v=o)]\,k' \qquad (10.3(a))$$

where k′ is the pseudo-first-order rate constant for the collisional deactivation of O_2 ($a^1\Delta_g$) (v=o).

The previous expression can be rearranged and then integrated to give;

$$[O_2(a^1\Delta_g)]_t = [O_2(a^1\Delta_g)]_o \exp -(k't) \qquad (10.4)$$

where $[O_2(a^1\Delta_g)]_t$ and $[O_2(a^1\Delta_g)]_o$ are the concentrations of $O_2(a^1\Delta_g)(v=o)$ at times t and t=o respectively.

The concentration of $O_2(a^1\Delta_g)(v=o)$ is measured using the emission at 634, 703 or 762 nm (Table 8.2). The 'dimol' emission at 634 nm arises from the reaction [112]:

$$O_2(a^1\Delta_g)(v=o) + O_2(a^1\Delta_g)(v=o) =$$

$$O_2(x^3\Sigma_g^-)(v=o) + O_2(x^3\Sigma_g^-)(v=o) + h\nu \qquad (10.5)$$

The intensity of this emission is expressed as a function of $[O_2(a^1\Delta_g)]$ by the relationship [31];

$$I(\text{dimol}) = C_o[O_2(a^1\Delta_g)]^2 \qquad (10.6)$$

where C_o is a contant, determined experimenally.

Substituting equation (10.6) into (10.4), the intensity of the dimol emissions at 634 and 703 nm as a function of time, t, is:

$$I_t(\text{dimol}) = I_o(\text{dimol}).\exp-(2k't) \qquad (10.7)$$

In flow tube experiments, the distance along the flow tube and the reaction time are linked by equation (4.3). The variation of the dimol emission as a function of flow tube length, l, is therefore;

$$I_l(\text{dimol}) = I_o(\text{dimol}).\exp-((2k'/v).l) \qquad (10.8)$$

or
$$I_l(\text{dimol}) = I_o(\text{dimol}).\exp-(2\alpha.l) \qquad (10.9)$$

where v is the linear flow velocity and α is a first order decay constant. By comparing (10.8) and (10.9);

$$\alpha = k'/v \qquad (10.10)$$

and rearrangement of equation (10.9) gives the expression;

$$\ln\left\{\frac{I_o(\text{dimol})}{I_l(\text{dimol})}\right\} = 2\alpha.l \qquad (10.11)$$

and so a plot of ln { I_o (dimol)/I_l (dimol) } as a function of l should give a straight line with a slope equal to 2α. The quantitiy k′ is then determined from α by using equation (10.10), the value consists of two rate constants (eqn. 10.3):

$$k' = k_d^m [m_i] + k_w \qquad (10.12)$$

If one quencher m_i, ie O_2, is used then a plot of k′ against $[O_2]$ should give a straight line of slope $k_d^{O_2}$ and intercept k_w. In the case of more than one quencher, eg O_2 and H_2, the pseudo - first order rate constant k′ becomes [28,30,31,117];

$$k'' = k_d^{O_2} [O_2] + k_d^{H_2} [H_2] + k_w' \qquad (10.13)$$

and k_w' is the wall rate constant in the presence of an O_2/H_2 mixture.

If k″ and k′ are determined at a constant value of $[O_2]$, then by using equations (10.12) and (10.13);

$$(k''-k') = k_d^{H_2} [H_2] + (k'_w - k_w) \qquad (10.14)$$

and so a plot of (k″−k′) against $[H_2]$ should give a straight line of slope $k_d^{H_2}$ with the provision that k'_w is equal to k_w.

The molecular state $O_2 (b^1\Sigma_g^+)$ is formed by the energy pooling reaction [109];

$$O_2 (a^1\Delta_g) + O_2 (a^1\Delta_g) \xrightarrow{k_p} O_2 (b^1\Sigma_g^+) + O_2 (x^3\Sigma_g^-) \qquad (10.15)$$

and is then rapidly removed by both wall and gas phase collisions;

$$O_2 (b^1\Sigma_g^+) + \text{wall} \xrightarrow{k_w^*} O_2 \qquad (10.16)$$

$$O_2 (b^1\Sigma_g^+) + m \xrightarrow{k_q^m} O_2 (a^1\Delta_g) + m \qquad (10.17)$$

and by the emission process (table 8.2), which is due to:

$$O_2 (b^1\Sigma_g^+) \longrightarrow O_2 (x^3\Sigma_g^-) + h\nu \qquad (10.18)$$

The last process (eqn. 10.18) has been shown to be slow compared to (10.16 and 10.17) [110]. The rate of production of $O_2 (b^1\Sigma_g^+)$ is therefore expressed by:

$$\frac{d[O_2(b^1\Sigma_g^+)]}{dt} = k_p[O_2(a^1\Delta_g)(v=o)]^2 -$$

$$[O_2(b^1\Sigma_g^+)]\{k_q^m[m] + k_w^*\} \qquad (10.19)$$

The quenching of $O_2(b^1\Sigma_g^+)$ has been shown to be rapid compared to $O_2(a^1\Delta_g)(v=o)$. Therefore $O_2(b^1\Sigma_g^+)$ can be considered to be in steady state [28,30,31,117]:

$$[O_2(b^1\Sigma_g^+)] = \frac{k_p[O_2(a^1\Delta_g)(v=o)]^2}{\{k_q^m[m] + k_w^*\}} \qquad (10.20)$$

The concentration of $O_2(b^1\Sigma_g^+)$ is dependent upon $O_2(a^1\Delta_g)(v=o)$; the emission intensity, ^{762}I, is therefore [28,30,31,117];

$$^{762}I = Co'[O_2(a^1\Delta_g)(v=o)]^2 \qquad (10.21)$$

at fixed pressure, where Co' is a constant determined experimentally.

The variation of the emission band at 762 nm therefore has the same functionality as the dimol emissions at 634 and 703 nm and as a consequence, equations (10.10) and(10.11) should be valid for this emission as well.

10.3 Room Temperature Determinations of the Rate Constants $k_d^{o_2}$ and k_w.

10.3.1 Experimental

Measurements were carried out initially at room temperature, to compare the determinations of $k_d^{o_2}$ and k_w with previous estimates and in this way the apparatus could be checked.

The variation in the concentration of $O_2(a^1\Delta_g)(v=o)$, as a function of distance along the flow tube, was measured by monitoring the output from a mobile photmultiplier fitted with an interference filter. Measurements were taken using the emission wavelengths at 634, 703 and 762 nm (table 8.2). Experiments were conducted in the pressure range 4 to 13 torr (linear flow velocity 0.3 to 1.2 ms^{-1}).

10.3.2 Results.

.Sample plots of $\ln\{I_o(\text{dimol})/I_l(\text{dimol})\}$ against flow tube length, at 634nm, are given in figure 10.1 . Good straight lines were obtained throughout the pressure range.

Figure 10.1 Variation in ln I(dimol) at 634 nm with flow tube length at 295K

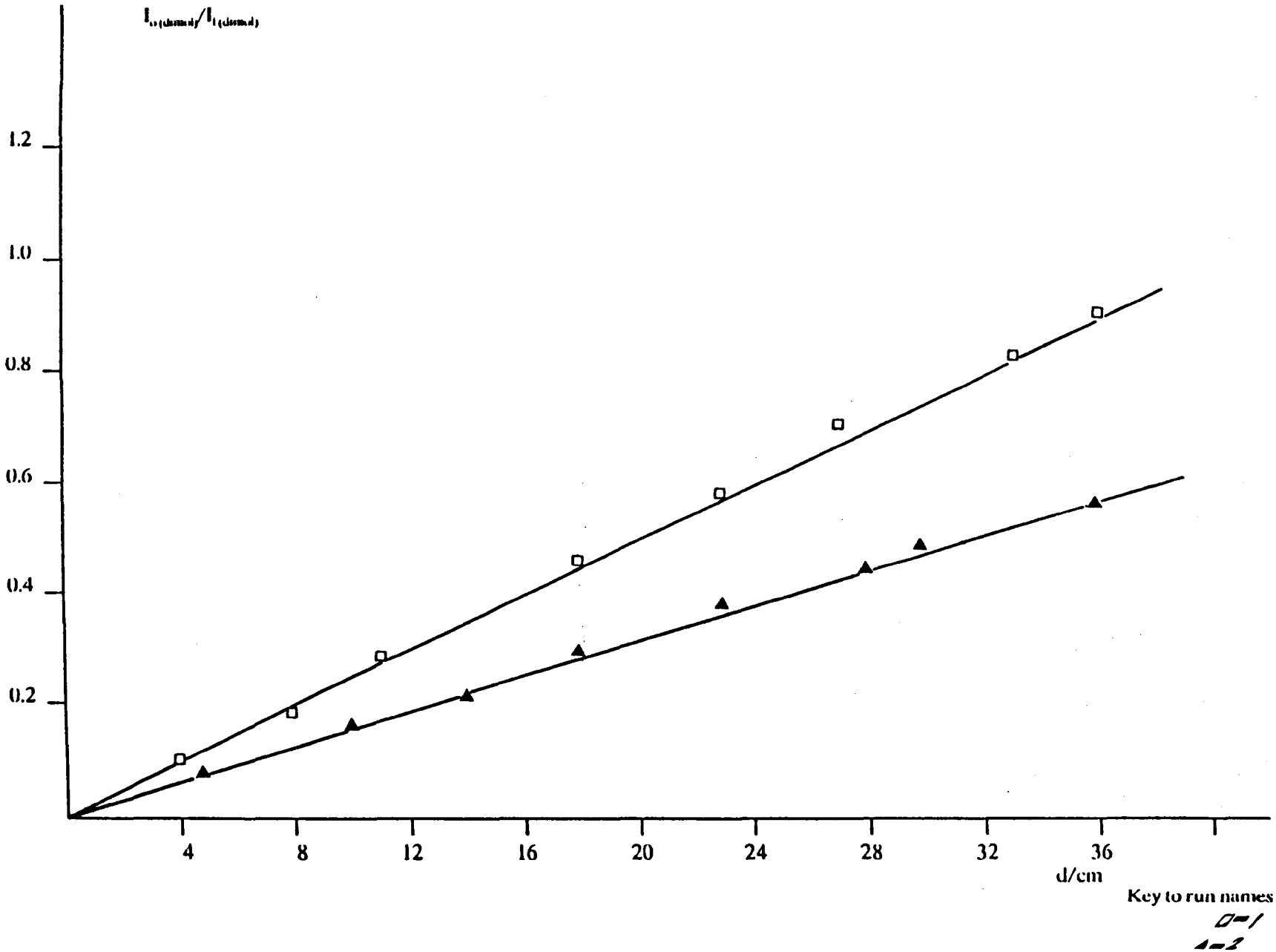

From the slope of each plot, α, the first order decay constant was calculated (eqn. 10.11).

In section 10.2 it was shown that;

$$\alpha = k'/v \qquad (10.10)$$

and

$$k' = k_d^{O_2}[O_2] + k_w \qquad (10.12)$$

where v is the linear flow velocity and k' is the psuedo first order rate constant. The valves of k', determined from each experiment, are given in table 10.1 . From a linear plot of k' against $[O_2]$ (or pressure), the rate constants $k_d^{O_2}$ and k_w can be calculated from the slope and intercept respectively. A good straight line was obtained and is shown in figure 10.2 . Linear least squares analysis of the data according to eqn. (10.12) gave the values;

$$k_d^{O_2}/dm^3\,mol^{-1}s^{-1} = (955 \pm 42)$$
$$k_w/s^{-1} = (0.178 \pm 0.02)$$

the error limits are 2σ (95%) confidence valves.

Measurements were also taken using the emission bands at 703 and 762nm. Semi-logarithmic plots (eqn. 10.11) gave good straight lines, an example is given in fig. 10.3 . The values of $k_d^{O_2}$ and k_w were then calculated by the method given, linear least squares analysis of the data (tables 10.2 and 10.3) gave the rate constants (fig. 10.4);

$k_d^{O_2}/dm^3\,mol^{-1}\,s^{-1}$	892 ± 85	: 703 nm
k_w/s^{-1}	0.203 ± 0.028	
$k_d^{O_2}/dm^3\,mol^{-1}\,s^{-1}$	973 ± 118	: 762 nm
k_w/s^{-1}	0.179 ± 0.057	

the error limits are 2σ (95%) confidence values.

10.3.3 Discussion of the Room Temperature Data.

Table 10.4(a) gives a number of recent results for the quenching of $O_2(a^1\Delta_g)(v=o)$ by O_2. The present result is in excellent agreement with the now accepted value of Borrell *et al.* [155]. In both experiments similar purfication

Table 10.1 \ Room Temperature Deactivation of O_2 ($a^1\Delta_g$)(v=o) by O_2 at 634 nm.

Run Name	P / torr	k′ / sec^{-1}	10^4 [O_2] / mol dm^{-3}	L.F.V / ms^{-1}
1	12	0.78	6.41	0.629
2	7	0.55	3.74	0.674
3	7.9	0.62	4.22	0.358
4	9	0.66	4.81	0.524
5	4	0.37	2.13	0.944
6	10.5	0.72	5.61	0.371
7	8	0.59	4.27	0.388
8	6.5	0.51	3.47	0.435
9	4.5	0.42	2.40	0.964

10.2 : 703 nm

703 1	12	0.79	6.41	0.629
703 2	4	0.4	2.13	0.944
703 3	9	0.65	4.81	0.524
703 4	8	0.61	4.27	0.388
703 5	6.5	0.55	3.47	0.435
703 6	7	0.50	3.74	0.674

10.3 : 762 nm

762 1	12	0.89	6.41	0.629
762 2	4	0.4	2.13	0.944
762 3	9	0.69	4.81	0.524
762 4	8	0.59	4.27	0.388
762 5	6.5	0.52	3.47	0.435
762 6	7	0.55	3.74	0.674
762 7	12	0.75	6.41	0.629

Figure 10.2 Room Temperature Deactivation of O_2 ($a^1\Delta_g$) (v=o) by O_2

λ= 634 nm.

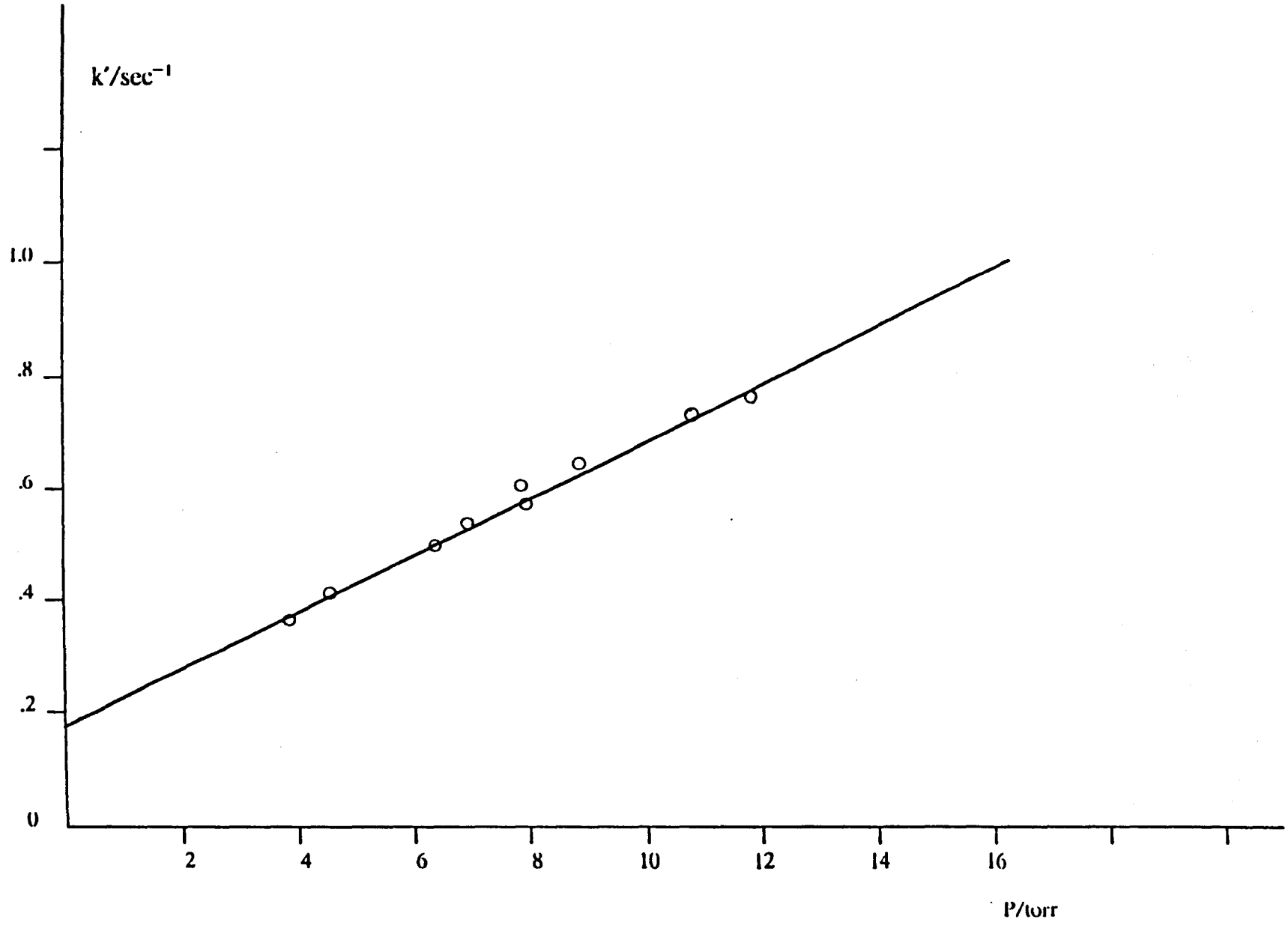

Figure 10.3 Semi Logarithmic plot for the emission band at 762 nm.

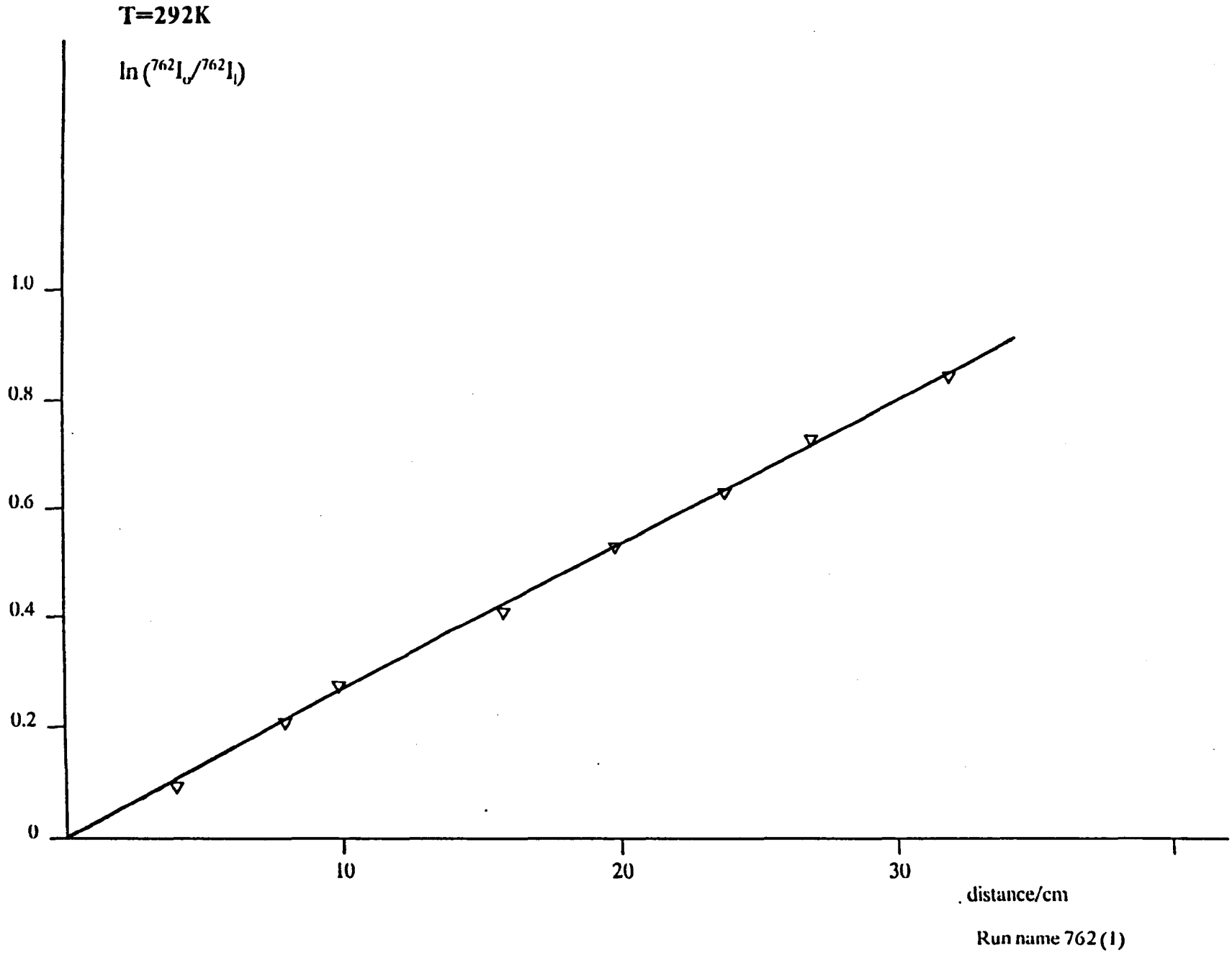

Figure 10.4 Room Temperature Deactivation of O_2 ($a^1\Delta_g$) (v=o) by O_2 at T=295K.

λ= 762 nm and 703 nm.

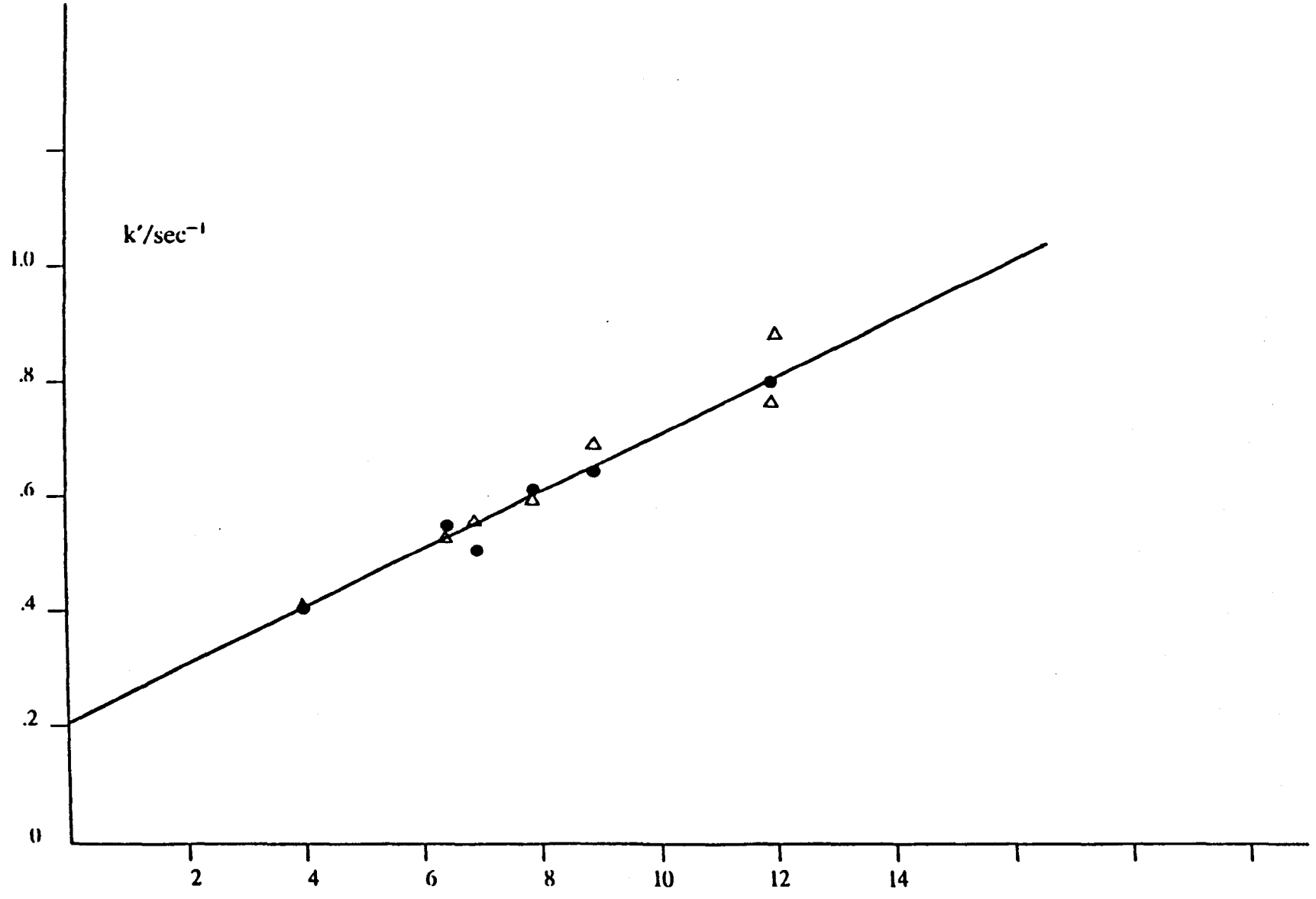

Run numbers 762(1-7)
703(1-8)

Table 10.4(a) Values for $k_d^{O_2}$ at T= 292K.

$k_d^{O_2}$ / $dm^3mol^{-1}s^{-1}$	Workers	Year	Reference
1445	Clark & Wayne	1969	153
1228	Steer, Ackerman and Pitts	1969	154
1337	Findlay and Snelling	1971	116
939	Borrell, Borrell and Pedley	1977	155
885	Leiss *et. al.*	1978	156
196	Murray *et. al.*	1984	157
955	This work 634 nm.	1985	

10.4 (b)

Wavelength	$k_d^{O_2}$/$dm^3mol^{-1}s^{-1}$	$\frac{k_w}{s^{-1}}$
703 nm	892	0.203
762 nm	973	0.179

techniques were used, the earlier work of Clark and Wayne, Steer *et al.* and Findlay and Snelling was therefore probably subject to a greater impurity. This work supports the lower values of $k_d^{o_2}$ listed, with the exception of Murray [157]. It is thought that this very low value could be due to a systematic error in their new technique.

The value of k_w represents a surface efficiency, γ, of 10^{-5} since [110];

$$k_w = 2r/\bar{c}\gamma \ s^{-1} \qquad (10.22)$$

where r = 1.60cm
and $\bar{c}$ = 44100 cms^{-1} at T = 292 K.
The present value of γ is in good agreement with previous workers who have also used pyrex wall surfaces [32,112].

The agreement between the values of $k_d^{o_2}$ and k_w, determined at 634, 703 and 762 nm (tables 10.4(a) and 10.4(b)), is in accord with the theory given in section 10.2 and the experience of previous workers [28,30,31,117].

10.4 Measurements of $k_d^{o_2}$ and k_w Between 100 and 440 K.

10.4.1 Experimental.

Measurements of the O_2 ($a^1\Delta_g$) (v=o) concentration gradient, as a function of distance along the flow tube, were then taken on the temperature range 100 to 440 K, using the method given in section 10.3.1 .

10.4.2 Results.

The semi logarithmic plots used to determine α, the first order decay constant (eqn. 10.11), were found to give good straight lines for all of the conditions used. A sample plot of this is given in fig. 10.5 , for the emission band at 634 nm.

Values of k , the psuedo-first-order rate constant determined from α (eqn. 10.10), have been listed for each temperature in table 10.5(a-h) . Plots of k′ against $[O_2]$ (or pressure) were then made and found to give good straight lines (fig. 10.6). The rate constants $k_d^{o_2}$ and k_w were determined from the slope and intercept respectively, the results analysed by least squares analysis are given in table 10.7(a) .

Figure 10.5 Variation of the Intensity with distance at T=150K.

λ= 634 nm.

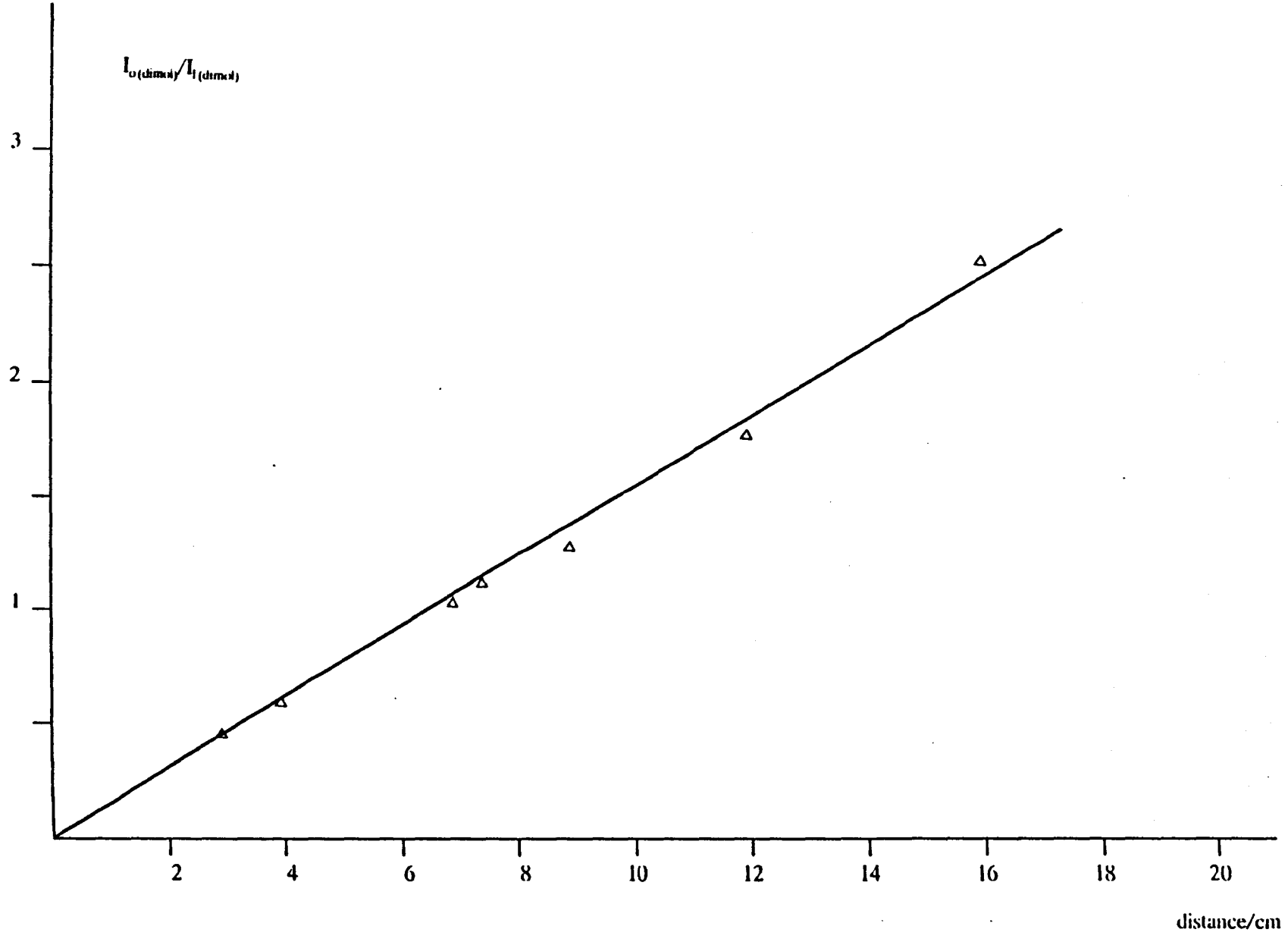

Table 10.5 The Deactivation of O_2 ($a^1\Delta_g$) (v=o) by O_2 Between 100 and 440K; 634 nm.

(a) T=100K

Run Name	P / torr	k' / sec^{-1}	10^4 [O_2] / mol dm^{-3}	L.F.V / ms^{-1}
77	10	1.54	15.27	0.129
78	7	1.31	10.69	0.184
79	3.5	1.16	5.34	0.158
80	11.1	1.60	16.95	0.243
81	12	1.58	18.32	0.269
82	9	1.44	13.74	0.269
83	3.5	1.39	5.34	0.215
84	8	1.53	12.21	0.303
85	3	1.23	7.636	0.258

(b) T=125K

68	5	1.2	6.41	0.242
69	6	1.22	7.95	0.260
70	7	1.35	8.98	0.231
71	9	1.45	1.154	0.224
72	7	1.30	8.98	0.288
73	10.7	1.55	13.72	0.188
74	11.5	1.43	14.75	0.211
75	7.5	1.23	9.62	0.242
76	4.8	1.12	6.15	0.336

(c) T=150K

60	5	0.93	5.34	0.179
61	7	1.06	7.48	0.195
62	10.1	1.12	10.79	0.163
63	7.1	0.87	7.59	0.186
64	10	1.17	10.69	0.146
65	11.1	1.16	11.86	0.194
66	5.1	0.16	5.45	0.212
67	6.5	0.99	0.94	0.218

(d) T=200K

46	11	0.89	8.82	0.228
47	12	1.13	9.62	0.262
48	6.7	0.67	5.37	0.375
49	5.9	0.62	4.73	0.320
50	7.3	0.68	5.85	0.345
51	4.5	0.65	3.61	0.279
52	8.0	0.74	6.41	0.275

(e) T=275K

Run Name	P / torr	k′ / sec^{-1}	$10^4[O_2]$ / mol dm^{-3}	L.F.V / ms^{-1}
32	5	0.5	2.93	0.692
33	7	0.59	4.11	0.494
34	10	0.76	4.87	0.432
35	12	0.85	7.049	0.432
36	10.7	0.765	6.285	0.404
37	8	0.64	4.69	0.432
38	6.5	0.55	3.81	0.53

(f) T=350K

Run Name	P / torr	k′ / sec^{-1}	$10^4[O_2]$ / mol dm^{-3}	L.F.V / ms^{-1}
10	5	0.41	2.291	0.665
11	4	0.36	1.833	0.831
12	7	0.52	3.207	0.475
13	10.5	0.70	4.811	0.476
14	9	0.60	4.124	0.615
15	8	0.38	3.665	0.692
16	13	0.79	5.956	0.512
17	12.7	0.554	5.498	0.50

(g) T=400K

18	9.3	0.61	3.728	0.475
19	3.9	0.37	1.504	0.532
20	10.1	0.70	4.05	0.260
21	7.5	0.53	3.00	0.332
22	6.7	0·49	2.68	0.619
23	8.2	0.52	3.28	0.725
24	7.9	0.54	3.16	0.744
25	10.8	0.68	4.33	0.55

(h) T=440K

26	8.9	0.56	3.24	0.639
27	5	0.41	1.82	0.853
28	10	0.64	3.64	0.426
29	5	0.34	1.82	0.853
30	7	0.47	2.551	0.609
31	4	0.35	1.45	0.711

Figure 10.6 The variation in k′ with $[O_2]$ at T=125, 200, 150 and 350K.

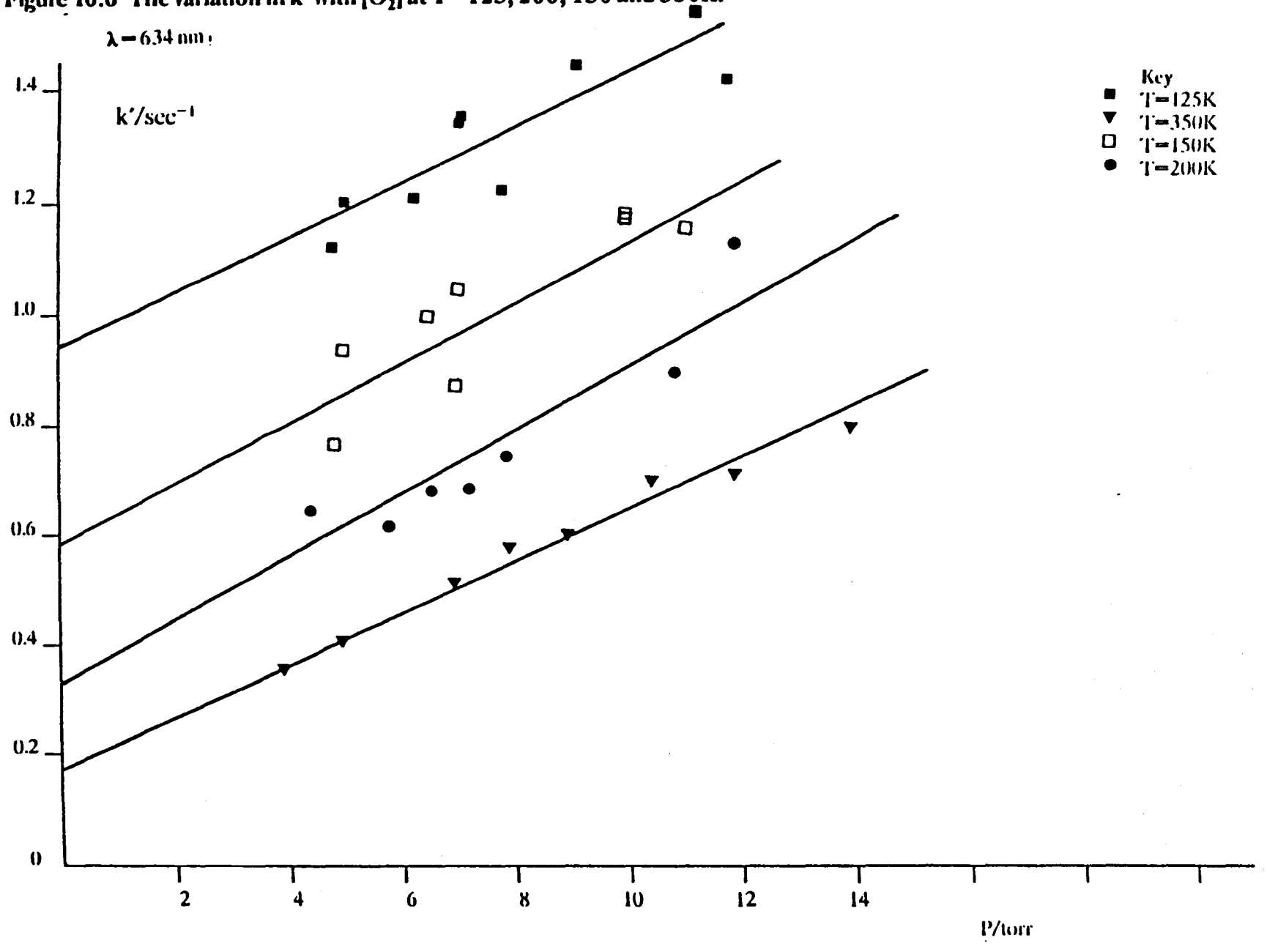

Measurements were also made by using the emission wavelengths at 703 and 762 nm. The semi-logarithmic plots (eqn. 10.11) were found to give good straight lines, an example is given in figure 10.7 .

The rate constants $k_d^{O_2}$ and k_w were calculated at each temperature by the method given above. Plots of k' (table 10.6) against the pressure also gave good straight lines (fig. 10.8), the results are listed in table 10.7 (b-c) .

The rate constant $k_d^{O_2}$ increases with temperature (fig. 10.9), the agreement between the results for all of the emission bands studied is excellent. Three error bars have been plotted, they were estimated statistically and represent $2\sigma^-$ values. They show that the error in the determination of $k_d^{O_2}$ is greatest at the extremities of the temperature range where conditions are hardest to maintain.

The results for k_w (table 10.7) have been plotted in fig. 10.10 . This shows that k_w increases as the temperature is reduced. The solid line through these points represents a linear least squares fit to an empirical plot of log (k_w) against log (T). The functionality was found to be:

$$\log(k_w/s^{-1}) = (2.94 \pm 0.23) - (1.45 \pm 0.05)\log(T/K) \qquad (10.23)$$

The error limits are 2σ (95%) confidence values.

10.4.3 Discussion of the Quenching Data.

An Arrhenius plot for the results of $k_d^{O_2}$ is given in fig. 10.11 . The data was fitted to a straight line with the equation;

$$k_d^{O_2}/dm^3mol^{-1}s^{-1} = (1896 \pm 65)\exp -(205 \pm 8/T) \qquad (10.24)$$

the error limits are statistical $2\sigma^-$ values.

The line extrapolated to 77K fits well with the estimate made by Huestis *et al.* [158] of the gas phase value, from experiments with laser excitation of liquid oxygen. Also shown are the early results of Findlay and Snelling [116], who studied the temperature dependence by flash photolysis between 290 and 350 K. Their result at 295 K is above the now preferred value [155], but the slope they obtained is in reasonable agreement with that obtained in this work. Extrapolation of the line to 1500 K lies well within the upper limit for the reaction of $3.8\times10^4 dm^3mol^{-1}s^{-1}$ found

Figure 10.7. Variation of the emission intensity with the distance at T=125K.

λ= 703 nm.

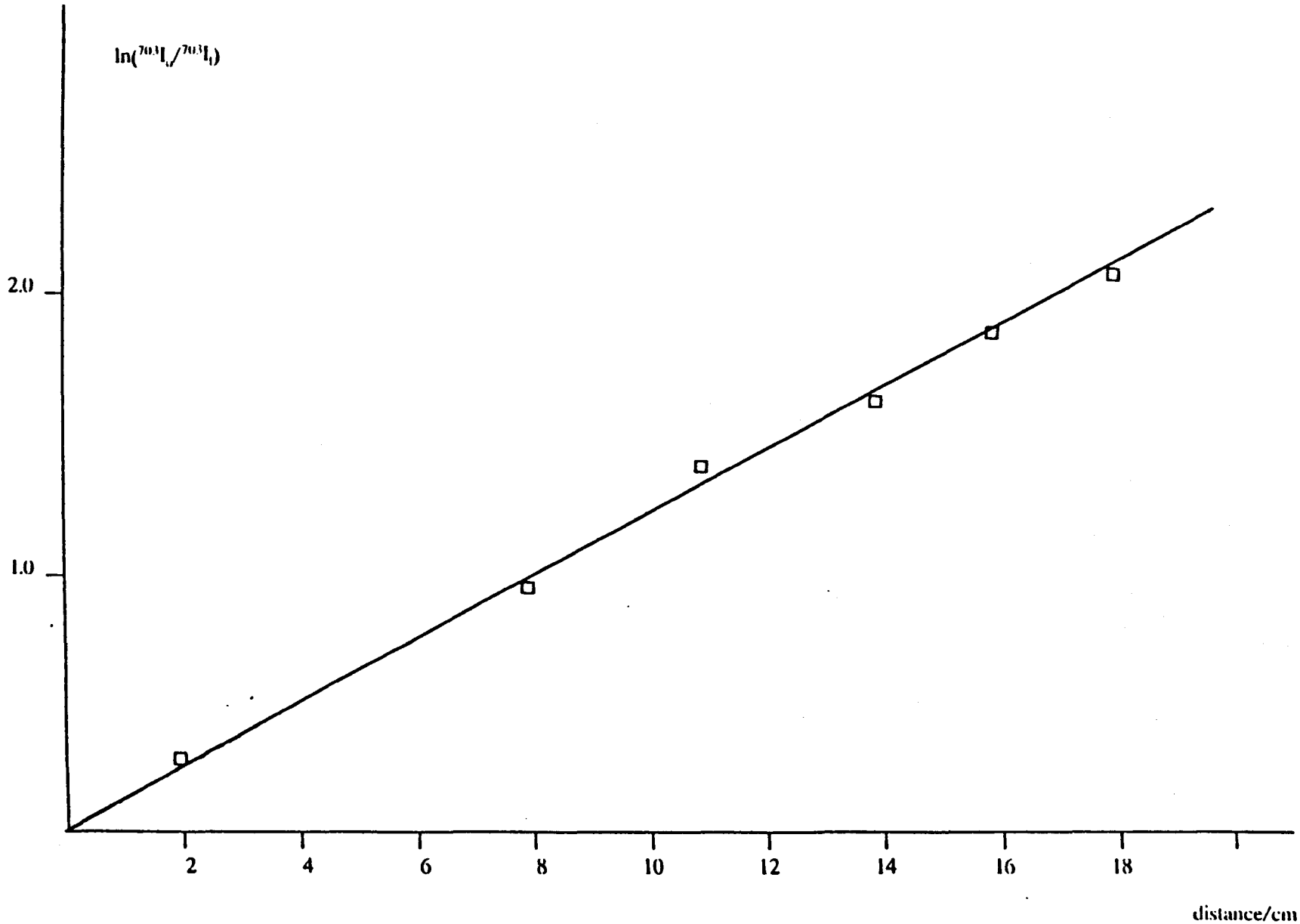

Table 10.6 The Deactivation of O_2 ($a^1\Delta_g$) (v=o) by O_2 Between 100 and 440 K.

λ=703 nm.

(a) T=400K

Run Name	P torr	k' sec^{-1}	10^4 [O_2] mol dm^{-3}	L.F.V ms^{-1}
703 7	10	0.70	4.00	0.440
8	6.7	0.50	2.68	0.244
9	11	0.70	4.41	0.40
10	4	0.36	1.60	1.10
11	8	0.50	3.20	0.55
12	7.8	0.54	3.10	0.56

(b) T=125K

13	5	1.25	6.41	0.283
14	9	1.42	11.54	0.158
15	7	1.30	8.98	0.202
16	11.5	1.45	14.7	0.123
17	4.8	1.30	6.13	0.294

λ=762 nm

(c) T=440K

762 8	4	0.32	1.458	1.24
9	9.3	6.57	3.39	0.535
10	11	0.66	4.00	0.452
11	8.2	0.53	2.98	0.607
12	6.7	0.47	2.44	0.743
13	8.2	0.55	2.98	0.607

(b) T=147K

14	5	0.92	5.45	0.332
15	10.1	1.17	11.10	0.164
16	10.0	1.20	10.90	0.166
17	6.5	1.00	7.09	0.255
18	11.0	1.18	11.99	0.151

Figure 10.8. Variation in k′ with the pressure

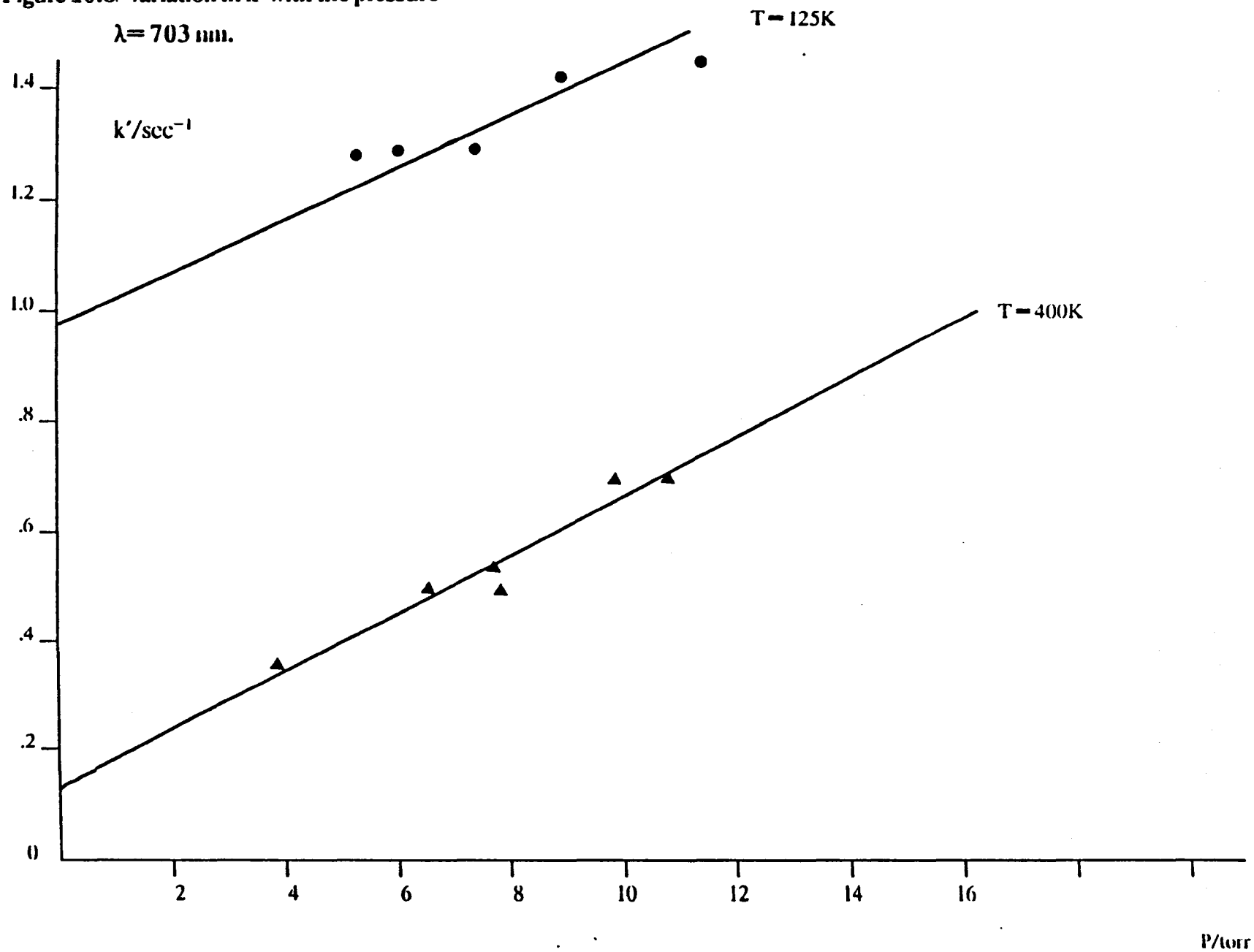

Table 10.7 The Rate constants $k_d^{O_2}$ and k_w Between 100 and 440 K.

10.7 (a)
634 nm

Temp / K.	$k_d^{O_2}$ / $dm^3mol^{-1}s^{-1}$	k_w / sec^{-1}
100	267±60	1.09±0.08
125	392±94	0.94±009
150	499±122	0.59±0.10
200	725±150	0.33±0.09
275	869±40	0.23±0.02
292	945±42	0.18±0.02
352	1010±54	0.18±0.02
400	1200±116	0.17±0.03
440	1335±122	0.14±0.03

10.7 (b)
703 nm

292	892±85	0.2±0.02
400	1279±161	0.14±0.05
125	351±93	0.97±0.09

10.7 (c)
762 nm

292	973±118	0.18±0.02
147	433±48	0.69±0.05
440	1292±72	0.14±0.03

The error limits are 2σ (95%) confidence values.

Figure 10.9 Variation of $k_d^{O_2}$ with temperature

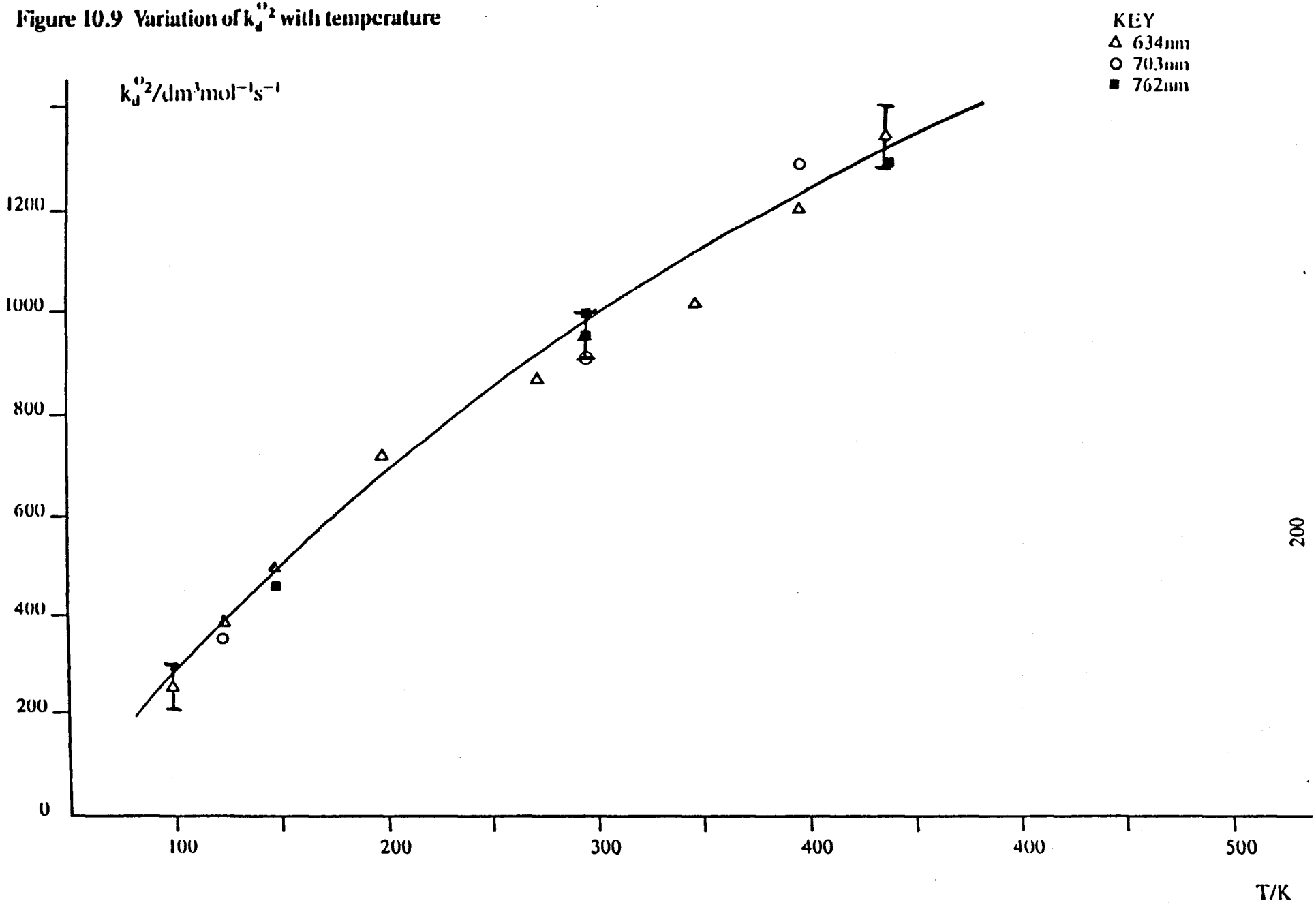

Figure 10.10 Variation of k_w with temperature

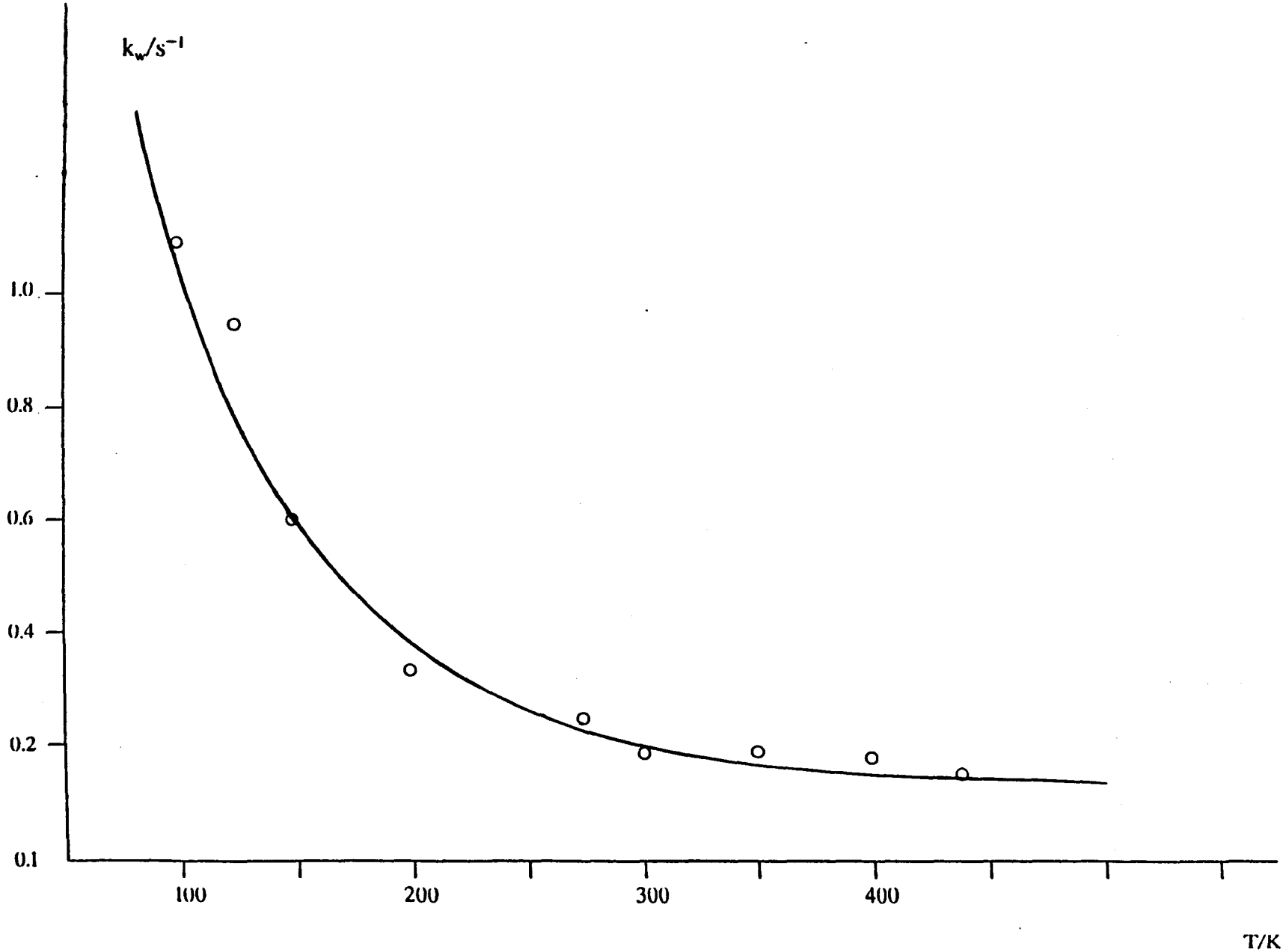

Figure 10.11 Arrhenius plot for k_d^{II}.

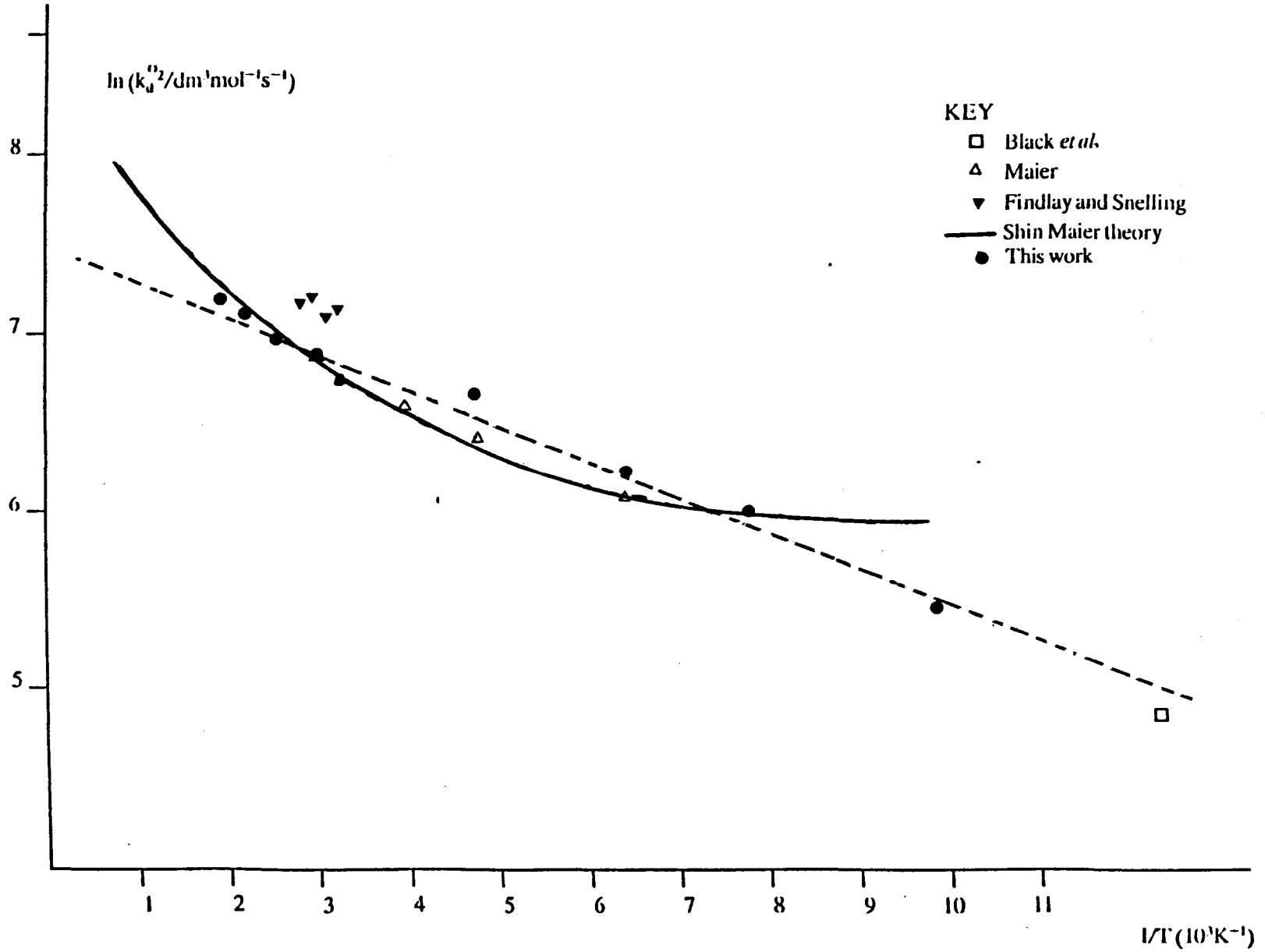

at 1650 K by Borrell *et al.* [30]. The results of Maier, obtained at 35 atmospheres using a laser, have also been plotted in figure 10.11 . The agreement between the results across the temperature range is good. The solid line in figure 10.11 represent the results from the Shin-Maier theory [147], and this fits the data reasonably in this temperature range. However it is is also clear that the curvature is different from the observed Arrhenius behaviour of the experimental data.

The wall constant k_w increases as the temperature is reduced. The surface efficiency at the lowest temperature is 10^{-4}, an increase of a factor of ten from the room temperature value. While the general trend for the increase in k_w was observed, in later experiments, the surface efficiency was found to be less. The value of k_w therefore depends on the surface history. Ogryzlo, using a discharge flow tube, observed an increase in k_w below 130K. This effect was attributed to the increased residence time of the O_2 ($a^1\Delta_g$) (v=o) molecule at low temperature [159].

10.5 The Temperature Dependence for the Quenching of O_2 ($a^1\Delta_g$) (v=o) by O_2.

An Arrhenius expression was derived to describe the variation of $k_d^{O_2}$ with temperature and was found to be;

$$k_d^{O_2}/dm^3mol^{-1}s^{-1} = (1896\pm65)\exp-(205\pm8/T) \qquad (10.24)$$

which represents an activation energy of 1.70 KJ mol^{-1}.

The observed variation of $k_d^{O_2}$ with temperature suggests that energy transfer in this quenching reaction takes place at long distances, where the intermolecular potential well is attractive in form [138,142].

Boodaghians has studied a series of quenchers for O_2 ($a^1\Delta_g$) (v=o) in the gas phase between 300 and 1500K [31]. He found a sharp increase in the quenching rate constant with temperature for the species HCL, NO and SO_2. This indicates that quenching takes place on the repulsive part of the potential well. However, the quenchers N_2, CO_2 and N_2O have also been studied, the quenching rate constants for these do not increase measurably with the temperature [160,161]. The quenching reaction may therefore be specific for a particular quenching species, i.e. there is a favoured channel above the already excited energy level. An activation energy is therefore required to facilitate energy transfer. Ogryzlo

and Thrush used infra red spectroscopy to study the vibrational energy distribution produced in NO by the quenching of $O_2(a^1\Delta_g)$ (v=o) in the gas phase [162]. They concluded that energy transfer occurs preferentially into the v=4 state of NO.

$$O_2(a^1\Delta_g)(v{=}o) + NO(v{=}o) \longrightarrow O_2(x^3\Sigma_g^-)(v{=}o) + NO(v{=}4) \qquad (10.25)$$
$$\Delta H = 6.53\,KJ\,mol^{-1}$$

The potential products for the quenching of $O_2(a^1\Delta_g)$ (v=o) by O_2 can be examined to see whether the activation energy corresponds to a particular reaction pathway.

For vibrational to vibrational energy transfer, the most probable reaction pathways are those that lie closest to resonance; the exothermic energy routes would be more dominant than the endothermic pathways.

For the relaxation of $O_2(a^1\Delta_g)$ (v=o) by $O_2(x^3\Sigma_g^-)$, all of the reaction pathways would be exothermic (see table 10.8). It is noted in equation (10.24) that a positive (endothermic) reaction pathway is required for the overall process.

The data was shown to fit the Arrhenius expression well, but no correlation is seen between any particular reaction pathway and the activation energy. This must cast some doubt on the interpretation of the slope of fig 10.11 as an activation energy.

An alternative approach that can be considered is that of simple collision theory. The probability, P, that a deactivation will take place on collision at a temperature T is given by [163];

$$P = k/\varphi \qquad (10.26)$$

where k is the rate constant ($dm^3mol^{-1}s^{-1}$) and
$\varphi = 2.751 \times 10^9 (\sigma\Delta m)^2 (T/\mu)^{\frac{1}{2}} (dm^3mol^{-1}s^{-1})$.

The quantity φ is the rate constant predicted if every collision gives rise to deactivation, $\sigma\Delta m$ is the 'hard sphere' collision diameter and μ is the reduced mass. Calculations show that at room temperature only one in 2×10^8 collision gives rise to deactivation. This low probability suggests that only 'head on' collision give rise to

deactivation. If simple collision theory is an accurate model for this system, then in the absence of a minimum energy barrier (Chapter One), the rate constant will vary with the square root of the temperature. The probability should be a constant and give the steric factor in the absence of a barrier. The probablity (eqn. 10.26) has been plotted as a function of temperature in figure '10.12 , and shows that P increases with the temperature. Thus, simple collision theory is inappropriate to describe this reaction.

The Landau-Teller relationship for vibrational relaxation is derived on the assumption that short range repulsive forces control the energy exchange process. It can be shown that the probability, $P_{10(T)}$, is related to the temperature according to the expression:

$$P_{10(T)} = B.\exp -(C/T)^{\frac{1}{3}} \qquad (10.27)$$

A plot of $\ln (P_{10(T)})$ against $T^{-\frac{1}{3}}$ should give a straight line of slope $-C$ and intercept $\ln (B)$. The probablity can be calculated by equation (10.26), the results have been plotted in figure 10.13 . It can be seen the results do not give a good straight line suggesting that vibrational relaxation is not important in the deactivation process.

A model for the relaxation of the $O_2 (a^1\Delta_g) (v=o)$ molecule has been developed by Maier from the earlier work of Shin [146,147]. In this approach, Schwartz, Slawsky and Herzfeld (S.S.H) theory [164] has been modified to include attractive forces.

For binary collisions, the rate constant, k, is related to the probability for the reaction, P, and collision frequency, Z, by the relationship:

$$k = PZ \qquad (10.28)$$

The collision frequency can be calculated from the known molecular parameters of the interacting species [165]. The probability is approached by considering the energy distribution in the product molecules. For the relaxation of $O_2 (a^1\Delta_g)(v=o)$ by $O_2 (x^3\Sigma_g^-) (v=o)$ the process is written:

$$O_2 (a^1\Delta_g) (v=o) + O_2 (x^3\Sigma_g^-) (v=o) =$$

$$O_2 (x^3\Sigma_g^-) (v=x) + O_2 (x^3\Sigma_g^-) (v=y) \qquad (10.29)$$

Figure 10.12 Variation of P with T for O_2

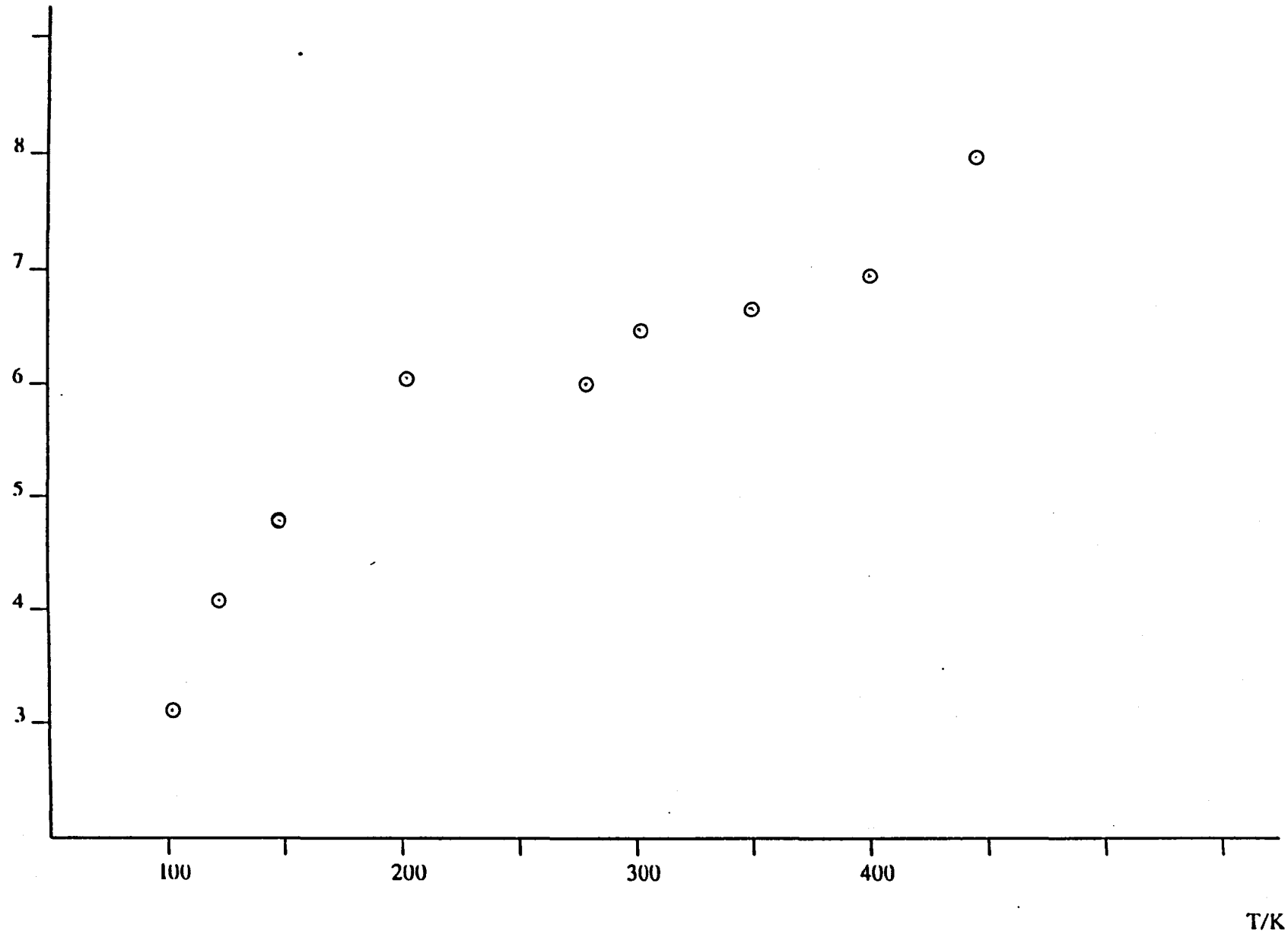

Figure 10.13 Landau Teller plot for the deactivation of O_2 ($a^1\Delta_g$) by O_2

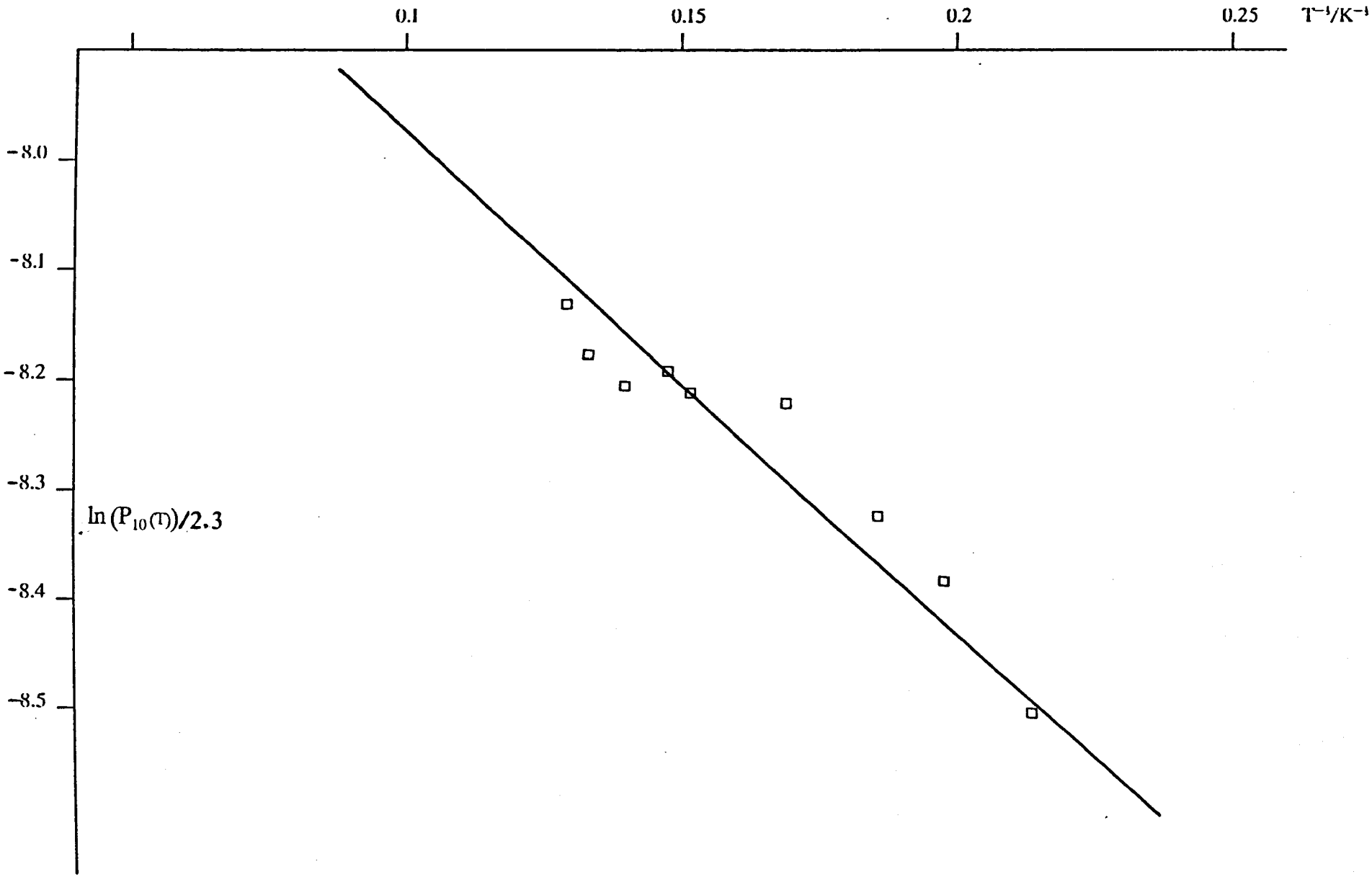

In this model, it is imagined that the maximum amount of electronic energy goes into the vibrational levels of the product molecules. The remaining energy must go into translation, this quantity, ΔE, is given by;

$$\Delta E = E_{\Delta} - \left\{ E_x + E_{(5-x)} \right\} \qquad (10.30)$$

where E_{Δ} is the electronic energy of O_2 $(a^1\Delta_g)$ (v=o) and E_x, $E_{(5-x)}$ are the energies of the x and (5−x) vibrational levels of O_2 $(x^3\Sigma_g^-)$. The values of ΔE for specific transitions in this reaction are given in table 10.8 and illustrated in figure 10.14.

The probability $P_{1,2}$ for a transition involving molecules 1 and 2 with an energy mismatch ΔE between them is given by;

$$P_{1,2} = P_{\Delta} \left\{ \frac{8\pi\mu\Delta E}{\alpha^2 h^2} \right\}^2 \Gamma^{\frac{1}{2}} \left(\frac{A_I}{V_{01}} \right)^V \left(\frac{A_{II}}{V_{02}} \right)^{(5-V)} \left(\frac{1}{V!(5-V)!} \right)$$

$$\exp - \left\{ 3\Gamma + \left(\frac{4E\Gamma}{\pi k_B T} \right)^{1/2} + \left(\frac{\Delta E}{2k_B T} \right) + \left(\frac{16E}{3\pi^2 k_B T} \right) \right\} \qquad (10.31)$$

where $$\Gamma = \left(\frac{2\pi^4 \mu (\Delta E)^2}{\alpha^2 h^2 k_B T} \right)^{1/3}$$

P_{Δ} is the crossover probability for $O_2(a^1\Delta_g)$ (v=o)

μ is the reduced mass of the colliding pair

ΔE is the energy mismatch

A_I, A_{II} are the vibrational frequency factors for molecules 1 and 2 respectively

V is the vibrational level (0 to 5)

V_{01}, V_{02} are the vibrational frequencies of molecules 1 and 2 respectively

T is the temperature

E is the well depth for the interacting pair.

and k_B and h are the Boltzmann and Planck constants respectively.

Figure 10.14 Simultaneous Transitions for $O_2(a^1\Delta_g)(v=o)$ Quenching

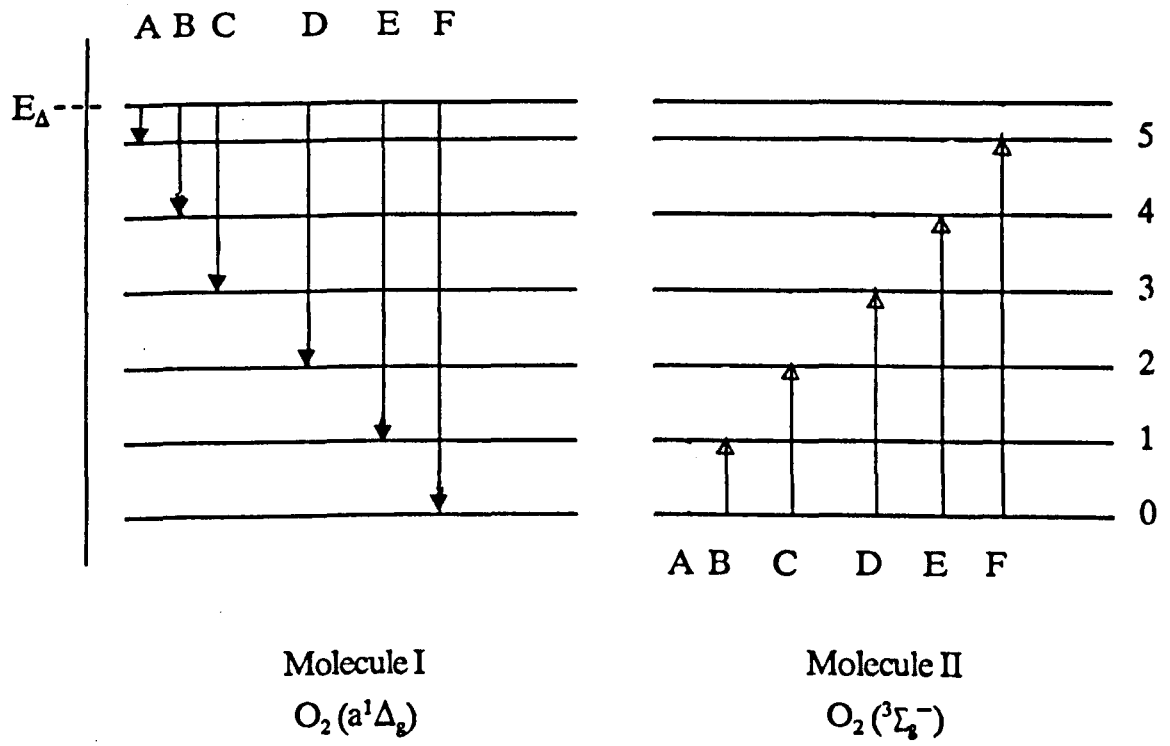

Table 10.8 Energy Mismatch for the Process

$$O_2(a^1\Delta_g)(v=o) + O_2(x^3\Sigma_g^-)(v=o) \longrightarrow O_2(x^3\Sigma_g^-)(v=x) + O_2(x^3\Sigma_g^-)(v=5-x)$$

Final vibrational level of $O_2(x^3\Sigma_g^-)$		Energy mismatch / cm^{-1}
A	0	- 313
B	1	-221
C	2	- 174
D	3	- 174
E	4	-221
F	5	-313

The quantity $P_{1,2}$ must be summed over all six of the simultaneous transitions (table 10.8), a value of k can then be calculated. It is necessary to calculate and then scale all of the values to one temperature to allow for the unknown P_{Δ}. Equation (10.31) was evaluated by using a B.B.C microcomputer, the program is given in appendix 4 and the results have been listed in table 10.9 , for k at each temperature. Values of $\alpha = 5.53E8\ cm^{-1}$ [146] and $E/K_B = 109$ K were used, the results for each transition are given in table 10.9 and are shown in figure 10.15 .

The agreement between the data and the calculation (fig. 10.11) is excellent considering the few adjustable parameters. The temperature dependence comes principally from the species ability to convert the mismatched energy into translational energy. However, the model makes no attempt to describe the relationship between P_{Δ} and the approach velocities of the colliding molecules. Any temperature dependence for this would be hard to estimate and so a more comprehensive treatment is therefore required [26].

Since the model of Maier fits the data well, this suggests that the majority of the electronic energy preferentially goes into the vibration of the products. This must cast some doubt on the suggestion of Thomas and Thrush, who from a surprisal analysis, concluded that as much as 25% of the energy went into translation of the product molecules [141] (Chapter Eight).

10.6 Introduction: The Collisional Quenching of O_2 ($a^1\Delta_g$) (v=o) by H_2 and D_2

Preliminary measurements were made of the rate constants $k_d^{H_2}$ and $k_d^{D_2}$, for the collisional quenching of O_2 ($a^1\Delta_g$) (v=o) by H_2 and D_2 respectively (Chapter Eight and section 10.0).

Measurements were taken using the variable temperature discharge flow tube in the temperature range 170 to 407K.

10.7 Experimental

The decrease in concentration of O_2 ($a^1\Delta_g$) (v=o) was measured by monitoring the voltage output from the mobile photomultiplier fitted with an interference filter at 762 nm. For a set initial pressure, the first measurements were taken in pure oxygen for the decay of O_2 ($a^1\Delta_g$) (v=o). Then the flow was mixed with a stream of the

Table 10.9 Scaled Rate Constants (to T=290K), for Various Vibrational Transitions of O_2 ($a^1\Delta_g$) to O_2 ($x^3\Sigma_g^-$)

$k_d^{O_2}$/dm^3 mol^{-1} s^{-1} (at Product vibrational level v)						$\frac{k_d^{O_2}}{dm^3mol^{-1}s^{-1}}$	$\frac{Temp}{K}$
v=o	1	2	3	4	5		
2.6	42.7	153.3	153.3	42.7	2.6	397.2	100
3.4	51.1	174	174	51.1	3.4	457	140
5.2	71	232	232	71	5.2	618.4	200
10	117	348	348	117	10	950	290
17.1	183	512	512	183	17.1	1424.2	400
26.5	260	695	695	260	26.5	1963	500

Figure 10.15 Rate constants for various vibrational products of $O_2(a^1\Delta_g)$ (v=o) quenched by O_2

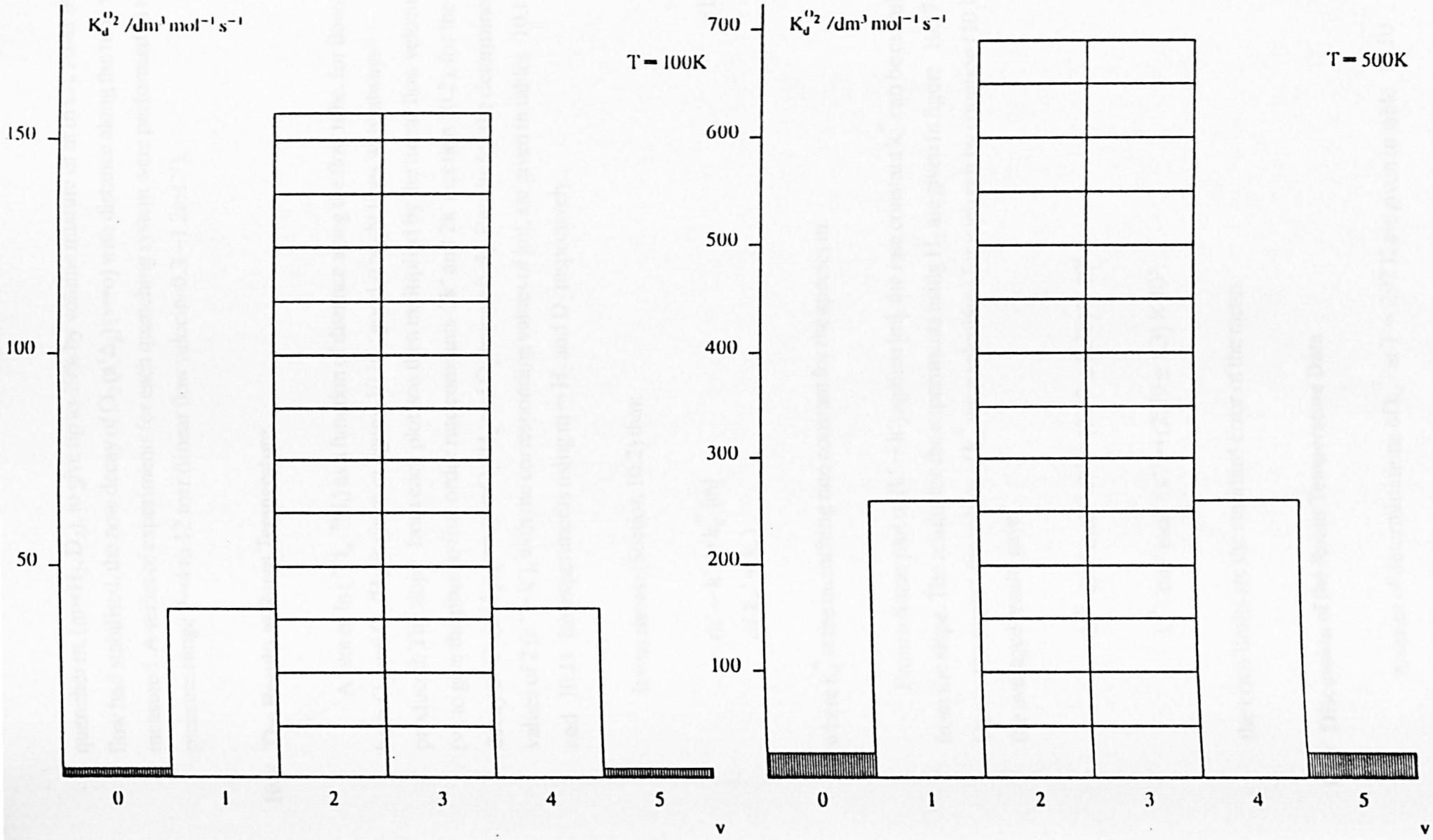

Figure 10.16 Variation of ln (I_o/I_t) as a function of flow tube length at 295K.
$\lambda = 762$ nm.

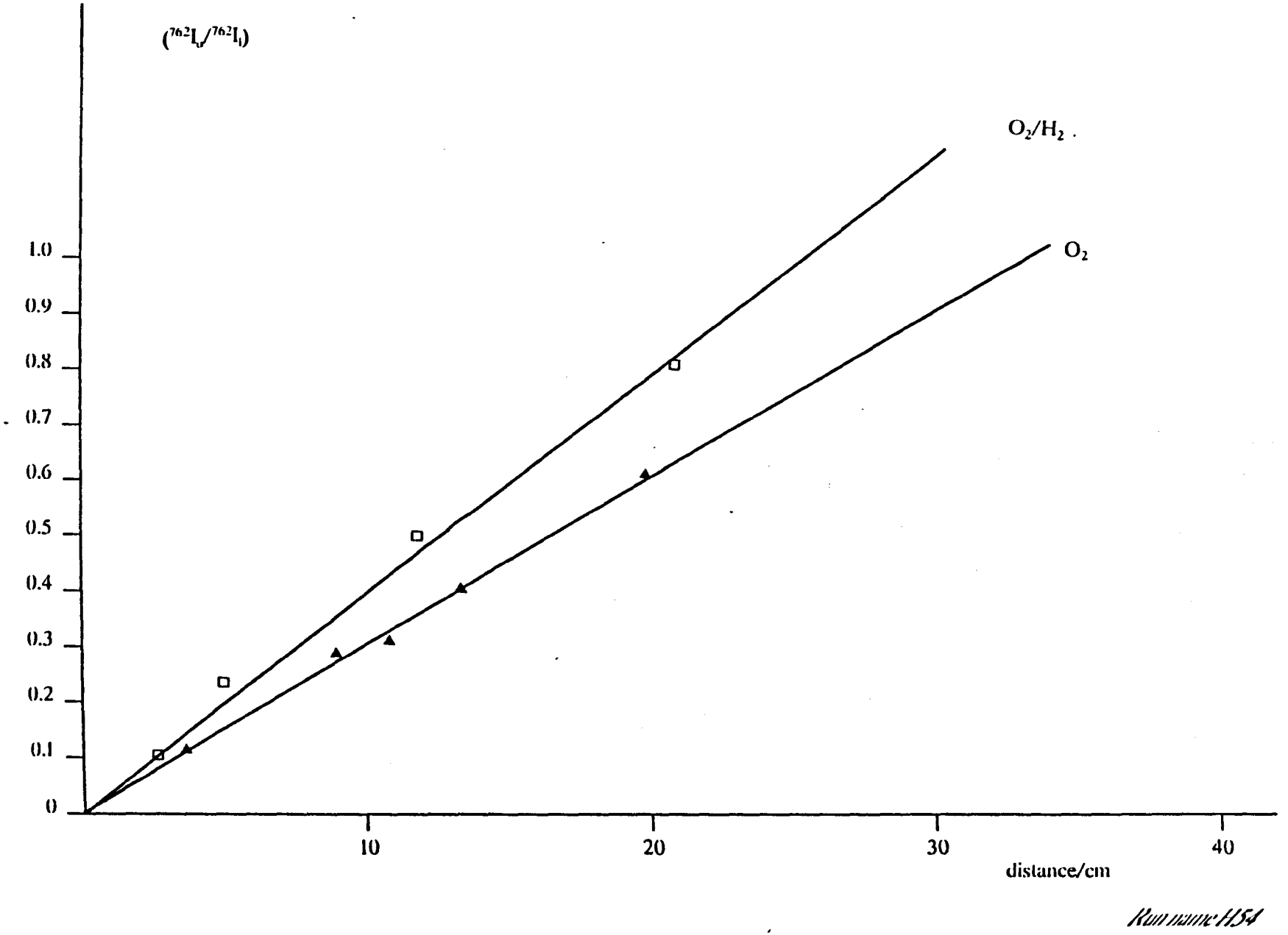

Runnine H54

quencher m, (m=H_2, D_2), to give up to 10% by volume mixture of m in O_2. After the flow had stabilised, the new decay of O_2 ($a^1\Delta_g$) (v=o) with distance along the tube was measured. A series of experiments for each quenching system were performed in the pressure range P=4 to 12 torr (linear flow velocity 0.3—1.2ms^{-1}).

10.8 The Results at Room Temperature.

A plot of ln ($^{762}I_v/^{762}I_1$) as a function of distance along the flow tube, for flows of both O_2 and O_2/H_2, is given in figure 10.16 ; good straight lines were always produced. The slope from each plot was then multiplied by the linear flow velocity (v), to give the psuedo first order rate constants $2k''$ and $2k'$ (section 10.2), for the decay of O_2 ($a\,^1\Delta_g$) (v=o) in O_2/H_2 and O_2 respectively. Results for the determined values of $2(k''-k')$, with the corresponding values of [m], are given in tables 10.10 and 10.11 for experiments using m = H_2 and D_2 respectively.

It was shown (Section 10.2) that;

$$(k''-k') = k_d^m\,[m] \qquad (10.14)$$

(if $k_w' = k_w$)

where k_d^m is the quenching rate constant for the species m.

From a linear plot of $(k''-k')$ against [m], the rate constant k_d^m can be calculated from the slope. The results for the experiments using H_2 are given in figure 10.17 . Due to the scatter, the values of k_d^m were calculated for each run by equation (10.14), the averaged results gave;

$$k_d^{H_2}/dm^3\,mol^{-1}\,s^{-1} = (3.37 \pm 0.38) \times 10^4.$$

$$k_d^{D_2}/dm^3\,mol^{-1}\,s^{-1} = (2.79 \pm 1.3) \times 10^3.$$

the error limits are the standard error of the mean.

10.9 Discussion of the Room Temperature Data

A series of determinations of $k_d^{H_2}$ at T = 292 K are given in table 10.10 ,

Table 10.10 Room Temperature Deactivation of O_2 ($a^1\Delta_g$)(v=o) by H_2, 762 nm.

Run Name	P/torr	$\frac{2(k''-k')}{sec^{-1}}$	$\frac{[H_2]\times10^6}{mol\ dm^{-3}}$	$\frac{k_d^{H_2}\times10^{-4}}{dm^3mol^{-1}s^{-1}}$
HD18	6.1	0.146	3.05	2.38
HD19	6.1	0.084	3.05	1.37
HD20	6.1	0.094	3.05	1.52
HD21	6.1	0.113	1.44	3.86
HD22	6.1	0.1639	1.44	5.86
HD23	6.1	0.151	1.44	5.15
HD24	6.1	0.198	2.81	3.88
HD25	6.1	0.169	2.51	3.32
HD26	6.1	0.198	2.51	3.88
HD27	6.1	0.113	1.08	4.42
HD28	6.1	0.113	1.08	4.42
HD29	6.1	0.113	1.08	4.42
51	5.5	0.56	6.04	4.68
52	5.3	0.92	6.04	7.59
53	8.9	0.159	2.17	3.57
54	7.9	0.236	8.2	1.445
55	6.8	0.183	9.54	0.955
56	3.8	0.363	3.44	4.51
57	6.10	0.18	8.19	1.10
58	7.3	0.147	4.45	1.65
59	9.0	0.109	5.49	1.00

Table 10.11 Room Temperature Deactivation of O_2 ($a^1\Delta_g$)(v=o) by D_2, 762 nm.

Run Name	P/torr	$\frac{2(k''-k')}{sec^{-1}}$	$\frac{[H_2]\times10^6}{mol\ dm^{-3}}$	$\frac{k_d^{H_2}\times10^{-4}}{dm^3mol^{-1}s^{-1}}$
D1	5.10	0.0833	26.9	0.31
D2	5.10	0.0645	26.9	0.25
D3	5.10	0.103	26.9	0.40
D4	8.0	0.0903	30.1	0.30
D5	8.0	0.064	43.0	0.15
D6	8.0	0.073	43.0	0.17
D7	10.0	0.178	51.0	0.35

Figure 10.17 Room Temperature deactivation of O_2 ($a^1\Delta_g$) (v=o) by H_2.

λ= 762 nm.

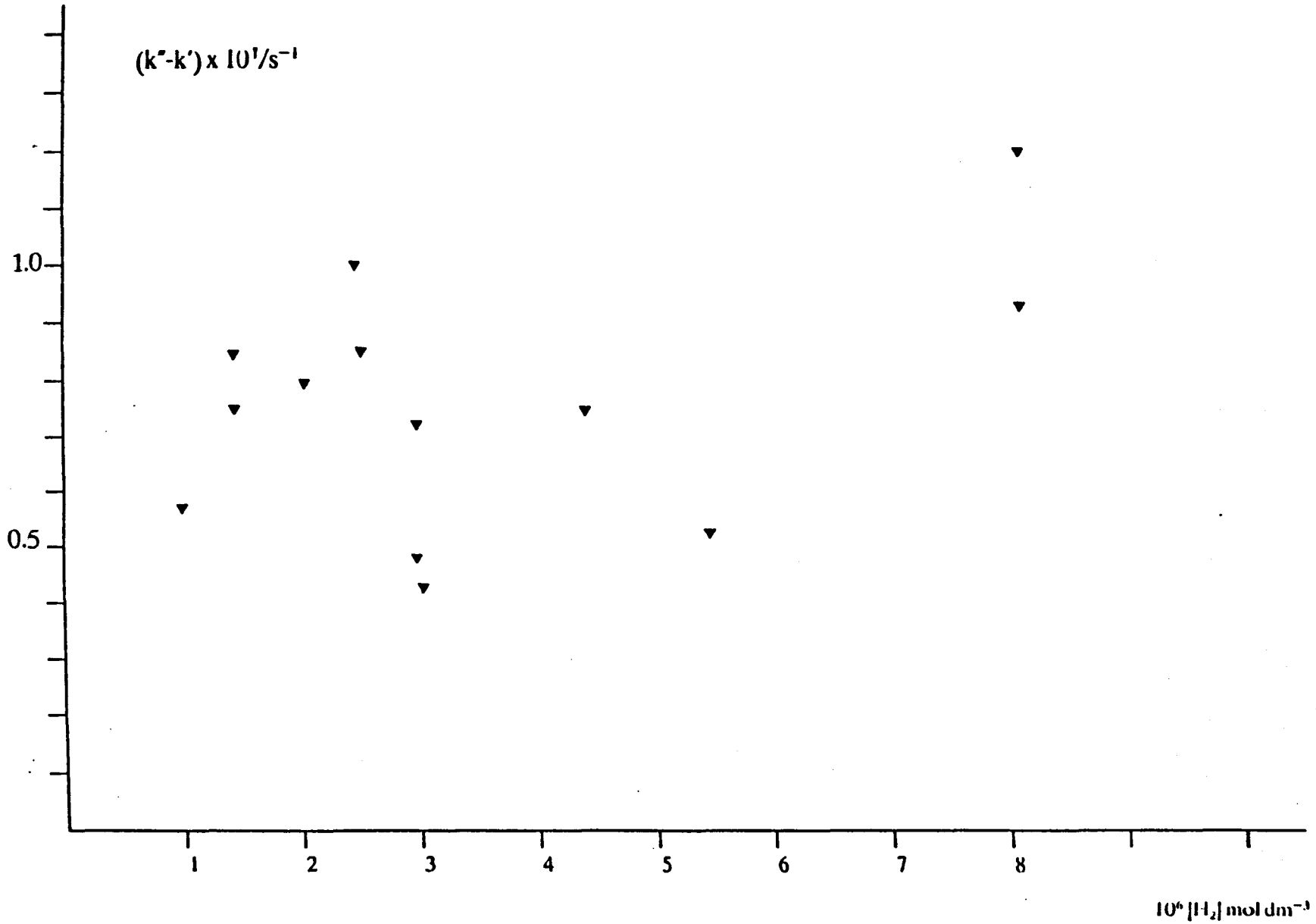

The result for $k_d^{H_2}$, obtained by averaging the data, agrees well with the value of Richards [28]. His rate constant was determined using a discharge flow tube and analysed by the method given in section 10.2 . Both Findlay and Snelling [116] and Becker [135] obtained values for $k_d^{H_2}$ an order of magnitude lower than Richards. In the former case, determinations were made by measuring the difference in decay constants for O_2 ($a\,^1\Delta_g$)(v=o) both with and without added H_2. High values for the O_2 decay contants were reported, and this may lead to a lower value of $k_d^{H_2}$. Becker *et al.* experienced problems with diffusion, and this could lead to an erroneous estimate.

Least squares analysis of the data, according to equation (10.14), yields a rate constant an order of magnitude lower than the averaged result. Further, this analysis also concludes that the wall constant in the presence of m (k_w'), is greater than the wall constant in O_2 alone (k_w). Richards obtained a linear plot according to eqn (10.14) and concluded that $k_w' = k_w$, and hence the wall was unmodified in the presence of H_2. This would be expected since H_2 is a non-polar species. The form of figure 10.14 is then probably attributable to experimental error.

Experimental determinations of $k_d^{H_2}$ are subject to error principally from two sources. There is a limited range of concentrations that can be used, as a consequence only small differences between the first order rate constants (k", k') can be obtained. Also there is a reduction in emission intensity when H_2 is added to the O_2 stream, this reduces the precision of the psuedo first order rate constant k".

The value of $k_d^{D_2}$, obtained by averaging the data in table 10.11 , agrees well with the value of Richards, who obtained [28]:

$$k_d^{D_2} = (2.56 \pm 1.3) \times 10^3 \text{ dm}^3 \text{ mol}^{-1} \text{ s}^{-1}.$$

Due to the availability of D_2, only a few estimates of $k_d^{D_2}$ were possible. In this case, Richards could not produce a linear plot according to eqn. (10.14). The scatter is attributable to the small differences in first order rate constant under these conditions.

In view of the difficulties of the experiment, and the disagreement between the previous estimates, the values of $k_d^{H_2}$ and $k_d^{D_2}$ reported here should be regarded as order of magnitude estimates.

10.10 Determinations of $k_d^{H_2}$ and $k_d^{D_2}$ in the Temperature Range 170 to 407K

10.10.1 Experimental

Measurements of the rate constants $k_d^{H_2}$ and $k_d^{D_2}$ were taken in the temperature range 170 to 407K, by using the technique given in section 10.7 .

10.10.2 Results

A plot of ln ($^{762}I_o/^{762}I_t$) as a function of flow tube length, with pure O_2 and for an O_2/H_2 mixture, is given in figure 10.18 . Good straight lines were produced throughout the temperature range Values of 2 ($k'' - k'$) from each plot with the corresponding quencher concentration are given in tables 10.12 and 10.13 .

A plot of 2 ($k'' - k'$) against m was made at each temperature. For both species, H_2 and D_2, a scattered plot was produced (fig. 10.19). The values of $k_d^{H_2}$ and $k_d^{D_2}$, calculated by equation (10.14),were therefore averaged, and are given in table 10.14 .

10.10.3 Discussion of the High and Low Temperature Data.

The values for $k_d^{H_2}$ and $k_d^{D_2}$, have been plotted against the temperature in figures 10.20 and 10.21 respectively. Also plotted is the data of Richards who obtained values for $k_d^{H_2}$ and $k_d^{D_2}$ using a discharge flow shock tube. It can be seen that both rate constants increase with temperature; the agreement between the two data sets using both $H_2$and D_2 is reasonable.

Both plots (figs. 10.20 and 10.21) illustrate an appreciable amount of scatter. The rate constants in this study were obtained under some difficulty (fig. 10.17), the data of Richards is also scattered and this was attributed to the nature of shock tube experimentation.

An Arrhenius plot was constructed from the data in table 10.14 and is given in fig. 10.22 . It can be seen that despite the scatter, the two plots have different slopes.

Figure 10.18 Variation of ln (I_o/I_t) as a function of flow tube length, T = 170K

λ= 762 nm.

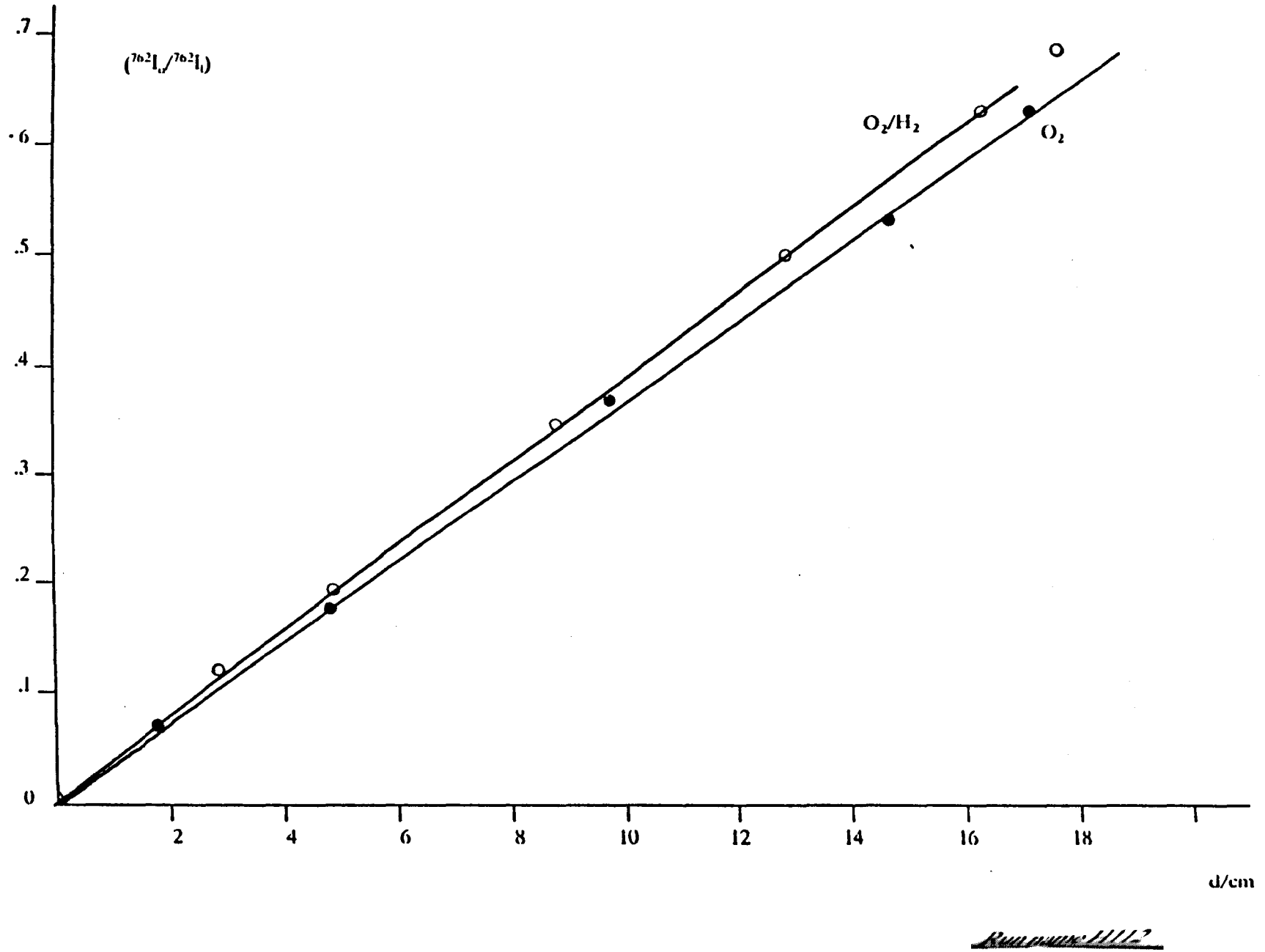

Table 10.12 Deactivation of O_2 ($a^1\Delta_g$)(v=o) by H_2 .λ 762 nm.

(a) T=407K

Run Name	P / torr	$2(k''-k')$ / s^{-1}	$10^6[H_2]$ / mol dm^{-3}	$10^{-4}k_d^{H_2}$ / $dm^3mol^{-1}s^{-1}$
HD63	7.30	0.356	2.2	8.1
64	7.30	0.320	2.2	7.26
65	7.30	0.369	2.2	8.37
66	7.30	0.369	2.2	8.37
67	7.30	0.282	1.4	10.10
68	7.30	0.272	1.4	9.66
69	7.30	0.272	1.4	9.66
70	7.30	0.292	1.4	9.66
71	7.30	0.285	1.6	8.84
72	7.30	0.295	1.6	9.23

(b) T=335K

34	7.50	0.071	2.7	1.25
35	7.50	0.071	2.7	1.25
36	7.50	0.115	2.5	2.04
37	7.50	0.195	5.6	1.67
38	7.50	0.168	5.6	1.44
39	7.50	0.177	5.6	1.81
40	7.50	0.097	3.9	1.20
41	7.50	0.106	3.9	1.30
42	7.50	0.138	3.9	1.72
43	7.50	0.079	2.2	1.72
44	7.50	0.097	2.2	2.1
45	7.50	0.097	2.2	2.1

Table 10.12 *(Continued)*

(c) T=362K

Run Name	P / torr	$2(k''-k')$ / s^{-1}	$10^6[H_2]$ / mol dm^{-3}	$10^{-4}k_d^{H_2}$ / $dm^3mol^{-1}s^{-1}$
HD3	7.7	0.0968	2.58	1.87
4	7.7	0.112	2.58	2.18
5	7.7	0.0968	2.58	1.87
6	7.7	0.0968	5.16	0.93
7	7.7	0.0968	5.16	0.93
8	7.7	0.150	5.16	1.45
9	7.7	0.0968	3.87	2.5
10	7.7	0.121	3.87	1.34
11	7.7	0.102	3.87	1.34
13	7.7	0.0833	2.58	1.7
14	7.7	0.0833	2.58	1.7

(d) T=355K

HD49	7.5	0.190	3.26	2.91
50	7.5	0.190	3.26	2.91
51	7.5	0.162	3.26	2.48
52	7.5	0.162	1.63	4.96
53	7.5	0.171	1.63	5.23
54	7.5	0.153	1.63	4.68
55	7.5	0.279	3.26	4.27
56	7.5	0.324	3.26	4.96
57	7.5	0.288	3.26	4.41
58	7.5	0.315	3.26	4.82

Table 10.12 *(Continued)*

(e) T=170K

Run Name	P / torr	$2(k''-k')$ / s^{-1}	$10^6[H_2]$ / mol dm^{-3}	$10^{-4}k_d^{H_2}$ / $dm^3mol^{-1}s^{-1}$
H110	5	0.055	29.0	0.095
111	5	0.06	29.0	0.1
112	5	0.04	22.0	0.091
113	5	0.04	22.0	0.091
114	5	0.02	15.0	0.066
115	5	0.02	15.0	0.066

Table 10.13 Deactivation of D_2 ($a^1\Delta_g$)(v=o) by D_2 :λ 762 nm.

(a) T=350K

Run Name	P / torr	$2(k''-k')$ / s^{-1}	$10^5[D_2]$ / mol dm^{-3}	$10^{-4}k_q^{D_2}$ / $dm^3mol^{-1}s^{-1}$
D8	5	0.75	1.22	3.1
D9	7	0.34	1.71	2
D10	10	0.76	2.95	2.6
D11	11	0.37	2.69	1.5

(b) T=400K

D12	6	1.2	0.69	9
D13	8	2	0.85	13
D14	10	1.6	1.07	8
D15	7	1.5	0.75	10

Figure 10.19 The Deactivation of O_2 ($a^1\Delta_g$) (v=o) by H_2 at T=170K.

λ= 762 nm.

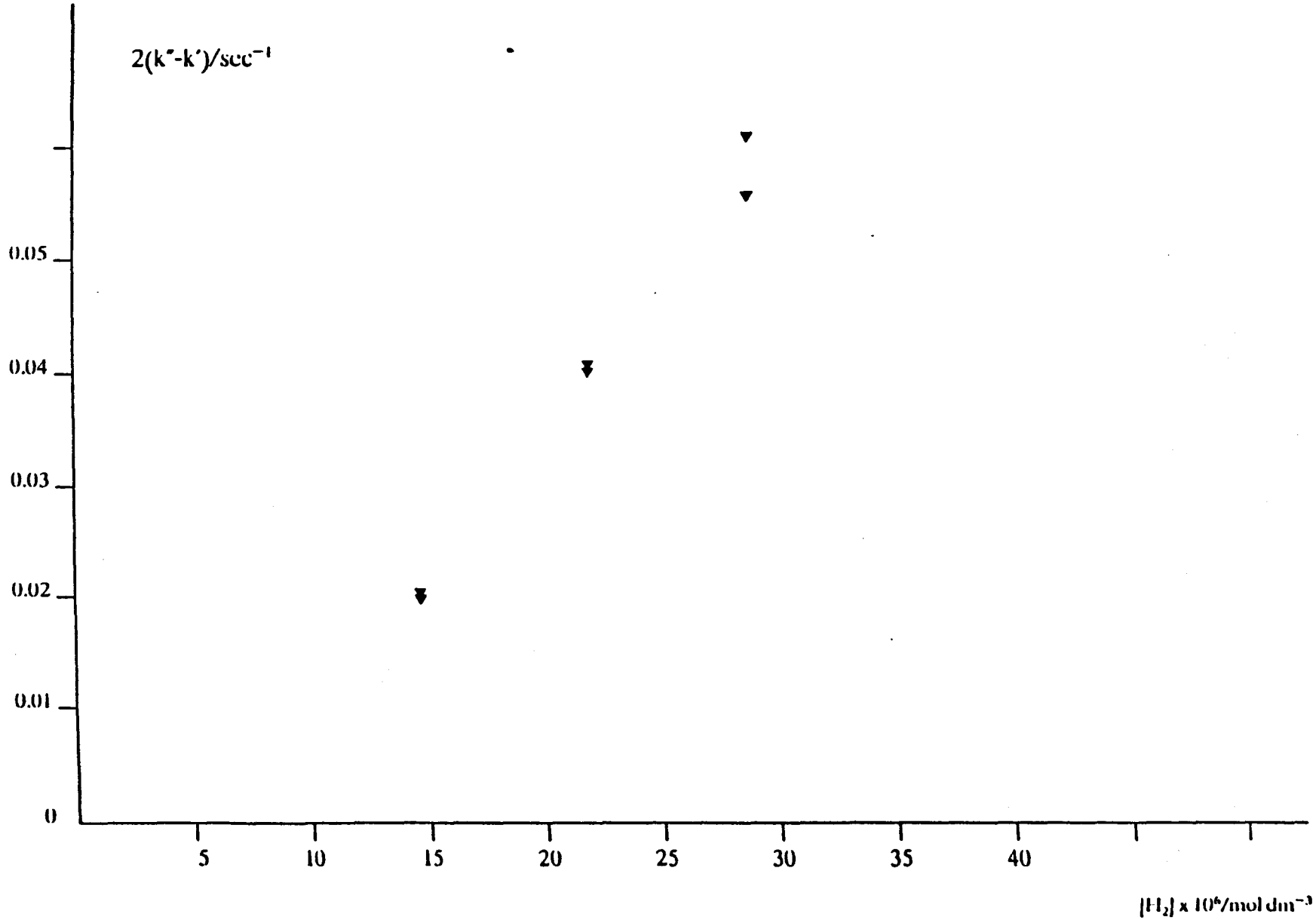

Table 10.14 The rate constants $k_d^{H_2}$ and $k_d^{D_2}$

(a) H_2

Temperature / K	$k_d^{H_2}$ / $dm^3mol^{-1}s^{-1}$
170	$(8.43\pm0.05)\times10^2$
292	$(3.39\pm0.38)\times10^4$
335	$(1.63\pm0.09)\times10^4$
355	$(4.16\pm0.3)\times10^4$
362	$(1.57\pm0.13)\times10^4$
407	$(8.92\pm0.26)\times10^4$

(b) D_2

T/K	$k_d^{D_2}$ / $dm^3mol^{-1}s^{-1}$
292	$(2.56\pm1.3)\times10^3$
350	$(2.3\pm1.0)\times10^4$
400	$(1.0\pm0.3)\times10^5$

The error limits are the standard error of the mean.

Figure 10.20 Rate constants for the deactivation of O_2 ($a^1\Delta_g$) by H_2

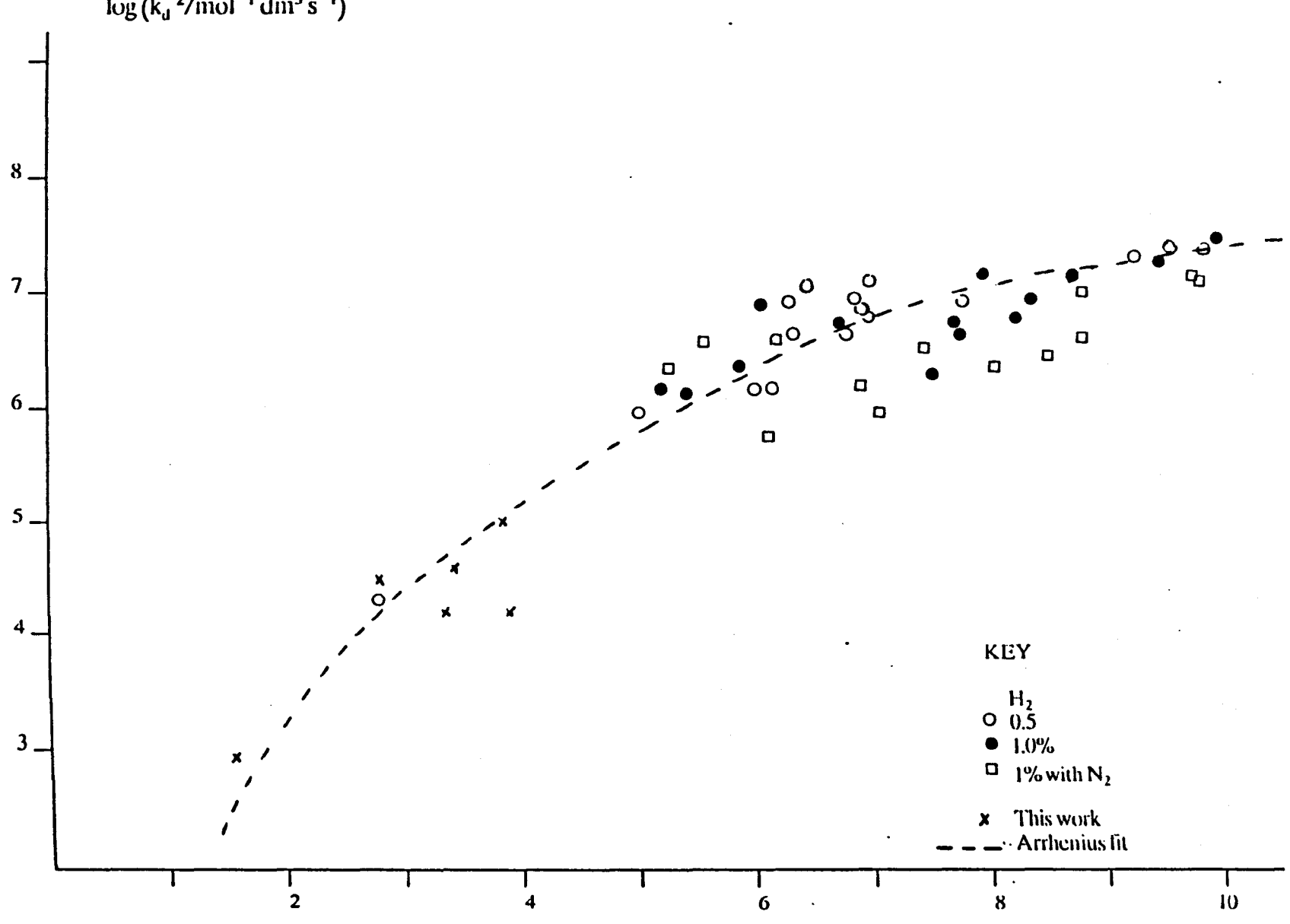

Figure 10.21 Rate constants for the deactivation of O_2 ($a^1\Delta_g$) by D_2

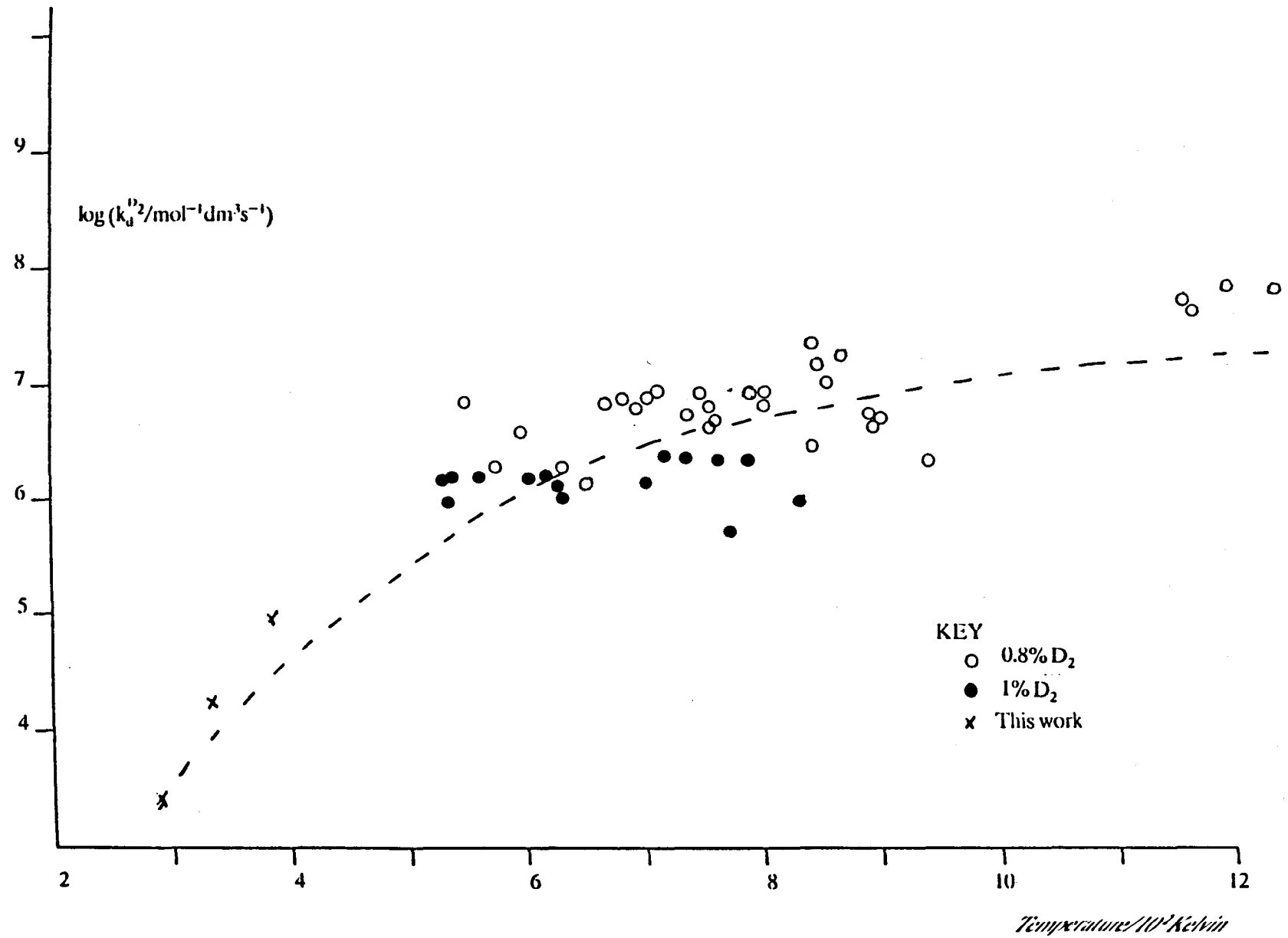

Figure 10.22 Arrhenius plot of $k_d^{H_2}$ and $k_d^{D_2}$

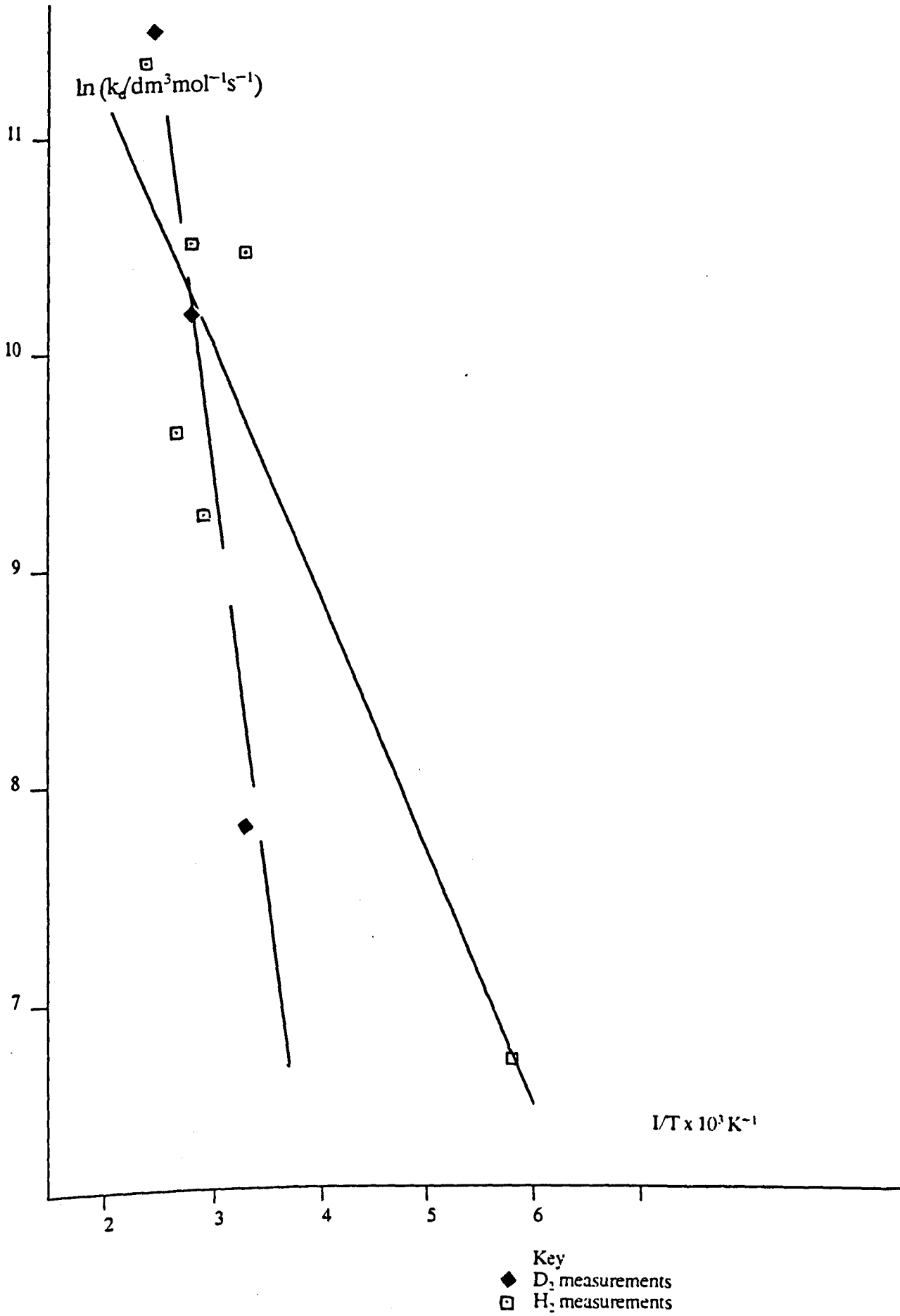

There is therefore a measurable difference in temperature dependence for the quenching of O_2 ($a^1\Delta_g$) (v=o) by H_2 and D_2.

In view of the difficulties of the experiment (section 10.9), considerable scatter of the experimental data was observed. It must be concluded that further experimentation is required to resolve the differences reported between these and previous measurements [166].

CHAPER ELEVEN

11.0 Low Temperature Spectral Measurements of the Co-Operative 'Dimol' Emissions From Singlet Molecular Oxygen.

11.1 Introduction

Measurements of both the spectra and emissivity of the co-operative, 'dimol', transitions from O_2 have been made using the temperature variable flow tube. These measurements were made to provide experimental data for the dimol emission at low temperature. This gives an extension to the work in emission already conducted at high temperature [106], and provides a comparison to the absorption measurements that have been made at low temperature [107]. Furthermore, these measurements may give information as to the nature of the interaction and the emitting species (Chapter Eight).

Observations were made by viewing the emission from a discharged flow of oxygen. The measurements were taken in the temperature range 100 to 300K.

11.2 Experimental

The dimol emission, centred at 634 nm, was viewed at a fixed location along the cooled discharge flow tube. The observation position was located 6cm downstream of the constricted inlet. Spectra was taken by using a monochromator (Bentham BN4), with a slit width of 0.5mm which gave a bandpass of 1nm. The emission was measured by photon counting (Ortec), using a low noise photomultiplier (E.M.I.9863) [32].

The relative emissivity of the dimol emissions located at 634 and 703 nm (table 8.2) was determined by viewing the emission with a photomultiplier (E.M.I.9558B), fitted with an interference filter. The output from the photomultiplier was fed to a digital voltmeter.

All of the experiments were taken in the pressure range P=4 to 12 torr, with a flow rate between 0.05 and 0.2 millimol sec^{-1}.

11.3 The Expected variation of the Emission Intensity with the Temperature for the Dimol Emission.

Measurements of the emission intensity were taken at a known location along the cooled discharge flow tube. As the temperature is changed the linear flow velocity, gas density and deactivation rate for $O_2(a^1\Delta_g)$ will also change. A model is therefore required that is capable of accounting for these variations, so that the intensity data can be correctly analysed.

The dimol emission occurs when two singlet molecular oxygen molecules interact. For the emission at 634 nm, the process is written:

$$O_2(a^1\Delta_g)(v=o) + O_2(a^1\Delta_g)(v=o) =$$

$$O_2(x^3\Sigma_g^-)(v=o) + O_2(x^3\Sigma_g^-)(v=o) + h\nu \qquad (11.1)$$

$$\lambda = 634\ nm$$

In these experiments, $O_2(a^1\Delta_g)(v=o)$ is produced by a discharge. It is then allowed to flow along the discharge flow tube. Deactivation of the species occurs by

both gas phase and surface collision; the emission intensity will therefore vary with the flow tube length and is given by (Chapter Ten);

$$[O_2(a^1\Delta_g)]_l = [O_2(a^1\Delta_g)]_o \exp -(k'l/v) \qquad (11.2)$$

where $[O_2(a^1\Delta_g)]_l$ and $[O_2(a^1\Delta_g)]_o$ are the $O_2(a^1\Delta_g)$ (v=o) concentrations at the observation position, l, and at the entrance to the flow tube, l=o, respectively. The quantity, v, is the linear flow velocity of the O_2 gas (Chapter Four) and k' is the psuedo first order rate constant for the deactivation of $O_2(a^1\Delta_g)$ which is given by (Chapter Ten):

$$k' = k_d^{O_2}[O_2] + k_w \qquad (11.3)$$

At room temperature the emission intensity at the observation position, $I_{(dimol)}$, can be written [167];

$$I_{(dimol)} = E_1 C [O_2(a^1\Delta_g)]_l^2 \qquad (11.4)$$

where E_1 is the emissivity for the emission and C is a geometrical constant, determined by experimental arrangement.

As the temperature of the flow tube is lowered, the value of $[O_2(a^1\Delta_g)]_l$ will change. The rate constants $k_d^{O_2}$ and k_w have already been determined in this system (Chapter Ten) and since there is a constant flow, $[O_2(a^1\Delta_g)]_o$ will remain unchanged. The value of the $O_2(a^1\Delta_g)$ concentration at the observation position at the lower temperature, $[O_2(a^1\Delta_g)]_l^*$ is given by;

$$[O_2(a^1\Delta_g)]_l^* = (292/T)[O_2(a^1\Delta_g)]_o \exp -((k')^*l/v^*) \qquad (11.5)$$

where * refers to the quantity at low temperature.

The emission intensity at temperature T, $I'_{(dimol)}$, and at room temperature, $I_{(dimol)}$, are given by using equations (11.2, 11.4 and 11.5);

$$I'_{(dimol)} = CE_2[O_2(a^1\Delta_g)]_o^2 (292/T) \exp -(2(k')^*l/v^*) \qquad (11.6)$$

$$I_{(dimol)} = C E_1 [O_2(a^1\Delta_g)]_o^2 \exp -(2k'l/v) \qquad (11.7)$$

where E_2 is the emissivity at low temperature.

Dividing equation (11.6) by (11.7) one obtains the emission ratio, γ;

$$\gamma = \frac{E_2}{E_1}\left(\frac{292}{T}\right)^2 \frac{\exp -(2(k')^* l/v^*)}{\exp -(2(k')l/v)} \qquad (11.8)$$

Equation (11.8) can be used to determine the ratio E_2/E_1 if the emission intensity ratio is measured and the quantities k', l, v, $(k')^*$, v^* and T are known.

11.4 Results

A spectrum of the dimol emission, centred at 634 nm, taken at 292K is given in figure 11.1 . Results were obtained with a maximum count rate of 20 scc^{-1}, each experiment took three minutes to perform.

This trace shows that the emission spectrum is broad, diffuse and structureless at this temperature. The full width at half maximum (F.W.H.M.) [107] was determined from the trace and found to have a value of 320cm^{-1}.

Measurements were then taken of the dimol emission below room temperature. A spectrum taken at 130K is given in fig. 11.1 . The narrowing of the peak as the temperature is reduced can clearly be seen. The F.W.H.M. was determined from a series of experiments conducted between 130 and 300K; this quantity was plotted as a function of the square root of the temperature [107], and is given in fig. 11.2 .

Further measurements were taken below 130K. In these cases the emission intensity was too low to produce a satisfactory spectrum.

The emission intensity was measured as a function of the temperature (section 11.2). A series of measurements, for the dimol emissions at 634 and 703 nm, are given in tables 11.1, 11.2 and 11.3 . Examples of the emission intensity relative to the room temperature value, γ, are plotted as a function of the temperature in figures 11.3 and 11.4 . The variation in γ has a complex dependence on the temperature (section 11.3), and this depends upon the experimental conditions. Also plotted in figures 11.3 and 11.4 are the calculated values for the relative emission ratio, γ', obtained by using equation (11.8) with a value of E_2/E_1 set to unity throughout the temperature range.

Figure 11.1 Variation of the emission intensity as a function of wavelength for the dimol transition at 634 nm.

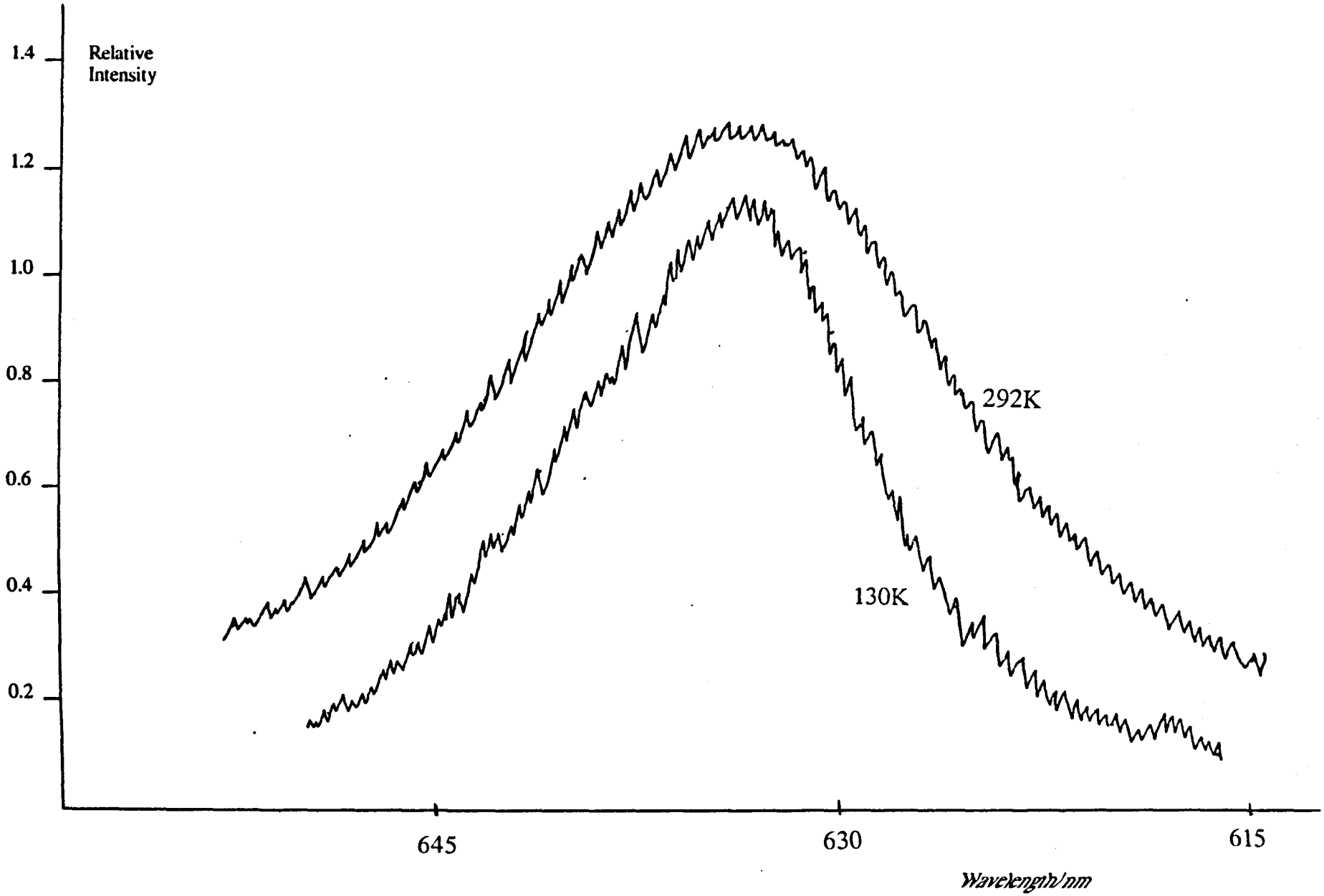

Figure 11.2 Co-operative Dimol band, λ=634.0 nm.

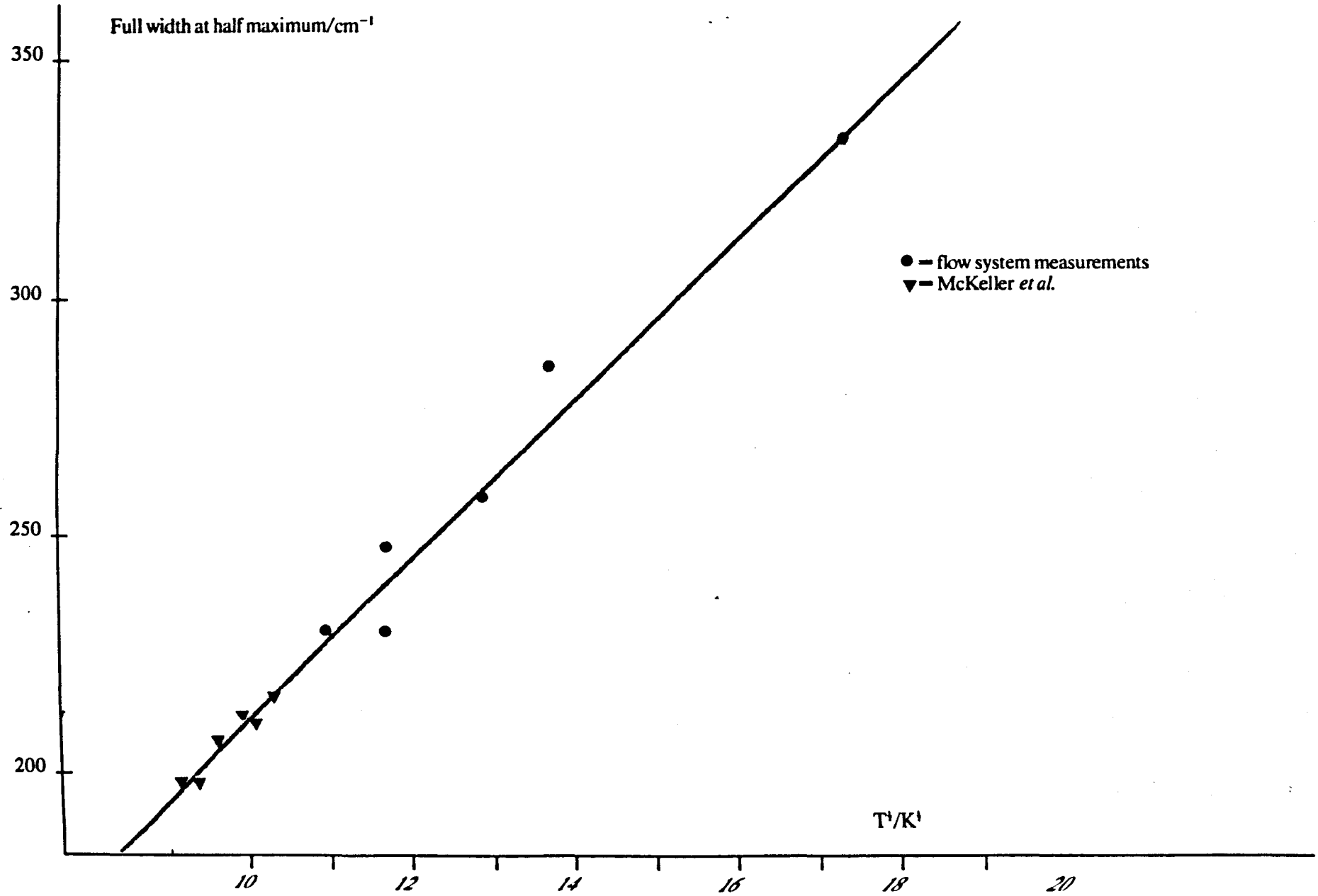

Table 11.1 Enhancement Factors for the Dimol Emission (634 nm)

(a): T=110K

Run Name	$\frac{I_{(dimol)}}{mV}$	$\frac{I_{(dimol)'}}{mV}$	γ	γ'
C1	110	42.6	.388	.359
C2	162	14.7	0.086	0.076
C3	100	23.7	.237	.217
C4	125	78.4	0.627	0.58
C9	225	530	2.35	2.17
C10	200	254	1.27	1.23
C11	193	230	1.189	1.10
C12	155	90.6	0.58	0.53
C13	150	400	2.67	2.48
C14	155	455	2.93	2.73
C15	150	402	2.68	2.48
C16	160	531	3.31	3.08

(b): T=200K

C1	110	138	1.25	1.21
C2	162	136	0.83	0.83
C3	100	113	1.13	1.08
C4	125	177	1.41	1.35
C5	144	185	1.28	1.23
C6	137	156	1.14	1.09
C7	104	80	0.76	0.73
C8	107	95	0.88	0.84
C9	215	404	1.88	1.78
C10	200	328	1.84	1.58
C11	192	312	1.62	1.54
C12	155	213	1.32	1.31

(c): T=175K

C1	110	132	1.21	1.17
C2	162	124	0.77	0.67
C3	100	113	1.13	1.00
C4	125	196	1.57	1.36
C5	144	195	1.36	1.18
C6	137	156	1.14	1.01
C7	104	70	0.67	0.58

11.1(c) *(Continued)*

C8	107	87	0.82	0.71
C9	225	495	2.220	2.00
C10	200	392	1.96	1.69

(d): T=125K

C1	110	84	0.76	0.6
C2	162	32.4	0.2	0.16
C3	100	44	0.44	0.4
C4	125	158	1.27	0.88
C5	144	118	0.82	0.65
C6	137	75	0.55	0.41
C7	104	13.5	0.13	0.10
C8	107	25	0.23	0.18

(e): T=275K

C1	110	114	1.04	1.04
C2	162	158	0.98	0.95
C3	100	100	1.0	0.96
C4	125	150	1.20	1.14
C5	144	172	1.20	1.16
C6	137	137	1.00	0.97
C7	104	101	0.97	0.95

(f): T=230K

C1	110	132	1.20	1.19
C2	162	160	1.0	0.96
C3	100	120	1.20	1.18
C4	125	156	1.25	1.27
C5	144	172	1.2	1.20
C6	137	1.50	1.1	1.12

(g): T=260K

C1	110	129	1.17	1.12
C2	162	170	1.03	1.01
C3	100	115	1.20	1.09
C4	125	150	1.20	1.16
C5	144	168	1.17	1.12
C6	137	157	1.15	1.10
C7	104	116	1.12	1.08

(h): T=150K

C1	110	114	1.03	0.96
C2	162	78	0.48	0.42
C3	100	86	0.86	0.74
C4	125	176	1.41	1.22
C5	144	163	1.13	0.98
C6	137	120	0.88	0.76
C7	104	39	0.37	0.32

(i): T=100K

C1	110	26	0.23	0.2
C2	162	6.5	0.04	0.03
C3	100	15.8	0.158	0.11
C4	66	0.52	0.32	0.37
C5	166	39	0.27	0.22
C6	137	20	0.145	0.12
C7	104	2.8	0.027	0.018
C8	107	46	0.642	0.03
C9	225	602	2.67	1.9
C10	200	241	1.21	0.93
C11	193	214	1.11	0.83
C12	135	65	0.42	0.33
C13	150	450	3.02	2.26
C14	155	257	3.4	2.55
C15	150	450	3.0	2.27
C16	160	636	3.96	2.98
C17	64	13	0.20	0.15
C18	60	17	0.28	0.23
C19	45	5.4	0.12	0.10

(j): T=200K

C13	150	278	1.83	1.82
C14	156	302	1.94	1.84
C15	150	283	1.88	1.81
C16	160	316	1.97	1.88
C17	64	80	1.24	1.19
C18	60	80	1.34	1.26
C19	45	61	1.13	1.04

Table 11.2 Enhancement Factors for the Dimol Emission (703 nm)

(a): T=150K

Run Name	$\frac{I_{(dimol)}}{mV}$	$\frac{I_{(dimol)'}}{mV}$	γ	γ'
C20	46	49.7	1.08	0.97
C21	40	14	0.35	0.31
C22	35	20	0.55	0.48
C23	42	36	0.86	0.78
C24	37	88	2.37	2.05
C26	32	48	1.50	1.34
C27	36	28	1.08	0.92
C28	26	28	1.08	0.92
C29	40	72	1.8	1.55
C30	48	78	1.63	1.139

(b): T=200K

C20	46	54	1.19	1.27
C21	40	32	0.81	0.78
C22	35	32	0.91	0.91
C23	42	49	1.16	1.16
C24	37	65	1.77	1.69
C26	32	45	1.4	1.42
C27	36	42	1.16	1.16
C28	26	30	1.14	1.18
C29	40	60	1.47	1.49
C30	48	60	1.25	1.29

(c): T=125K

C20	46	34	0.74	0.57
C21	40	5	.125	0.10
C22	36	9.5	0.27	0.21
C23	42	22	0.53	0.44
C24	37	91	2.46	2.0
C26	32	43	1.33	1.06
C27	36	19	0.53	0.44
C28	26	19	0.73	0.60
C29	40	64	1.60	1.30
C30	48	45	0.95	0.77

(d): T=110K

C20	46	19	0.4	0.3
C21	40	1.6	0.04	0.03
C22	36	3.5	0.10	0.08
C23	42	14.0	0.30	0.23
C24	37	88	2.38	1.96
C26	32	2.9	0.9	0.69
C27	36	12	0.34	0.23
C28	26	10	0.38	0.35
C29	40	54	1.39	1.00
C30	48	30	0.63	0.47

(e): T=230K

C20	46	55	1.21	1.24
C21	40	37	0.93	0.94
C22	35	35.7	1.01	1.01
C23	42	46	1.1	1.14
C24	37	53	1.43	1.36
C26	32	40	1.25	1.31
C27	36	40	1.12	1.41
C28	26	31	1.18	1.17
C29	40	53	1.33	1.34
C30	48	58	1.21	1.26

Table 11.3 Experimental Conditions for the Runs.

(a): $\lambda = 634$ nm

Run name	Pressure torr	Flow rate cm^3sec^{-1}(N.T.P)	Observation position cm
C1	7	4	25
C2	10	4	25
C3	8	4	25
C4	6	4	25
C5	7	5.2	33
C6	8	5.2	33
C7	11	5.2	33
C8	10	5.2	33
C9	4	3	12
C10	5.7	3	12
C11	6	3	12
C12	8	3	12
C13	5	3	7
C14	6	4	7
C15	6.5	4	7
C16	6.8	5	7
C17	5.3	3	28
C18	6.2	4	28
C19	9.1	5	28

(b): $\lambda = 703$ nm

Run name	Pressure torr	Flow rate $cm^3 sec^{-1}$(N.T.P)	Observation position cm
C20	5	3	25
C21	5	1.25	25
C22	7	2.7	25
C23	7	3.5	25
C24	6	3.8	10
C26	5.7	2	10
C27	8	2	10
C28	9	3.8	18
C29	7	4	18
C30	5	2	15

Figure 11.3 Variation of the Emission intensity as a function of temperature. λ=634 nm

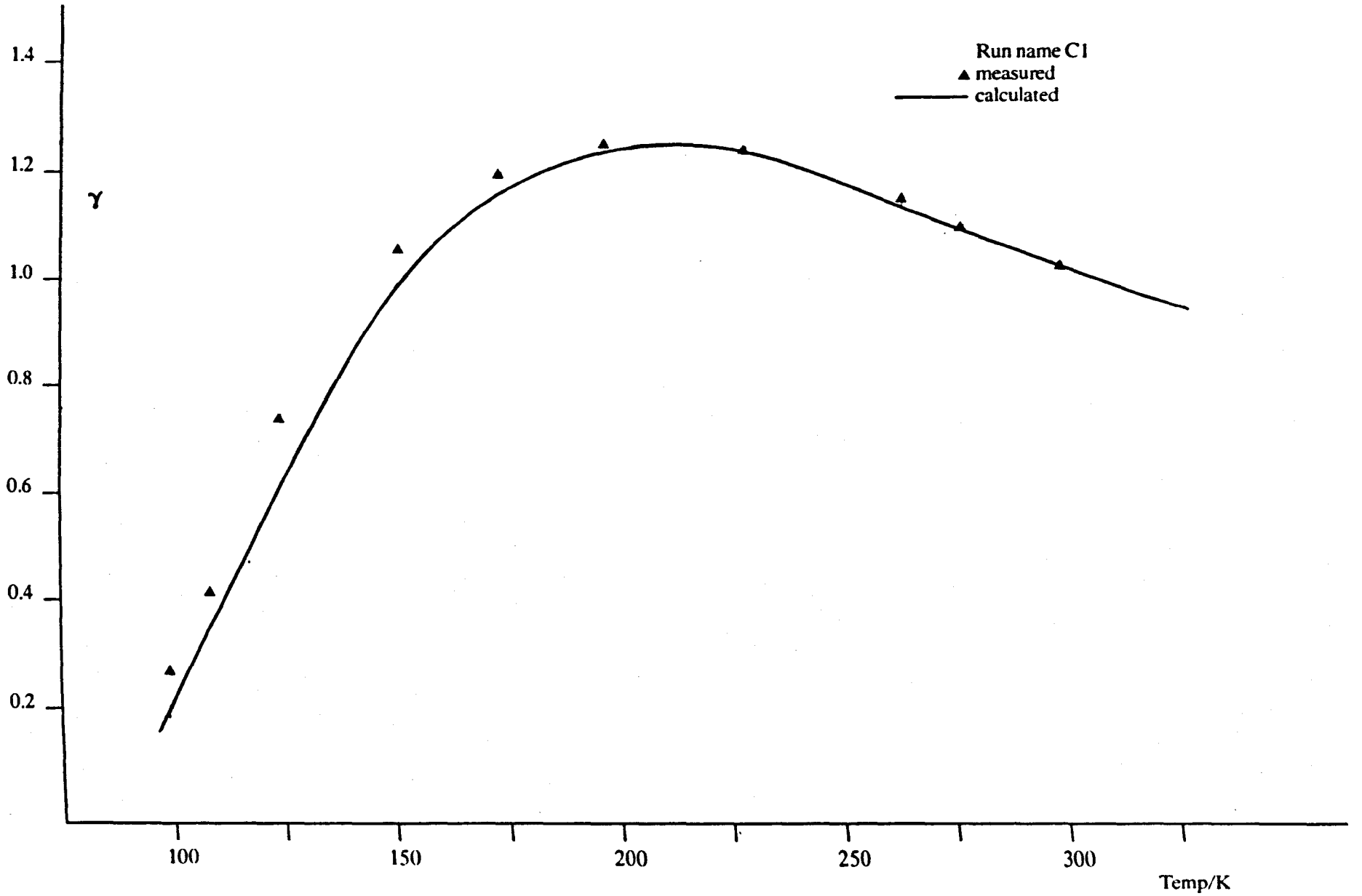

Figure 11.4 Variation of the Emission intensity as a function of temperature. λ=703 nm

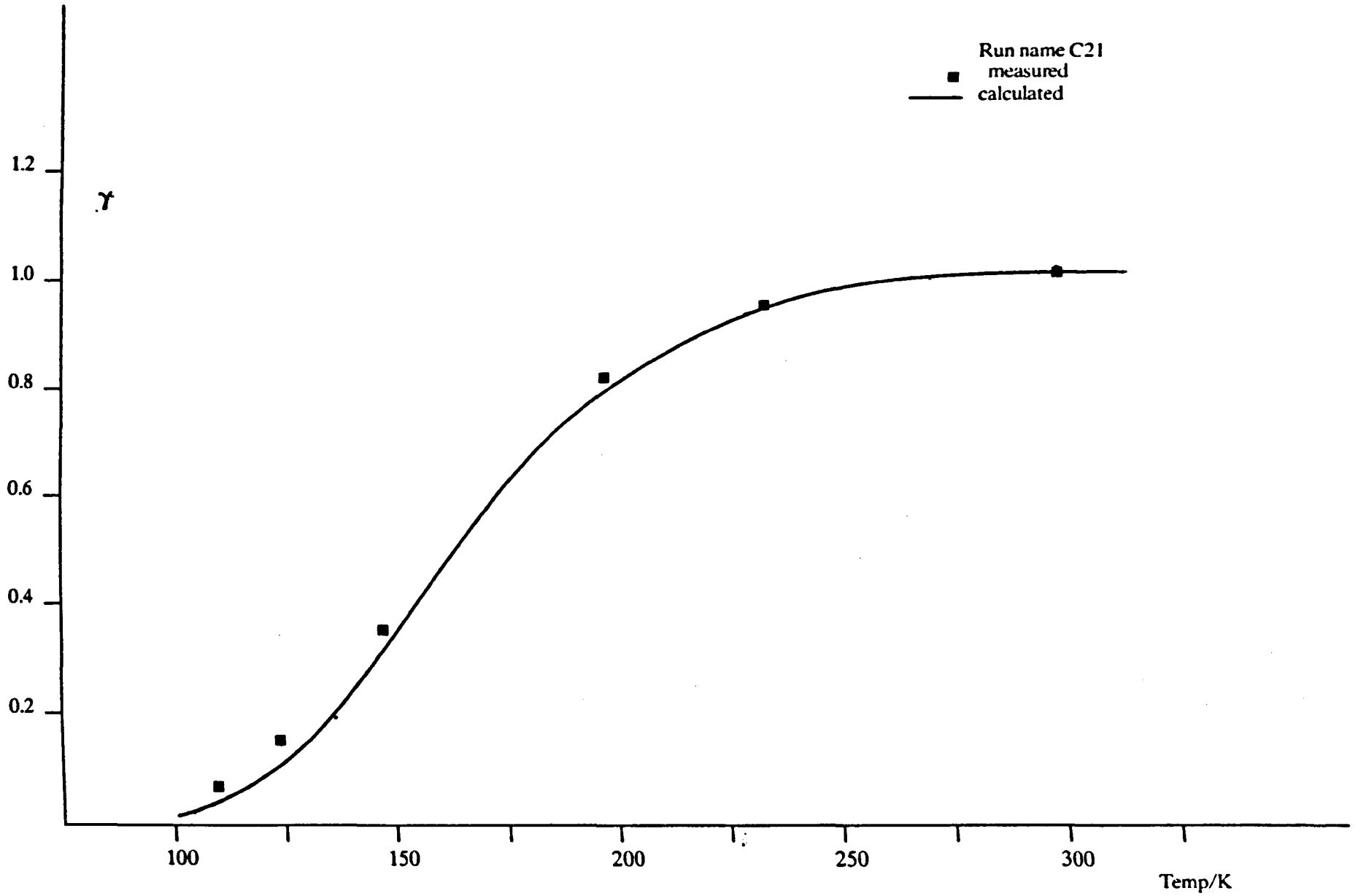

From these plots it is seen that the intensity ratio can be modelled well down to 150K. Below this, the observed intensity is greater than that predicted by the calculation.

Although the values of γ are close to those predicted by using equation (11.8), the values are always greater at lower temperature and the discrepancy increases as the temperature is reduced. Averages of the values, under different experimental conditions, were taken (tables 11.1 and 11.2) and at each temperature found to agree with one another, and thus the increase is statistically significant.

11.5 Discussion of the Results

In section 11.4 , it was shown that the emission spectrum for the dimol emission at 634 nm was broad, diffuse and structureless. There is good agreement between these measurements and those of Ogryzlo *et al.* [168,104], obtained by observing the emission in a discharge flow tube. There is also excellent agreement with the results of McKellar, Rich and Welsh [107], taken by measuring the absorption as a function of the wavelength at high pressure. Both spectra have the same general shape and the same F.W.H.M value at room temperature. The F.W.H.M was shown to vary with the temperature, the results were plotted in figure 11.2 . From this plot it is seen that there is an excellent agreement between the measurements reported here and the absorption measurements of McKellar *et al.* [107]. This dependence is reasonable since the width of an individual collision induced transition is inversely proportional to the duration of the collision, which will be proportional to $\sqrt{T}$.

The variation of the F.W.H.M. must be considered when examining the emission intensity measurements. The emission is seen by a photomultiplier which is fitted with an interference filter of half height bandwidth, s. The total emission observed will be effected as the temperature changes since the spectral distribution alters (fig. 11.2). The effect has been considered and is presented in appendix 5 . If the spectrum can be described by a Gaussian distribution (fig. 11.1) [169], with a F.W.H.M, f, the total observed emission, E, is related to the incident emission, E_o, by:

$$\frac{E}{E_o} = \frac{s}{(s^2+f^2)^{\frac{1}{2}}} \qquad (11.9)$$

Corrections were made to the data (table 11.4) by applying eqn. (11.9), using a value of $s=250cm^{-1}$. The corrected data has been plotted in fig. 11.5 and this shows that the emissivity is virtually independent of the temperature between 100 and 300K.

Table 11.4 Correction for the Relative Emissivity ($\lambda = 634nm$)

Temp/K	Relative Emissivity	$\frac{f}{cm^{-1}}$	$c = s/(s^2 + f^2)^{\frac{1}{2}}$	Corrected Relative Emissivity
292	1	325	0.61	1
275	1.05	317	0.619	1.05
260	1.03	308	0.63	1.0
230	1	290	0.653	0.93
200	1.1	282	0.66	1.0
175	1.06	262	0.69	0.93
150	1.16	247	0.71	1.0
125	1.27	232	0.73	1.06
110	1.08	218	0.75	0.87
100	1.38	210	0.76	1.09

value of s used = $250cm^{-1}$

Table 11.5

Temp/K	Relative Emissivity	Corrrection Factor	Corrected Relative Emissivity
292	1	1	1
230	0.96	0.9	0.89
200	1.0	0.92	0.92
150	1.15	0.85	0.97
125	1.36	0.83	1.12
110	1.21	0.80	0.96

Figure 11.5 Variation of the Dimol transition at 634 nm.

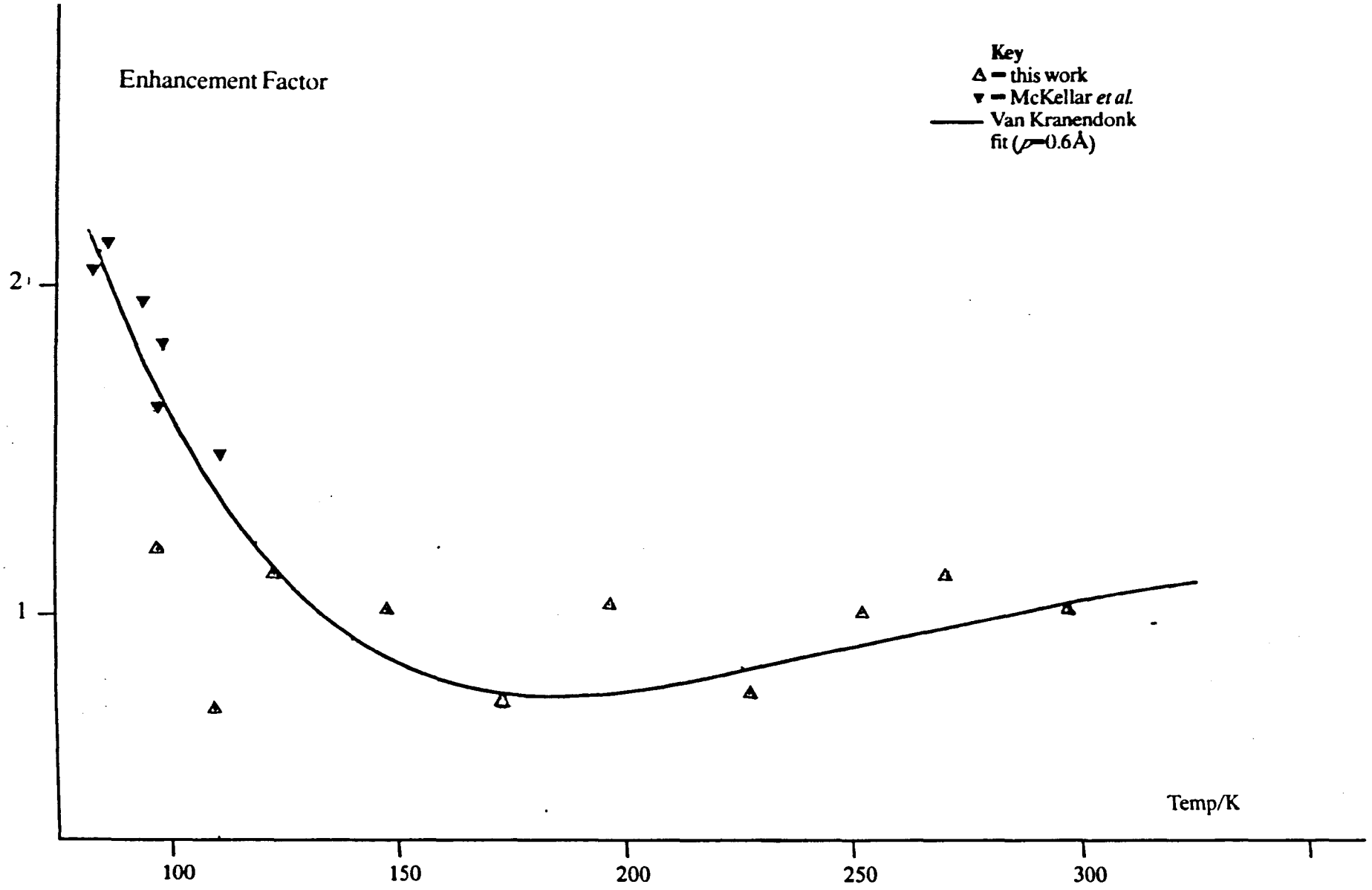

Figure 11.6 Enhancement factors for the dimol emission from O_2

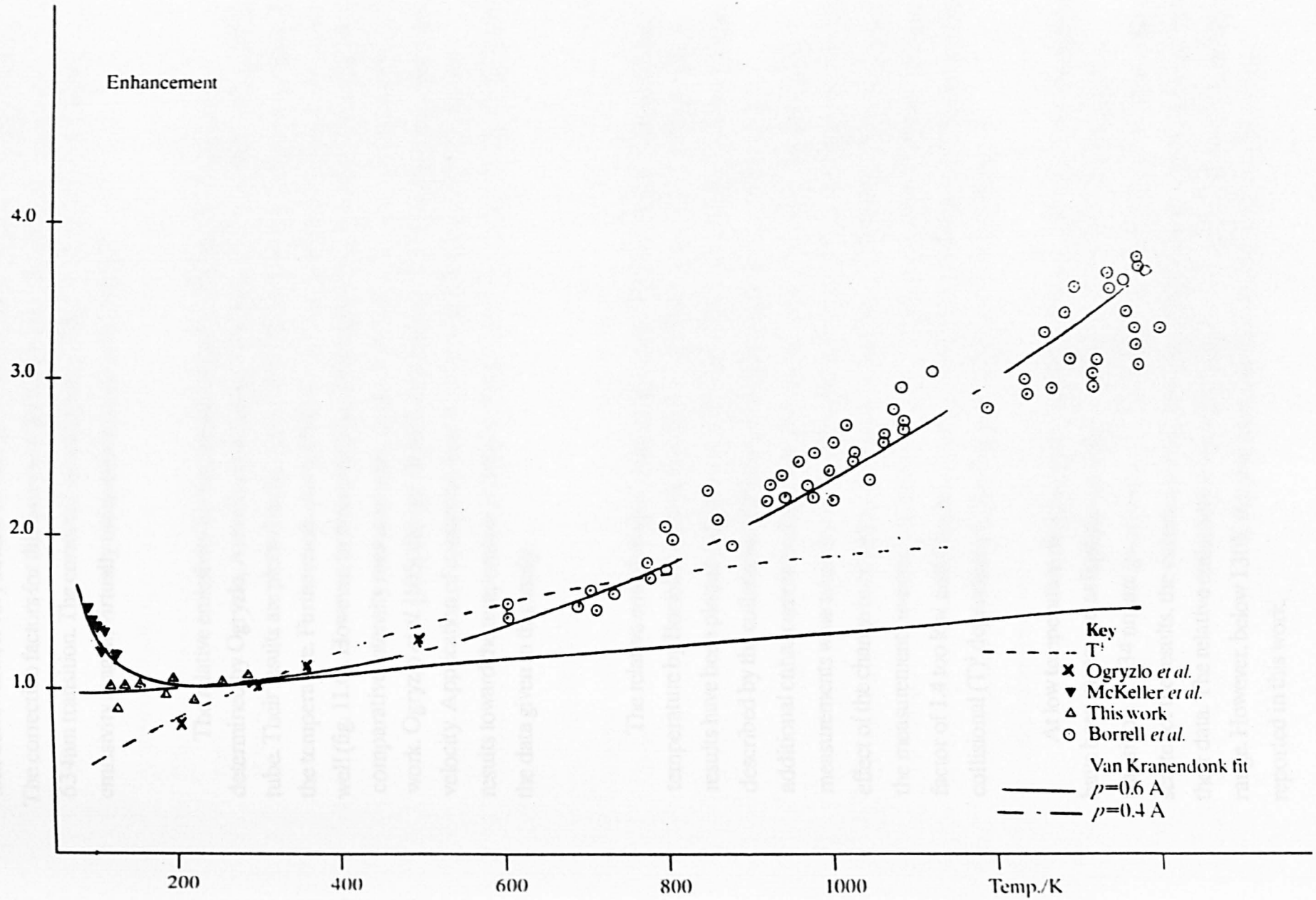

Corrections were also made to the data at 703nm. It is known that bandshape, and bandwidth, is very similar to that of the transition at 634nm [104,159,168,107]. The correction factors for this band will therefore be very similar as those for the 634nm transition. The corrected data is given in table 11.5 and shows that the emissivity is again virtually independent of the temperature.

The relative emissivity for the emission band at 634 nm has also been determined by Ogryzlo, Arnold and Browne [105], who used a cooled discharge flow tube. Their results are plotted in fig. 11.6 and it is clear that the emissivity varies with the temperature. Furthermore, the collisional, $(T)^{\frac{1}{2}}$, dependence describes their data well (fig. 11.6). However, in their experiments the emissivity was determined by taking comparative intensity measurements, in much the same way as they were taken in this work. Ogryzlo *et al.* [105] did not allow for variations in the quenching rates and flow velocity. Application of correction factors to account for these would move their results toward the temperature independent form, and so would be in agreement with the data given in this study.

The relative emissivity (or enhancement factor) has been determined at high temperature by Borrell *et al.* [106], in the temperature range 300 to 1650K. Their results have been plotted in figure 11.6 : between 300 and 1000K their data can be described by the collisional $(T)^{\frac{1}{2}}$ form, at temperatures above 1000K there is additional enhancement and this was attributed to vibrational 'hot bands'. These measurements were taken by viewing the emission through an interference filter. The effect of the change in emission distribution was not considered (fig. 11.1) and so put the measurements in error. Calculations (eqn. 11.9) show that at 1000K their data is a factor of 1.4 too low, and thus the corrected enhancement factors move away from the collisional $(T)^{\frac{1}{2}}$ dependence in the temperature range 300 to 1000K.

At low temperature the absorption coefficients for a number of dimol transitions have been measured at high pressure by McKellar *et al.* [107]. The results for the transition at 634 nm are given in fig. 11.5 . It is clear that down to 130K, within the scatter of the results, the current measurements fit with the general trend exhibited by their data. The relative emissivity is virtually independent of the temperature in this range. However, below 130K the absorption measurements lie above the values reported in this work.

The relative emissivity determined in this study relies heavily on the quality of the values of $k_d^{o}{}^2$ and k_w, and upon the precision of the measurements of the pressure and flow rate. The greatest source of error would be due to the low temperature wall rate constant, k_w*. The surface activity depends upon the history, cleanliness and treatment of the glass (Chapter Ten). The intensity measurements were made shortly after the determination of $k_d^{o}{}^2$ and k_w and should therefore be considered as part of the same set of experiments. Also, subsequent work has shown that the wall becomes conditioned with age and the wall constant reduces with continued experimentation. The calculation (eqn. 11.8) probably underestimates the calculated relative intensity ratio (γ). The data should therefore be regarded as providing an upper limit to the relative emissivity, particularly below 150K.

11.6 Discussion of the Temperature Dependence of the Dimol Emission.

The dimol emission occurs when two singlet molecular oxygen molecules interact (section 11.3), and the temperature dependence of the emissivity and spectral distribution should provide an insight into the nature of the interaction.

Simple collision theory can be applied to the emissivity measurements. If two oxygen molecules collide and this alone gives rise to the emission, the temperature dependence for the emission rate constant, k_E, will vary with the square root of the temperature. Inspection of fig. 11.5 shows clearly that this is not the case, and so simple collision theory is inappropriate to describe this reaction.

McKellar, Rich and Welsh were able to fit their measurements in absorption (fig. 11.5), by applying a theory which was developed by Van Kranendonk [170] for the absorption in H_2 in the presence of inert gases at high pressure. Collision induced dipoles in the molecule give rise to the observed transition. Quadrupoles are neglected in this approach and it assumed that induction varies exponentially with the intermolecular separation, x. The emissivity, $I_{(T)}$, depends upon the dimensionless configuration integral;

$$I_{(T)} = 4\pi \int_0^{\infty} \exp -(2(x-1)\sigma/p)\, g_o(x)\ .\ x^2\, dx \qquad (11.10)$$

where $g_o(x) = \exp - [V(x)/k_B T]$

$$V(x) = 4E\{x^{-12} - x^{-6}\}$$

and $E/k_B = 109K$.

In order to fit this theory to their measurements, McKellar, Rich and Welsh used a Lennard-Jones parameter, σ, of 346pm and a value of p equal to 60pm. This experimental fit, normalised to room temperature, is given in figure 11.5 . This describes the absorption measurements well, and similar fits worked for other dimol transitions in the visible and infra red. However, the fit does not describe the high temperature emission measurements of Borrell; it can also be seen that it does not fit the current measurements in emission at low temperature (fig 11.6).

The measurement of Borrell *et al.* [106] and the present work can be described well by using equation (11.10), with values of $\sigma = 346$pm and $p = 40$pm; the fit is given in figure 11.6 (see appendix 6). All of the emission measurements can be described by this fit, and this must cast some doubt upon the absorption measurements of McKellar *et al.* [107], since the emission and absorption measurements should show the same temperature dependence.

The existence of a bound O_4 dimer has been postulated since the early paramagnetic studies made on oxygen by Lewis [171]. It is of interest to enquire whether the emitting species is a pair of bound singlet molecular oxygen molecules.

The dimol interaction can be represented by the following simple reaction sequence;

$$O_2(a^1\Delta_g) + O_2(a^1\Delta_g) \underset{k_2}{\overset{k_1}{\rightleftharpoons}} 2O_2(a^1\Delta_g) \qquad (11.11)$$

$$2O_2(a^1\Delta_g) \xrightarrow{k_3} 2O_2(x^3\Sigma_g^-) + h\nu \qquad \lambda = 634\text{nm} \qquad (11.11(a))$$

and the emission intensity is given by:

$$I = (k_1/(k_2+k_3))k_3 [O_2(a^1\Delta_g)]^2 \qquad (11.12)$$

If the value of $k_2 >> k_3$ then the above expression reduces to;

$$I = (k_1/k_2)\, k_3\, [O_2(a^1\Delta_g)]^2 \qquad (11.13)$$

where (k_1/k_2) is the equilibrium constant for the first reaction (eqn. 11.11).

As the reaction is exothermic, then the ratio k_1/k_2 will decline with the temperature [172], and so the emission should reduce as the temperature is increased. However ΔH, the enthalpy, is very small in this case, therefore;

$$\Delta H/RT << 1 \qquad (11.14)$$

and

$$\exp -(\Delta H/RT) \simeq 1 \qquad (11.15)$$

and so the emission would hardly vary at all with the temperature.

So the presence of an O_4 dimer could give rise to a temperature independent emissivity and this would be capable of explaining the results reported here (fig. 11.5), but could not encompass the high temperature results of Borrell *et al.* [106].

Falik and Mahan suggested that the only binding energy available for dimer formation would have to come from the Vand der Waals forces that exist for that exist between the oxygen molecules [173]. Spectroscopic evidence for binary cluster formation shows, at room temperature, that the species would necessarily be in low concentration [174].

Borrell and Rich have studied the symmetry of the likely emitting dimol species [175]. They concluded that this must be of planar symmetry by analogy with the work of Goodman and Brus in the solid state at 4.2k [176]. Bandari and Falikov [177] have used a nearest neighbour approach, of D_2h symmetry, to calculate the intensity of the electric dipole transitions for parallel molecules. They found that these transitions could be attributed to terms in the Hamiltonian [178] which describes electron tunneling from a π orbital in one molecule to a π in the other. For this effect, it is clear that the spatial alignment of the molecules would be of paramount importance. The

low transition probability (one in every 10^{12} collisions) is probably the result of three contributory factors:

(a) The very short interaction time

(b) The steric requirement needed for obtaining D_2h symmetry.

(c) The low oscillator strength for the transition.

The low transition probability suggests that there is a very short interaction time, and so the emitting species is unlikely to be a bound dimer.

CHAPTER TWELVE

12.0 Suggestions for Further Work

12.1 Introduction

This chapter outlines further work that can be made using the combined discharge flow shock tube and variable temperature discharge flow apparatus.

12.2 Further Studies with the Combined Discharge Flow Shock Tube

In Chapter Six, a variation of the relative emissivity for several (1+) emission bands of N_2 was reported. The spectral distribution for this band system is temperature dependent and this is due to the recombination mechanism. An extension of this work would be to carry out measurement on other emissions that originate from the lower vibrational levels of $N_2(B^3\pi_g)$.

The temperature dependence of the rate constant for the $N + O_2$ reaction was given in Chapter Seven. There have been numerous studies of this but there still remains uncertainty as to the nature of the reaction. Clark and Wayne attempted to investigate the temperature dependence for the $N + O_2(^3\Sigma_g^-)$ and $N + O_2(a^1\Delta_g)$ reactions [42]. It is now accepted that for the second reaction, they in fact measured the collisional deactivation rate constant for $O_2(a^1\Delta_g)$ by N atoms [97]. A repeat of these experiments would be of use; the excess energy of the $O_2(a^1\Delta_g)$ molecule may give a different temperature dependence for the rate constant and so provide clues to the reaction mechanism.

The reactions of oxygen atoms, at room temperature, were given in Chapter Seven. It would be of use to extend these studies to high temperature, since they are of interest in combustion chemistry [115]. In order to study these reactions, methods are required for generating and detecting the species. Oxygen atoms could be produced in the discharge flow shock tube by the hot wire pyrolysis of N_2O [179]. Slanger and Ogryzlo have reported visible emission that results from oxygen atom recombination [180]. This could be used to monitor the concentration of the species at high temperature.

The temperature dependence of the rate constant and emissivity for the $O + NO$ reaction could also be studied in the discharge flow shock tube. This would be of interest since it may provide another method by which oxygen atom concentrations could be determined. This was the first reaction to be studied using a discharge flow shock tube [181]. However, the rise time, pre shock decay and vibrational relaxation were not accounted for thus giving somewhat unrealistic results.

12.3 Studies using the Variable Temperature Discharge Flow Tube

The deactivation of singlet molecular oxygen, $O_2(a^1\Delta_g)$, can now be investigated in the temperature range 100 to 440K.

In this study (Chapter Ten), the collisional deactivation rate constants for $O_2(a^1\Delta_g)$, by the collision partners O_2, H_2, D_2, were determined. In the cases of H_2 and D_2, difficulties were experienced which gave rise to uncertainties in the reported values. It would be worthwhile repeating these experiments to resolve this problem. The major difficulty with these experiments is obtaining a sufficiently large difference in the first oder decay constants for the O_2 and mixed flow. It was shown that the Shin Maier theory works well for the deactivation of $O_2(a^1\Delta_g)$ by O_2. With accurate data for the deactivation of $O_2(a^1\Delta_g)$ by H_2 and D_2, a further test of this theory can be made.

A study of the temperature dependence for the quenching of O_2 $(b^1\Sigma_g^+)$ would allow an invaluable addition to the work already conducted at high temperature by Borrell *et al.* [10,11,12]. To approach this, the energy pooling rate constant, k_p, must be known in the temperature range 100 to 400K. Heidner [148] has been able to determine this over a limited temperature range by selectively deactivating $O_2(b^1\Sigma_g^+)$ by an aluminium wire. There is scope for extension of this experiment in the variable temperature flow tube.

There are several dimol emissions, for example;

$$O_2(a^1\Delta_g)\,(v=1) + O_2(a^1\Delta_g)\,(v=o) =$$

$$O_2(x^3\Sigma_g^-)\,(v=o) + O_2(x^3\Sigma_g^-)\,(v=o) + h\nu \qquad (12.1)$$

$$\lambda = 579\ \text{nm}$$

$$O_2(a^1\Delta_g)\,(v=o) + O_2(b^1\Sigma_g^+)\,(v=o) =$$

$$O_2(x^3\Sigma_g^-)\,(v=o) + O_2(x^3\Sigma_g^-)\,(v=o) + h\nu \qquad (12.2)$$

$$\lambda = 475\ \text{nm}$$

that could be studied in the variable temperature flow tube. Here, the problem may be that the intensity level of the emission may not be high enough to measure adequately with a photomultiplier. Furthermore, a simple interference filter may not provide sufficient discrimination; a preliminary survey of the dimol emission (12.1) proved this to be the case.

There are several modifications that can be made to the apparatus to assist measurement taking. In future studies the discharge flow tube could be immersed in an isothermal bath, temperature reduction is achieved by the use of cooling mixtures [21]. This arrangement would give a longer experimental run time.

For spectroscopic studies (Chapter Eleven), it would be advisable to construct an entirely new observation tube. To gather more of the emission, the walls of the tube could be made reflective and photomultiplier mounted so that the vessel is viewed longitudinally.

References

1. J. H. Vant Hoff, Etudies de Thermodynamique Chemique, F. Muller and Co., Amsterdam (1884).
2. P. W. Atkins, "Physical Chemistry", Oxford, (1978).
3. J. J. Hood, Philos. Mag., **20**, 323, (1885).
4. A Fontijn and M. A. A. Clyne, Reactions of Small Transient Species, Kinetics and Energetics, Academic Press, London (1983).
5. M. Menzinger and R. Wolfgang. Agnew — Chem. Int. Ed., **8**, 438, (1969).
6. R. L. Le Roy, J. Chem. Phys., **73**, 4338, (1969).
7. S. P. Walch and H. Dunning, J. Chem. Phys., **72**, 3221, (1980).
8. H. Eyring, J. Chem. Phys., **3**, 107, (1935).
9. J. D. Lambert, "Vibrational and Rotational Relaxation in Gasses", Oxford, (1977).
10. R. B. Boodaghians, P. M. Borrell and P. Borrell, Journal of Petrochem., **31**, 29-36, (1985).
11. R. B. Boodaghians, P. M. Borrell and P. Borrell, J. Chem. Soc., Faraday Transactions II, **80**, 817, (1984).
12. R. B. Boodaghians, P. M. Borrell P. Borrell and D. S. Richards, Bull. Soc. Chem. Belg., **92**, 651, (1983).
13. R. W. Nicholls, J. Chem. Phys., **20**, 1040, (1952).
14. J. M. Benson, J. Appl. Phys. **23**, 757-63, (1952).
15. J. Ankatell and R. W. Nicholls, Rep. Prog. Phys., **33**, 269, (1970).
16. D. S. Jackson and H. I. Schiff, J. Chem. Phys., **23**, 2333-8, (1955).
17. J. Berkowitz, W. A. Chupka and G. B. Kistiakowsky, J. Chem. Phys., **25**, 457-66, (1956).
18. U. H. Kurzweg and H. P. Broida, J. Molec. Spectrosc., **3**, (1959).
19. K. D. Bayes and G. B. Kistiakowsky, J. Chem. Phys., **32**, 992-1000, (1960).
20. Lord R. S. J. Rayleigh, Proc. R. Soc. A, **85**, 219-29, (1911).
21. I. M. Campbell and B. A. Thrush, Proc. Roy. Soc. A, **296**, 201-21, (1967).
22. P. A. Young and R. L. Sharpless, J. Chem. Phys., **39**, 1071-102, (1983).
23. P. W. F. Gross, J. Chem. Phys., **48**, 1302, (1968).
24. A. G. Gaydon, Dissociation Energies, 1st edition (London: Chapman and Hall), p156, (1947).
25. S. Benson, J. Chem. Phys., **48**, 1765-8, (1968).
26. N. F. Mott, W. H. Massey, "The Theory of Atomic Collisions", (Oxford University Press, Oxford, 1969).
27. H. Hartridge and F. J. W. Roughton, Proc. Roy. Soc. A, **104**, 376, (1923).
28. D. S. Richards, Ph. D. Thesis, University of Keele, 1985.
29. R. L. Belford and R. A. Strenlow, American Review of Physical Chemistry, **247**, (1967).
30. M. D. Pedley, Ph.D. Thesis, University of Keele, (1978).

31. R. B. Boodaghians, Ph.D. Thesis, University of Keele, (1983).
32. Photomultipliers (E.M.I. Ltd., Hayes, Middlesex, (1979).
33. Radio Spares Catalogue, (1983).
34. "Hazards in the Chemical Laboratory", SGL, (1984).
35. Tandy Electronics Catalogue, (1984).
36 M. Nelkon, "A Level Physics", Oxford, (1978).
37. J. N. Bradley, "Shock Waves in Chemistry and Physics", (London: Methuen), (1962).
38. J. K. Wright, "Shock Tubes", (London: Methuen), (1961).
39. G. M. Barrow, "Physical Chemistry", McGraw-Hill, (1979).
40. "Handbook of Chemistry and Physics, Chemical Rubber Company, 156th edition, (1977).
41. J.A.N.A.F. Thermodynamic tables, Dow Chemical Company, Michigan, (1965).
42. M. A. A. Clyne and B. A. Thrush, Proc. Roy. Soc. Lond. A, **261,** 259 (1961).
43. I. D. Clark and R. P. Wayne, Proc. Roy. Soc. Lond. A, **316,** 539-550, (1970).
44. J. T. Merron, J. Chem. Phys., **35,** 1138, (1961).
45. J. P. Monat, R. K. Hanson and C. H. Kruger, 17th Symposium on Combustion.
46. I. M. Campbell and B. A. Thrush, Proc. Roy. Soc. Lond. A, **296,** 222, (1967).
47. R. Pearse, "Identification of Molecular Spectra", Lond., (1968).
48. G. Hancock, G. W. Ketley and A. J. McRobert, J. Phys. Chem., **88,** 2104, (1984).
49. L. Elias, E. A. Ogryzlo and H. I. Schiff, Can. J. Chem., 37, (1959).
50. S. W. Benson and E. A. Axworthy, J. Chem. Phys., **26,** 1718, (1957).
51. F. Kaufman, "Reactions of O Atoms", Prog. in Reaction Kinetics, Vol. 1, Editor G. Porter, (1961).
52. P. Borrell, Comput. Chem., **4,** 131, (1980).
53. J. Sheppard, "Mathematics for Chemists", McGraw-Hill, (1980).
54. N. Cohn and R. F. Gross, J. Chem. Phys., **50,** 3119, (1969).
55. G. B. Kistiakowsky and G. G. Volpi, J. Chem. Phys., **31,** 1030, (1959).
56. W. Brennon and E. C. Shane, J. Phys. Chem., **75,** 1552, (1971).
57. F. Kaufman and L. J. Decker, 17th Symposium on Combustion, (1959).
58. P Harteck, R. P. Reeves and G. Manella, J. Chem. Phys., **29,** 1333, (1958).
59. P. Harteck, R. P. Reeves and G. Manella, J. Chem. Phys., **29,** 608, (1958).
60. J. F. Herron, J. Franklin, P. Brandt and V. H. Dibeler, J. Chem. Phys., **30,** 879, (1959).
61. M. A. A. Clyne and D. H. Stedman, J. Phys. Chem., **71,** 3071, (1969).
62. H. B. Dunford, J. Phys. Chem., **67,** 258 (1965).
63. C. B. Kretchmer and H. L. Peterson, J. Chem. Phys., **39,** 1772, (1963).
64. T. Marshall and R. A. Kawcyn, Physics Fluids, **5,** 1657, (1962).
65. B. Brockelhurst and R. W. Nicholls, Nature, Vol. 223, No. 5208, (1969).
66. G. E. Beale and H. P. Broida, J. Chem. Phys., **31,** 1030, (1959).
67. O. Oldburg, Bull. Amer. Phys. Soc., **12,** 217, (1969).

68. P. M. Borrell, private communication.
69. M. F. Golde and B. A. Thrush, Rep. Prog. Phys., **33**, 269, (1970).
70. P. G. Wilkinson and R. S. Mulliken, J. Chem. Phys, **31**, 674, (1959).
71. I. M. Campbell and B. A. Thrush, Chem. Comm., **250**, (1965).
72. M. Jeunhomme and A. B. F. Duncan, J. Chem. Phys., **41**, 1692, (1964).
73. N. Sadeighi and D. W. Setser, J. Chem. Phys., **79**, (1983).
74. A. Rotem, I. Nadler and S. Rosenwaks, Chem. Phys. lett., **83**, 281, (1981).
75. D. L. Baulch, D. D. Drysdale, D. G. Horne and A. C. Lloyd, "High Temperature Reaction Rate Data", (1969).
76. I. A. Miller and V. E. Bondeyby ', J. Chem. Phys., **69**, 3579, (1978).
77. K. M. Evenson and D. S. Burch, J. Chem. Phys., **45**, 2450, (1966).
78. K. H. Becker, W. Groth and D. Kley, Zeitschrift fur Naturforschung A, **24**, (1969).
79. C. B. Kretchmer and H. C. Peterson, J. Chem. Phys., **39**, 1172, (1963).
80. W. E. Wilson, J. Chem. Phys., 46, 2017, (1967).
81. P. Harteck and R. R. Reeves Jr., AFOSR. TR-57-50, ASTIA No. AD-136-421.
82. C. B. Kretchmer., AFOSR. TR-59-66, ASTIA No. 217-008, Aerojet Report No. 1611.
83. W. M. Jones and N. Davidson, Abstract of papers, 135th meeting Amer. Chem. Soc., 37, (1959).
84. H. B. Urbach, F. Leighton, J. A. Wojtowicz and J. A. Zaslosky, Abstract of Papers, 136th Meeting Amer. Chem. Soc., 46-48, (1959).
85. F. Kaufman, Proc. Roy. Soc. Lond., A, **247**, 123, (1958).
86. H. Enzo, K. Glazner and J. Troe, J. Phys. Chem., **83**, 2053, (1979).
87. H. J. Ball and G. S. Larkin, Nature (London), **245**, 63, (1973).
88. C. W. von Rosenberg and P. W. Trainor, J. Chem. Phys., **61**, 2442, (1974).
89. J. E. Morgan, L. Elias and H. I. Schiff, J. Chem. Phys., **33**, 930, (1960).
90. P. G. H. Marsden and J. W. Linnett, Proc. Roy. Soc., **A234**, 489, 504.
91. C. W. Wilson Jr., J. Chem. Phys., **62**, 4842, (1975).
92. P. A. Benioff and G. Das, Chem. Phys. letts., **75**, No. 3, (1980).
93. P. A. Benioff, G. Das, and A. C. Wahl, J. Chem. Phys., **67**, 2449, (1977).
94. M. Nicolet, J. Geophysics. Res., **70**, 679, (1965).
95. P. B. Norton, "essa" Technical Memorandum IERTM — ITSA 60, U.S. Department of Commerce (1967).
96. E. E. Ferguson, F. C. Fehsenfen, P. D. Goldan and A. L. Schmeltekopf, J. Geophysics Res., **70**, 679, (1965).
97. A. A. Westenberg, J. M. Roscoe and N. De Haas, Chem. Phys. letts., **7**, 597, (1970).
98. D. P Kearns, Chem. Rev., **71**, 403, (1971).
99. L. Herzberg and G. Herzberg, Astrophys. J., **105**, 353, (1947).
100. J. S. Griffith, "Oxygen in Animal Organisms", F. Dickens and E. Niel, Ed., Pergamon Press, Oxford, 481, (1964).

101. G. Herzberg, "Spectra of diatomic molecules", Van Nostrand, New York, N.Y., (1950).
102. R. M. Badger, A. C. Wright and R. F. Whitlock, ibid, **43**, 4345, (1965).).
103. L. Wallace and D. M. Hunter, J. Geophys. Res., **73**, 4813, (1968).
104. L. W. Bader and E. A. Ogryzlo, Disc. Farad. Soc., **37**, 46, (1964).
105. S. J. Arnold, R. J. Browne and E. A. Ogryzlo, Photochem. Photobiol., **4**, 963, (1965).
106. R. Boodaghians, P. M. Borrell, P. Borrell and K. R. Grant, J. Chem. Soc., **78**, 1195, (1982).
107. A. R. W. McKellar, N. H. Rich and H. L. Welsh, Can. J. Phys., **50**, 1, (1972).
108. G. Black and T. G. Slanger, J. Chem. Phys., **74**, 6517, (1978).
109. R. A. Young and G. T. Black, ibid., **44**, 341, (1966).
110. R. Wayne, Adv. Chem. Ser., **7**, 311, (1967).
111. R. E. March, S. G. Furnival and H. I. Schiff, Photochem. Photobiol., **4**, 971, (1965).
112. R. Wayne, "Singlet Oxygen", Chemical Rubber Company, **1**, (1984).
113. I. B. C. Matheson, J. Lee, R. S. Tammanchi and M. L. Volbersht, Chem. Phys. letts., **27**, 355, (1974).
114. K. Kohse-Hoinghaus and F. Stuhl, J. Chem. Phys., **72**, 3720, (1980).
115. R. P. Wayne, "Chemistry of Atmospheres", Oxford, (1985).
116. F. D. Findlay and D. R. Snelling, J. Chem. Phys., **55**, 545, (1971).
117. Patricia Borrell, Ph.D. Thesis, University of Keele.
118. J. A. Davidson, K. E. Kear and K. V. Abrahamson, J. Photochem., **1**, 307, (1973).
119. E. McKeown and W. A. Wates, J. Chem. Soc. B., 1040, (1960).
120. K. Gollnick, advan. Chem. Ser., **77**, 78, (1968).
121. A. M. Falik, D. M. Mahan and R. J. Myers, J. Chem. Phys., **42**, 1835, (1965).
122. S. J. Arnold, M. Kubo and E. A. Ogryzlo, Adv. Chem. Ser., **77**, 133, (1968).
123. P. B. Carins and J. A. R. Samson, Phys. Rev., **39**, 403, (1966).
124. R. G. McNeal and G. R. Cook, J. Chem. Physs., **45**, 3469, (1966).
125. R. G. McNeal and G. R. Cook, ibid., **47**, 5385, (1967).
126. I. D. Clark and R. P. Wayne, Chem. Phys. letts., **3**, 93, (1969).
127. E. A. Ogryzlo and A. E Pearson, J. Phys. Chem., **72**, 2913, (1968).
128. S. J. Arnold, N. Finlarson and E. A. Ogryzlo, J. Chem. Phys., **44**, 2529, (1966).
129. S. H. Whitlow and F. D. Findlay, Can. J. Chem., **45**, 2087, (1967).
130. P. M. Borrell, P. Borrell and K. R. Grant, J. Chem. Soc. Farad. II, **2**, 76, 923, (1980).
131. R. J. Collins, D. Hussain and R. J. Donovan, J. Chem. Soc., Faraday II, **69**, 145, (1973).
132. M. Yaron, A. von Engel and P. H. Vidaud, Chem. Phys. letts., **37**, 159, (1976).
133. D. J. Giachardi, G. W. Marns and R. P. Wayne, J. Chem. Soc. Faraday II, **72**, 619, (1976).

134. R. G. O. Thomas and B. A. Thrush, Proc. Roy. Soc. Lond. A, **356**, 287 (1979).

135. K. H. Becker, W. Groth and U. Schurath, Chem. Phys. letts., **8**, 259, (1971).

136. L. R. Martin, R. B. Cohen and J. F. Schatz, Chem. Phys. letts., **8**, 259, (1971).

137. S. V. Filseth, A. Zia and K. H. Welge, J. Chem. Phys., **52**, 5502, (1970).

138. K. Kear and E. W. Abrahamson, J. Photochem., **3**, 409, (1975).

139. E. A. Ogryzlo, Photophysiology, **5**, 35, (1970).

140. J. A. Davidson and E. A Ogryzlo, "Chemiluminesence and Bioluminescence", M. J. Cormier, D. M. Hercules and J. Leeds., Plenum Press N.Y., (1973).

141. R. G. O. Thomas and B. A. Thrush, Proc. Roy. Soc. Lond. A, **356**, 307, (1977).

142. M. P. Braithwaite, E. A. Ogryzlo, J. A. Davidson, J. Chem. Phys., **65**, 771, (1976).

143. M. P. Braithwaite, E. A. Ogryzlo, J. A. Davidson and H. I. Schiff, J. Chem. Soc. Faraday II, **72**, 2075, (1976).

144. M. P. Braithwaite, E. A. Ogryzlo, J. A. Davidson and H. I. Schiff, Chem. Phys. letts., **42**, 158, (1976).

145. M. Maier, Chem. Phys. letts., in press.

146. M. K. Shin, J. Chem. Phys., **42**, 59, (1965).

147. E. Wild, H. Klingshirn and M. Maier, J. Photochem., **25**, 131, (1974).

148. R. F. Heidner III, C. E. Gardner, T. M. El-Sayed, G. I. Segal and J. V. V. Kaspar, J. Chem. Phys., **74**, 5618, (1981).

149. R. G. O. Derwent and B. A. Thrush, Chem. Phys. lett., **9**, 591, (1971).

150. W. Hack, private communication.

151. B.B.C. Users Guide, (1983).

152. B.B.C. Disc Manual, Computer User Club, (1983).

153. I. B. Clark and R. P. Wayne, Proc. R. Soc. Lond. A., **314**, 111, (1969).

154. R. P. Steer, K. A. Ackerman and J. M. Pitts, J. Chem. Phys., **51**, 843, (1969).

155. P. M. Borrell, M. D. Pedley, P. Borrell and K. R. Grant, Proc. Roy. Soc. Lond. A., **367**, 395, (1979).

156. A. Leiss, U. Schurath, K. H. Beck and E. H. Fink, J. Photochem., **8**, 211, (1978).

157. W. C. Eisenberg, A. Snelson, R. Butler, K. Taylor and R. W. Murray, J. Photochem., **25**, 439, (1984).

158. D. L. Huestis, G. Black, S. A. Edelstein and R. L. Sharpless, J. Chem. Phys., **60**, 4471, (1974).

159. E. W. Gray and E. A. Ogryzlo, Chem. Phys. lett., **3**, 658, (1969).

160. K. R. Grant, Ph.D. Thesis, University of Keele.

161. P. Borrell, M. D. Pedley, P. M. Borrell and K. R. Grant, J. Chem. Phys., **78**, 748, (1983).

162. E. A. Ogryzlo and B. A. Thrush, Chem. Phys. lett., **32**, 34, (1973).

163. "Physical Chemistry", Daniels, McGraw Hill, (1980).

164. R. N. Schwartz, Z. I. Slawsky and K. F. Herzfeld, J. Chem. Phys., **20**, 1591, (1952).

165. J. O. Hirschfelder, C. F. Curtiss and R. B. Bird, "Molecular Theory of Gases and Liquids", (Wiley: New York), (1964).

166. D. S. Richards, Private Communication.

167. F. A. Fisk and G. N. Hays, Chem. Phys. letts., **79**, 331, (1981).

168. S. J. Arnold, E. A. Ogryzlo and H. Witzke, J. Chem. Phys., **40**, 1769, (d1964).

169. Handbook of Mathematics, Dept. of Physics, University of Keele, (1982).

170. J. Van Kranendonk, Physica, **24**, 347, (1958).

171. G. N. Lewis, J. Amer. Chem. Soc., **46**, 2031, (1924).

172. J. Nicholas, "Chemical Kinetics", Harper and Row, (d1970).

173. A. M. Falik and B. M. Mahan, J. Chem. Phys., **47**, 4778, (1967).

174. R. P. Bickensfelder and G. E. Ewing, J. Chem. Phys., **47**, 4778, (1967).

175. P. Borrell and N. H. Rich, Chem. Phys. lett., **99**, 144, (1983).

176. J. Goodman and L. E. Brus, J. Chem. Phys., **67**, 4398, (1977).

177. R. Bandari and L. M. Falicov, J. Phys. Chem., **6**, 493, (1973).

178. W. M. Hanna, "Quantum Mechanics In Chemistry", (W. A. Benjamin: London), (1965).

179. O. R. Lundell, R. D. Ketchesen and H. I. Schiff, 12th Symposium on Combustion, (1969).

180. T. G. Slanger, Science, **202**, 751, (1978).

181. R. A. Hartunian, W. P. Thompson and E. A. Hewitt, J. Chem. Phys., **44**, 165, (1966).

APPENDIX 1

Non linear least squares subroutine for the solution of equation (5.30) (Chapter Five),

```
      DOUBLE PRECISION FUNCTION NLSF(X)
C
      COMMON/PKINET/P(6)
C
      DOUBLE PRECISION P,X,Y
C
      Y = (1.0D0 + P(1))*DEXP-((2P(2) + P(3)))*X) -
      P(1)*D EXP - (4P(2))*X)
C
      NLSF = Y
C
      RETURN
C
      END
C
```

APPENDIX 2

Non linear least squares subroutine for the solution of equation (6.9)

```
      DOUBLE PRECISION FUNCTION NLSF(X)
C
      COMMON/PKINET/P(6)
C
      DOUBLE PRECISION P,X,Y
C
      Y = P(1) + P(2)*X + P(3)*X*X
C
      NLSF = Y
C
      RETURN
C
      END
C
```

APPENDIX 3

Least squares data analysis program.

```
 10 REM
 20 REM*********************************************
 30 REM****LEAST SQUARES PROCEEDURE***
 40 REM****BY A.P.BILLINGTON*****************
 50 REM*********************************************
 60 REM
 70 REM SEE SHEPPERD:MATHEMATICS FOR
 80 REM CHEMISTS FOR APPROPRIATE
 90 REM VERSION
100 REM*********************************************
110 REM ACCESSING THE FILE
120 PRINT"WHAT IS THE NAME OF YOUR FILE?"
130 INPUT R$
140 PRINT
150 N=OPENIN R$
160 REM*********************************************
170 REM DEFINITION OF LOOP ZEROS
180 A=0
190 B=0
200 C=0
210 D=0
220 REM***FILE SEQUENCE LOOP*******
230 REM
240 FOR E=1 TO 220 STEP 1
250 INPUT#N,I
260 INPUT#N,XO
270 LET Y=LN(I)
280 LET X=78—1.097E6/XO
290 LET A—A+Y
300 LET B=B+X
310 LET XY=X*Y
320 LET C=C+XY
330 LET X2+X^2
340 LET D=X2+D
350 NEXT
360 CLOSE#N
370 REM**DONT FORGET******
380 REM D=SUM(X^2)
390 REM B=SUM(X)
400 REM C=SUM(X*Y)
410 REM A=SUM(Y)
420 LET X3=B^2
430 REM
440 CLS
450 PRINT
460 PRINT"*************************************"
470 PRINT
480 PRINT"RUN NAME is "R$
490 PRINT"————————————————————"
```

```
500 PRINT
510 PRINT"DATA FOR THE RUN"
520 PRINT
530 PRINT"///////RESULTS//////"
540 PRINT
550 REM
560 REM***********************************************
570 REM CALCULATION OF THE INTERCEPT
580 REM***********************************************
590 REM
600 LET IN=(A-(B*C/D))/(200-(B^2/D))
610 PRINT
620 PRINT"THE INTERCEPT Y(O)=";IN
630 REM**************************************
640 REM THE GRADIENT
650 PRINT
660 M= (C-B*IN)/D/2
670 PRINT"THE RATE CONST.=";M;"/CM"
680 REM
690 REM**************************************
700 REM THE CORRELATION COEFFICIENT
710 REM**************************************
720 REM
730 H=O
740 BB=O
750 LET YB=£/220
760 LET XD1=O
770 LET YD1=O
780 N=OPENIN R$
790 LET XB=B/220
800 FOR G=1 TO 220 STEP 1
810 INPUT#N,I
820 INPUT#N,XO
830 LET Y=LN(I)
840 LET X=78-1.097E6/XO
850 LET XD=(X-XB)
860 LET XD2=(XB-X)^2
870 LET XD1=XD1+XD2
880 LET YD=(Y-YB)
890 LET YD2=(YB-Y)^2
900 LET XC=XD*YD
910 LET BB=BB+XC
920 LET YD1=YD1+YD2
930
940 NEXT
950 CLOSE#N
960 LET SY=(YD1/220)^0.5
970 LET SX=(XD1/220)^0.5
980 LET SXY=1/SY*SX)
990 PRINT
1000 LT CORR=BB/220*SXY
1010 PRINT"///////THE ERRORS//////////"
```

```
1020 PRINT
1030 PRINT
1040 PRINT "CORRELATION COEFFICIENT=";CORR
1050 REM**************************************
1060 REM CALCULATION OF THE ERRORS
1070 REM**************************************
1080 REM
1090 REM NORMAL DISTRIBUTION ERRORS
1100 REM GRADIENT ERRORS
1110 REM
1120 2 SIGMA CALCULATION
1130 REM
1140 REM ERROR=1/218*(Y-C-M*X)
1150 REM
1160 N=OPENIN R$
1170 K=0
1180 FOR J=1 TO 220 STEP 1
1190 INPUT#N,I
1200 INPUT#N,X0
1210 LET Y=LN(I)
1220 LET X=78-1.097E6/X0
1230 LET YN=(Y-IN-M*X*2)^2
1240 LET K=K+YN
1250 NEXT
1260 CLOSE#N
1270 LET XCOR=(220*K/(220*D-B^2))^0.5/M/2*-100
1280 PRINT
1290 PRINT"ERROR OF THE LINE=";XCOR;"%"
1300 PRINT
1310 REM****STANDARD ERRROR OF Y(0)***
1320 LET YU=((B^2/(220*D-B^2)+1/220)*K)^0.5
1330 PRINT"ERROR OF THE INTERCEPT=";YU
1340 PRINT
1350 PRINT"*****************************"
1355 *GDUMP 1 2 0 1
1360 FOR ERT=0 TO 10000
1370 NEXT
1380 FOR GH=0 TO 30
1390 FOR IO=0 TO 60
1400 NEXT
1410 PRINT
1420 NEXT
```

```
1430 REM************************************
1440 REM****THE GRAPHICS SECTION****
1450 REM************************************
1460 REM
1470 REM SEE THE B.B.C. HANDBOOK
1480 REM @%=10
1490 ZX=2
1500 TYU=0
1510 MODE4
1520 REM****DRAWING THE GRAPH*******
1530 CLS
1540 MOVE 80,120
1550 DRAW 80,900
1560 LT ZX2=1/IN
1570 PRINT TAB(2,4);"REL.DECAY(1-LN(I/IN))      SLOPE ";ZX
1580 MOVE 80,120
1590 DRAW 1500,120
1600 PRINT TAB(4,6);R$
1610 LETC=30
1620 FOR X=0 TO 30 STEP 2
1630 3=1-((X/10-0.80)/2)
1640 LET C7=C/2
1650 IF X3>0.050 AND X3<1.10 THEN PRINT TAB(0,X);X3
1660 LET C=C-2*1/ZX
1670 NEXT
1680 LET C2=0
1690 FOR X=0 TO 12
1700 NEXT
1710 PRINT TAB(G2,30);C2
1720 LET C2=C2+4
1730 NEXT X
1740 PRINT TAB (32,28);"DIST/CM"
1750 N=OPENIN R$
1760 REM
1770 REM**********************************
1780 REM**SETTING THE SCALES UP****
1790 REM**********************************
1800 REM
1810 LET AJ=EXP(IN)
1820 FOR Q=1 TO 229 STEP 1
1830 INPUT#N,I
1840 INPUT#,X
1850 LET Y2=700*(1+(LN(I/AJ)*ZX))+120
1860 IF 0.1>Y2 THEN GOTO 1900
1870 NEXT
1880 CLOSE#N
1890 GOTO 1940
1900 CLOSE#N
1910 TYU=TYU+1
```

```
1920 ZX=2—TYU*0.200
1930 GOTO 1530
1940 =OPENIN R$
1950 REM****PLOTTING THE VALUES*******
1960 FOR 0=1 TO 220 STEP1
1970 INPUT#N,I
1980 INPUT#N,X
1990 LET I2=650*(1+(LN(I/AJ)*ZX))+120
2000 LET X2=(78—1.097E6/X)*24+80
2010 PLOT 70,X2,I2
2020 NEXT
2030 CLOSE#N
2040 REM
2050 REM*****************************
2060 REM**FITTING THE SLOPE**********
2070 REM*****************************
2080 REM
2090 MOVE 80,770
2100 LET DF=650*(1+2*M*ZX*40)+120
2110 DRAW 1040,DF
2120 LET DF2=700*(1+YU/IN)
2130 LET DF3=700*(1—YU/IN)
2140 MOVE 80,DF2+120
2150 LET DF4=(DF2*(1+2*M*ZX*40)
2160 PRINT
2170 @%=&2030C
2180 PRINT"RATE CONST*100=";—M*100;"/CM"
2190 PRINT"ERROR OF LINE=";XCOR;"%"
2200 *GDUMP 1 2 1 0
2210 GOTO 10
2220 PRINTXB
```

APPENDIX 4

```
 10 CLS
 20 REM SHIN PROGRAMME
 30 PRINT
 40 PRINT"**********************************"
 50 PRINT
 60 REM CALCULATION OF SHIN–MAIER
 70 REM PROBABILITIES FOR
 80 REM THE DELTA RELAXATION
 90 W=O
100 PRINT"PROGRAMME TO CALCULATE THE"
110 PRINT"SHIN-MAIER RELAXATION RATE"
120 PRINT"OF SINGLET DELTA"
130 PRINT
140 PRINT"**********************************"
150 PRINT
160 PRINT
170 PRINT"LOWER TEMPERATURE IN RANGE?(K)"
180 INPUT T1
190 PRINT
200 PRINT"UPPER TEMPERATURE IN RANGE?(K)"
210 PRINT
220 INPUT T2
230 DIM E(6)
240 DIM V(6)
250 PRINT
260 PRINT"HOW MANY SIMULTANEOUS TRANSITIONS"
270 PRINT"ARE TO BE CONSIDERED?"
280 INPUT X
290 PRINT
300 FOR Y=1 TO X
310 PRINT"GIVE THE ENERGY GAP/eV  "
320 PRINT"AND THEN SUPPLY THE "
330 PRINT"FREQUENCY FACTORS"
340 INPUT E(Y)
350 INPUT V(Y)
360 NEXT
370 PRINT
380 PRINT
390 PRINT
400 PRINT"TEMPERATURE IS PRINTED AND"
410 PRINT"THEN THE RELEVANT PROBABILITIES"
420 FOR T=T1 TO T2 STEP 10
430 PRINT
```

APPENDIX 4 *(Continued)*

```
440 PRINTT
450 FOR Y=1 TO X
460 LET A=58.901/T
470 LET B=5.7968E3*E(Y)/T
480 LET C=-5.7825E2*(E(Y))^(2/3)/T^0.3333
490 LET D=1.845E2*E(Y)^(0.3333)/T^0.6666
500 F=A+B+C+D
510 LET G=EXP(F)
520 LET H=1.340E5*E(Y)^2.3333/T^0.16666   *V(Y)
530 LET I=H*G
540 PRINT I
550 NEXT
570 NEXT
```

APPENDIX 5

The Effect of the Slitwidth on the Dimol Emission

The effect of an alteration in the band profile for the dimol emission under fixed slit conditions is considered. The model adopted for the emission profile is Gaussian, and the definative F.W.H.M. has been measured in section 11.5 .

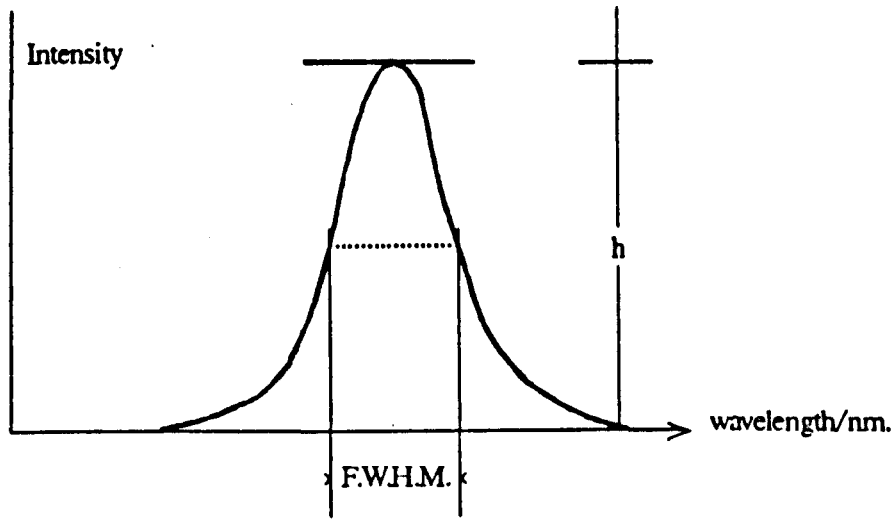

Let the F.W.H.M. [107] be equal to f,

The total emission E^{tot}, is given by:

$$E^{tot} = \int_{-\infty}^{+\infty} h\exp -(y^2/f^2)\ dy \qquad = hf\sqrt{\pi} \tag{A1}$$

With a uniform transmission, t, under the experimental conditions:

$$E^{tot} = thf\sqrt{\pi} \qquad (A2)$$

Now let us consider a slit function, working in conjunction with the emission profile:

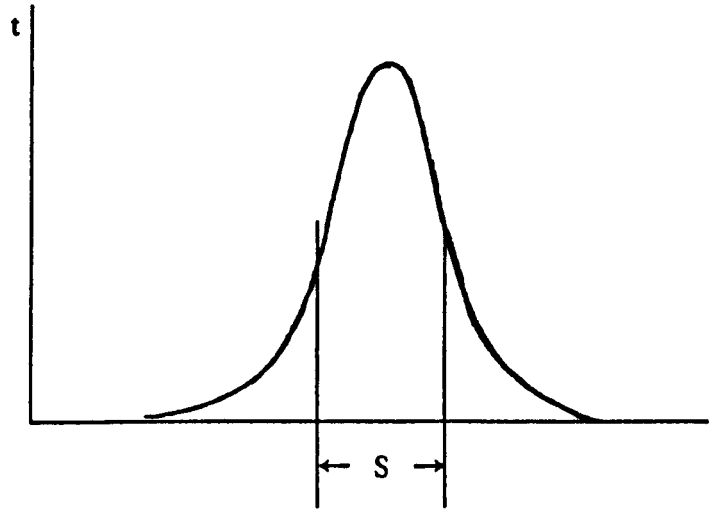

t = transmission
s = slit width

E_{obs} must now become a function of both the emission and the slit, so equation (A1) becomes:

$$E_{obs} = \int_{-\infty}^{+\infty} h\exp -(y^2/f^2)\, t\exp -(y^2/s^2)dy \qquad (A3)$$

$$E_{obs} = \int_{-\infty}^{+\infty} ht\exp -(y^2(1/f^2+1/s^2))dy \qquad (A4)$$

$$= \sqrt{\pi}ht/(1/f^2+1/s^2)^{1/2}$$

$$E_{obs} = \frac{\sqrt{\pi}\,hfts}{(s^2+f^2)^{1/2}} \qquad (A5)$$

Condition variation:

(a) If s is very large, $s \longrightarrow \infty$; $(s^2+f^2)^{1/2} \longrightarrow s$

$E_{obs} = \sqrt{\pi}$ hft, as before.

(b) If f is very large, $f \longrightarrow \infty$; $(s^2 + f^2)^{1/2} \longrightarrow f$

$= \sqrt{\pi} hts$

Using equations (A2) and (A5):

$$\frac{E}{E_{tot}} = \frac{S}{(S^2 + f^2)^{1/2}} \qquad \text{(A6)}$$

APPENDIX 6

```
10REM
20 REM NUMERICAL INTEGRATION OF THE
30 REM VAN KRANENDONK CONFIGURATION
40 REM
50 PRINT"LOWEST TEMP. ?"
60 INPUTT1
70 PRINT"HIGHEST TEMP. ?"
80 INPUTT2
90 PRINT"RANGE PARAMETER ?"
100 INPUTR
110 CLS
120 PRINT
130 PRINT
140 PRINT"THE CONFIGUATIONS ARE"
150 PRINT
160 FOR T=T1 TO T2 STEP 20
170 LET M=0
180 FOR D=0.5 TO 1.79 STEP 0.01
190 LET F=0
200 FORX=D TO (D+0.01) STEP 0.01
210 LET A=EXP(427/T*(X^-12-X^-6))
220 LET B=EXP-(2*(X-1)*4.35/X*0.6/R)
230 LET E=A*B*X^ 2
240 LET F=F+E
250 NEXT
260 LET M=M+F
270 NEXT
280 LET M=M*PI*0.02
290 PRINT"INT ";M ;"AT TEMP. T=";T
300 PRINT
310 NEXT
```

APPENDIX SEVEN

Shock parameters for the work in Chapter 6

Run name	Pre shock decay 10^{-3} x cm^{-1}	Post shock decay 10^{-3} x cm^{-1}	Integration time μ sec.
39B	5.3	6.1	8
39A	6.3	4.3	8
36B	9	12.6	8
34B	12	11.3	8
28B	—	7.17	8
26B	—	12.6	16.9
25B	—	11.1	12.1
23B	8.8	10.1	10.0
22B	8.2	10.3	13.9
19B	14.4	9.98	8
18B	8.1	8.03	8
17B	11.6	12.0	10
15B	10	12.4	13.1
14B	10	16.0	10
13B	—	13.6	12.9
12B	—	11.4	10.9
11B	—	16.4	15.9
9B	—	13.3	8
71B	6.5	5.8	13.2
72B	3.4	4.6	12
65B	6.7	5.0	14.7
63B	6.8	6.25	16.3
43B	8.1	4.18	10.0
44B	8.7	5.23	13.6
53B	7.7	6.3	13.0
54B	8.1	6.9	13.6
55B	8.5	7.13	11.3
60B	7.87	6.67	12.5

APPENDIX SEVEN *(Continued)*

Run name	Pre shock decay $10^{-3} \times cm^{-1}$	Post shock decay $10^{-3} \times cm^{-1}$	Integration time μ sec.
61B	8.3	6.2	10
62B	6.5	6.1	17
47B	5.3	5.4	14
49B	8.0	7.6	14.4
57B	7.1	6.0	14.8
58B	7.4	4.7	16
59B	7.6	4.7	13
66B	7.1	7.0	10
68B	8.2	6.8	12.9
69B	7.1	5.0	13.2
70B	8.0	6.5	14.1
80B	7.5	7.0	12
79B	7.5	7.0	12
78B	7.7	5.83	18
77B	6.6	3.1	8.6
76B	7.43	5.6	15
75B	7.9	5.8	14
48B	5.64	5.16	11.9
7B	—	20	10
6B	16.1	16.1	13
5B	—	13.5	10
4B	—	9.1	9.7

APPENDIX SEVEN *(Continued)*

Run name	Pre shock decay $10^{-3} \times cm^{-1}$	Post shock decay $10^{-3} \times cm^{-1}$	Integration time μsec^{-1}
38A	10	12.4	25
37A	6.9	5.1	4.1
36A	12.1	12.4	25
34A	10	8.13	8
32A	9	7.1	8
28A	5.2	5	10
27A	8.3	6.5	10
26A	6.4	8.4	10
25A	7.0	5.0	8
23A	6.9	5.45	8
22A	10.0	9.0	8
20A	11.5	8.0	8
29A	—	10	10
18A	13.8	11.6	25
17A	13.6	10	8
16A	8	8.5	10
15A	11.5	10.3	10
14A	7.0	10.8	10
13A	9.0	11.3	15.8
12A	7.3	6.23	11.5
11A	8.0	9.9	10
8A	10.4	11.0	8

APPENDIX SEVEN *(Continued)*

Run name	Pre shock	Post shock	Integration time μ sec.
80A	8.7	8.6	14.3
79A	7.5	7.3	7.3
78A	7.7	7.0	17
77A	6.6	6.5	4.1
76A	7.4	7.8	21
75A	7.9	7.0	10
74A	6.2	6.3	5.1
73A	7.0	7.4	6.9
71A	6.5	6.3	11.5
75A	7.5	6.0	17
65A	6.7	6.7	11
64A	7.1	7.5	14
63A	6.8	8.0	11
43A	7.4	5.0	10
44A	6.0	4.3	8
53A	7.7	5.9	7
54A	8.1	8.3	11
55A	8.5	7.7	14
60A	7.8	6.2	6.4
61A	8.3	8.2	15
62A	6.5	6.4	12
47A	5.3	4.6	10

APPENDIX SEVEN *(Continued)*

Run name	Pre shock	Post shock	Integration time μ sec.
49A	8.0	8.34	14.3
57A	7.1	7.7	8.9
58A	7.4	6.1	16.1
59A	7.6	4.4	8.1
66A	7.1	5.9	23
68A	8.2	7.2	8.9
70A	8.0	8.0	10

Appendix 8

Shock parameters for the work in Chapter Seven.

Run name	Pre Shock glow mV	Shock speed Km s^{-1}	p_{21}
122A	233	1.465	5.00
113B	436	0.780	3.00
113A	180	0.780	3.00
118A	263	0.9510	3.58
119A	182	0.93	3.59
114B	131	0.772	2.97
115A	200	0.79	3.06
115B	514	0.79	3.06
114A	318	0.772	2.97
121A	214	1.12	4.00
116B	67	0.73	2.81
129A	592	1.54	5.11
116A	27	0.73	2.81
124A	177	1.54	5.10
117B	135	0.757	2.91
117A	56	0.757	2.91
111A	83	0.76	2.93
111B	200	0.76	2.93
112B	147	0.74	2.86
112A	61	0.74	2.86
120A	189	0.98	3.69
123A	323	1.53	5.15
126A	296	1.63	5.33
104A	74	1.01	3.78
105A	202	1.06	3.91
100A	149	0.93	3.52
107A	359	1.537	5.14
106A	142	1.08	3.94
102A	325	0.922	3.49
109A	396	0.968	3.63
122B	277	1.46	5.00

Appendix 8 *(Continued)*

Run name	Pre Shock glow mV	Shock speed Km s^{-1}	p_{21}
108B	237	1.47	5.02
93B	475	1.15	4.12
125B	592	1.52	5.12
96B	410	1.468	5.01
101B	90	0.929	3.52
94B	163	1.42	4.92
93A	224	1.15	4.12
120B	75	0.93	3.52
123B	300	1.53	5.15
119B	269	0.93	3.5
104B	174	1.01	3.78
95A	268	1.16	4.15
91A	183	0.99	3.72
91B	391	0.99	3.72
109B	337	0.968	3.63
105B	312	1.06	3.91
87B	208	0.980	3.67
95B	410	1.468	5.01
96A	149	1.468	5.01
106B	213	1.08	3.94
107B	314	1.537	5.14
88B	257	0.88	3.38
103B	198	1.47	5.03